Current kinematics in the Northern Andes by GPS

Paúl Jarrín Tamayo

Sorbonne Université

ED 398 - Géosciences, ressources naturelles et environnement

Istep / Équipe Dynamique et évolution des Marges et des Orogènes

Cinématique actuelle dans les Andes du Nord par GPS

Par Paul Alberto Jarrin Tamayo

Thèse de doctorat de Géophysique

Dirigée par Frédérique Rolandone et Jean-Mathieu Nocquet

Présentée et soutenue publiquement le 08/12/2021

Devant un jury composé de:

M. VIGNY Christophe	Directeur de Recherche	ENS Paris	Rapporteur
M. JOUANNE François	Professeur	ISTerre	Rapporteur
Mme. D'ACREMONT Elia	Professeure	ISTeP	Examinatrice
Mme. SAILLARD Marianne	Chargée de recherche	Géoazur	Examinatrice
Mme. ALVARADO Alexandra	Professeure	EPN-Equateur	Examinatrice
Mme. ROLANDONE Frédérique	Maître de Conférences	ISTeP	Directrice de Thèse
M. NOCQUET Jean-Mathieu	Directeur de Recherche	Géoazur	Co-directeur de Thèse

À David et Alicia
À mes Parents
À ma sœur Helen

Remerciements

Je tiens tout d'abord à remercier fortement ma directrice et mon co-directeur de thèse, Frédérique Rolandone et Jean-Mathieu Nocquet. Ce fut un grand plaisir pour moi de travailler sous votre supervision. Je vous remercie également pour votre patience, votre générosité, la confiance que vous m'avez accordée, vos encouragements et pour les conseils transmis tout au long de la thèse et en général tout au long de ces 13 dernières années où j'ai eu l'opportunité d'interagir avec vous. Ceci est, et a été, très enrichissant et gratifiant pour moi.

Je remercie les membres du jury, les examinatrices, Marianne Saillard, Alexandra Alvarado, Elia D'Acremont, et les rapporteurs, Christophe Vigny et François Jouanne, d'avoir accepté de lire mon manuscrit et d'évaluer mon travail.

Mes remerciements vont aussi à la Senescyt et au gouvernement d'Equateur pour la bourse de thèse que j'ai obtenue, bien qu'il y ait eu de nombreuses difficultés administratives et financières, cette bourse de thèse m'a permis de réaliser ce travail de recherche.

Je voudrais remercier l'Institut de Recherche pour le Développement (IRD) et l'Agence Nationale de la Recherche dans le cadre du project IRD/ANR-S5 pour le soutien pendant la crise sanitaire du Covid.

Des remerciements spéciaux à Yvonne Font, Marc Regnier, Xavier Martin, Aurore Laurendeau, Elsa Rainbon et son mari Willy pour leur amitié et leur aide pour résoudre les problèmes logistiques depuis mon arrivée et l'arrivée de ma famille en France. Mes remerciements vont aussi à Caroline Ramel, Laure Schenini, Philippe Charvis, Francoise Courboules, et tous mes autres collègues qui m'ont aidé pour mon installation, merci beaucoup à vous tous.

J'adresse aussi mes remerciement à Caroline Ramel et à toute l'équipe informatique pour leur soutien face aux problèmes informatiques. À Jelena Giannetti pour l'accès au matériel bibliographique. À Jenny Trevisan pour l'accueil dans le laboratoire. À Valerie, Sandrine, Magali, Emilie, et à toute l'équipe administrative et à l'équipe de direction du

laboratoire Géoazur. À l'équipe Séismes de Géoazur et à l'équipe Dynamique et Evolution des Marges et des Orogènes de l'ISTeP.

Je remercie également Loïc Labrousse, Sylvie Leroy, Dovy Tristani, Laurence Pastor, et toute l'équipe de l'ISTeP et de l'ED 398.

Merci à tous les collègues, doctorants et "María Jose y los come piedras" avec lesquels on a partagé ces dernières années de très bons souvenirs. À Hector Mora pour sa générosité et son support pendant la thèse. Aux collègues de l'équipe de sismologie de l'IG pour leur générosité et leur amitié. À David Cisneros, Juan Carlos Villegas ainsi que l'Institut de Géophysique d'Équateur pour l'accès aux données GPS.

Finalement, je voudrais remercier énormément Alicia, ma femme, pour sa générosité, sa confiance, son amour, qui a tout laissé derrière elle pour venir avec moi en France, pour son soutien inconditionnel pendant ces années. À mon fils David qui est la lumière de ma vie et qui a affronté avec courage tous ces changements de vie. À ma sœur Helen pour son aide avec toutes les lourdes démarches administratives de la bourse en Equateur et son soutien familial pendant ces années.

Résumé

La région des Andes du Nord est un domaine continental situé à l'extrême nord-ouest de la plaque sud-américaine. Cette region, longue de ∼2200 km et large de 300 à 1000 km, est un laboratoire naturel pour l'étude du partitionement de la déformation, du cycle simique, et de la collision des domaines continentaux. La convergence rapide et oblique de la plaque Nazca sous l'Amérique du sud induit (1) une déformation élastique associée au blocage partiel de l'interface de subduction le long de la marge équatoriano-colombienne et (2) une contrainte de cisaillement à long-terme, qui se traduit par un mouvement de translation du Sliver Nord Andin (NAS) vers le nord-est par rapport à la plaque Sud-Amérique. De plus, la convergence du NAS produit également une diversité de la sismicité interplaque et intraplaque, observée depuis la fin du 19ème siècle. Par ailleurs, la collision vers l'est du bloc Panama et la subduction de la plaque Caraïbe induisent des déformations qui dominent la cinématique dans la partie nord du NAS. Les techniques de géodésie spatiale, en particulier les mesures par GPS/GNSS, permettent de quantifier les mouvements à la surface terrestre avec une précision millimétrique. L'intégration de ces mesures avec des modèles élastiques nous permet d'apporter des informations sur la cinématique et sur le niveau de couplage inter-sismique le long de l'interface de subduction. Cette thèse est consacrée à l'étude de la phase inter-sismique du cycle sismique avec un intérêt particulier pour la déformation continentale autour et au sein du NAS. L'objectif est d'affiner la cinématique de la plaque Nazca et du Sliver Nord Andin. Pour cela, les mesures GPS acquises par divers instituts de recherche et la collaboration Franco-équatorien (projets ADN et S5, Laboratoire Mixte International SVAN), entre 1994.0 et 2019.9 sont utilisées pour dériver un nouveau champ de vitesse horizontale à l'échelle continentale. L'analyse et la modélisation de ce champ de vitesse sont centrées sur deux axes principaux qui conduisent à la construction du premier modèle cinématique de blocs élastiques pour le NAS et les régions voisines. Ce modèle résout simultanément les rotations rigides des blocs et la distribution de couplage inter-sismique sur les interfaces de subduction, fournissant des taux de glissement des failles crustales cohérents avec la cinématique dérivée.

En ce qui concerne la plaque océanique Nazca, nous proposons un nouveau pôle d'Euler qui décrit son mouvement actuel par rapport à l'Amérique du sud. Ce pôle a été estimé à partir de 5 sites GPS continus qui couvrent la quasi-totalité de la plaque. Notre analyse montre que les données sont compatibles avec la cinématique d'une seule plaque rigide (wrms = 0.6 mm/an). Notre pôle prédit un taux de convergence maximal de 65.5 ± 0.8 mm/an à la latitude ∼30°S le long de la fosse chilienne, qui diminue à 50.8 ± 0.7 mm/an au nord de la Colombie, et à 64.5 ± 0.9 mm/an au sud du Chili. Cette étude révèle aussi que la composante est de la vitesse à l'île de Robinson Crusoé (latitude ∼33.6°S) est ∼4 à 5 mm/an plus rapide que le mouvement général de la plaque, en raison de la

relaxation visco-élastique à la suite du séisme de Maule au Chili de magnitude Mw 8.8 en 2010.

Le modèle cinématique obtenu pour les Andes du Nord confirme que les mouvements relatifs entre les plaques Nazca/SOAM et Caraïbes/SOAM ne sont pas accommodés sur le continent par un seul système de failles. Nous mettons en évidence une déformation interne de 2-4 mm/an, localisée sur des failles secondaires actives (les systèmes de failles Oca-Ancon, Santa Martha-Bucarmanga, Romeral et Latacunga-Quito-El Angel). Ces failles limitent des blocs tectoniques et définissent la rotation de 6 blocs. La limite orientale du NAS est définie par un système transpressif latéral dextre qui accommode 5 à 17 mm/an. Notre modèle quantifie l'ordre de grandeur des mouvements accommodés par la collision du bloc Panama avec le NAS sur des structures que nous proposons comme nouvelles limites de ces deux domaines continentaux à 6 mm/an (la faille de Uramita) et 15 mm/an (la East Panama Deformed Zone). On note également que $\sim$1 cm/an de mouvement du bloc Panama est transféré vers l'intérieur de la Colombie et rapidement accommodé sur une distance de $\sim$100km vers le nord, à la latitude 6°N, sur le système de plis de San Jacinto (San Jacinto fold belt). À l'extérieur du NAS, le domaine Subandin accommode un raccourcissement crustal de 2-4 mm/an à travers la ceinture de chevauchements (Eastern Subandean Belt) le long de l'Equateur et au nord du Pérou. Cette déformation pénètre à l'intérieur de plaque Sud-Américaine en Amazonie parfois sur plusieurs centaines de kilomètres.

Notre modèle confirme l'existence d'une subduction oblique et lente de la plaque Caraïbe sous le NAS le long de la marge nord Colombienne. Cette convergence est accommodée partiellement sur l'interface de subduction (3 mm/an) sans couplage inter-sismique significatif, mais elle est aussi accommodée par des structures actives (failles et plis) à l'intérieur du continent. Notre modèle confirme également que la subduction de la plaque Nazca sous le NAS induit un couplage spatiallement hétérogène, limité à 30-40 km de profondeur dans le nord de l'Équateur, $\sim$20km dans la partie centrale de l'Equateur et nul au sud de la latitude $\sim$2.5°S et au nord de la latitude $\sim$5°N. Notre modèle montre une bonne corrélation du couplage fort avec les grandes ruptures sismiques passées. Il montre aussi une corrélation entre couplage faible ou partiel avec des zones de transition où l'on observe la présence d'épisodes de glissements asismiques transitoires récurrents. Dans l'ensemble, le travail presenté dans cette thèse fournit des résultats importants qui contribuent à une meilleure compréhension des processus de déformation long-terme et de la tectonique active crustale dans les Andes du Nord. Ces résultats fournissent également une image de haute qualité de la déformation inter-sismique, un ingrédient essentiel pour les futures évaluations du risque sismique à l'échelle régionale.

Abstract

The Northern Andes is a continental domain located at the northwestern edge of the South American Plate. This ∼2200 km long and 300 to 1000 km wide region defines a natural laboratory for various studies of divers processes, including deformation partitioning, inter-seismic coupling, and continental collision. The oblique and fast convergence of the Nazca plate beneath South America induces (1) elastic deformation induced by spatially variable locking at the subduction interface along the Equatorian-Colombian margin and (2) long-term shear stress, which results in a translation-like motion of the North Andean Sliver (NAS) towards northeast with respect to the South American plate. Furthermore, Nazca plate convergence also produces a diversity of interplate and intraplate seismicity, which has been observed since the 19th century. In the northwestern Andes, eastward collision of the Panama block against the NAS and the Caribbean subduction induce deformation that dominates the kinematics at the northern part of the NAS. Spatial geodesy techniques, in particular GPS/GNSS measurements, make it possible to quantify movements on the earth's surface with millimeter accuracy. The integration of these measurements with elastic models allows us to provide information about the kinematics and the inter-seismic coupling distribution at the subduction interface. This thesis focuses on studying the inter-seismic phase of the seismic cycle with a particular interest in the continental deformation along and within the NAS. The aim is to improve the kinematic models for the Nazca plate and the North Andean Sliver. For that, GPS measurements collected by several research institutes and the Franco-Ecuadorian collaboration (ADN & S5 projects, SVAN International Joint Laboratory), between 1994.0 and 2019.9 are used to derive a new and more refined horizontal velocity field at the continental scale. The analysis and modeling of this velocity field is centered on two main axes allowing to build the first kinematic elastic block model for the NAS and neighboring regions. This model simultaneously solves for rigid block rotations and spatially variable coupling at the subduction interfaces, providing crustal fault slip rates consistent with the derived kinematics.

First, we propose a new Euler pole that describes the current motion of the Nazca plate with respect to South America. This pole is estimated from continuous measurements at 5 GPS sites, spatially sampling the entire plate. Our results show that GPS data are compatible with the kinematics of a single rigid plate (wrms = 0.6 mm/yr). Our pole predicts a maximum convergence rate at 65.5 ± 0.8 mm/yr at latitude ∼30°S along the Chile trench, decreasing to 50.8 ± 0.7 mm/yr in northern Colombia, and 64.5 ± 0.9 mm/yr in southern Chile. A second-order result for the Nazca plate is that the velocity east component of Robinson Crusoe Island (latitude ∼33.6°S) is ∼4-5 mm/yr faster than the overall motion of the plate, which is induced by the visco-elastic relaxation following the

Maule Mw 8.8 2010 earthquake in Chili.

Secondly, our kinematic model for the northern Andes confirms that the Nazca/SOAM and Caribbean/SOAM relative motions are not accommodated inland by a single fault system. We find internal deformation at 2-4 mm/yr accommodated on active secondary faults (the Oca-Ancon, Santa Martha-Bucaramanga, Romeral, and Latacunga-Quito-El Angel faults). These faults bound tectonic blocks and define the rotation of 6 blocks. The NAS eastern boundary is found to be a right-lateral transpressive system accommodating 5 to 17 mm/yr of motion. Our model also quantifies the motion accommodated by the Panama block with respect to the NAS on active structures that we propose as new boundaries for these two continental domains. Relative motions take place at 6 mm/yr along the Uramita fault and 15 mm/yr in the Eastern Panama Deformed Zone. We also note that $\sim$1 cm/yr of the Panama motion is transferred inside northwestern Colombia and is accommodated over a distance as far as $\sim$100km towards the north (at latitude 6°N) across the San Jacinto fold belt. Outside the NAS, the Subandean domain accommodates crustal shortening at 2-4 mm/yr across the Eastern Subandean Belt along Ecuador and northern Peru, which induces deformation by tens of kilometers penetrating the Amazonia basin.

Our model confirms the existence of oblique and slow subduction of the Caribbean plate below the NAS along the northern Colombian margin. This convergence is partially accommodated along the subduction interface (3 mm/yr) without significant inter-seismic coupling. It is also accommodated on faults and folds inside the continent. Our model also confirms that the subduction of the Nazca plate beneath the NAS induces heterogeneous spatial coupling, with high coupling restricted to 30-40 km depth in northern Ecuador, $\sim$20km in central Ecuador and null coupling south of latitude $\sim$2.5°S and north of latitude $\sim$ 5°N. This coupling shows first-order correlations. High coupling patches are located at the rupture area of large historical and recent earthquakes. Weak or partial coupling within transition zones correlates with the location of recurrent transient aseismic episodes (Slow Slip Events). Overall, the work presented in this thesis provides important results that contribute to a better understanding of the long-term deformation process and active crustal tectonics along the Northern Andes. The obtained velocity field and model provide a high-quality image of the inter-seismic deformation, an essential input for future seismic hazard studies at the regional scale.

Contents

CHAPTER 1

Introduction

1.1 Contexte scientifique des Andes du Nord et de la thèse

Les Andes du Nord, on parlera dans cette thèse du bloc Nord Andin (ou Sliver Nord Andin, NAS), sont localisées à l'extrémité nord-ouest de la plaque continentale Sud-Amérique depuis le Golfe de Guayaquil en Equateur jusqu'en Colombie et à l'ouest du Vénézuela. Cette zone est le siège de déformations actives et complexes dues (1) à la subduction oblique de la plaque océanique Nazca sous la plaque Sud-Amérique, (2) aux interactions de la plaque Sud-Amérique avec la cinématique de la plaque Caraïbe, (3) à la collision avec le bloc du Panama au nord-ouest de la Colombie (Figure 1.1). La zone de subduction Equateur-Colombie a connu l'une des plus grandes séquences sismiques jamais documentées. Tous les séismes de cette séquence ont eu lieu à l'interface de subduction entre la plaque Nazca et le Sliver Nord Andin. Cette séquence a débuté avec un séisme de magnitude Mw 8.5-8.8 qui a rompu un segment de plus de ∼500 km de la zone de subduction (Abe 1979, Kanamori and McNally 1982, Ye et al. 2016). Durant les décennies suivantes, le même segment a de nouveau rompu lors de trois séismes de magnitude Mw 7.7 à 8.2 en 1942, 1958 and 1979 (Figure 1.1). En avril 2016, un séisme de magnitude Mw 7.8 a étendu la séquence et soulevé des questions en terme de budget du cycle sismique de la zone de subduction car la zone de rupture du séisme de 2016 coïncide en grande partie avec celle du séisme de 1942 (He et al. 2017, Nocquet et al. 2016, Ye et al. 2016), (Figure 1.1).

La déformation mesurée par GPS à la surface dans les Andes du Nord provient de la contribution de deux processus distincts : (1) la déformation élastique associée au blocage partiel de l'interface de subduction le long de la marge équatoriano-colombienne, et (2) la cinématique du bloc nord-andin par rapport à la plaque Sud-Amérique. J'ai travaillé sur

ces deux thématiques lors de ma thèse.

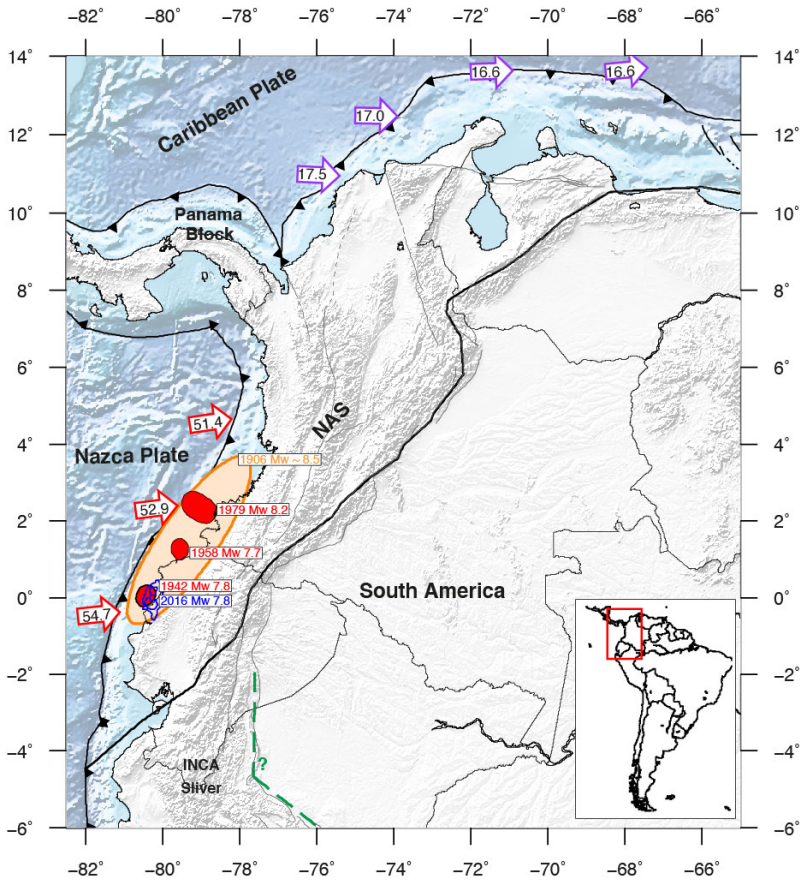

FIGURE 1.1 – Configuration tectonique du Sliver Nord Andin. Les flèches rouges indiquent la vitesse de convergence Nazca/Sud-Amérique prédite par Kendrick et al. (2003). Les flèches violettes indique la vitesse de la plaque Caraïbe par rapport à la plaque Sud-Amérique prédite par Symithe et al. (2015). Les ellipses indiquent la région de glissement élevé des sources sismiques de 1942, 1958, et 1979. (Beck and Ruff 1984, Sewnson and Beck 1996). La courbe bleue est la zone de rupture cosismique du séisme de 2016 selon Nocquet et al. (2016). L'ellipse orange est la zone de rupture proposée pour le séisme de 1906 (Kanamori and McNally 1982). Les lignes en noir indiquent la limite du sliver nord-andin et en tirets vert la limite est du sliver Inca proposée par Nocquet et al. (2014).

La géodésie spatiale, et en particulier le Global Positioning System (GPS), permet de quantifier les mouvements de la surface terrestre et apporte des informations essentielles pour modéliser les processus responsables de la déformation crustale. En Equateur, les premières campagnes de mesures GPS réalisées en 1994 et 1996 (Trenkamp et al. 2002, White et al. 2003) ont permis de contraindre au premier ordre l'accumulation des contraintes le long de l'interface de subduction. Puis, dans le cadre de la collaboration franco-équatorienne, un réseau GPS permanent a été développé en Equateur depuis 2007. Travaillant à l'Institut de Géophysique (IG-EPN) depuis 2008, j'ai participé à la mise en place du réseau géodésique GNSS permanent (Mothes et al. 2013). La première station GPS permanente pour l'étude de la subduction a été installée en

2007 à Esmeraldas. Le réseau GNSS permanent comprend aujourd'hui 76 stations permanentes. Dans mon travail de thèse, j'ai également utilisé les données GPS provenant de différents instituts sur la plaque Sud-Amérique et les plaques voisines (Figure 2.1), ainsi que des mesures de campagnes réalisées dans le cadre de la collaboration entre l'IRD et l'IG-EPN. Le jeu de données final analysé dans cette thèse comprend 330 stations GPS. Le détail des stations utilisées est donné dans le chapitre 2 et la figure 2.1.

Je travaille sur le traitement des données GPS depuis 2009, une période où j'ai également participé activement au développement du centre de traitement des données GPS à l'institut de Géophysique en Equateur. En tant que responsable du réseau GPS et du centre de traitement des données, j'ai eu l'expérience de travailler et d'étudier avec des chercheurs de laboratoires français pendant 10 années. Cela m'a permis d'apprendre, de comprendre non seulement la partie instrumentale des réseaux d'observation, mais aussi d'analyser, de discuter et de réfléchir sur les premiers résultats sur le fonctionnement du cycle sismique en Equateur. En ce qui concerne le traitement de données GPS, j'utilise les logiciels développés au MIT GAMIT/GLOBK (Herring et al. 2015; 2018), ainsi que PYACS un outil pour l'analyse des données géodésiques développé par Jean-Mathieu Nocquet (Nocquet 2017). Je détaillerai le traitement et l'analyse des données GPS dans le chapitre 2 de cette thèse.

Les résultats, avec des mesures GPS réalisées entre 2008 et 2012 en Equateur et au Pérou, ont permis de déterminer le premier ordre du fonctionnement de la subduction et de la déformation continentale à l'échelle des Andes du Nord (Nocquet et al. 2014). En ce qui concerne la déformation crustale à terre, les résultats GPS (Figure 1.2) identifient deux domaines continentaux (les slivers Nord-Andin et Inca) comprenant la Cordillère Andine et sa marge occidentale qui divergent autour du Golfe de Guayaquil. Ces domaines sont larges de plusieurs centaines de km et long de 2000 km, depuis l'Equateur jusqu'au Venezuela pour le sliver Nord-Andin et de l'Equateur à l'Altiplano bolivien pour le sliver Inca. Leurs mouvements accommodent l'obliquité de la subduction, structurent la déformation actuelle des Andes et contrôlent au premier ordre l'aléa sismique à terre. Les premiers résultats montrent que la cinématique au premier ordre du bloc Nord-Andin est dominée par un mouvement vers l'Est-Nord-est à une vitesse comprise entre 8 et 11 mm/an (Nocquet et al. 2014).

Sur le fonctionnement de la subduction, les premiers résultats obtenus ont montré que le couplage mécanique est spatialement hétérogène. Il est fort et relativement profond ($\sim$35km) au nord de l'Equateur, superficiel (<20km) au centre et pratiquement nul au sud du pays et au nord Pérou où aucun séisme n'est connu depuis le début des archives

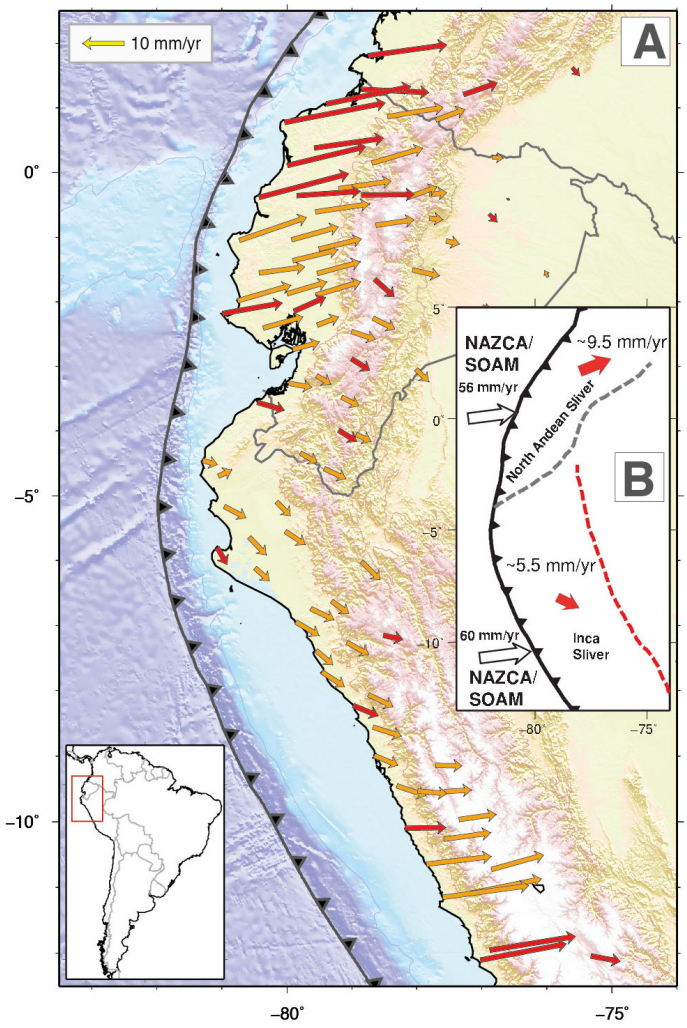

FIGURE 1.2 – A) Champ de vitesse horizontal intersismique par rapport à la partie stable de l'Amérique du Sud. Les flèches rouges et oranges sont les vitesses estimées à partir des sites GPS continus et de campagne respectivement (Nocquet et al. 2014). **B**) Schéma cinématique indiquant le mouvement du sliver Nord-Andin et du sliver INCA (Nocquet et al. 2014).

historiques datant de 5 siècles (Figure 1.3) (Chlieh et al. 2014, Nocquet et al. 2014).

Par ailleurs en Equateur, nous observons des glissements lents (SSE pour Slow Slip Event) fréquents. Ces SSEs sont des épisodes de quelques jours à quelques semaines pendant lesquels les contraintes se relâchent de manière asismique le long de l'interface de subduction. Nous avons détecté le premier SSE en 2008 au Nord de l'Equateur grâce à la première station GPS continue installée à Esmeraldas (Mothes et al. 2013). En 2010, nous avons identifié un SSE dans la région de l'Ile de la Plata (Vallée et al. 2013). Le SSE de 2010 avait une magnitude équivalente Mw entre 6.0 & 6.3 et était associé à une micro-sismicité intense (Vallée et al. 2013). Cependant, le processus de relâchement des contraintes lors des SSEs se fait de manière presque totalement asismique avec une contribution très faible en terme de moment de la micro-sismicité associée. La région de La Plata est le siège d'essaims sismiques réguliers. Lors de mon Master, j'ai travaillé à caractériser le SSE de 2005 à l'aide de données GPS de campagne initialement réalisées pour des besoins de topographie. La modélisation des déplacements estimés à partir de cet ensemble de données nous a permis d'estimer un SSE de magnitude équivalente Mw 7.2-7.3, qui a été associé à un essaim sismique qui ne représente que 10% du moment total libéré par le SSE. D'autres SSEs y ont été analysés depuis (Segovia et al. 2015) ainsi que dans différentes régions de la subduction équatorienne (Vaca et al. 2018). L'observation de ces nombreux SSEs souligne l'importance de ces glissements asismiques dans le cycle sismique de la zone de subduction équatorienne.

D'autre part, j'ai participé activement à l'étude du séisme de Pedernales de magnitude Mw 7.8 du 16 avril 2016. Grâce au réseau d'observation géodésique que j'ai décrit précédemment mais aussi au réseau sismologique développé depuis 2008 en Equateur, nous avons pu étudier les phases co-sismique et post-sismique du séisme de Pedernales. Pour la phase co-sismique, nous avons caractérisé l'évolution spatiale et temporelle de la rupture de ce séisme (Nocquet et al. 2016). La rupture s'est propagée du nord vers le sud sur 110 km en rompant successivement deux zones le long de la côte équatorienne entre 15 et 30 km de profondeur le long de l'interface. La seconde zone est caractérisée par un pic de glissement atteignant 6 m (Figure 1.4). Pour la phase post-sismique, nous avons mis en évidence un glissement asismique (afterslip) durant le premier mois qui suit le séisme de Pedernales, qui se développe principalement en deux zones discrètes au nord et au sud au-dessus de la rupture. Cet afterslip apparaît plus rapide que celui observé lors d'autres séismes de subduction et les zones de glissement important après le séisme de Pedernales ont toute été le lieu de SSEs avant le séisme (Rolandone et al. 2018). Je ne vais pas détailler les résultats de ces deux études. Je souhaite mettre l'accent sur leurs implications en termes de budget du cycle sismique. Nos observations GPS indiquent un temps de récurrence pour des séismes de magnitude

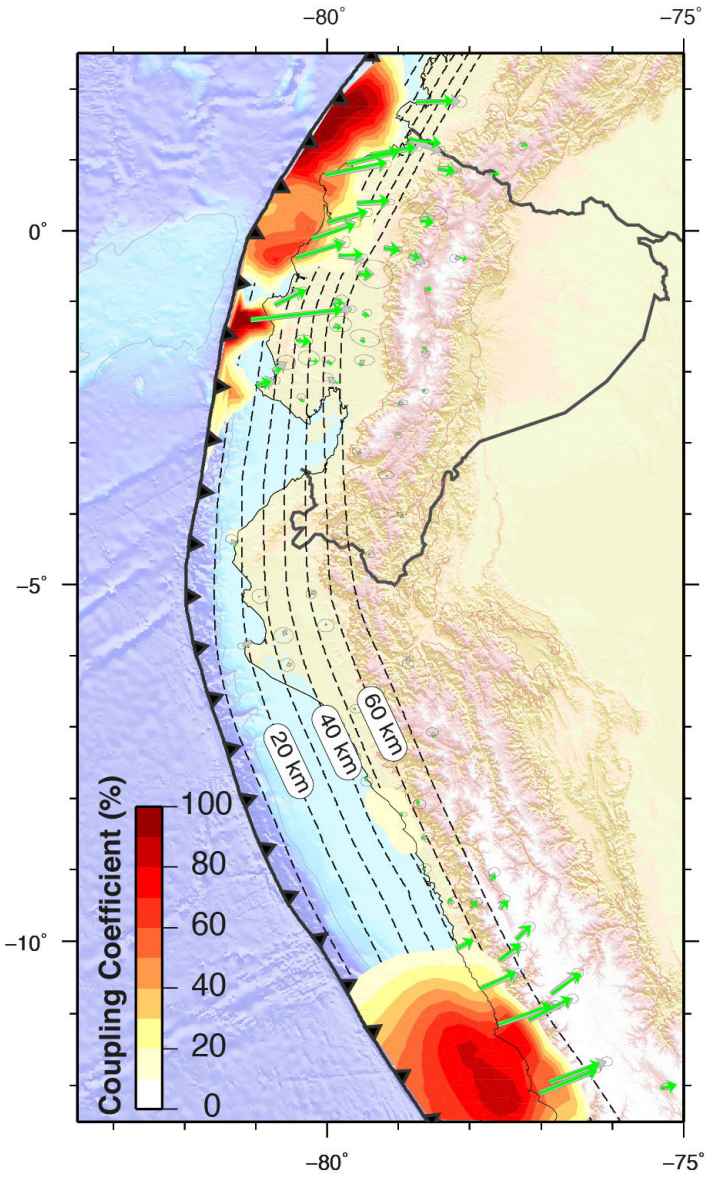

FIGURE 1.3 – Distribution spatiale du couplage interseismique au long de la zone de subduction entre le centre du Pérou et le nord d'Equateur (Nocquet et al. 2014)

Mw 7.8 de 140±30 ans dans la zone du séisme de Pedernales (Chlieh et al. 2014). Le séisme de 2016 a rompu en partie la zone de rupture estimée du séisme de 1942 et le pic de glissement de 6 m excède les 3.5 m de déficit de glissement accumulés sur l'interface par la subduction de la plaque Nazca avec une vitesse de 47.5 mm/an par rapport au bloc Nord-Andin, en considérant un couplage total. Notre étude a donc proposé que la subduction nord-Equateur & sud-Colombie semble suivre un "supercycle" de séismes avec de longues périodes de quiescence sismique (Nocquet et al. 2016). De plus, l'estimation du moment relâché de manière asismique durant les trois années de déformation post-sismique montre qu'il est du même ordre de grandeur que le moment sismique du séisme de Pedernales. Ainsi, le glissement asismique, durant les SSEs et l'afterslip, contribue de manière significative au budget de glissement sur l'interface de subduction équatorienne.

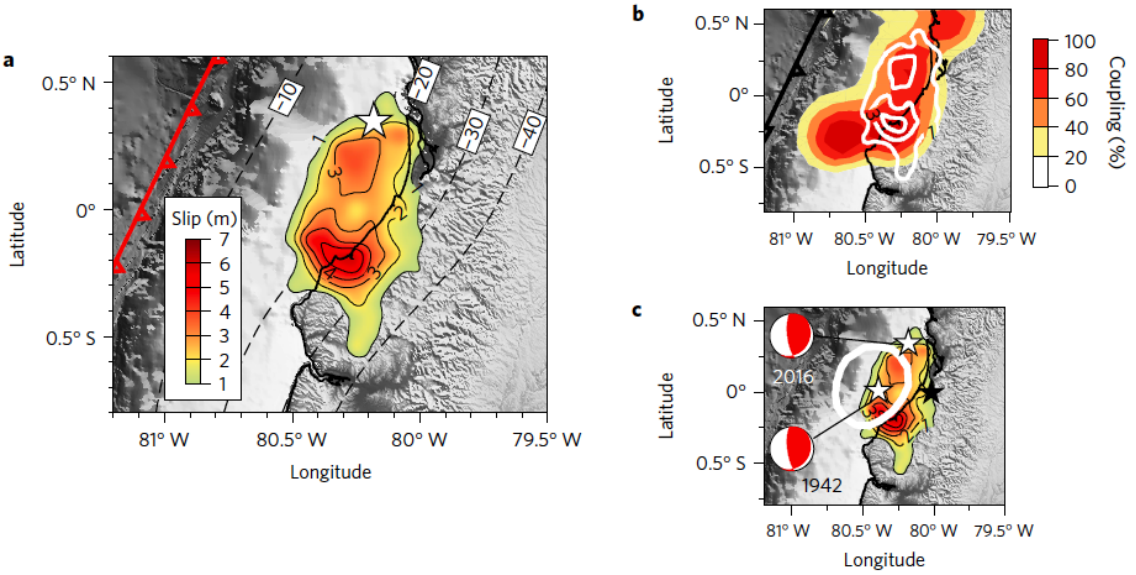

FIGURE 1.4 – a) Distribution du glissement cosismique pour le séisme de 2016. L'étoile blanche est l'épicentre du séisme. b) Couplage intersismique avec le glissement cosismique. c) Superposition du glissement cosismique du séisme de 2016 et de la zone estimée de libération maximale du moment sismique du séisme de 1942 (Nocquet et al. 2016).

1.2 Les questions scientifiques et le plan de la thèse

J'ai obtenu une bourse de thèse du gouvernement équatorien et j'ai commencé ma thèse en juin 2018. L'état de l'art des connaissances que j'ai décrit précédemment sur les déformations dans les Andes du Nord, amène plusieurs questions. Comme je l'ai souligné dans le paragraphe précédent, cette déformation est la conséquence de deux contributions différentes l'accumulation des contraintes élastiques induites par la subduction de la plaque Nazca sous le bloc Nord-Andin et la cinématique du bloc Nord-Andin. Séparer ces deux contributions reste un problème difficile.

Pour la partie du cycle sismique en zone de subduction, les questions suscitées par nos observations sont les suivantes :

- Quels sont les facteurs qui contrôlent le couplage et ses variations le long de l'interface de subduction et la genèse des grands séismes ?
- Quel est le rôle des SSEs et de la déformation asismique dans le budget global du cycle sismique ?
- Comment évaluer le potentiel sismique et le couplage de la subduction équatorienne à la lumière de ces observations ?

Si l'organisation à grande échelle de la cinématique du bloc Nord Andin vers le nord, nord-est est établie, de nombreuses questions restent ouvertes :

- Quel est le fonctionnement des segments du système de failles qui délimitent ce bloc ?. On note une grande diversité de la sismicité historique et instrumentale. Est-ce que cela peut s'expliquer par des variations de taux d'accumulation de contraintes et des profondeurs de blocage très variables entre les différents segments, ou bien par une déformation accommodée par plusieurs failles ?
- Y a-t-il de la déformation interne au bloc Nord-Andin ?
- Quelles sont les conséquences sur l'aléa sismique ?

Pour tenter de répondre à ces questions, j'ai traité et analysé plus de 300 stations GPS continues pendant ma thèse, et j'ai travaillé sur deux axes :

1. Améliorer la cinématique de la plaque Nazca.
2. Améliorer la cinématique du sliver Nord-Andin.

La détermation de la cinématique de la plaque Nazca est importante car elle définit les conditions cinématiques aux limites du sliver Nord-Andin. Dans une seconde étape, j'ai construit un modèle de blocs élastiques du sliver Nord-Andin cohérent à l'échelle des Andes du Nord, qui rend compte des observations tectoniques, et intègre la cinématique précise de la plaque Nazca que j'ai determinée. Ce modèle me permet de proposer des vitesses de glissement le long des principales failles crustales qui séparent les blocs. Ces résultats sont importants pour les études d'aléa sismique. De plus, l'approche en blocs élastiques permet de résoudre simultanément la rotation des blocs qui constituent le sliver Nord-Andin et l'accumulation des contraintes élastiques induites par la subduction de la plaque Nazca sous ce sliver. J'étudie donc de manière cohérente et simultanée les deux processus à l'œuvre dans les déformations des Andes du Nord. Je propose ainsi un

nouveau modèle cinématique pour le sliver Nord-Andin ainsi qu'un modèle de couplage inter-sismique le long de l'interface de subduction.

Ce manuscrit de thèse est structuré en cinq chapitres incluant ce chapitre introductif.

Le Chapitre 2 décrit tout d'abord les données GPS continues utilisées dans mon travail de thèse qui proviennent de centres de données régionaux et globaux à l'échelle des Andes du Nord et des regions voisines. Puis, je décris la stratégie de traitement adoptée au cours de cette thèse pour obtenir des séries temporelles géodésiques. Je discute ensuite de l'analyse des séries temporelles et de l'analyse du bruit pour estimer le champ de vitesse régional par rapport au référencenciel Sud-Américain ainsi que les incertitudes associées.

Le Chapitre 3 est consacré à revisiter la cinématique de la plaque océanique Nazca à l'aide des données continues GPS. Nous évaluons la possible déformation de la plaque Nazca et proposons un nouveau pôle d'Euler qui décrit le mouvement relatif actuel Nazca/Amérique du Sud basé sur les vitesses de 5 sites : 2 anciens sites situés sur l'île de Pâques et l'île de Santa Cruz et 3 nouveaux sites situés sur les îles de Malpelo au large de la Colombie, San Cristobal à l'Est de l'archipel des Galapagos, et Salas y Goméz à l'Est de l'île de Pâques. Ensemble, ils couvrent spatialement la totalité de la plaque Nazca. En plus du bruit géodésique formel, nous avons estimé les incertitudes de vitesse réelle à partir de modèles directs élastiques pour prendre en compte des processus tectoniques et volcaniques. L'analyse détaillée de ces vitesses a révélé que les estimations précédentes des pôles d'Euler utilisant les anciens sites EISL et GLPS sont biaisées de plusieurs mm/an. Ces résultats ont été soumis au Geophysical Journal International.

Le chapitre 4 est le coeur de cette thèse. Il présente un nouveau modèle cinématique à l'échelle régionale pour le sliver Nord-Andin basé sur l'approche de modélisation par blocs élastiques. Dans cette formulation, une inversion des données GPS a été effectuée pour résoudre simultanément le couplage inter-sismique sur les interfaces de subduction et les rotations rigides des blocs. Ce chapitre décrit la démarche de construction du modèle, les résultats obtenus pour la partie continentale, et la validation du modèle cinématique en utilisant des données indépendantes telles que les taux de glissement géologiques des failles et les mécanismes au foyer des séismes. Les résultats obtenus dans cette étude sont présentés sous la forme d'un article qui est en cours de corrections finales. Il devrait donc être soumis à une revue dans les prochains mois.

Le chapitre 5 présente la distribution de couplage inter-simique le long de la zone de subduction d'Equateur-Colombie qui a été estimée par le modèle de blocs décrit dans le chapitre précédent. Ces résultats sont présentés sous la forme d'un article en cours

de rédaction. Ce chapitre décrit les cartes de couplage obtenues, ainsi qu'une première interprétation sur la relation entre le couplage et le cycle sismique le long de la subduction en Equateur-Colombie.

Enfin, dans le chapitre 6 de conclusions et perspectives, je résume les résultats les plus importants obtenus lors de ma thèse. La contribution principale de mon travail est de fournir des modèles cinématiques de référence pour les études tectoniques et pour les études du cycle sismique dans les Andes du Nord. Je propose également dans ce chapitre quelques pistes de recherche pour les prochaines années.

CHAPTER 2

GPS Data Processing and Analysis

2.1 GPS Data

For this thesis, the data set used includes 76 permanent stations from the Instituto Geofísico of Ecuador (RENGEO network) (Alvarado et al. 2018, Mothes et al. 2013), 21 permanent stations from the Insituto Geográfico Militar of Ecuador (REGME network), 13 permanent stations provided by the Servicio Geológico Colombiano (GeoRED network) (Mora-Páez et al. 2018), 38 permanent stations from the Insituto Geográfico Agustin Codazzi (IGAC) of Colombia, 11 permanent stations from the Low Latitude Ionospheric Sensor Network (LISN) provided by Instituto Geofísico del Peru (IGP), 1 permanent station from the Servicio Sismológico Nacional (Báez et al. 2018) located in the Nazca plate, 45 permanent stations from the Instituto Geofísico del Peru (IGP), 39 permanent stations from the COCONet Project (Community 2008) distributed in northern Colombia, Venezuela and Panama, 7 permanent stations from the RAMSAC network (Piñón et al. 2018) distributed in Argentina, and regional IGS stations from the global network of the International GNSS Service for Geodynamics (Dow et al. 2009).

The final GPS data set comprises 330 permanent stations located on the Nazca, Cocos, South America, Caribbean, Pacific and Nubia plates. The location of the analyzed GNSS network is shown in figure 2.1. Figure 2.2 shows general statistics of the data collected between 1994 and 2019.9. All mentioned GPS data have a minimum of 2.5 years of measurements to mitigate the impact of seasonal variations on the velocity estimates (Blewitt and Lavallée 2002).

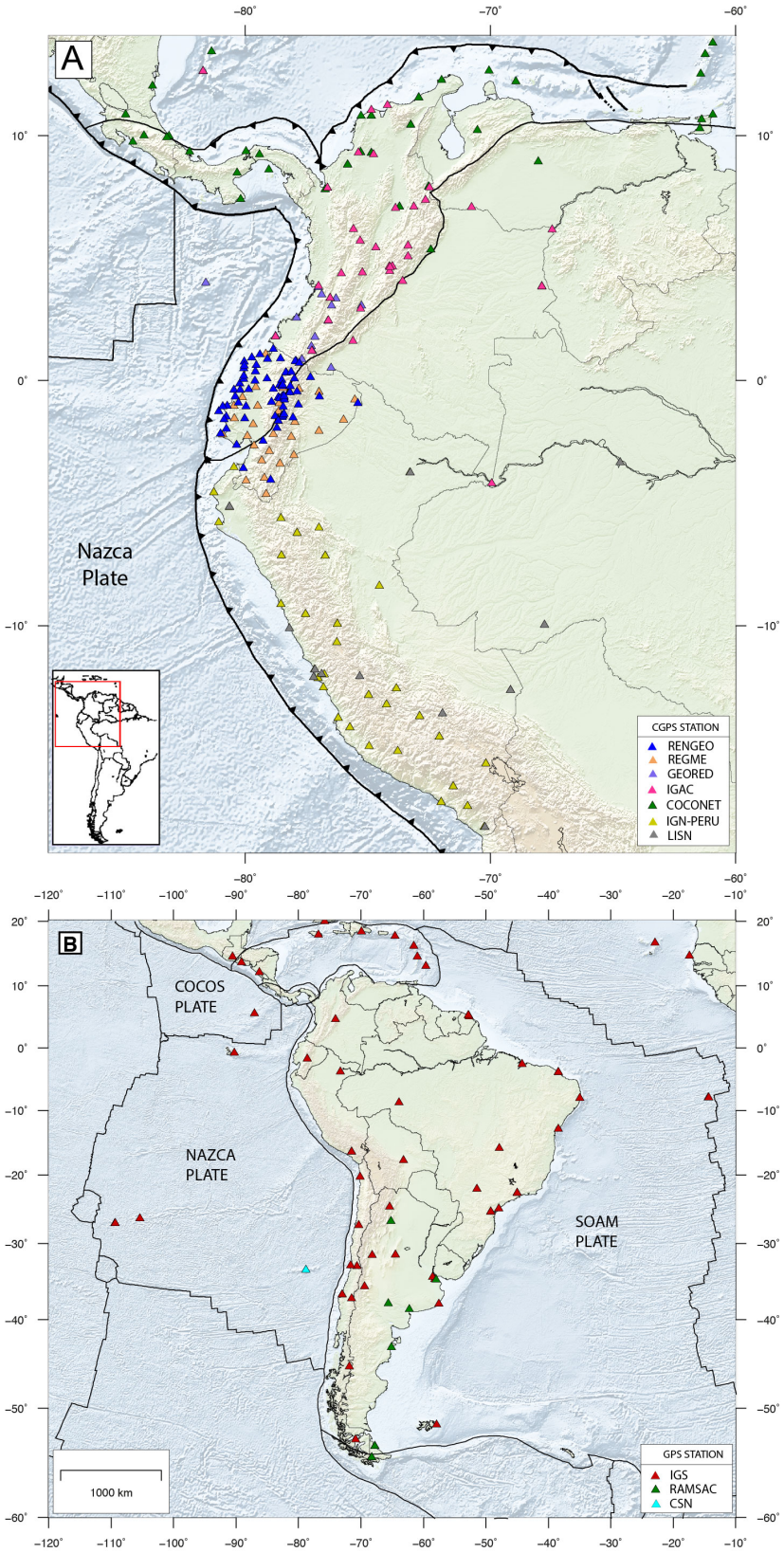

Figure 2.1 – Distribution of permanent GPS stations per network: **(A)** Peru, Ecuador, Colombia, Venezuela, and Panama. **(B)** Nazca, Cocos, Caribbean, South American, and Nubia plates

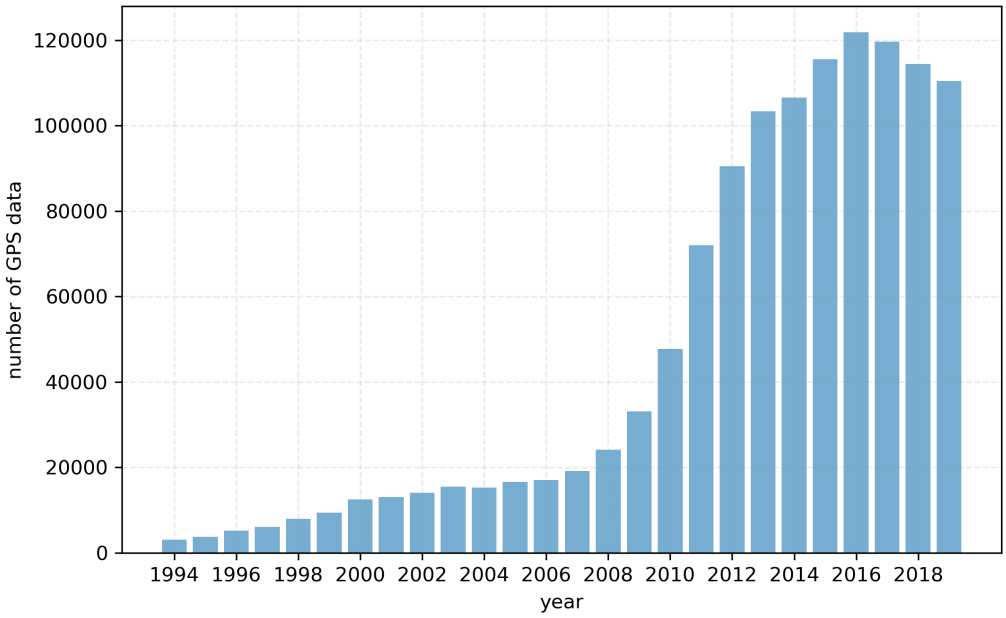

Figure 2.2 – Summary of continuous GPS data collected per year between 1994 and 2019.9

2.2 Gamit / Globk Processing

GAMIT is a collection of programs that allows to process code and phase observables using the double difference approach to estimate relative positions of a set of ground stations. In practice, the free GAMIT solution is not used directly to obtain the final estimates of station positions from a survey, rather it is computed in two stages. The first one produce estimates and an associated co-variance matrix (quasi-observations) of station positions and Earth-rotation parameters within a few decimetric precision, which are in the second one the input to GLOBK or other similar programs to combine the data with those from other networks under a defined and appropriate reference frame to estimate a final solution of positions and velocities.

2.3 PYACS Framework

PYACS software package is a set of tools written in python to analyze and model geodetic data (Nocquet 2017). It does not replace more complex software package like GAMIT/GLOBK, but rather PYACS interacts with them. PYACS is composed of several modules that are detailed below:

- **GECA module** allows to do an automatic Gamit processing of a local, regional or continental network by using a subnetworks strategy in a cluster computing environment.

- **SOL module** allows to estimate a 7-parameters Helmert transformation between daily free solutions and a reference solution (ITRF). This transformation is expressed in local coordinates. It implements an approach, which allows to isolate the vertical component from the horizontal ones and remove it from the estimation when an outlier is detected (more information in section 2.4.3).

- **GTS module** provides a set of functions to perform operations on time series. These operations are defined as primitives, which ones contain several models to detect outliers or offsets, to remove outliers and period of times, to compute robust velocities and seasonal terms through the use of L2 norm (Least Squares) approach, or Automatic velocity estimates using the Median approach. It also provides a versatile visualization of time series.

- **GVEL module** provides a set of models to compute Euler poles, slip rates on faults, elastic models, etc.

- **MODEL module** provides a set of tools to perform slip inversions applied to deformation studies (inter-seismic, co-seismic and time dependent deformation).

2.3.1 Parameters Considered in the Processing

GPS observations are processed in sessions of 24 hours to average errors such as the effect of alternation (day/night) in the troposphere and ionosphere, as well as the effect of geometric variation in the satellite constellation. We have considered earth rotation (EOPs) and its variations during GPS measurements as well as precise orbits models from the International GNSS service for Geodynamics (IGS) (Dow et al. 2009). The position variation of antenna phase centres as a function of satellite motion (elevation and azimuth) was modelled using the phase centre offsets (PCOs) and variations (PCVs) tables recommended by the IGS, and the elevation cut-off angle from the observations is 10°. Elastic response effects to ocean tides were modelled using FES2004 model (Lyard et al. 2006), as well as polar and solid-earth tides following IERS/IGS (1996) standards (McCarthy 1996). We have used the linear combination (LC) of L1 and L2 frequencies known as "ionosphere-free" to eliminate the wave delay across the ionosphere. Double difference of LC phase measurements is performed to eliminate clock errors in receivers and satellites. We also used the Vienna Mapping Function model (VMF1) together with a zenithal delay every 2 hour to model the GPS signal delay in the troposphere (Boehm et al. 2006). Others specific parameters (apriori coordinates of sites) and control files are described in section 2.3.2.

2.3.2 Processing Strategy and Automatic Processing

A differential approach requires a significant computing power and time because the computational burden increases with the square of the number of geodetic sites (Nocquet 2011). A hard coded constraint is that, Gamit is configured to process networks with a limit of 80 sites by project. In practice, it is more efficient to process a regional or global network that exceeds $\sim$ 50 sites in sequential subnetworks (Herring et al. 2018). For processing time considerations, each sub-network is set to a maximum of 25 sites using PYACS. Every subnetwork shares 4 common tie sites with the other networks. The subnetwork are processed sequentially and generates an individual solution. Then, all individual subnetwork solutions are recombined into a single daily solution. This processing strategy was applied uniformly to the 24 years of data analysis.

In order to use the GECA module of PYACS, it is necessary to prepare all inputs files that Gamit needs. This stage is very important and has been sub-divided in two steps. The first one is to have ready all rinex data files, broadcast files, orbit files and atmospheric grids in an specific directory structure and the second one is to create a project directory, within this a configuration directory is created where the control files are copied and edited.

A quick description of the control files is detailed below:

1. **Process.defaults** file specifies the directory architecture for internal GNSS data, orbit files, broadcast files, atmospheric grids, start time and sampling interval, and instructions for archiving the results.
2. **Sites.defaults** file specifies local and IGS stations used in the processing.
3. **Station.info** file contains the receiver and antenna type as a function of time for all occupations of the stations.
4. **Sestbl.** file defines the models used in data processing, for example: atmospheric parameters, orbit parameters, etc.
5. **Sittbl.** file specifies a priori constraints and appropriate options for the analysis
6. **Coordinate** file contains the cartesian coordinates (position and velocity) of stations.

2.4 Time series positions and velocities

From the point of view of Geodynamics, two approaches are proposed to obtain velocities from GPS observations. In the first classical approach, the velocities and its uncertainties are estimated from time series of positions. Performing a seven-parameters transformation

between the free daily solutions and a reference solution we produce time series, allowing to evaluate day-to-day repeatability. The advantages of this one lies in the ability to perform an outliers detection, transient signals detection, and a rigorous noise analysis. However, its disadvantage lies in neglecting the correlations between components (e.g. north and east) of solutions. On the contrary, the second approach uses a mathematical model called Kalman filter which extends the classical seven-parameter transformations to complex 14-parameter formulations (7 parameters with their time derivatives). This model takes into account correlated noise in the form of a Markov noise to estimate velocity uncertainties. The result of this approach is to simultaneously obtain an estimate of station coordinates and velocities.

In the remainder of this chapter, I describe the methodology adopted to obtain the inter-seismic velocity field. A first iteration is performed to compute a 7-parameters Helmert transformation with the PYACS software in order to produce time series of positions. All time series (component-by-component) are then visually inspected to remove any artificial or geophysical signal that could cause bias in the estimated secular velocities. From these clean time series, we simultaneously estimate velocity, annual and semiannual terms, offsets and noise components with the aim of to quantify the uncertainties associated with the velocity estimations.

2.4.1 Reference Frame Definition

Before to express free daily solutions in a geocentric reference solution, it is necessary to define a set of stations whose position and velocity are precisely known. These stations usually belong to an international network (Internacional GNSS service, IGS) and are distributed throughout the world.

The International Terrestrial Reference System ITRF2014 is the most accurate and current reference frame adopted by the scientific community. It has demonstrated to be superior to its previous version ITRF2008, due to the modeling of nonlinear station motions like postseismic deformation (PSD) for sites that were affected by major earthquakes, like for example: the Chile (2010) and Japan (2011) earthquakes (Altamimi et al. 2016).

On the other hand, the International GNSS Service has adopted a new reference frame at the end of january 2017, called IGS14, as the basis of its products. IGS14 is basically an extraction of 252 well-suited reference frame stations (long and stable position time series) from the ITRF2014 (fig. 2.3). At the same time, an updated set of satellite and ground antenna calibrations have also been adopted, replacing the previuos IGS08 and

igs08.atx framework by IGS14 and igs14.atx (Rebischung et al. 2016).

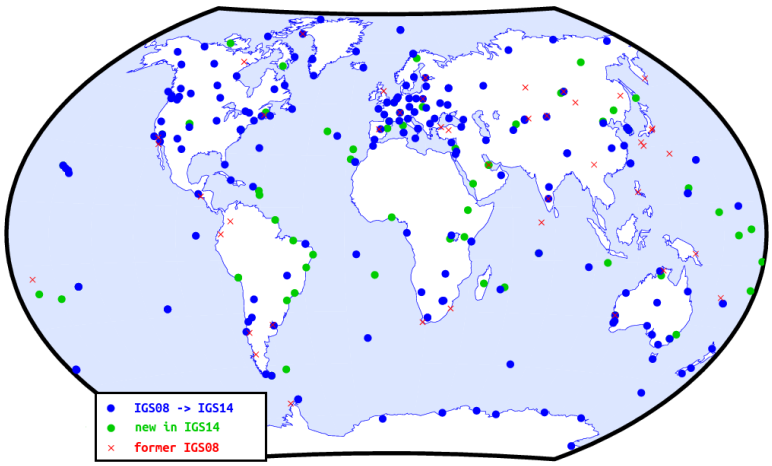

Figure 2.3 – Distribution of the IGS14 and the former IGS08 reference frame stations (Rebischung and Schmid 2016)

The advantages of using an IGS solution is mainly due to:

1. It is generally a cumulative solution and more up to date than the current implementation of the ITRF.

2. It is derived from the high quality ITRF stations whose coherence as a reference solution is higher than current ITRF solution (Rebischung et al. 2016).

3. The quality of the solution takes into account the information of discontinuities and non-linear predictions models in the sites used to reference the solution.

Based on the advantages mentioned above, we chose the most current and cumulative IGS solution provided by the IGN of France (Institut National de l'Information Géographique et Forestiére) as a reference solution to express our free solutions in an International terrestrial reference frame.

2.4.2 Helmert Transformation between two reference systems

The standard relation of transformation between two terrestrial reference systems $\mathbb{R}_1$ and $\mathbb{R}_2$ is a similarity involving seven parameters: three translations, one scale factor, and three rotations (figure 2.4). In general, the transformation of a point i of coordinates $X_1^i = (x_1^i, y_1^i, z_1^i)$ expressed in a reference system $\mathbb{R}_1$, into a coordinate $X_2^i = (x_2^i, y_2^i, z_2^i)$, expressed in a reference system $\mathbb{R}_2$ under the condition that the coordinates are fixed in space (no velocities are involved), is given by:

$$X_2^i = T + \lambda \Re X_1^i \tag{2.1}$$

Where T is a vector consisting of the three translation parameters, λ is the scaling factor and $\Re$ is a rotation matrix.

$$T = \begin{bmatrix} T_x & T_y & T_z \end{bmatrix} \tag{2.2}$$

$\Re$ is composed of three rotation matrices: R_x, R_y and R_z one for each axis. Therefore, they can be combined in one:

$$\Re = R_x R_y R_z \tag{2.3}$$

$$\Re = \begin{bmatrix} 1 & 0 & 0 \\ 0 & Cos(R_x) & -Sin(R_x) \\ 0 & Sin(R_x) & -Cos(R_x) \end{bmatrix} \begin{bmatrix} Cos(R_y) & 0 & -Sin(R_y) \\ 0 & 1 & 0 \\ Sin(R_y) & 0 & Cos(R_y) \end{bmatrix} \begin{bmatrix} Cos(R_z) & Sin(R_z) & 0 \\ -Sin(R_z) & Cos(R_z) & 0 \\ 0 & 0 & 1 \end{bmatrix}$$

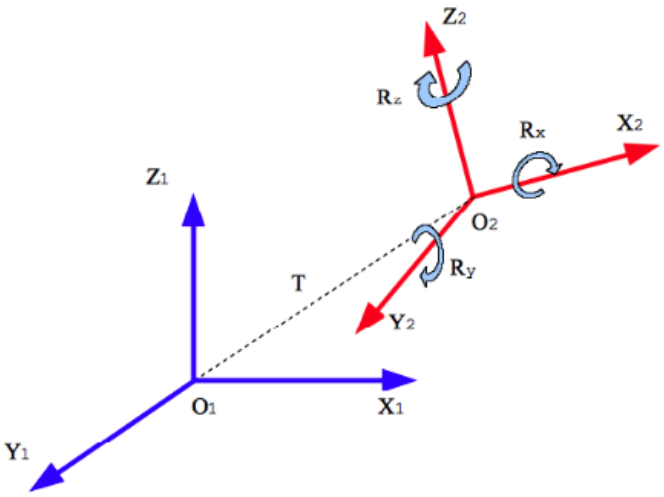

Figure 2.4 – Helmert transformation schema. T is the translation along of axe origins, R_x, R_y, R_z are the respective rotations for each axis. (Tran 2013)

Equation (2.1) is not linear because the matrix $\Re$ includes circular functions. In space geodesy techniques, small values are expected for translations, rotations and scale parameters. Indeed, origin differences are around of few meters, and differences in scale and orientation parameters are of the order of 10^{-5}. Thus, making a first order Taylor-Young expansion, we can write $Sin(R_i) \approx R_i$ *and* $Cos(R_i) \approx 1$ (Altamimi et al. 2002, McCarthy and Petit 2003). We obtain:

$$\Re = \begin{bmatrix} I \end{bmatrix} + \begin{bmatrix} R \end{bmatrix}^t = \begin{bmatrix} I \end{bmatrix} + \begin{bmatrix} 0 & R_z & -R_y \\ -R_z & 0 & R_x \\ R_y & -R_x & 0 \end{bmatrix} \tag{2.4}$$

The superscript t stands for transpose, $[I]$ denotes the 3×3 unit matrix, and $\left[R\right]^t$ is a skewsymmetric (anti-symmetric) matrix containing the rotation parameters. Moreover, by writing $\lambda = 1 + D$, equation (2.1) is written in the most common version of the Helmert transformation:

$$X_2^i = X_1^i + T + \Re X_1^i + DX_1^i \tag{2.5}$$

Least squares adjustment based on at least three points in common between both reference systems is commonly used to estimate the seven transformation parameters. For this purpose, equations (2.5) is rewritten in the form of the linear system:

$$X_2 = X_1 + A\theta \tag{2.6}$$

where θ is the vector of the seven transformation parameters. A is the nx7 design matrix of partial derivatives constructed upon approximate station positions (..., X_0^i, ...) where 1 < i < n and n is the number of stations

$$\theta = \begin{bmatrix} T_x & T_y & T_z & R_x & R_y & R_z & D \end{bmatrix}$$

$$A = \begin{bmatrix} . & . & . & . & . & . & . \\ . & . & . & . & . & . & . \\ 1 & 0 & 0 & 0 & z_i^1 & -y_i^1 & x_i^1 \\ 0 & 1 & 0 & -z_i^1 & 0 & x_i^1 & y_i^1 \\ 0 & 0 & 1 & y_i^1 & -x_i^1 & 0 & z_i^1 \\ . & . & . & . & . & . & . \\ . & . & . & . & . & . & . \end{bmatrix}$$

Now, we can rewrite equation 2.6 in terms of an international terrestrial reference frame (ITRF) and an epoch associate at a (t_D) datum t_D, which is common for the two sets of coordinates. (Soler and Marshall 2003)

$$[X_{t_D}]_{ITRF_{yy}} - [X_{t_D}]_{ITRF_{00}} = A\theta \tag{2.7}$$

Where $ITRF_{00}$ is the initial frame and $ITRF_{yy}$ is the desired frame.

2.4.3 Helmert Transformation using PYACS

Tran [2013] presents a rapid and robust methodology to estimate 7 parameters of the Helmert transformation between two reference systems. The robustness of this methodology is based on the successively detection of atypical values (outliers) in the set of common sites during the combination through the extensive use of the L1 norm (Dikin estimation approach). Then, the final estimation is performed by least squares

(L2 norm) on validated data. On the other hand, the rapidity is achieved by avoiding the reading and manipulation of the variance-covariance matrix (VCV) of the free and reference solutions. This makes sense, because the main GPS problems come from offsets in the time series and errors associated with reference systems. Therefore the VCV matrix contains secondary information (Nocquet 2017). With this methodology, it is possible to generate high-quality time series which we will be inspected them in section 2.5.2.

Using the recently mentioned methodology, we express our free Gamit solutions in the ITRF. As mentioned in section 2.4.1, we choose as the refence the most current cumulative IGS reference solution (ex: *IGS18P21.ssc.Z*), the discontinuity file (*soln.snx*), the models of prediction and non-linear evolution of station positions (*psd_IGS.snx*), the IGS domes number file (*codomes_gps_coord.snx*), and of course the free Gamit solutions in h-file or international sinex format. All these input files are processed by the PYACS package, which generates residual time series in a long format of various coordinate systems (Geocentric, Geodetic and Local) so-called pos-file.

2.5 From Time Series to Velocitiy

2.5.1 Linear Parameters

In order to accurately estimate the geodetic velocity, it is necessary to model first-order features observed in a time series. Thereby any time series of n positions can generally be modeled by a combination of a linear term representing secular velocity, an annual and semi-annual oscillations and instantaneous jumps (Bevis and Brown 2014, Langbein 2004). The time series expression is written as:

$$y_{t_i} = y_{trend} + y_{cycle} + y_{jumps} \tag{2.8}$$

$$y_{t_i} = a_R + b(t_i - t_R) + [c\,Sin(2\pi t_i) + d\,Cos(2\pi t_i)] + [eSin(4\pi t_i) + f\,Cos(4\pi\, t_i)] + \sum_{j=1}^{n_j} g_j H(t_i - t_j) + \varepsilon_{y_{t_i}} \tag{2.9}$$

Where:

- y_{t_i} is the measurement at time t_i.
- t_i for i=[1, n] is the time of position i of the daily solution.

- t_R is a reference time. (adopted by convention)
- a is the reference position to a t=t_R
- b is the linear velocity.
- (c, d) and (e, f) are the magnitude of annual and semi-annual periodic motions respectively.
- g_j characterize the offsets of amplitude g which occur at time t_j as a instantaneous displacement. n_j is the number of offsets. H is the Heaviside step function, which equals 1 for $t_i \geqslant t_j$ and 0 otherwise.
- $\varepsilon_{y_{t_i}}$ is the difference between the observed and the predicted (residual error term).

Assuming that the offset epoch is known, the model y_{t_i} is linear with respect to the coefficients.

2.5.2 Visual Inspection of Time Series

As mentioned in section 2.4, the visual inspection of the GPS time series allow us to remove signals associated or not to any geophysical processes. The criteria used to perform this task is to first define co-seismic and post-seismic displacements, slow slip events, and other type of transient signal by example volcanic activity. The second criteria is defined in terms of atypical values such as outliers and offsets.

The offsets are caused by earthquakes, antenna changes, equipment malfunctioning, phenomena related to the environment changes such as trimming a tree nearby the station or a shock on the antenna. Others offsets can be linked to changes in the processing strategy adopted (e.g.: selection of atmospheric models or input information) (Williams 2003b). On the contrary, the outliers (isolated or grouped) may be related to an antenna problem, hardware failure, changing the size of the vegetation nearby the antenna, bad measurements (few hours of gps observations), or simply atypical weather conditions (snow on the antenna). Finally, others causes may be due to a change of the reference stations, either in number or in observation time (network effect), or simply a problem in the processing strategy adopted (Tran 2013).

The cleaning process and velocity estimation at each time series was performed in 4 stages. Firstly, a robust outlier detection algorithm was applied a each time series of positions which considers as outliers residuals (difference between the observed data and the predicted) larger than 10 mm on the vertical component and 5 mm on the horizontal component. Secondly, a manual detection of undetected outliers was performed. Thirdly,

the date of the offsets were fixed, and problematic periods of data (includes no-linear motion) was excluded, based on the correlations of dates between nearby stations and information extracted from publications. Finally, the velocity, annuals and semi-annuals terms and amplitude of offsets displacement were simultaneously estimated using Least squares approach.

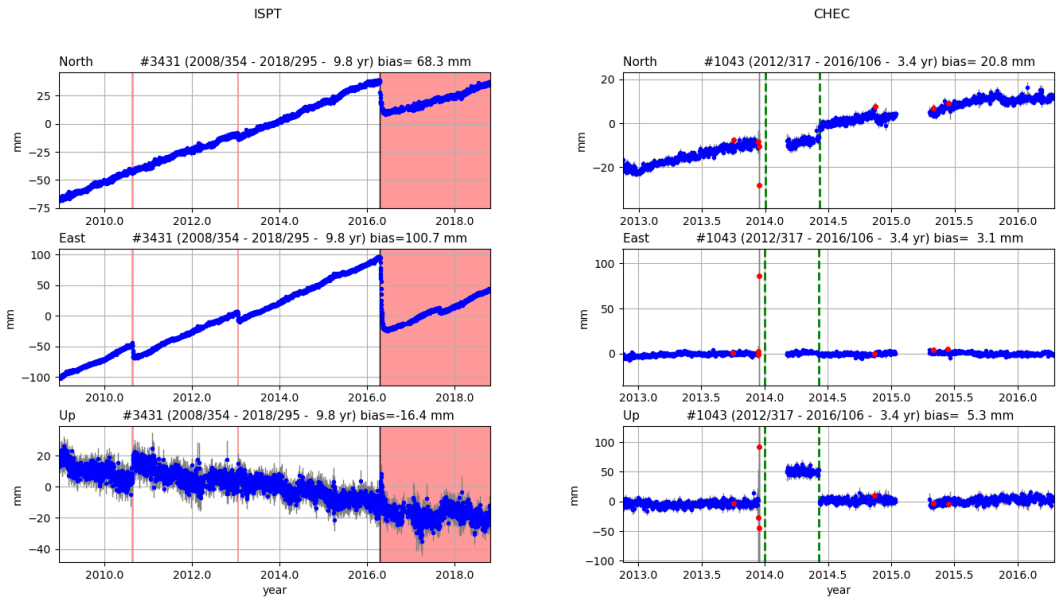

Figure 2.5 – Example of the cleaning process of time series. The time series of ISPT station (left plot) shows two no-linear displacements related with two slow slip events in 2010.7 and 2013 (Vallée et al. 2013), and a coseismic and post-seismic displacement related with the 2016 Pedernales earthquake (pink filled strips) (Nocquet et al. 2016) The time series of CHEC station (right plot) shows the presence of offsets (dashed green lines) related with the antenna changes and outliers (red dots). These stations are located in Ecuador.

Figure 2.5 shows the identification process of outliers and offsets in the time series of CHEC station. In the time series of ISPT station, we identify non-linear displacements related with two slow slip events in 2010 and 2013 and a coseismic and post-seismic displacement related with an earthquake in 2016 (Pedernales earthquake).

In order to evaluate the quality of our clean time series, we focus on daily repeatability, which is an average indicator of positions dispersion and it is defined as the weighted residual mean squared (WRMS) of daily positions around the detrended average position for each component (east, north and vertical) of each site (Nocquet 2011).

$$WRMS = \sqrt{\frac{\sum_{i=1}^{n} \frac{(x-\bar{x})^2}{\sigma^2}}{\sum_{i=1}^{n} \frac{1}{\sigma^2}}} \tag{2.10}$$

where n is the number of positions, $\bar{x}$ is the weighted average of the daily solutions of x_i or the value predicted by an evolution model, σ_i is the daily position variance of x_i.

The WRMS is calculated from the time series of positions by removing first the slope and secondly the annual and semi-annual terms. Figure 2.6 shows the WRMS values estimated for the time series of ISPT and CHEC stations. Values between 1.0 and 1.2 mm are estimated for north and east components and values of 3.1 and 3.6 mm are estimated for the vertical component.

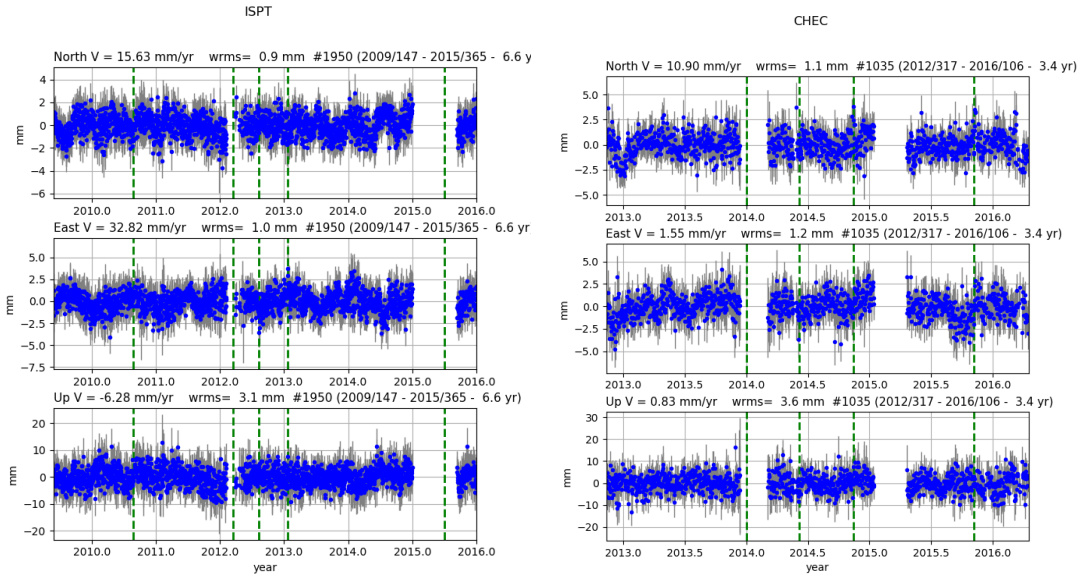

Figure 2.6 – Evaluation of WRMS after cleaning process from the time series of figure 2.5. The time series of ISPT station shows a WRMS of 0.9 and 1.0 mm for north and east components respectively and 3.1 mm for the vertical component. The time series of CHEC station shows a WRMS of 1.1 and 1.2 for north and east components respectively and 3.6 mm for the vertical component. Dotted green lines are offsets fixed due to antenna replacements and jumps in the time series.

2.5.3 Seasonal Motion

A considerable number of seasonal variations (in particular annual signals) from different sources are present in global and regional time series of continuous GPS measurements causing variations in the estimated site positions. These signals may be attributed to gravitational excitation, hydrological loading, atmospheric pressure and various errors related with GPS data processing. (Blewitt et al. 2002, Dong et al. 2002, van Dam et al. 2001). For example, the gravitational excitement from sun and moon induces displacements due to solid Earth tides, ocean tides, and atmospheric tides. Hydrological loading comes from the weight of water stored in the land, including water stored in the first meters of soil (soil moisture), aquifers, glaciers and rivers. van Dam et al. (2001)

found that the water storage load induce vertical surface displacements reaching 30 mm, particularly in tropical areas of South America and Africa, in the Asian monsoon region and along the coasts of western Canada and southern Alaska. Dong et al. (2002) studied seasonal variations in time series of 4.5 years from a global GPS network. They found that the primary cause for annual vertical variations of site positions is attributed to surface mass redistribution (atmosphere, ocean, snow, and soil moisture) and particularly to atmospheric loading, which produces the highest annual amplitudes in sites located in the Eurasian plate and the Arabian Peninsula and particularly in Siberia and Canada. Blewitt et al. (2002) detect a global mode of vertical deformation attributed to annual mass redistribution. Their results reveal a pattern of compression (downward) in the northern hemisphere between February and March with maximum of 3.0 mm in sites close to the north Pole, and the south Pole during August and September. At these periods of times, a lateral deformation of 1.5 mm is observed near the Equator. Besides these physical models, other errors such as orbital and atmospheric models, phase center variation models, noise, and environmental errors related with local multipath (trees with/without leafs), can also cause apparent variations (Dong et al. 2002).

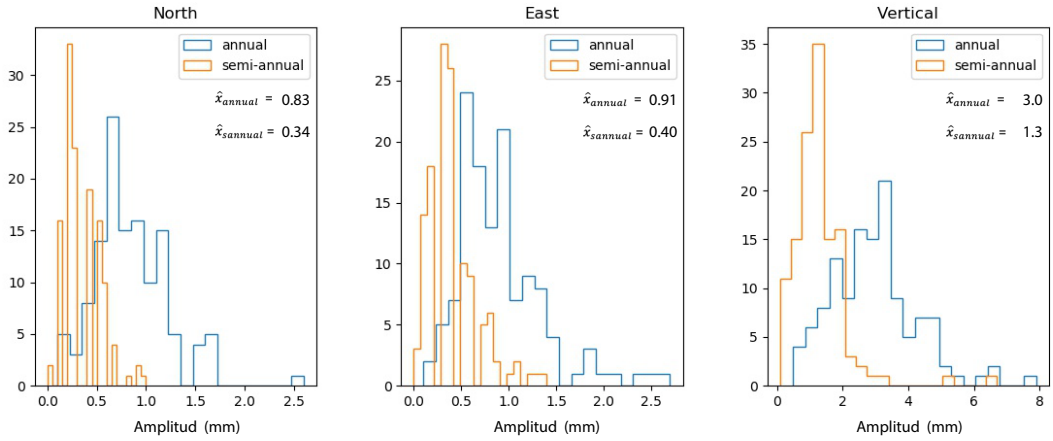

Figure 2.7 – Histograms of Annual and Semi-annual amplitudes for horizontal and vertical components in Ecuador and south of Colombia. Annual and Semi-annual amplitudes are plotted in blue and orange respectively. In each chart, the median value $\hat{x}$ is specified. The number of sites evaluated were 127, and are located in Ecuador and southern Colombia.

Blewitt and Lavallée (2002) studied the effect of seasonal components in continuous GPS time series of a global network through of the simultaneous estimation of velocity, annual and semi-annual terms. This analysis determined annual amplitude values of 2 mm and 4 mm for horizontal and vertical components respectively and semi-annual amplitude values of 1 mm and 2 mm for horizontal and vertical components respectively. However, these amplitudes could twice larger in several sites. At the same time, it was observed that the influence of seasonal variations in velocity estimations

is minimum from 2.5 years of data span and negligible for time series with 4.5 years of data.

Histograms of Figure 2.7 shows the amplitudes of annual and semi-annual variations for horizontal and vertical components of an array of 127 sites located in Ecuador and southern Colombia. The results show annual amplitudes of $\sim$ 1 mm and 3 mm for horizontal and vertical components respectively, and semi-annual amplitudes of $\sim$ 0.5 and 1.3 mm for the same components.

Figures 2.8 and 2.9 show the distribution of annual and semi-annual variations for vertical and horizontal components located in Ecuador and south of Colombia respectively, whose phase and amplitude are plotted in individual phase diagrams in figure 2.10. Vectors have lengths proportional to amplitude of seasonal variations and point in the direction of zero cosine phase. All sites of figure 2.8 show a clear downward vertical motion (annual terms) that exhibits a spatial correlation. This fact suggests that the difference between estimating and removing seasonal terms could be performed by a direct method such as common mode filtering (Wdowinski et al. 1997). The annual periods have maximum amplitudes between February and April, the middle of the winter. Spatial correlations between semi-annual terms are less obvious. However, it appears to occur between May 15 and June, and between November 15 and December. Annual variations in the east component have maximum amplitudes during August and September. However, two sites are maximum in May (figure 2.10). Around 95% of these sites are well correlated, they show a coherent motion towards the northeast, which in not the case for annual variations of the north component (figure 2.9), where $\sim$ 60% of sites show a movement towards southwest and the remaining sites toward southeast (maximum amplitudes between March and April). Although semi-annual phases in the east and north components are largely uncorrelated, a considerable number of sites (north component) show maximum variations in June and December. In conclusion, the annual variations are well spatially correlated, whose maximum amplitude values occur between February and April, when the winter period is in its strongest stage.

2.5.4 Least squares Approach

One of the most commonly methods used to estimate velocities from time series of GPS positions is Least Squares (LS). This method is optimal if the observations are errors following a normal distribution. For example, in least squares analysis the presence of outliers, offsets, and particularly seasonal signals in short time series, are problems that can significantly bias velocity estimates. Thus, the least squares method is not optimal and advisable to use if a previous work of inspection and cleaning has not been performed.

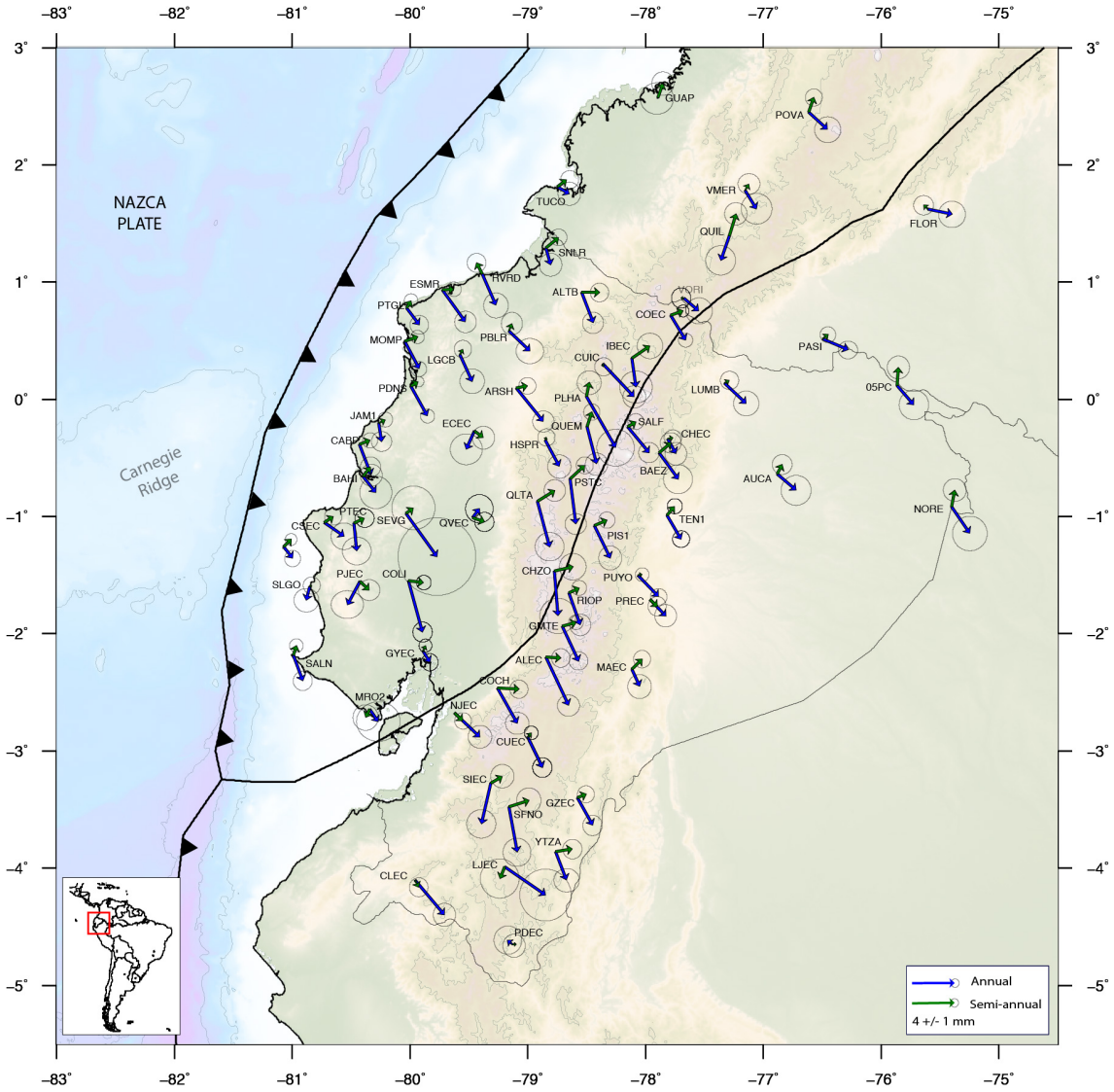

Figure 2.8 – Annual and Semi-annual variations for vertical component in Ecuador and southern Colombia. Blue and green arrows are the annual and semi-annual terms. Vectors have lengths proportional to amplitude of seasonal terms and point in the direction of zero cosine phase (figure 2.10). Ellipse errors are given at a 95% confidence level.

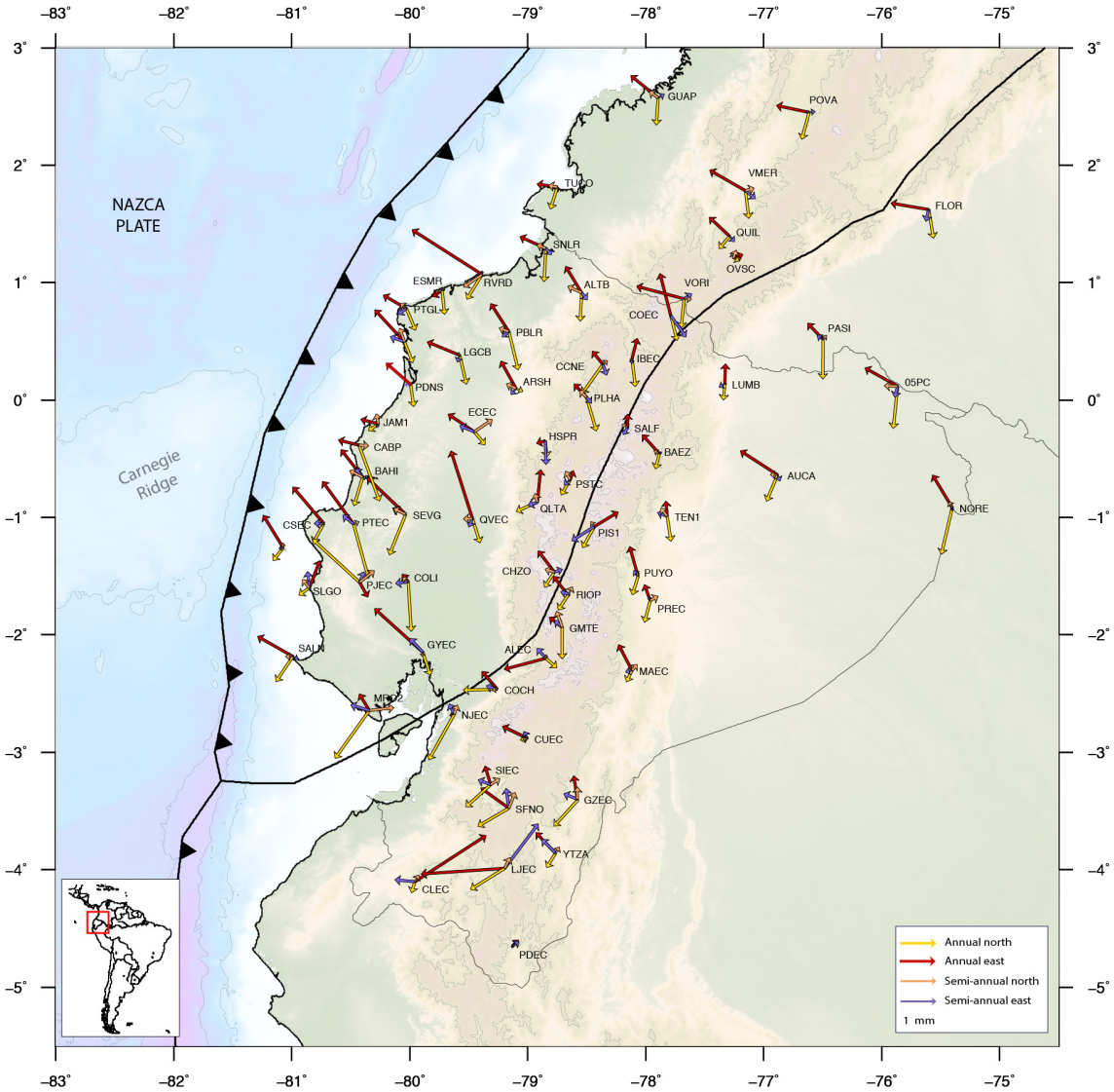

Figure 2.9 – Annual and Semi-annual variations for horizontal components in Ecuador and southern Colombia. Red and violet arrows are the annual and semi-annual terms of east component respectively, yellow and orange arrows are the annual and semi-annual terms of north component respectively. Vectors have lengths proportional to amplitude of seasonal terms and point in the direction of zero cosine phase (figure 2.10).

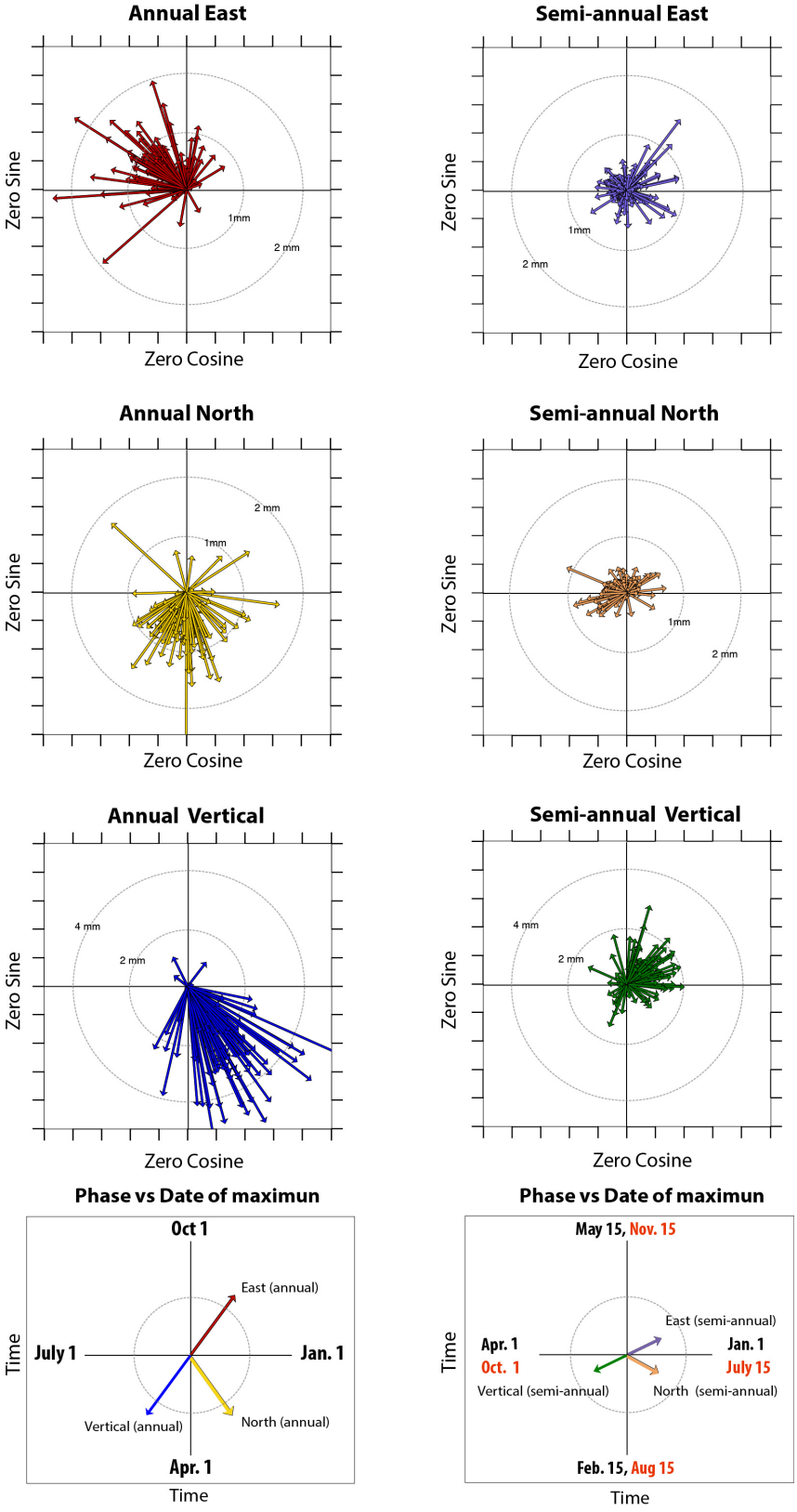

Figure 2.10 – Phasor diagram of annual and semi-annual variations for vertical and horizontal components of figure 2.8 and 2.9. Amplitudes of the estimated sine and cosine parameters are plotted for east, north and vertical components. Annual Phase angle is relative to 1 January - 1 January cycle and Semi-annual phase angle is relate to 1 January - 1 July cycle. The lower plots are the key to correlate phase direction with the date (months of the year) of maximum direction. Phases are referenced to January 1 and time increases clockwise.

2.5.5 Median Approach

Blewitt et al. (2016) proposed a robust approach to estimate velocities for continuous time series of GPS positions in the presence of unknown offsets. It is based on the annual median slopes determination from pairs of data points. The advantage of this approach is that the number of data pairs goes linearly with the number of data $O_{(n)}$. In this way, it does not take into account outliers and offsets elimination, as well as the seasonal terms estimation. Some limitations remain when the GPS station really does have a non-constant velocity (earthquake followed by post-seismic deformation) or when large periodic signals that do not repeat exactly from 1 year to the next, or signals of other frequency. The uncertainties are computed by scaling the median of absolute deviation (MAD) by a factor of 1.4826 with respect to the median trend of data pairs.

2.5.6 Comparison between Least Squares and Median approaches

Figure (2.11) shows horizontal and vertical velocity values comparison between Median and Least Square approaches for a final array of 310 time series. The velocity estimations by Least squares approach was performed following the process described in subsection (2.5.2). The Median approach was automatically performed using an algorithm implemented on PYACS software. Five stations with large data gaps (data gaps upper to 80% of the length of the time series) were removed. Plots **(A)** and **(B)** show a very good agreement on velocity estimates. The east (80%) and north (83%) components show differences less than $\pm$ 0.5 mm/yr. Histograms of plots **(D)** and **(E)** quantify also differences between 1.3 and 2 mm/yr for 10 specific sites which do not have a constant velocity (post-seismic deformation after earthquakes dominates time series) and 5 sites have differences of velocity magnitude larger than 2 mm/yr, which they have not been considered in this analysis. 1 site (BDOS) shows a difference of 1.86 mm/yr in east component due to an exponential increase signal equivalent to 20% of the length of its time series, 1 site (ALEC) shows a difference of 1.63 mm/yr in north component due possibly to the presence of a periodical strange signal (every 2 years), etc. The remaining 20% (east component) and 17% (north component) show differences of maximum $\pm$ 1.2 mm/yr. On the other hand, plot **(C)** and **(F)** show agreements on vertical velocity estimates for $\sim$ 68% of time series at $\pm$ 1.5 mm/yr (plot **F**). The remaining 32% shows values that are quantified in two different ranges: 24% is between 1.5 and 6 mm/yr, and 8% is larger than 7 mm/y (these differences are not registered in plot **(C)** nor plot **(F)**).

Considering; that (1) median approach needs minimum 3 years of data span to be resistant to a single step and tolerate 17% of data being outliers (Blewitt et al. 2016), and (2) least squares approach needs 2.5 years of data to have a minimum influence of seasonal

variations (Blewitt and Lavallée 2002), we attribute velocity differences bigger than 1.0 mm/yr in horizontal components and 2.5 mm/yr in vertical component at the presence of non-linear motions such as post-seismic displacements, data gaps in time series, and maybe when trends involve significant and sustained accelerations. On the contrary, we attribute velocity differences less than 0.5 mm/yr and 1.5 mm/yr in the horizontal and vertical components respectively to the mathematical method used by each technique. Velocity differences between 0.5 and 1 mm/yr in horizontal components are attributed to time series between 2.5 and 3.5 years of data span, which present complicated combinations of offsets, outliers, data gaps, etc. (as is the case of several time series of REGME network).

Figure 2.12 shows an example of GPS time series between 2.5 and 3.1 years of data spam, which have offsets (PREC) and considerable quantity of outliers (SIMI). North component of SIMI station gives a difference of 0.55 mm/yr, east component of PREC station gives a difference of 0.82 mm/yr and east component of PDEC station gives a difference of 1.02 mm/yr.

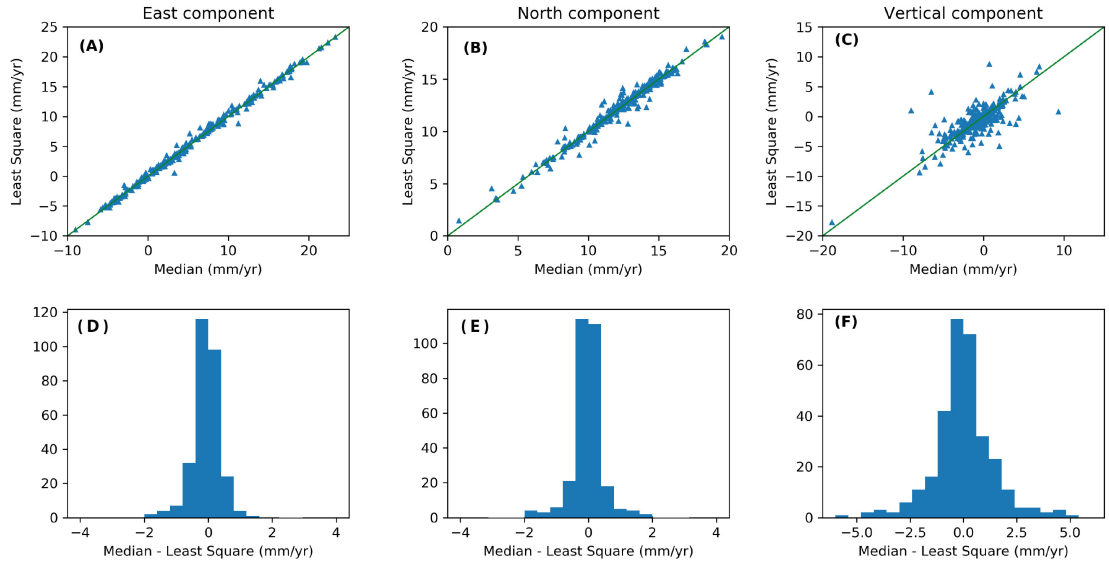

Figure 2.11 – Velocities values comparison: **(A), (B), (C)** show the comparison of velocity values between Median and Least square approaches for east, north and vertical components. Histograms of plots **(D), (E), (F)** show the difference of velocity values between Median and Least square approaches for east, north and vertical components respectively.

Finally, comparing the two approaches from the point of view of computation time, we can mention that median approach allows to perform an automatic velocity estimation of 320 time series in around 3 minutes (calculation performed in a Macbook i7). Otherwise least square approach demands a previous work (inspection and cleaning of time series) before final estimation, which meant a time investment of around 5 weeks. In conclusion, median approach presents $\sim$ 95% of agreement in the velocity estimates at a level of 1

mm of precision for the horizontal components. This precision drops by $\sim 30\%$ in the vertical component. Considering that our objective is to produce a horizontal and vertical interseismic velocity field as accurate as possible, we adopt velocity results obtained from the least squares approach.

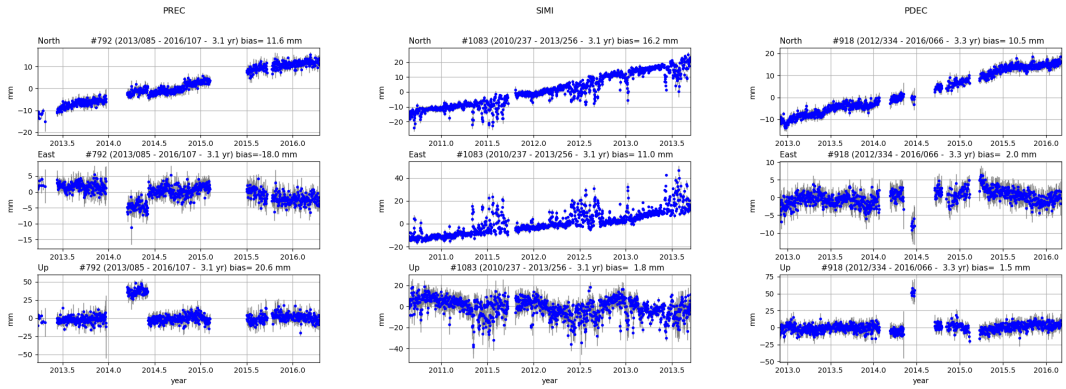

Figure 2.12 – Example of different configurations found in time series with a data span from 2.5 and 3.1 years. PREC station shows 2 offsets relate to antenna replacements and 2 periods of data gaps. SIMI station shows a considerable percentage of outliers and a little data gap. PDEC station shows 2 offsets relate to antenna replacements and 2 data gaps

2.6 Noise Analysis

2.6.1 Noise Characteristics

Long time series of continuous GPS measurements include a significant colored noise due to temporal correlations that finally impacts velocity estimation and its associated uncertainties. These correlations can be characterized by computing a power spectrum. At the highest frequencies the power is frequency independent and at lower frequencies the power increases (amplitude) and can be represented by a power-law (Agnew 1992, Mao et al. 1999, Nocquet 2011, Williams 2003a). The power spectrum has the form:

$$P_{x(f)} = P_\phi \left(\frac{f}{f_\phi} \right)^k \tag{2.11}$$

Where f is the frequency, f_ϕ is the frequency from which the correlated noise is observed, P_ϕ is the spectral power at the frequency f_ϕ and k is the spectral index that reflects the increase of the power as a function of the frequency. k is a real number. For most physical processes, k lies within the range from -3 to 1. Specials cases occur when k takes integer values: for $k = 0$ we have classical white noise, $k = -1$ we have flicker noise and $k = -2$ we have random walk. The geodesic literature uses the term coloured noise to refer to power-law process other than classical white noise (Agnew 1992, Mao et al. 1999, Williams 2003a).

Analyses of global and regional geodetic networks converge to recognize that the noise is best modelled by a combination of *white noise* (random signal with a constant power spectral density) and *flicker noise* (Calais 1999, Mao et al. 1999, Zhang et al. 1997). Other studies have revealed increase on the white noise amplitudes in the vertical component of GPS stations located in South America, which suggest a latitude dependence with a maximum at the Ecuador, possibly related to environment effects, ionospheric or tropospheric water vapor variations (Mao et al. 1999, Williams et al. 2004). Noise amplitudes are generally lower for regional networks than for global networks, thereby white noise is typically in the order of 1-4, 2-5 mm/yr (horizontal and vertical components respectively) in global networks and 0.5-2 and 2-5 mm/yr in regional networks. Flicker noise is in the order of 2-10, 7-23 $mm/y^{1/4}$ for global networks and 3-5, 7-12 $mm/y^{1/4}$ for regional networks (Nocquet 2011, Williams et al. 2004). On the contrary, time series from strainmeters and electronic distance-meters in California, as well as short baseline GPS data from Pinon Flat observatory have showed a power-law process at low frequencies in the horizontal components that are close to random walk process. Although not very well understood until now, random walk noise appears to be related with monument instability due to non-tectonic forces action (such as weathering) near to the surface. Random walk amplitudes can be as high as 3 $mm/y^{1/2}$ for some geodetic data. Whether or not the random walk noise is detectable depends on the length of the time series, the sampling frequency, and the relative amplitudes of the other noise components (Williams 2003a).

In the last years, several researches have focused on studying power-law noise in GPS time series. Most of them consider the methodology proposed by Williams (2003a) and implemented in the CATS software (Create and Analyse Time Series) as one of the most accurate techniques to determine realistic uncertainties. CATS uses a Maximum Likelihood Estimator (MLE) which simultaneously estimates the velocity, annuals and semi-annuals terms, offsets, white noise level, and colored noise level associated to fickler noise (k = -1) and random walk noise (k = -2). It also allows to compute the spectral index k of any time series at the price of increasing computational burden and processing time.

Figure 2.13 shows the estimated spectral index of time correlated noise with CATS software for east, north and vertical components (plots ***A, B*** and ***C***) of our array of 330 stations, in which 20 time series were not processed due to failure of the MLE algorithm. All histograms show that flicker noise is the appropriate choice of power-law noise for all stations evaluated. Histograms of figure 2.14 show amplitudes estimated for east, north and vertical components of the same array of figure 2.13. The mean white noise amplitudes for east, north and vertical components are 0.96, 1.24 and 3.70 mm respectively, and mean amplitudes for power law noise are 2.62, 3.36 and 8.60 mm for the same components.

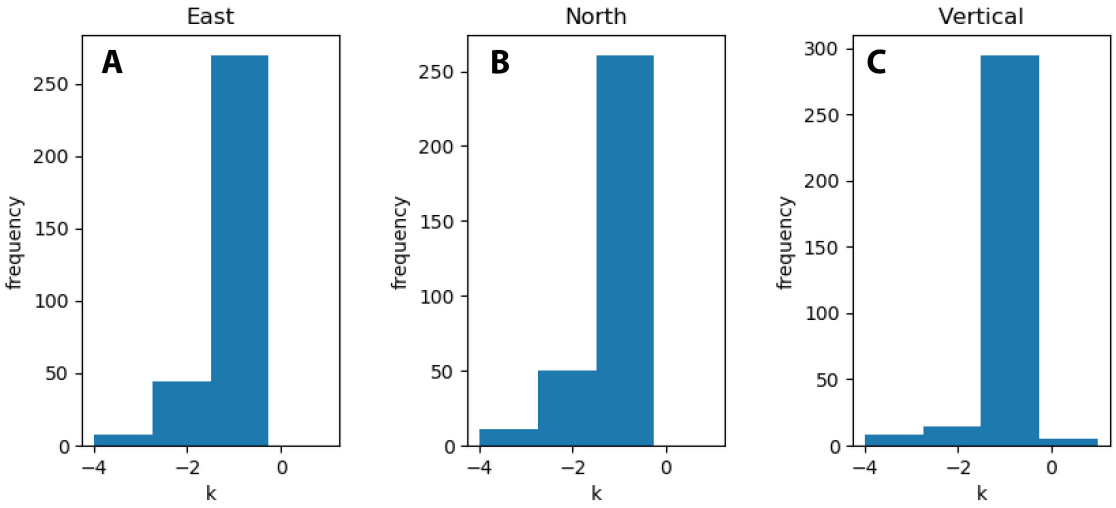

Figure 2.13 – Histograms of the estimated spectral index of time correlated noise for east (plot **A**), north (plot **B**) and vertical (plot **C**) components content within GPS time series. The number of sites analyzed was 310. The histograms show that flicker noise is a suitable coloured noise model for the time series analysed.

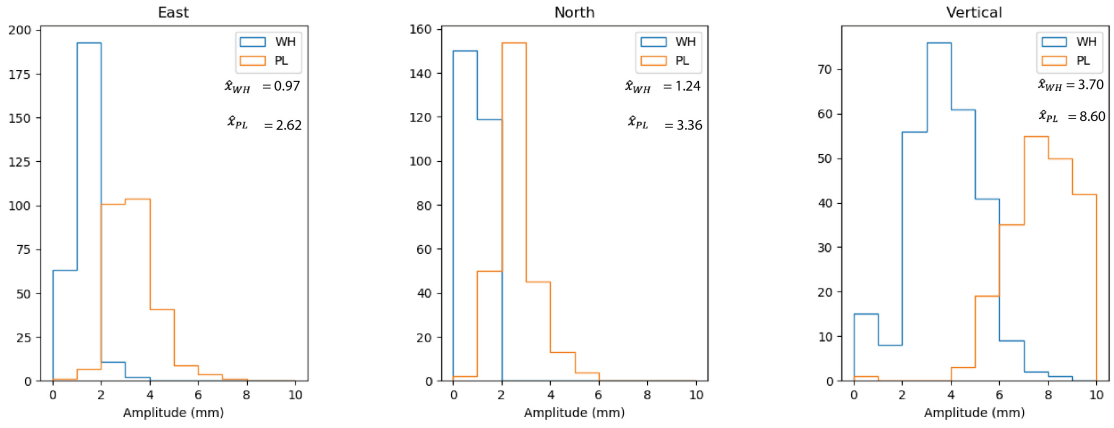

Figure 2.14 – Histograms of white noise and colored noise for north, east and vertical components. Blue and orange lines are white noise and power law amplitudes. *y* axis is the number of sites. A 15 specific stations have power law noise and white noise amplitudes greater than 10 mm which have not been considering neither in the plot nor in the estimation of average value due to these ones possibly have antenna problems (excessive data gaps and/or outliers).

2.6.2 Velocity uncertainties comparison between Least Squares and Median

Figure 2.15 shows horizontal and vertical standard deviation values comparison between Median and Least Squares approaches from the estimated velocities. Standard deviations by Least Square approach was performed with CATS without fixing a priori spectral indices, and standard deviations with Median approach was performed using PYACS software. Plots **(A)** and **(B)** show little scatter values for $\sim$ 90% of sites, which are concentrated in differences of $\pm$ 0.5 mm for horizontal components (plots **D** and **E**). The remaining 10% shows maximum differences of 2 mm for the same components. Conversely, plot **(C)** shows considerable scatter values for $\sim$ 70% of sites that are concentrated in differences of $\pm$ 1.5 mm in the vertical component. The remaining 25% shows maximum differences of 5 mm (plot **F**).

Plots **C** and **F** show that the standard deviation computed with median approach tends to be slightly pessimistic. A possible reason for that could be median approach assumes time series have a constant velocity and their data uncertainties has a gaussian PDF distribution with a minority being outliers (Blewitt et al. 2016). Likewise, a considerable percentage of large uncertainties belong to larger velocity differences discussed in section 2.5.6. A possible explanation could be that these sites have been more influenced by white noise and power law noise, which could be evaluated by looking at the weigthed residual mean squared (WRMS) of each approach. For example: CN33 site has a WRMS of 6 mm with Least squares approach and 10.1 mm with median approach.

On the other hand, CATS shows $\sim$ 85% of sites are subject to a similar type of power law noise (flicker noise) for horizontal components, and $\sim$ 93% for vertical component. However, there is a little percentage of sites suggesting the existence of random walk noise. In general, uncertainties for horizontal ($\sim$ 95%) and vertical ($\sim$ 80%) components have values $\leq$ 1 mm, implying uncertainties in the range of their WRMS. The remaining 5% and 20% (horizontal and vertical components respectively) corresponds to time series that have specific configurations related with antenna problems or maybe sites instabilities.

2.7 Velocity Field

2.7.1 Euler Pole Estimation

The plate tectonics theory has been grounded in describing the relative motion between two plates (rigid bodies) as a rotation around an Euler pole (Lowrie 2007, Stein and Wysession 2003). Using Euler's theorem, it is also possible to fix a plate in space and to find a rotation pole (location) to analyse its intraplate motion. The relative rotation pole can be located using geological and geophysical data records such as spreading

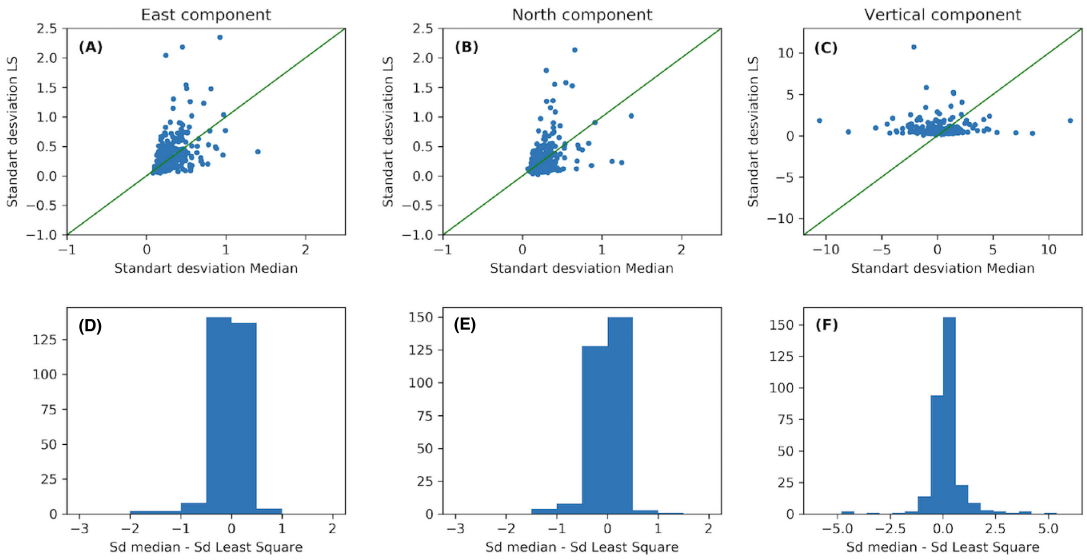

Figure 2.15 – Standard deviation comparison: **(A), (B), (C)** show the comparison of standard deviation values between Median and Least square approaches for east, north and vertical components respectively. Histograms of plots **(D), (E), (F)** show the difference of standard deviation values between Median and Least square approaches for east, north and vertical components respectively.

rates at mid-ocean ridges, transform faults azimuths, earthquake slip vectors and spatial positioning techniques specially global positioning systems (GPS) (Altamimi et al. 2012; 2017, Argus et al. 2010, DeMets et al. 2010; 1990; 1994). The increase of accuracy and density of geodetic measurements in the last years, allow now to quantify plate movements at the level of sub-millimetre par year. It also allows to test the plate rigidity hypothesis at a level better than one millimeter per year for the main tectonic plates (Altamimi et al. 2017). In order to define the stable plate interior of continental or regional studies, the GPS velocities are usually mapped relative to a supposedly stable plate or block close to the region of interest, defined from: either an existing plate motion model or the inversion of velocities at a subset of geodetic sites for a rigid rotation and removing that rotation from the original velocity field (Nocquet et al. 2001).

The basic equation used to estimate a rotation pole (angular velocity) located on the rigid part of the plate p with latitude φ and longitude λ showed in figure 2.16, is expressed by the relation (e.g. Stein and Wysession (2003)):

$$v_{(M)} = \dot{\omega}_p \times r_{OM} \tag{2.12}$$

where v is the horizontal velocity vector of a point M at the Earth surface belonging to the plate p, $\dot{\omega}$ is the angular velocity vector (Euler vector) described by its rotation rate $|\omega|$ that is usually expressed in degrees per million years (°/My) and

pole (θ, ϕ) expressed in degrees. r_{OM} is the vector joining the center of the Earth in point M.

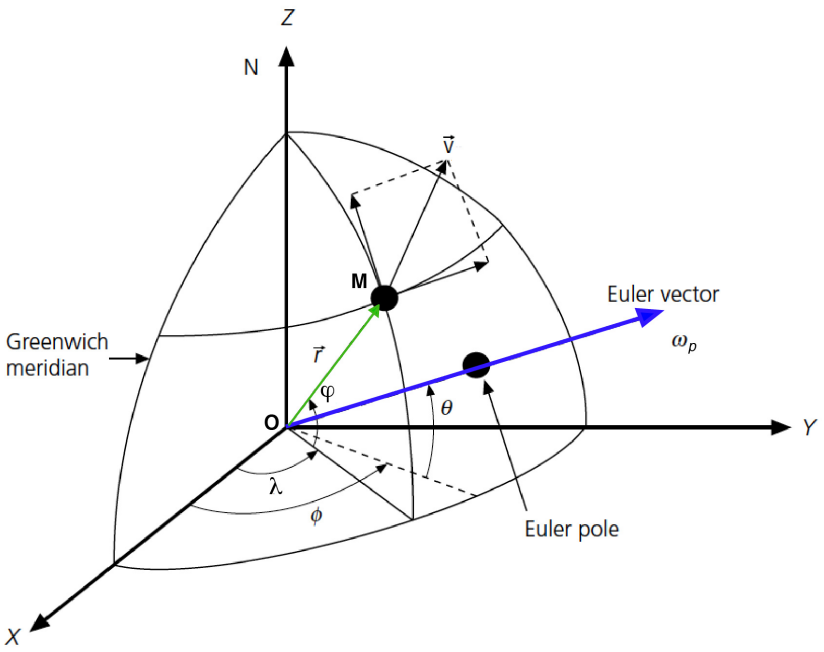

Figure 2.16 – Sketch of rotation pole. The Euler pole (blue arrow) is the intersection of the Euler vector with the earth's surface, and linear velocity at point M is given by equation 2.12, green arrow is the vector joining the center of the Earth in point M. $\vec{v}$ is the velocity vector of M point on the sphere's surface. Modified after (Stein and Wysession 2003)

Equation 2.12 is the fundamental relationship used to determine plate kinematics. If we have a geodetic velocity field v^i with $i \in [1,n]$ and taking into account that spatial geodesy measurements provides 3D velocities in a geocentric Cartesian frame, we determine the $\dot{\omega}_p$ such as (Nocquet 2002):

$$\sum_{i=1}^{n} \left\| \dot{\omega} \times r_{OM} - v^i \right\| \text{ is minimum}$$

$$\text{Where: } v^i = \begin{bmatrix} v_x^i \\ v_y^i \\ v_z^i \end{bmatrix} \text{ and } r_{OM} = \begin{bmatrix} x^i \\ y^i \\ z^i \end{bmatrix}$$

We can expand the cross product of equation 2.12 and rewrite it as a linear equation:

$$v = (z\omega_y - y\omega_z)\,\widehat{x} + (x\omega_z - z\omega_x)\,\widehat{y} + (y\omega_x - x\omega_y)\,\widehat{z}$$

$$\begin{bmatrix} 0 & z^i & -y^i \\ -z^i & 0 & x^i \\ y^i & -x^i & 0 \end{bmatrix} \begin{bmatrix} \dot{\omega}_x \\ \dot{\omega}_y \\ \dot{\omega}_z \end{bmatrix} = \begin{bmatrix} v_x^i \\ v_y^i \\ v_z^i \end{bmatrix} \tag{2.13}$$

Now, we can rewrite equation 2.13 in the form of a linear system:

$$A^i \, \dot{\omega} = v^i \tag{2.14}$$

The model of a rigid rotation on the sphere only predicts the values of the horizontal components (v_e^i, v_n^i). We therefore modify the equation 2.12 using a transition matrix H^i to converts from the geocentric cartesian coordinates to local coordinates (Nocquet 2002). In figure 2.16 at the point M, λ and φ are the geographical longitude and latitude respectively, then:

$$H^i_{geo \to loc} = \begin{bmatrix} -sin(\lambda_i) & cos(\lambda_i) & 0 \\ -sin(\varphi_i)cos(\lambda_i) & -sin(\varphi_i)sin(\lambda_i) & cos(\varphi_i) \\ cos(\varphi_i)cos(\lambda_i) & cos(\varphi_i)sin(\lambda_i) & sin(\varphi_i) \end{bmatrix}$$

$$H^i A^i \, \dot{\omega} = H^i v^i = \begin{bmatrix} v_e^i \\ v_n^i \end{bmatrix} \tag{2.15}$$

Finally, equation 2.15 is solved using weighted least-squares estimation (L2 norm).

2.7.2 Definition of the Stable South America reference frame

The GPS velocity field solution estimated in section 2.5.2 is expressed with respect to a global reference frame (IGS14). This velocity field shows the plate motion in a no-net rotation (NNR) reference frame (Altamimi et al. 2016; 2002), that does not allow us to retrieve signals of tectonic origin (crustal deformation). Therefore, it is necessary to express this solution with respect to stable South America plate (SOAM). In order to perform that, we use the criteria proposed by Nocquet et al. (2001) and Altamimi et al. (2012) for selection of sites to be used in the SOAM Euler pole determination: (1) define a group of stable sites in time (time spam of observations per site greater than 3 years), (2) select sites located on rigid parts of SOAM plate, far away from deforming zones (i.e. plate boundaries), and (3) select sites operating continuously. In the case of south America, sites along the west coast of continent cannot be selected due to large coseismic displacements and long postseismic deformation related to either past or recent big earthquakes like Arequipa (2001) (Perfettini et al. 2005), Maule (2010) (Vigny et al. 2011), Iquique (2014) (Duputel et al. 2015), Illapel (2015) (Klein et al. 2017). Most of the stations located in Argentina and Bolivia does not meet the criteria mentioned above lacking data before the Maule earthquake.

We select an initial set of 40 sites between 1994 and 2019.9, located in the southernmost Argentina, northeast of Bolivia, Brazil, Amazon of Venezuela, Peru and Colombia. We first compute a rigid rotation for the selected sites by means of the equation 2.12. We then remove sites with residuals velocities $\geq$ 1 mm/yr. On an iterative process, we then explore all possible combinations of sites that satisfies a condition of rigid rotation,

Figure 2.17 – Large scale of GPS stations used to define the stable South America (SOAM) reference frame. 17 sites (labelled in red with its corresponding horizontal velocities values) was used to compute the rotation vector, which is located at 18.41°S, 133.28°W, 0.121 °/Myr. Ellipses show 95% of confidence (see table 2.1). Yellow arrows are sites velocities in Nazca, Cocos and Caribbean plates relative to SOAM.

Table 2.1 – Euler Pole and residuals velocities computed to define the stable South America reference frame. R_ve, R_vn, S_ve, S_vn are residuals velocities and formal errors for the east and north components respectively, they are expressed in mm/yr. RN_ve, RN_vn are normalized residuals for the east and north components

```
ROTATION RATE VECTOR
Wx (rad/yr): -1.3718E-09 +- 1.0414E-11
Wy (rad/yr): -1.4564E-09 +-  1.501E-11
Wz (rad/yr): -6.6597E-10 +- 7.2744E-12

ASSOCIATED VARIANCE-COVARIANCE MATRIX (rad/yr)**2
        Wx           Wy            Wz
----------------------------------------
Wx | 1.0846E-22  -1.332E-22  -3.4946E-23
Wy |              2.2531E-22  5.209E-23
Wz |                          5.2916E-23
----------------------------------------

EULER POLE :
longitude (dec. degree)    : -133.29
latitude  (dec. degree)    : -18.41
angular velocity (deg/Myr ):  0.121
ASSOCIATED ERROR ELLIPSE
semi major axis            :  0.47
semi minor axis            :  0.17
azimuth of semi major axis : -32.6
std(angular velocity)      : 0.000

STATISTICS
Number of sites     =         17
Chi**2              =       40.8
Reduced Chi**2      =        1.1
Deg. of. freedom    =         31
A post. var. factor =        1.1

RESIDUALS
site         R_ve       R_vn       S_ve       S_vn      RN_ve      RN_vn
-------------------------------------------------------------------------
ARCA         0.17      -0.04       0.17       0.07       1.02      -0.59
ASC1        -0.22      -0.02       0.40       0.20      -0.54      -0.09
BRAZ         0.04      -0.15       0.11       0.07       0.40      -2.11
CHPG         0.16      -0.18       0.29       0.15       0.55      -1.15
CHPI        -0.02      -0.17       0.11       0.10      -0.20      -1.74
IQTS         0.16      -0.14       0.25       0.10       0.65      -1.43
IQUI        -0.03      -0.13       0.27       0.30      -0.09      -0.42
KOU1         0.17       0.28       0.27       0.48       0.62       0.59
NEIA         0.24       0.06       0.15       0.13       1.58       0.45
PARA         0.29      -0.18       0.22       0.27       1.35      -0.68
POVE        -0.08       0.20       0.11       0.06      -0.74       3.36
PUIN        -0.16       0.18       0.20       0.34      -0.79       0.53
RECF        -0.19       0.15       0.44       0.46      -0.43       0.32
SALU        -0.09       0.18       0.35       0.18      -0.24       1.00
SAVO         0.04       0.14       0.10       0.11       0.40       1.25
TEFE        -0.20      -0.11       0.11       0.23      -1.81      -0.49
UFPR        -0.19       0.26       0.22       0.22      -0.86       1.17
-------------------------------------------------------------------------
rms =       0.16 mm/yr    wrms =       0.15 mm/yr
```

that means a posteriori variance factor near to 1 and residual velocities < 1 mm/yr. We identify a final subset of 17 sites located on the Brazilian craton (12 sites), Ascension island (1 site), French Guyana (1 site), Amazon of Colombia, Peru and Venezuela (4 sites) that satisfies a rigid rotation with residual velocities $\leq$ 0.35 mm/yr, a posterioi variance of 1.1. Therefore, they provide a very good and stable reference frame (see figure 2.17). The motion of the SOAM plate relative to the IGS14 is defined by an Euler pole located at 133.28°W, 18.41°S with an angular velocity of 0.121 °/Myr (see table 2.1).

Comparing our Euler pole location with solution of Altamimi et al. (2017) (see Table 2.2), we can see that both Euler poles are very close (differences of 1.39° in longitude and 0.69° in latitud) as well as the residual velocities ($\leq$ 0.35 mm/yr) suggesting that both solutions are strongly consistent. We can also notice that the angular velocity difference is negligible (0.002 °/Myr).

Table 2.2 – Comparison of Euler pole solutions for South American plate. Table columns list the position in decimal degrees and angular velocity ω in degrees per million years.

	Plate Rotation Pole			Statictics			# Sites
	Lon (°)	Lat (°)	ω (°/My)	WRMS (mm/yr)	A post. factor	χ^2	
ITRF14:Altamimi et al. (2017)	-131.892	-19.097	0.119 + 0.001	0.48			40
This study	-133.28	-18.41	0.121 + 0.000	0.15	1.1	40.9	17

2.7.3 Regional Interseismic Velocity Field

Figure 2.18:**A** shows the obtained regional GPS velocity field relative to the South America reference frame in Colombia, Ecuador and Peru from continuous GPS observations performed from 1994.06 to 2019.9. The density of sites in Ecuador is $\sim$ 50 km from latitude 3°S to latitude 1°N and 70km for the southern. Southern Colombia has a limited number of sites from latitude 1°N to 4°N and from 4°N to 12°N (sites increase inland). In northern and southern Peru, the number of sites are scarce.

The velocity field shows that sites located in southern Ecuador and northern Peru (between latitudes 3°S and 8°S) do not show a deformation gradient in the plate convergence direction, rather these ones indicate a constant pattern of motion directed southeastern with rates of 4 to 5 mm/yr as was previously determined by Nocquet et al. (2014) and Villegas-Lanza et al. (2016b), suggesting a negligible contribution of elastic strain induced by locking in plate convergence. Contrary, in central Peru (between latitudes 11.8°S and 13°S), we found larger velocities in the direction of the plate convergence whose decrease inland. On the coast line, rates of 20 to 22 mm/yr are observed. In southern

Peru, scarce velocities seem to be in the range of 12 to 16 mm/yr, decreasing inland.

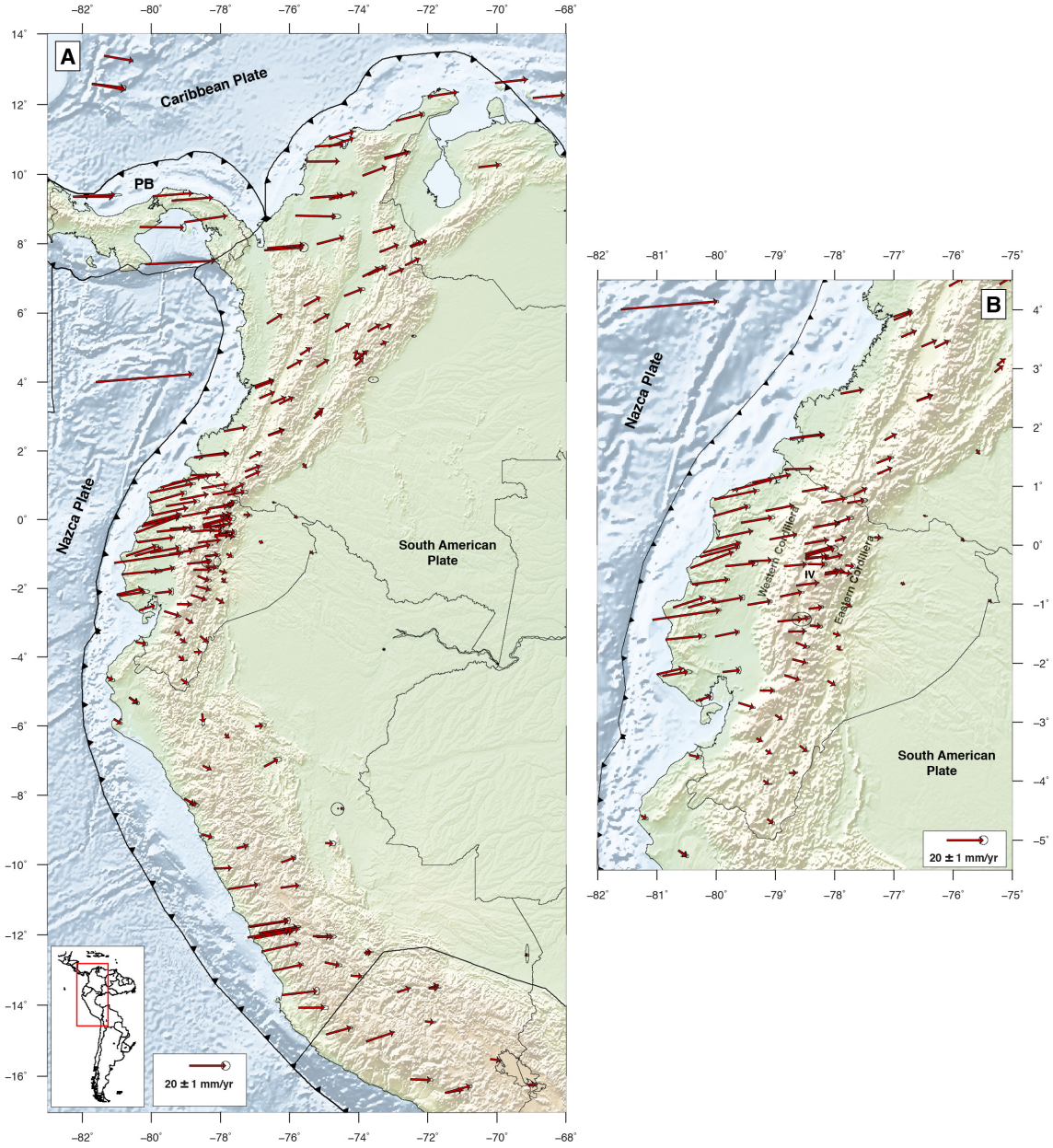

Figure 2.18 – (A) Large scale horizontal velocity field relative to stable South American plate (SOAM). Red arrows are velocities from continuous stations described in 2.1.Ellipses show 95% of confidence. The GPS velocity field is less dense in Peru than in Ecuador and Colombia. GPS Velocities from volcanoes in Ecuador are not present in plot A and plot B. **(B)** Horizontal Velocity field relative to SOAM in Ecuador and southern Colombia. Ellipses show 95% of confidence. IV: Interandean Valley

In Ecuador (between latitudes 2°S and 1°N,) larger velocities directed to northeastward (in the convergence direction) whose magnitude decreases with increasing distance from the trench are observed, that reflect the contributions of two effects: (1) elastic strain induced by locking along the convergence of the Nazca oceanic plate toward South

America and (2) internal long-term deformation of the overriding continental plate as was previously found by Nocquet et al. (2014). Velocities range from 20 to 25 mm/yr along coast line (figure 2.18: **B**) and sites located in the Western cordillera are in the range of 12 to 14 mm/yr. 6.5-8.5 mm/yr for sites in the Interandean valley and 3-4.5 mm/yr for sites in the Eastern cordillera (subandean fold-and-trust belt), defining thus a velocity gradient in the eastern component of the velocity field.

CHAPTER 3

Uncertainties in the Present-Day kinematic of the Nazca plate from GPS observations

Previous models derived from geological data like the Morvel model have left large uncertainties for the recent (since 0.78 Myr) Nazca plate kinematics, questioning the hypothesis of a single rigid plate. For the present-day kinematics, previously published geodetic models were based on continuous GPS observations at only two islands or episodic measurements in the 90's. Such a scarce sampling of the whole plate or lack of redundancy leaves space for several mm/yr biases in the Nazca kinematics estimates. Accurately knowing the present-day kinematics of the Nazca plate is however essential, because it directly impact interseismic models at the Andean margin and controls the slip budget estimates along the Nazca/South America subduction zone.

As part of my research, we re-visit the motion of the oceanic Nazca plate with respect to the South American plate. Our aim is to define a more accurate present-day kinematic model based on new and old continuous GPS observations from 5 sites providing an improved spatial sampling of the entire plate. This chapter has been reviewed by my co-authors and will be submitted for publication at the Geophysical Journal International.

Uncertainties in the Present-Day kinematic of the Nazca plate from GPS observations

P. Jarrin[1*], J.-M. Nocquet[2,3], F. Rolandone[1], H. Mora-Páez[4], P. Mothes[5], D. Cisneros[6]

[1] Sorbonne Université, Institut des Sciences de la Terre Paris, ISTeP, UMR 7193, F-75005 Paris, France.

E-mail*: paul.jarrin@sorbonne-universite.fr

[2] Université Côte d'Azur, IRD, CNRS, Observatoire de la Côte d'Azur, Géoazur, 06560 Valbonne, France

[3] Institut de Physique du Globe de Paris, Université de Paris, Paris, France

[4] Colombian Geological Survey, Space Geodesy Research Group, Bogotá, Colombia

[5] Escuela Politécnica Nacional Instituto Geofísico, Ladrón de Guevara E11-253 Apartado 2759 Quito, Ecuador

[6] Instituto Geográfico Militar de Ecuador IGM-EC, Sector El Dorado, 2435 Quito, Ecuador

SUMMARY

We use a new GPS solution to determine an updated Euler pole describing the present-day motion of the oceanic Nazca plate. We first produce a velocity field including continuous GPS (cGPS) measurements at Malpelo Island offshore Colombia, two sites in the Galapagos archipelago, Easter Island and Salas y Gomez Island in the western part of the plate and Robinson Crusoe Island offshore Chile. Careful analysis of geodetic time series reveals that (1) previous estimates using former cGPS site EISL are biased by several mm/yr eastward due to station malfunctioning (2) velocity north component of cGPS site GLPS at Santa Cruz Island in the Galapagos is impacted by volcanic deformation at the 1-2 mm/yr level, probably caused by the recurrent volcanic activity of the Sierra Negra volcano. Shortening rate of ∼1 mm/yr is observed between Easter Island (cGPS ISPA) and Salas y Gomez Island (ILSG). We attribute this deformation to the elastic deformation induced by rapid opening at the East Pacific rise. Robinson Crusoe Island appears to have ∼4-5 mm/yr abnormally fast East velocity induced by the visco-elastic relaxation following the Maule Mw 8.8 2010 megathrust earthquake. Using this information, we propose a new Euler pole (longitude: -90.93°E, latitude 56.19°N, 0.588 deg/Myr) describing the present-day Nazca/South America plate motion, using horizontal velocity from 5 sites at Malpelo Island, two sites in the Galapagos archipelago, Easter Island and Salas y Gomez Island, with their uncertainty accounting for potential volcanic/tectonic deformation. The proposed Euler pole has a weighted root mean square (wrms) of residual velocities of 0.6 mm/yr, slightly higher than usually observed for other major tectonic plates. Our model predicts a maximum convergence rate at 65.5 ± 0.8 mm/yr at latitude ∼30°S along the Chile trench decreasing to 50.8 ± 0.7 mm/yr in northern Colombia and 64.5 ± 0.9 mm/yr in southern Chile. A comparison with the geological models NUVEL1A and MORVEL indicates constant ∼5 mm/yr per Myr decrease since 3.16 Myr of opening rate along the Nazca/Antarctic plate boundary spreading

centers. Combined with the ITRF2014 pole for the Pacific and Antarctic plates, our derived Euler pole predicts closure at the ∼1mm/yr level for Pacific/Antarctic/Nazca plate circuit. Geodetic velocity at Malpelo Island does not support the hypothesis of an independent Malpelo microplate offshore Colombia. Combining geodetically derived Euler poles with MORVEL estimates for the Cocos plate, non-closure of the Pacific/Cocos/Nazca plate circuit is 9.7 ± 1.6 mm/yr, 30% lower than the 14 ± 5 mm/yr reported in MORVEL model, but still significant. Because our solution spatially samples the whole plate and does not find significant internal deformation, it suggests that non-closure arises from the Cocos plate motion determination in MORVEL.

Key words: Plate motion, Nazca, South America, Pacific, Satellite Geodesy.

3.1 INTRODUCTION

Among the major tectonic plates, the kinematics of the oceanic Nazca plate remains the less well determined. At geological time scales, the kinematics of the Nazca plate is determined from the seafloor spreading rates along its diverging boundaries with the Pacific, Antarctic and Cocos plates, together with the direction of relative motion provided by transform fault azimuths. In the MORVEL model (DeMets et al. 2010), the seafloor spreading rates estimated over the past 0.78 Myr are systematically slower than the estimates based on anomaly 2A averaging the motion over 3.16 Myr that was used in the NUVEL-1A model (DeMets et al. 1994). This result is consistent with a slowdown of the Nazca plate of 5-6 mm/yr since 3.16 Myr, and at longer term, with a progressive slowdown of the Nazca plate motion since at least 20 Myr (DeMets et al. 2010, Norabuena et al. 1999). However, while the Pacific–Nazca–Antarctic plate circuit closure shows agreement with the derived kinematics and plate rigidity hypothesis, closure for the Pacific-Cocos-Nazca circuit at the Galapagos triple junction has a residual of 14 ± 5 mm/yr (95 per cent confidence level), the largest misfit found on all the plate circuits in MORVEL (DeMets et al. 2010), questioning the hypothesis of a single rigid Nazca plate. Subsequently, Zhang et al. (2017) revised the Cocos-Nazca transform fault azimuths at four locations along the Cocos-Nazca plate boundary and found a 3° bias clockwise with respect to the values used in MORVEL. In order to explain this small but systematic discrepancy with respect to the relative Nazca/Cocos motion predicted by MORVEL, Zhang et al. (2017) introduce a new microplate in the northeastern part of the Nazca plate, referred as the Malpelo microplate (see figure 1). However, no clear seismicity or identified active fault separates the hypothetized Malpelo microplate from the Nazca plate, leading Zhang et al. (2017) to propose a diffuse oceanic boundary, approximatively located between the southern tip of the Panama transform fault and extending eastward to the trench offshore southern Colombia. Nonethless, introducing a Malpelo microplate only marginally reduces the non-closure for the 0.78 Myr Nazca-Cocos-Pacific plate motion circuit, leaving 11-12 mm/yr to be explained.

An alternative explanation for the non-closure problem is that the Nazca plate is not rigid and undergoes internal deformation. As the oceanic lithosphere moves away from the spreading centre, the progressive cooling should induce thermal contraction resulting in horizontal intraplate contractional strain rates. One-dimensional models suggest strain rates as large as 10^{-9} yr^{-1} for a 1

Myr old oceanic lithosphere (Kumar and Gordon 2009), decreasing to 10^{-10} yr^{-1} for a 10 Myr old lithosphere, a value in agreement with slight systematic deviations of the relative motion observed between right- and left-lateral transform faults (Mishra and Gordon 2016). Integrated over the whole Nazca plate which has a size of 5000x4000 km^2, such strain rates could convert into 0.5-1 mm/yr departure from a rigid motion. Although still too small to solve the Pacific-Cocos-Nazca circuit non-closure issue, thermal contraction should now be detectable from spatial geodesy as longer time series are available.

The present-day kinematics of the Nazca plate has been estimated using spatial geodesy. Most of the studies relied on only two sites located at Easter Island and at Santa Cruz Island in the Galapagos Archipelago (figure 3.1) (Altamimi et al. 2012; 2017, Angermann et al. 1999, Norabuena et al. 1999, Sella et al. 2002, Vigny et al. 2009). The latest estimate from Altamimi et al. (2017) finds negligible residuals estimating an Euler pole using these two sites (weighted root mean square, wrms=0.23 mm/yr). Fitting an Euler pole (3 parameters) using only two GPS sites provides 4 observations to estimate 3 parameters, resulting in a poor control of the results. Indeed, although significant relative motion along a great circle joining the two islands would be seen in the residuals, any abnormal velocity for the component perpendicular to the great circle would not be detectable. Alternatively, GPS survey mode measurements at San Felix and Robinson Crusoe islands offshore Chile (figure 3.1) providing a better spatial sampling of the Nazca plate were used by Angermann et al. (1999). Then, Kendrick et al. (2003) use longer time series and an additional campaign site in the Galapagos. They find residual velocities with respect to the best fitting rotation pole are up to 2-3 mm/yr at most sites, but become less than 0.5 mm/yr if the site at Easter Island is excluded. In that latter case San Felix, Robinson Crusoe islands and sites on two Galapagos islands are assumed to represent the stable part of the Nazca plate. In that view, the residual velocity of EISL site in Easter Island is 6.6 mm/yr, suggesting that Easter Island is located in a deforming zone.

Although the impact of excluding Easter Island from the Nazca plate kinematics estimate has minor influence on the Nazca/South America convergence rate along the northern and central Andes, it leads to differences as large as 8 mm/yr (10-15% of the convergence rate) along the southern Andes margin (Vigny et al. 2009), potentially inducing biases in interseismic models and slip budget estimates along the Chilean subduction zone.

In the present study, we use a new GPS velocity field (figure 3.1) to revisit the motion of the Nazca plate with respect to South American plate and discuss additional geodetic uncertainties in terms of possible tectonic and volcanic deformations. Compared to previous studies, we first benefit from longer time series over a period of time where noise in GPS time series has been reduced compared to the 1990's, allowing more reliable velocity estimates. Replacement of historical GPS sites, EISL at Easter Island by ISPA and GALA in the Galapagos (Santa Cruz Island) by GLPS further highlight how equipment and site change can impact velocity estimates. Two new cGPS sites allow us to re-evaluate the ability of Easter Island and Santa Cruz Island in the Galapagos

archipelago to witness the overall kinematics of the Nazca plate. A cGPS site on the Robinson Crusoe Island reveals the contribution of large scale viscoelastic relaxation from past great earthquakes at the southeastern tip of the plate. Finally, a site on the Malpelo Island offshore Colombia provides constraint on a possible independent microplate. Given the small number of available sites, each time series is carefully analyzed and we perform simple elastic models to evaluate the potential impact of several deformation processes. This study allows us to present a best selection of sites, with velocities and realistic uncertainties, to propose new values for the Nazca/South America Euler pole.

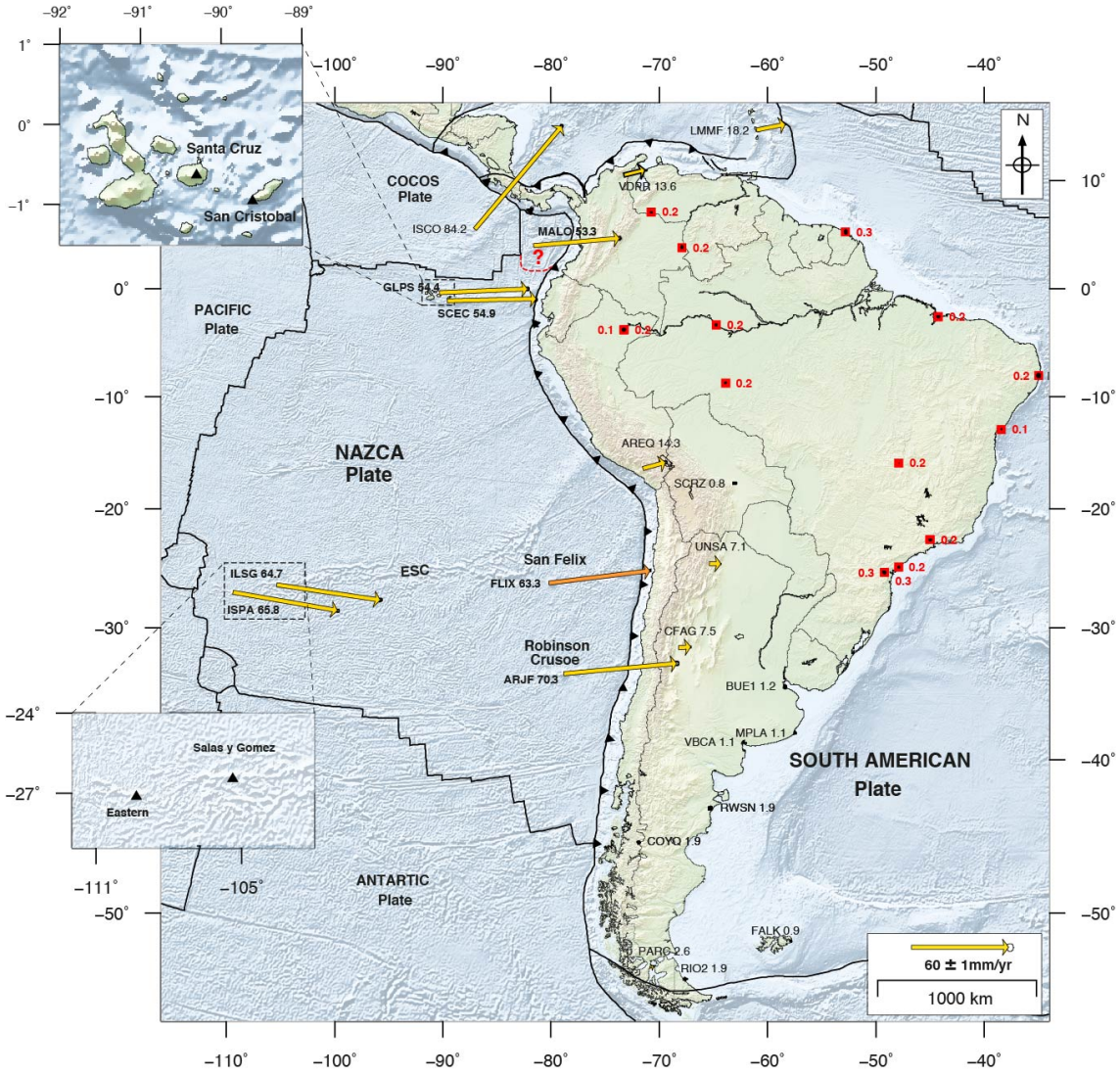

Figure 3.1 – Large scale GPS stations used to define the stable South America (SOAM) reference frame. Red squares are sites used to compute the SOAM pole. Yellow arrows are velocities relative to SOAM reference frame. Ellipses show 95% confidence. Red dashed line is the Malpelo microplate boundary proposed by Zhang et al. (2017). Black triangles, inset plots, are the location of Eastern, Salas y Gomez, Santa Cruz, and San Cristobal islands. Orange arrow is the velocity reported by Kendrick et al. (2003) at the San Felix Island. ESC: Easter Seamount Chain.

3.2 GPS DATA ANALYSIS

Our data set includes observations from regional continuous stations operated by the Instituto Geofísico of Ecuador (Alvarado et al. 2018, Mothes et al. 2013), the Instituto Geográfico Militar of Ecuador, Servicio Geológico Colombiano (Mora-Páez et al. 2018), Centro Sismológico Nacional (Báez et al. 2018), Red Argentina de Monitoreo Satelital Continuo (Piñón et al. 2018), COCONet Project (Community 2008), and well distributed IGS stations from the global network of the International GNSS Service for Geodynamics (Johnston et al. 2017). In total, the final data set is composed of 57 permanent sites located on Nazca, Cocos, South America, Caribbean, Pacific and Nubia plates.

Daily GPS observations were processed in sessions of 24 hours using the GAMIT/Globk software package release 10.71 (Herring et al. 2015; 2018) following a classical approach for geodynamic consisting in two steps. We first obtain free daily solutions by reducing double-difference of phase to coordinates. At this step, we used earth orientations parameters provided by the IERS, final combined orbits models from the International GNSS service for Geodynamics (IGS) (Dow et al. 2009). We account for position variation of antenna phase centres as a function of satellite elevation and azimuth using the phase centre offsets (PCOs) and variations (PCVs) tables recommended by the IGS. Elastic response effects to ocean tides were modelled using the FES2004 model (Lyard et al. 2006), as well as polar and solid-earth tides following IERS/IGS (1996) standards McCarthy (1996). We use the ionosphere-free combination to eliminate the wave delay induced by the ionosphere, and a double difference in LC phase measurements is performed to eliminate clock errors in receivers and satellites. We use the Vienna Mapping Function model (VMF1, (Boehm et al. 2006)) together with a zenithal delay every 2 hour to model the GPS signal delay in the troposphere. In the second step, we express our regional solutions with respect to the cumulative up-to-date solution from the global International GNSS Service (IGS) network (Rebischung et al. 2016). This IGS solution is up-to-date of the documented discontinuities and offers a parametric model for reference sites impacted by post-seismic deformation. Daily Helmert parameters are estimated through an L1 estimator implemented in the PYACS software. Finally, our solution spans the 1994-2019.9 period and includes 8 sites located on the Nazca plate: MALO (Malpelo Island), GLPS and GALA (Galapagos: Santa Cruz Island), SCEC (Galapagos: San Cristóbal Island), ILSG (Salas y Gomez Island), EISL and ISPA (Easter Island), and ARJF (Juan Fernandez Island) (figure 3.1).

In order to ensure a reliable interpretation, we only retain time series of positions of at least 2.5 years of measurement to avoid bias due to seasonal variations in the secular velocity estimates (Blewitt and Lavallée 2002). Time series of positions are then visually inspected in order to identify discontinuities or offsets caused by undocumented antenna changes, to remove remaining outliers and to exclude specific time window showing a non-linear evolution in the general trend. For sites on the South America plate, we remove periods of non-linear post-seismic motion following large subduction earthquakes. We then simultaneously estimate velocity, annual and semi-annual terms, and offsets using the formulation proposed by Bevis and Brown (2014). Spectral index of colored

noise and noise magnitude are estimated using the maximum likelihood estimator implemented in the CATS software (Williams 2008) to deduce realistic velocity uncertainties. Results show spectral indices about -1 for ∼95% of the time series evaluated, showing a combination of white noise and flicker noise as found in many studies worldwide.

Table 3.1 – GPS velocities with respect to South America for sites located on the Nazca plate. Longitude and Latitude in decimal degrees. Ts: time span of observation in years

Site	Lon.	Lat.	Ve	Vn	σVe	σVn	Ts	WRMS Ve	WMRS Vn
	deg	deg	mm/yr	mm/yr			yr	mm	mm
ARJF[a]	-78.833	-33.629	70.0	6.4	0.48	0.57	6.2	3.2	2.7
EISL[b]	-109.383	-27.148	66.0	-12.1	0.51	0.37	7.0	6.0	1.9
FLIX[c]	-80.088	-26.297	62.8	7.7	0.2	0.2	7.3		
GALA	-90.304	-0.742	55.2	1.5	0.53	0.45	6.3	1.7	2.0
GLPS	-90.304	-0.743	54.4	2.3	0.40	0.31	8.5	1.6	1.0
ILSG	-105.362	-26.473	64.0	-9.5	0.51	0.41	5.0	2.9	2.5
ISPA	-109.344	-27.125	64.8	-11.3	0.28	0.38	13.0	2.0	3.0
MALO	-81.606	4.003	53.1	4.6	0.39	0.40	5.2	1.8	2.1
RBSN[c]	-78.840	-33.630	62.5	7.8	0.40	0.60	6.7		
SCEC	-89.615	-0.903	54.9	1.3	0.32	0.42	4.0	2.3	1.4

[a] Value estimated accounting for an offset at the time of the Illapel Mw 8.3 2015.71 earthquake
[b] Value estimated excluding the 2001.5-2003.1 period
[c] Values reported by Kendrick et al. (2003)

We validate our results against the velocity estimates published by the Nevada Geodetic Laboratory (Blewitt et al. 2018). In overall, we find non-significant differences (< 0.3 mm/yr) except at ARJF, EISL, GALA, and GLPS sites where differences of 0.5-1 mm/yr are due to the presence of large periods of non-linearity that we discuss in the following sections. This comparison indicates a very small influence on velocity estimates of our regional reference frame realization compared to a global network solution. We then compute a rigid rotation by minimizing the horizontal velocities from 17 sites sampling the stable part of the South American plate (SOAM) [ARCA, ASC1, BRAZ, CHPG, CHPI, IQTS, IQUI, KOU1, NEIA, PARA, POVE, PUIN, RECF, SALU, SAVO, TEFE, UFPR] (figure 3.1, table 2 in the supporting information). The wrms is 0.15 mm/yr, with a reduced chi-square of 1.1 indicating a good agreement between velocity uncertainty and the residuals. Our Euler pole in the ITRF2014 for the South America plate is -133.28°E, 18.4°S, 0.121°/Myr close to the value proposed by Altamimi et al. (2017).

3.3 ANALYSIS OF POSSIBLE SOURCES OF DEFORMATION

Unlike the South America plate where many sites provide a high redundancy and allow outliers detection, the oceanic Nazca plate hosts only 6 different measurements locations at 8 GNSS sites. In the following section, we describe a careful analysis of the velocity estimates for each site and

assess the order of magnitude of potential sources of deformation before to proceed to the Euler pole calculation.

3.3.1 Easter and Salas y Gomez Islands

Geodetic velocity

On Easter Island, EISL site has been operating from 1994 to 2005 and ISPA site from 2004.12 to present. Both sites are located ∼4.0 km one from the other. We find that, regardless of the period considered to estimate the velocity, EISL and ISPA, have a north velocity component which is consistent at the sub-millimeter per year level. On the contrary, the east component of velocity appears to be dependent on the selected period. During EISL lifetime, equipment changes are documented at three dates for which offsets parameters are added to the least-squares estimate of trend. For the observation period 1994-2002.0, we find a velocity of Ve=66.9 mm/yr and Vn=-11.6 mm/yr (norm=67.9 mm/yr) in agreement at a 1 mm/yr level with the values proposed by Kendrick et al. (2003) (Ve=67.9, Vn=-12.0, norm=69 mm/yr) using the same observation window. However, figure 3.2 also shows that the trend during the 2001-2003.1 period appears to be abnormally large compared to the trend observed during the 1994-2001 period. Velocity estimates range from 66.2 mm/yr when excluding the 2001-2003.1 period to 67.9 mm/yr when including it.

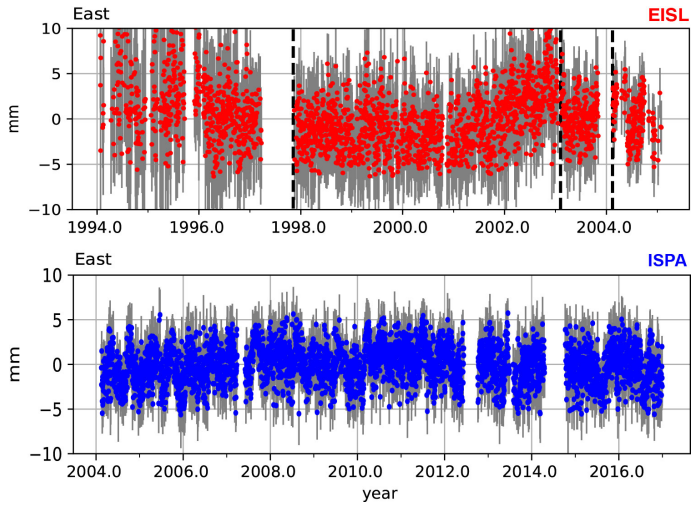

Figure 3.2 – Detrended time series of daily positions for the east component of EISL and ISPA cGPS sites. Vertical dashed lines show antenna replacement dates according to the International GNSS service.

ISPA benefits from ∼13 years of continuous observation from 2004.1 to 2017 without any documented potential offset (except antenna cable replacement) nor obvious transient behavior during this period (figure 3.2). The estimated velocity using least-squares is Ve=64.8 and Vn=-11.3 (norm=65.8 mm/yr). This value is in agreement within the uncertainty with the lowest estimates for EISL. We checked that the dependence of the east velocity estimate on the considered period does not arise from artefact in our solution by performing the same analysis using UNR ((Nevada University) (Blewitt et al. 2018) and IGS time series, and found a similar range of velocity

estimates at EISL and ISPA.

In addition to the influence of the selected period on the estimated east velocity, we investigate the noise property of the residual time series. For both sites, we compute the Power spectral density (hereinafter PSD) using the Hector package (Bos and Fernandes 2015, Bos et al. 2013). The obtained PSDs are similar to previous findings for global and regional cGPS networks, with a flat spectrum at high frequencies indicating white noise, and a spectra slope of roughly -1 at frequencies lower than 20 cpy (cycles per year), consistent with flicker noise (see Figure 1 and Table 3 in the supporting information). No random-walk that could suggest a monument instability is detected. The PSD obtained for EISL has a power value about twice the one for ISPA, at all frequencies. Lower noise for the 2004-2017 period compared to 1994-2003 is consistent with the progressive densification of the IGS network, the improvement of satellite tracking capabilities of GPS receivers, and the improvement of orbits accuracy through time (Griffiths 2019).

Aside this improvement observed worldwide, figure 3.3 shows the daily average multipath Root-Mean-Square (RMS) values for MP1 and MP2, that are data quality indicators of the raw data collected by the receiver together with the residual east time series at EISL. The visual comparison highlights correlations between anomalous values or trend changes of MP1 and MP2 with apparent transients or increased noise in the EISL time series. This likely suggests that the non-linear behavior of EISL time series arises from EISL receiver tracking problems or from changes in the environment surrounding the antenna (UNAVCO 2004).

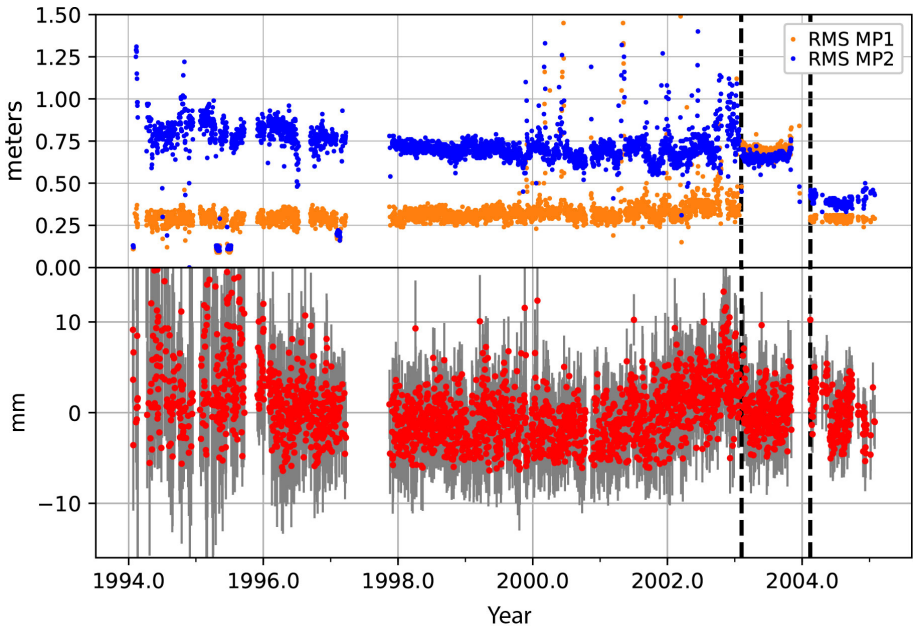

Figure 3.3 – Comparison between Average multipath daily values and the detrended daily positions time series from the east component of EISL site. Black dashed lines are the antenna replacement dates.

This comparison suggests that previous velocity estimates for EISL might be biased at a few millimeters per year level, explaining some discrepancies among previous studies. Therefore, the velocity estimate for ISPA is more robust and is a few mm/yr slower than previously published results (Altamimi et al. 2012, Angermann et al. 1999, Kendrick et al. 2003).

Possible source of deformation

Kendrick et al. (2003) interpret EISL velocity as being not consistent with a rigid motion defined by sites in San Felix, Robin Crusoe islands and Galapagos (GALA). We saw in the previous section that using the more reliable ISPA velocity explains about 50% of their residual (6.6 mm/yr). The deformation in that part of the plate may be evaluated using the results for ILSG site, located on the Salas y Gomez Island, 400 km east of Easter Island. We first evaluate the rate of length change along a great circle joining ISPA to ILSG, a quantity which is insensitive to rotation on the sphere. We find a shortening rate of 1.1 ± 0.5 mm/yr, still significant at a 95% confidence level and equivalent to 2.7 ± 1.2 nstrain/year. This value is one order of magnitude larger than the possible effect of oceanic thermal contraction as we discussed in the introduction (Kumar and Gordon 2009). Both islands are emerged parts of the Easter Seamount Chain, a ∼2500 km long structure made of volcanic material and numerous seamounts, extending east of the East Pacific Rise, to the southern tip of the Nazca Ridge offshore southern Peru (figure 3.1). At Easter Island, the latest stage of volcanic activity was dated at 110 kyr (Vezzoli and Acocella 2009), but the most recent lava flows on Easter Island are thought to be less than 2000 years old (Global Volcanism Program, Smithsonian Institution). While most of the Easter Seamount Chain hosts little or no seismicity, the ISC seismic reviewed catalog from 1976 to 2018 (Engdahl et al. 2020) highlights an average of 2-4 earthquakes per year occurring between and around both islands (Figure 3.4). A swarm of 12 shallow (<15 km depth) earthquakes occurred within 20 days in December 2000 between the two islands (∼200 km from both island) where sonar images and bathymetric data have shown evidence of volcanic activity (Lui 1996, Rodrigo et al. 2014). Seismicity distribution therefore probably witnesses several spots of more active magmatism or volcanism at the Eastern Seamount Chain. The diversity of focal mechanisms (figure 3.4) indicates heterogeneous stress induced by magmatic activity rather than by a regional tectonic stress. In the absence of additional measurements, the size and magnitude of the volcanic deformation occurring at the Easter Seamount Chain between Easter Island and Salas y Gomez island remains unknown. We can only comment that the large (∼200 km) distance between the seismicity location and both islands most probably prevents significant volcanic deformation to bias velocity at a 1 mm/yr level. As an element of comparison, no strain would be detected at 200 km away for the active volcano centers in the Galapagos for instance (see section 3.3.2).

As an additional attempt to understand the cause of the contractional strain rate observed between ISPA and ILSG, we evaluate the effect resulting from the far field elastic deformation induced by continuous magma injection at the fast spreading center located ∼350 km west of Easter Island. At a first glance, such a distance appears to be very large to cause a significant effect at Easter Island, but opening rates are among the largest on Earth almost reaching 15 cm/yr

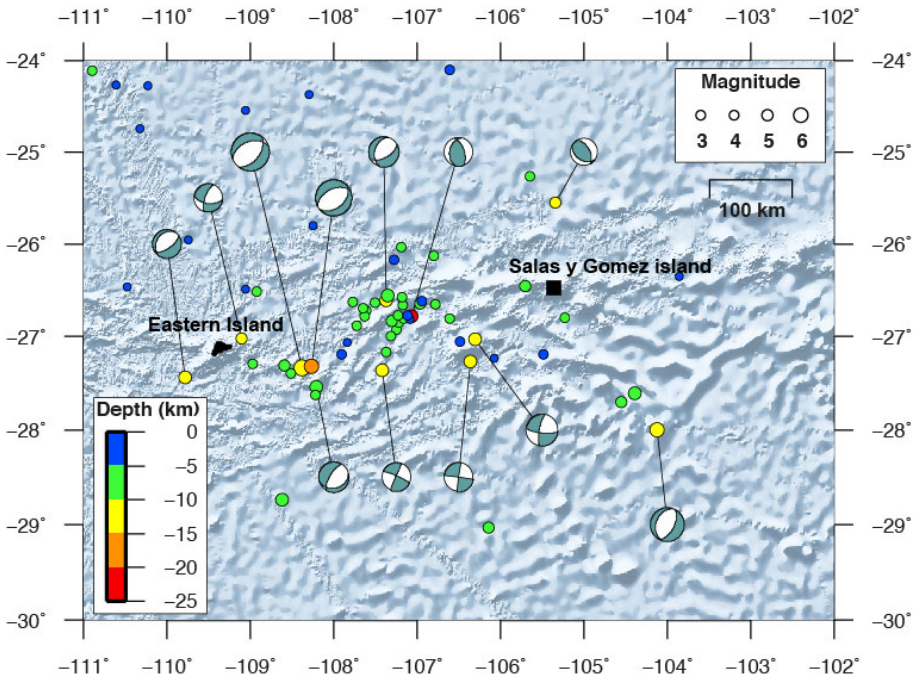

Figure 3.4 – Intraplate seismicity in areas surrounding to the Easter and Salas y Gomez Islands. mb $>$ 3.0 earthquakes are plotted by small color-filled circles. Earthquake reviewed catalog is from the International Seismological Centre (ISC) (Engdahl et al. 2020) and focal mechanism solutions are from the Global Centroid Moment Tensor (gCMT) (Ekström et al. 2012)

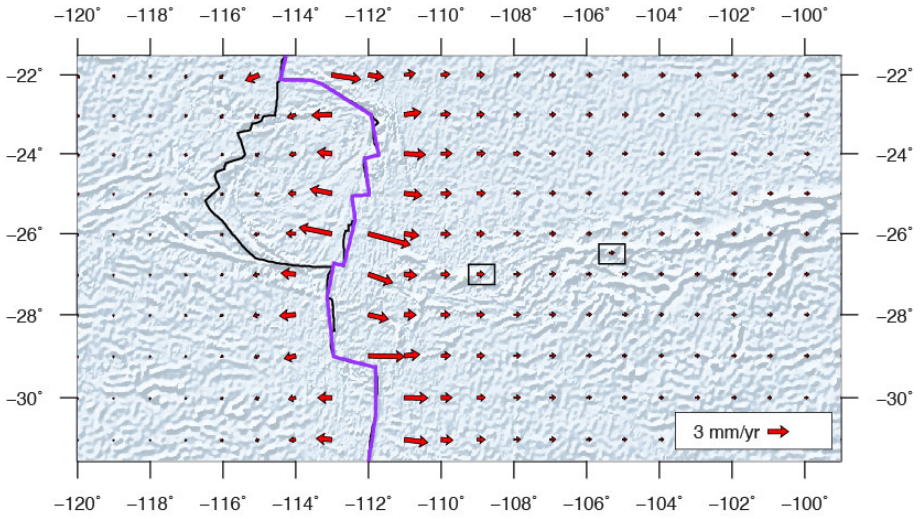

Figure 3.5 – Dyke model at the southwestern end of the Pacific/Nazca plate boundary. Red arrows are the predicted elastic contributions by locking rectangular dislocation elements. Unfilled black squares are the Easter and Salas y Gomez islands location.

(DeMets et al. 2010), potentially resulting in a wide area impacted at the mm/yr level. The most similar geodynamic environment where geodetic observations are available is Iceland where the relative motion of Eurasia with respect to North America results in an opening rate of ∼20 mm/yr. Geodetic results from Árnadóttir et al. (2009) show that contractional strain rates are observed at 100-200 km away from the spreading centers. Contractional strain rates, that is decreasing velocity magnitude with increasing distance from the spreading center are caused by the elastic response of the crust to the pressure induced by magma intrusion at the spreading center. This effect can be simply modelled using vertical dislocation with tensile slip, where the depth extension of the dislocation controls the spatial extend over which significant effect will be observed at the surface. For Iceland, Árnadóttir et al. (2009) obtained dislocation bottom depth in the range of 5-10 km. Compared to Iceland, the fast spreading rates along the East Pacific Rise certainly results in reduced elastic thickness, both at the spreading center and away of it as Nazca oceanic lithosphere travels faster. Elastic thickness of the lithosphere near the East Pacific Rise on the Easter and Salas y Gomez islands (along the Easter Seamount Chain) have been estimated from bathymetry and gravity data to ∼2.5 ± 1 km (Kruse et al. 1997, Lui 1996), a value consistent with 2-3 km at the Mid-ocean ridge axis proposed by flexural studies, geological interpretations, and thermo-mechanical models (Behn and Ito 2008, Engeln and Stein 1984, Mooney 2015).

In order to explore the potential impact of elastic deformation that would add to the Nazca plate velocity at ISPA and ILSG, we simulate the velocity field induced by tensile slip extending from the surface to 3 km depth using an opening rate of 140 mm/yr (DeMets et al. 2010). Between latitudes 22°S and 27°S, several studies identified an independent Easter microplate, embedded between the Nazca and Pacific plates, whose boundary accommodates a fraction of the Nazca/Pacific motion. Because the precise kinematics of the Easter microplate is uncertain and because our aim is to evaluate the order of magnitude of possible elastic deformation, we choose to attribute the whole Nazca/Pacific motion as the tensile slip along the Easter microplate/Nazca boundary. Results show elastic contributions of 1.1 and 0.7 mm/yr at ISPA and ILSG sites respectively, mainly impacting their East components (figure 3.5). This contribution increases to 1.4 and 0.8 mm/yr if we extend the depth of vertical dislocations to 4.0 km. For the horizontal baseline length rate of change between ISPA and ILSG, we obtain 0.4-0.6 mm/yr, a value that is consistent with the GPS results (1.1 ± 0.5 mm/yr). This calculation indicates that ISPA east velocity might be faster than the motion of the Nazca plate at the level of 1mm/yr and ILSG at the level of half a mm/yr. These potential effects can be accounted for either as additional uncertainties or as a priory correction to test their influence in the calculation of the Nazca plate rotation pole. We discuss the impact of these corrections on the Nazca Euler pole estimation in section 3.4.

3.3.2 Galapagos Archipelago

Similarly to Easter Island, geodetic measurements on the Galapagos archipelago have been used in all estimates of the Nazca plate motion. GALA site on Santa Cruz Island provided data starting in 1994, with daily data from 1996.1 to 2002.9. It has then been replaced by GLPS installed

33 m from GALA, with continuous data since 2003.0. Here, we use 4 years of data from an additional cGPS site SCEC operated by the National Geographical Institute of Ecuador (IGM). SCEC is located on San Cristóbal Island, about 90 km east from Santa Cruz and ∼170 km away from the active volcanic centers. Thus, SCEC allows to evaluate potential bias in GALA and GLPS velocities induced by volcano deformation.

Geodetic Time Series

SCEC benefits from 4 years of observations from 2013.8-2017.75, with only one documented offset. The velocity estimate is 54.9 mm/yr (Ve=54.9 mm/yr and Vn=1.3 mm/yr). Figure 3.6 shows the time series at the three sites in the Galapagos detrended using the velocity estimated for SCEC. As for EISL and ISPA, the newest site GLPS time series shows a much lower level of noise compared to GALA. Visual inspection of the GALA time series highlights a departure from constant linear motion with a 5-6 mm northward transient during the 1997-1998 period. It is then followed by a ∼2 mm/yr southward motion. Smaller changes of velocity might also exist for the 2000-2002 period on the East component. For GLPS, without any documented antenna change, a slight reversal of motion is observed around 2008 for the north component. Pre-2008 and post-2008 velocity differs by ∼1 mm/yr on the north component.

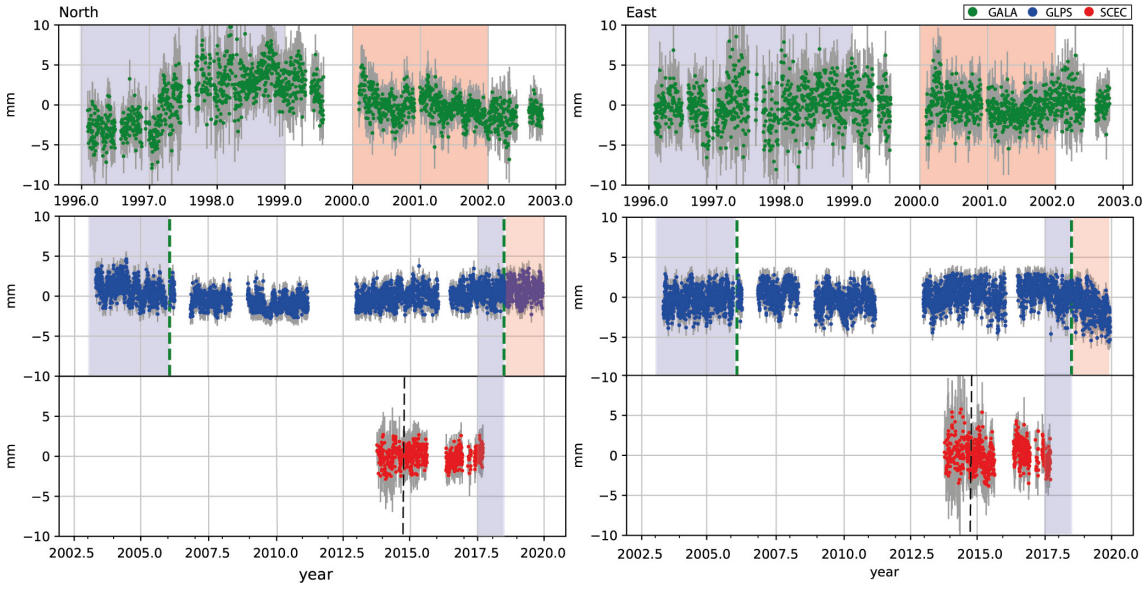

Figure 3.6 – Residuals of Daily horizontal position GPS time series of GALA, GLPS, and SCEC. The SCEC velocity is removed from the trend of GALA and GLPS. Light pink and light blue stripes are time windows of volcanic deflation and inflation observed at Sierra Negra volcano respectively. Green dashed lines depict the onset of Sierra Negra's eruptions in 2005.8 and 2018.7. Black dashed line is the antenna replacement date.

Volcanic Deformation

In the Galapagos archipelago, active volcanic centers are located on Fernandina and Isabella islands, at 140 and 90 km west to southwest from GALA/GLPS and 170 and 220 km west

from SCEC. During the 1994-2018 period, Fernandina volcano and Sierra Negra volcano on Isabella Island have experienced several episodes of large deformation at their calderas. Most of them ended in volcanic eruptions while for a few others high seismicity rate, degassing, and ground deformation occurred without eruption (figure 3.7). Interferometric synthetic aperture radar (InSAR) and GNSS data identified large inflation and deflation processes at the Fernandina, Sierra Negra and Alcedo volcanoes, suggesting complex magmatic systems composed of one or two shallow magma reservoirs (Bagnardi and Amelung 2012, Baker 2012, Chadwick et al. 2006, Galetto et al. 2019, Geist et al. 2008). Although many studies have focused on estimating the geometry and volume of these shallow magma reservoirs, their deeper portions that would induce larger scale surface deformation remain uncertain. Past and recent volcanic processes at the Fernandina-Alcedo, and Sierra Negra-Cerro Azul volcanoes suggest interactions between them that could possibly fed by a common deep magma reservoir (Baker 2012).

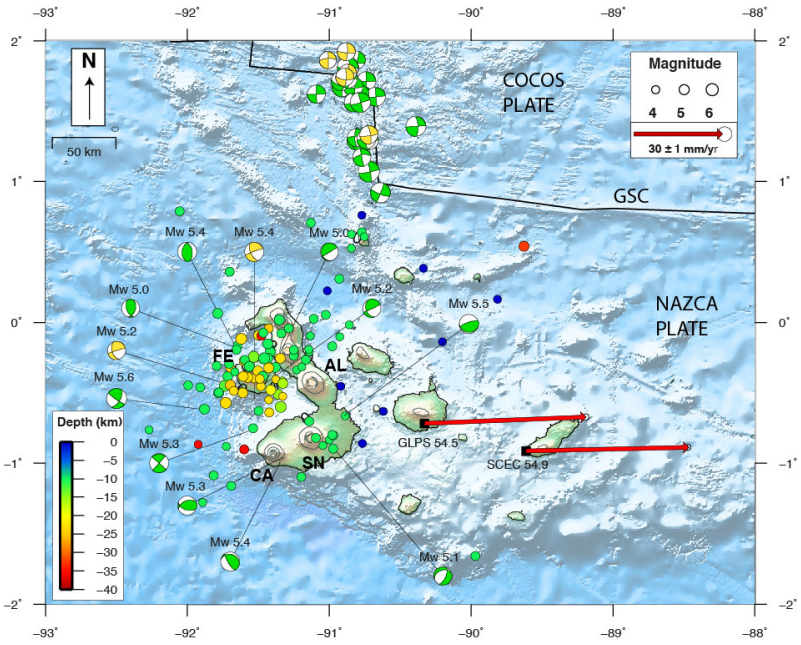

Figure 3.7 – Seismic activity in the Galapagos Archipelago. Mb $>$ 4.0 earthquake reviewed catalog restricted to 40 km depth between 1976 and 2018 is from the International Seismological Centre (ISC) (Engdahl et al. 2020) and Mw $\geq$ 4.5 focal mechanism solutions are from the Global Centroid Moment Tensor (gCMT) (Ekström et al. 2012). Earthquake depths and focal mechanism depths are depicted by the color scale (bottom left). Red arrows are GPS velocities with respect to stable South America reference frame (SOAM). Ellipses show 95% confidence. SN: Sierra Negra, FE: Fernandina, CA: Cerro Azul, and AL: Alcedo volcanoes. GSC: Galapagos Spreading Center.

Deformation at Sierra Negra produced faulting on an intra-caldera preexisting fault system and caldera floor uplift cumulative ∼5 meters (between 1992-2005.8) prior to the October 2005 eruption. ∼2.7 m uplift took place between 1992-1999, including intra-caldera faulting causing ∼1.2 m of slip (equivalent to a Mw 5.7 earthquake) during ∼1997-1998, followed by subsidence from ∼2000 to 2002, and then ∼2.3 m of uplift during the 2003-2005.8 period (Amelung et al. 2000, Chadwick et al. 2006, Geist et al. 2008). New deformation phases (uplift and subsidence of

the caldera floor) were recorded in all geodetic stations at Sierra Negra volcano after the 2005.8 eruption. The last one, recorded by InSAR and local cGPS measurements reached ∼0.9 m of caldera floor uplift (uplift cumulative > 6.5 m between 2006 and 2018) with the fastest inflation rates (∼70 cm/yr) ever recorded worldwide between June 2017 and June 2018. This deformation was accompanied by intense seismicity located below 16 km depth, with additional shallow seismicity around the caldera prior to the June 2018 eruption (reports: Instituto Geofísico of Ecuador).

Figure 3.6 shows several correlations between non-linear motions observed in geodetic observations and deformation processes of Sierra Negra volcano. We note a good correlation between the inflation and deflation occurring at Sierra Negra from 1997 to 2002 (Chadwick et al. 2006, Geist et al. 2008) with variations in the north component of GALA time series. For GLPS, the negative slope observed between the 2003-2006 corresponds to the 2003-2005.8 volcanic inflation period at Sierra Negra. Another change visible on the east component during 2017.5-2019.8 correlates with the pre-co and post-eruption period at Sierra Negra. In the meantime, despite only scarce data are available for SCEC, no change is visible during the first three months after the onset of the 2018 pre-eruptive activity, suggesting that San Cristobal Island is located far enough to remain unimpacted by volcanic deformation.

Removing the deformation periods of Sierra Negra, we find a velocity estimate of Ve=54.4 mm/yr, Vn=2.3 mm/yr (norm=54.5 mm/yr) for the 2008.5-2017 period for GLPS. We estimate the velocity for GALA using the 1996-2003 period, but removing the 1997-1998 period during which the ∼7 mm 1997-1998 northward transient is observed and solve for an offset during this period. This procedure provides a velocity of Ve=55.2 mm/yr, Vn=1.5 mm/yr (55.2 mm/yr) that agrees (difference is 0.7 mm/yr) with GLPS velocity estimates.

We further evaluate the consistency between GLPS and SCEC velocities. The baseline rate is 0.7 ± 0.5 mm/yr, not significant at the 95% confidence level. However, the relative motion between the two sites has a significant component perpendicular to the baseline. Given the short distance (80 km) between SCEC and GLPS together with the large distance of the Nazca/South America poles (∼90-98°W, 54-61°N) from the Galapagos archipelago, we can compare the velocity change predicted by previously published Euler poles and the relative residual velocities. The velocity of GLPS with respect to SCEC expected from a rigid motion is -0.4 mm/yr and -0.1 mm/yr for the east and north component respectively. Our best estimates (removing periods of known volcanic deformation described above) is -0.3 mm/yr and +1 mm/yr. This result suggests that the north component of GLPS velocity might be impacted by volcanic deformation at the 1 mm/yr level.

As for the Easter Island area, we also evaluate the possible contribution of elastic deformation associated with magma intrusion at the Nazca/Cocos plate boundary. Between longitudes 91°W and 85°W, seafloor spreading rates along the Galapagos Spreading Center is ∼58 mm/yr (DeMets et al. 2010) with a magma intrusion capacity from 5 to 50 million m^3 every 500 years (Perfit and

Chadwick Jr. 1998). Both GALA/GLPS and SCEC are located 180 km from it. Using a 3 km the bottom depth for tensile dislocations, the model predicts ∼0.3 mm/yr southward velocity at GLPS and SCEC sites. This displacement value is within the range of the GLPS and SCEC velocity uncertainties, so we discard this contribution.

In summary, correlations between velocity changes for the cGPS sites on Santa Cruz Island and eruptions periods suggest a potential impact of volcanic deformation at the 1 mm/yr level on the north component. Using velocity estimates for SCEC, located on San Cristobal to ∼170 km away from the active volcanic centers, provide a more reliable estimate of the Nazca plate motion.

3.3.3 San Felix and Robinson Crusoe Islands

Geodetic Velocity

In the southeastern part of the Nazca plate, velocity estimates from survey GPS measurements in distinct sites within San Felix (ISFE, FLIX) and Robinson Crusoe (IRBS, RBSN) islands published by Angermann et al. (1999) and Kendrick et al. (2003) highlight discrepancies of ∼3 mm/yr between them (FLIX=63.3 mm/yr, RBSN=63 mm/yr for Kendrick et al. (2003) versus ISFE=60.1 mm/yr and, IRCR=66 mm/yr for Angermann et al. (1999)). These differences may come from different data sets and observation spans, different reference frame (ITRF) adopted in the data analysis and will result in a different estimates of rotation pole for the Nazca/South American plates. Both studies only used two epochs of measurements, potentially leading a bias of a few mm/yr. Since 2013.8, a new continuous GPS site (ARJT) has been installed on the Robinson Crusoe Island, but has a large data gap between 2016.5 and 2019.7. A 15 mm eastward offset is observed (see figure 3.8) at the time of the Mw 8.3 September 16, 2015 megathrust Illapel earthquake located ∼700 km east-northeast of ARFJ. Pre-Illapel earthquake velocity estimated from 2 years of measurements is 70.3 mm/yr (Ve=70.1 mm/yr, Vn=5.0 mm/yr) and post-Illapel estimated from 2016 to 2019.8 is 69.9 mm/yr (Ve=69.6 mm/yr, Vn=6.6 mm/yr), but suffers from the data gap between 2017.6 and 2019.7. Despite their uncertainty, the velocity change is consistent with the expected motion for post-seismic deformation with increased velocity towards the Illapel earthquake rupture.

Post-seismic Deformation

Robinson Crusoe Island is currently converging toward South America at a rate 4 to 7 mm/yr faster during the 2013.5-2020 period than estimates obtained from surveys conducted during the 1990's. This change is significant even taking a conservative error budget for survey mode GPS measurements collected in the 1990's. Viscoelastic relaxation following the 2010 M_w 8.8 February 27 Maule great earthquake in Chile is the most likely explanation. Robinson Crusoe Island is located 700 km offshore in front of the northern extent of the Maule earthquake rupture area. Previous studies have shown that the viscoelastic relaxation in the asthenosphere during

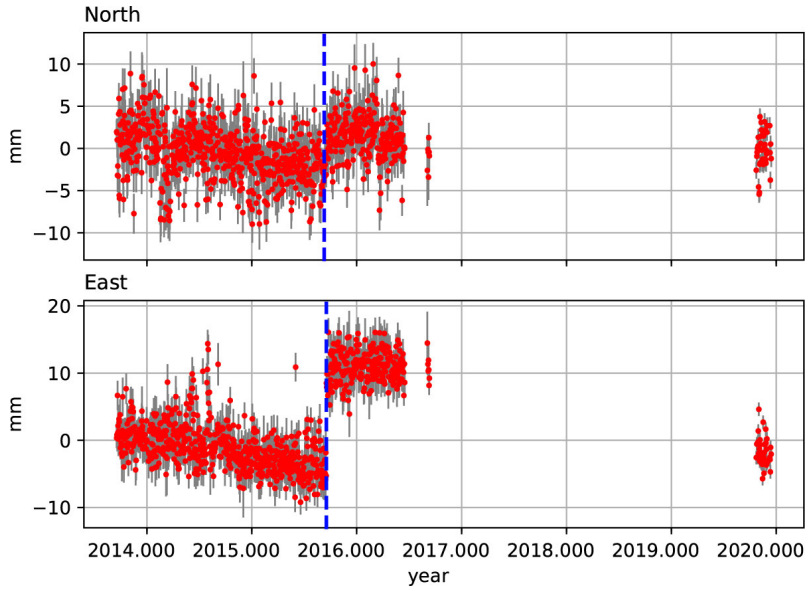

Figure 3.8 – Daily position time series at the ARJF site (Robinson Crusoe Island) after applied linear regression using least square. Blue dashed lines are the date of Illapel earthquake.

the 5 years following the 2010 M_w 8.8 Maule earthquake has induced a widespread horizontal deformation pattern extending ∼2000 km from the trench between latitudes ∼32°S and 40°S (Klein et al. 2016). According to viscosity values derived from several studies, several decades are required before visco-relaxation induced deformation becomes below the 1 mm/yr level even for sites located several hundreds of kilometers from the rupture area (Khazaradze et al. 2002, Klein et al. 2016, Suito and Freymueller 2009, Wang et al. 2007). These results have been constrained using the GPS data only available inland on the South America continent. Although large asymmetry in the shape of the viscoelastic relaxation pattern is expected due to (1) the dip of the fault which creates asymmetry of the co-seismic stress change in the asthenosphere and (2) the viscosity structure below the Andes and the South America continent (Klein et al. 2016) that is different below the oceanic Nazca plate, Figure 3.9 shows simple velocity estimates (without applying any correction) for the 2016-2020 period expressed with respect to stable South America, as a proxy of the ongoing post-seismic deformation 6 to 10 years after the Maule earthquake. This is an approximation since locking along the subduction is neglected, but should be small at several hundred kilometers away from the trench. Interestingly, we notice that the difference of geodetic velocities pre- (Kendrick et al. 2003) and post- (this study) Maule earthquake at Robinson Crusoe has the same order of magnitude (∼5 mm/yr) as the velocity for onshore sites located at equivalent distance from the Maule rupture area (Figure 3.9).

The observed large impact of the Maule earthquake on the velocity at Robinson Crusoe Island raises the question of the possible impact of even greater megathrust earthquakes along the Chilean subduction on pre-Maule velocities. Indeed, the northern extent of the Valdivia M_w 9.5 1960 rupture is thought to abut against the southern part of the Maule earthquake rupture area, being only 10% further away (750 km) from Robinson Crusoe Island than the Maule earthquake. Influence of the viscoelastic relaxation has been document for 40 years

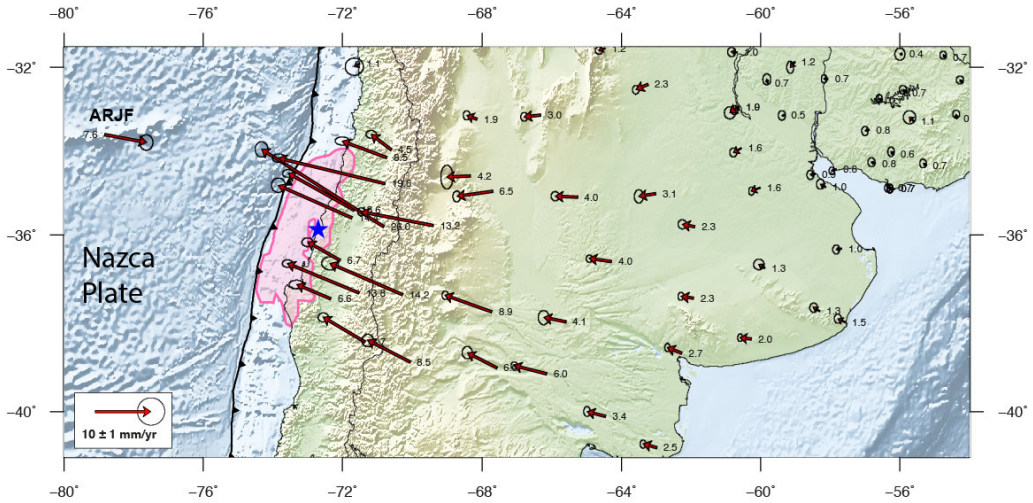

Figure 3.9 – Velocity estimates during the 2016-2020 period with respect to South America. Blue star is the epicenter of the 2010 Maule earthquake. Ping line is the 4 m iso-contour of co-seismic slip distribution from Vigny et al. (2011). Velocity in the Robinson Crusoe Island at ARJF is computed by the difference of velocities pre- (Kendrick et al. 2003) and post- (this study) Maule earthquake.

following the earthquake (Khazaradze et al. 2002, Wang et al. 2007). Thus, some influence on the 1990's derived velocity cannot be ruled out. In conclusion, because ARJF is likely impacted by post-seismic deformation, ARJF data cannot be used to constrain the Nazca plate motion. In addition, pre-Maule velocities at Robinson Crusoe Island (RBSN and IRCR, Kendrick et al. (2003) and Angermann et al. (1999)) are also suspected to be biased by the Valdivia 1960 mega-earthquake.

3.3.4 Malpelo Island

Geodetic Velocity

Malpelo Island is located offshore Colombia at the northeastern tip of the Nazca plate (figure 3.10:A). This part of the Nazca plate is squeezed between the Panama transform fault, active spreading centers north of the Galapagos Archipelago, the boundary with the proposed Coiba microplate (Adamek et al. 1988, Lonsdale and Klitgord 1978, Pennington 1981) to the north and the subduction zone. We do not find any impact from the 2016 Mw 7.8 Pedernales earthquake (Nocquet et al. 2016) that ruptured a 110 km long segment of the subduction, ∼400 km southeast of Malpelo island.

Possible sources of Deformation

We assess possible elastic contributions to the velocity at Malpelo Island using the prediction from a regional kinematic elastic block model (Mccaffrey 2002, Meade 2007, Meade and Hager 2005). Our model includes the Panama Transform Fault separating the Nazca plate from the Cocos plate, and modeled at a vertical fault. The locking depth is fixed to 13 km based on the average of hypocentres depth provided by the ISC-GEM global instrumental earthquake catalog (version

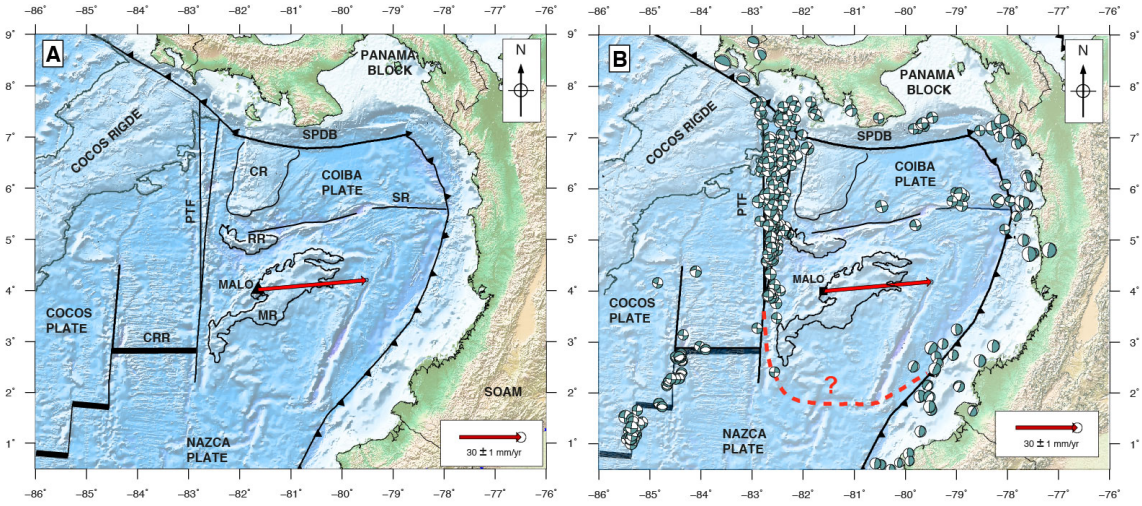

Figure 3.10 – A: Main features of the northeastern end of the Nazca Plate. CR: Coiba Ridge, MR: Malpelo Ridge, RR: Regina Ridge, PTF: Panama Transform Fault, SPDB: South Panama Deformed Belt, CRR: Costa Rica rift, SR: Sandra ridge. Black triangle is the Malpelo Island location. After Pennington (1981), Lonsdale (2005), and Adamek et al. (1988). **B**: Mw > 4.5 focal mechanism solutions reported by the Global Centroid Moment Tensor (gCMT) (Ekström et al. 2012) from 1976 to 2018 restricted to 40 km depth. Red dashed line is the Malpelo/NAZCA plate boundary proposed by Zhang et al. (2017).

7.0) (Di Giacomo et al. 2015). As before, we model the elastic effect from the spreading centers northeast of the Galapagos using outward tensile dislocation from the surface down to 3 km depth. Since 1906, large megathrust earthquakes have occurred in Colombia and Ecuador (Kanamori and McNally 1982, Nocquet et al. 2016), as a result of significant locking along the subduction interface. We model the interseismic effect using a uniform coupling of 80% down to a depth of 50 km, consistently with the results of previous studies (Mora-Páez et al. 2019, Nocquet et al. 2014, Trenkamp et al. 2002). We impose the Euler Pole for the Cocos plate from the MORVEL model (DeMets et al. 2010), from the ITRF2014 model for the Nazca plate (Altamimi et al. 2017), and for Panama block from the model of Kobayashi et al. (2014). The subduction separates the subducting Nazca plate from the North Andean Sliver (NAS), a continental domain moving with respect to South America at ∼1 cm/yr (Pennington 1981). We model the NAS motion using the Euler pole proposed by Nocquet et al. (2014).

Figure 3.11 shows the predictions of our forward model. The dominant elastic contribution comes from the Panama Transform fault located ∼110 km west of Malpelo Island, where the relative Nazca/Cocos plate motion is ∼66 mm/yr (dextral:figure 3.11B), inducing 1.3 mm/yr mainly northward at Malpelo Island. This amount reduces to 1.1 mm/yr taking a locking depth of 10 km. Elastic contribution induced by locking at the subduction interface is 0.7 mm/yr pointing out N-NW at the Malpelo site, hence reducing the effect from the Panama Transform Fault.

Adamek et al. (1988) suggest the existence of the Coiba microplate, squeezed between the northeastern edge of the Nazca plate and the Panama Block. North of Malpelo Island, an east-west trending shear zone seems to coincide with the Sandra ridge, which is proposed as

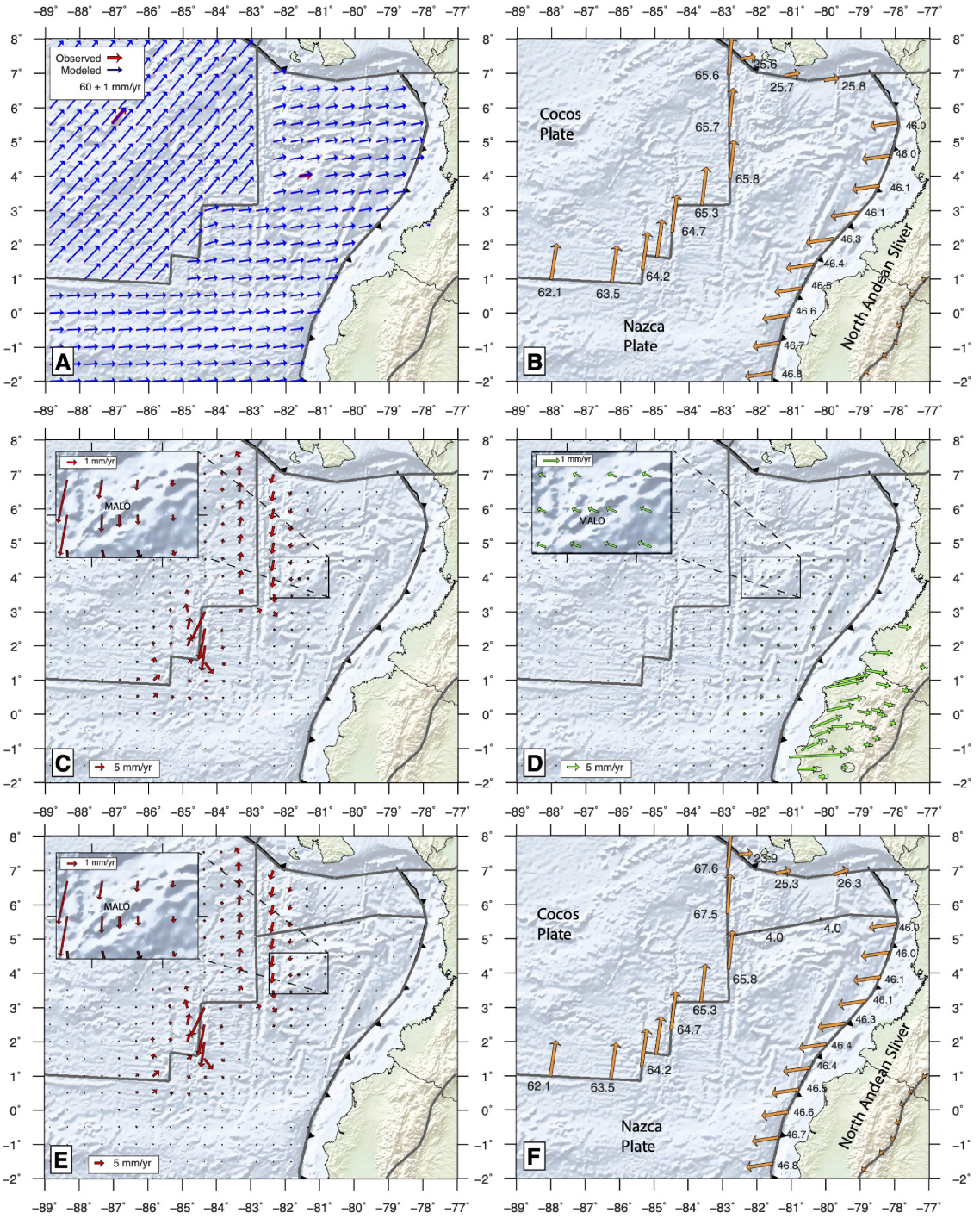

Figure 3.11 – Forward Elastic Block model results for the northern part of the Nazca plate. **A**: Observed (red arrows) and predicted (blue arrow) velocities with respect to South America. **B**: Plate motion at the Nazca plate boundaries. Values are in mm/yr. All arrow are with respect to the Nazca plate. **C**: Predicted elastic contribution from the Nazca/Cocos plate boundaries. **D**: Elastic contribution from the Nazca/North Andean Sliver subduction zone. **E**: Same as figure C but including the Coiba microplate. **F**: Same as figure B but including a priory slip of 4 mm/yr at the Coiba/Nazca plate boundary.

the Coiba/Nazca plate boundary (Adamek et al. 1988, Lonsdale and Klitgord 1978, Marcaillou et al. 2006). This plate boundary has been classified as active since ∼1 Myr and seismicity is regularly recorded from global network (figure 3.10:B). Regional seismotectonic analyzes conclude that if this microplate exists, its southern boundary would accommodate a small fraction of the relative motion between Nazca plate and Panama block (Adamek et al. 1988). In order to assess possible influences from the Coiba microplate in the regional kinematics and subsequently at the Malpelo velocity, we perform a second block model including the Coiba microplate and assigning left-lateral strike slip rate at the Coiba/NAZCA boundary from 1 to 8 mm/yr by steps of 1 mm/yr. The upper value of 8 mm/yr is constrained by the fact that the slip rate at the South Panama Deformed Belt must be similar to the motion observed by several cGPS within Panama (∼22 mm/yr: This study and Mora-Páez et al. (2019)). All models indicate negligible variations (∼0.1 mm/yr) in the previously elastic contribution (example: see figure 3.11:F and E), so effects from the Coiba plate motion along the Sandra ridge can be safely discarded.

The subduction segment along northern Ecuador and southern Colombia experienced a series of 5 megathrust earthquakes with Mw $\geq$ 7.7 that started with the Mw 8.6-8.8 1906 earthquake, which broke a ∼500km long segment of the megathrust (Kanamori and McNally 1982, Nocquet et al. 2016, Ye et al. 2016). In northern Ecuador and southern Colombia, the last documented earthquake is the 1979 Mw 8.2 (Tumaco earthquake). Previous studies suggested the effect of postseismic deformation following the 1979 earthquake has decayed from ∼3 mm/yr in the 1990s to 0.5-1 mm/yr (from 2009 to 2019) on inland sites located at latitude 2.5°N, ∼300 km away from its proposed rupture area based on simple viscoeleastic models (Mora-Páez et al. 2019, White et al. 2003). Malpelo Island is located ∼300 km northwest of the 1979 rupture area. Contributions from the viscoelastic relaxation processes in the asthenosphere is expected to be small, but would induce motion for MALO towards the rupture in an east-southeast direction.

In Summary, we find ∼1.0 mm/yr of possible elastic contribution to the Malpelo velocity from the Cocos/Nazca and Nazca/NAS relative motions and a negligible influence of Coiba microplate.

3.4 NAZCA-SOUTH AMERICA EULER POLE

Based on the results of the previous section, we consider three strategies for calculating the Nazca/South America Euler pole. The first strategy considers that deformation models are speculative and might introduce more bias in Euler pole calculation than corrections. Only geodetically derived velocities and associated uncertainties are used. The second strategy considers that previous models, although possibly incorrect, can still be used to add reasonable uncertainties to the geodetically observed velocities. Geodetically derived velocities are used with uncertainties based on the deformation analysis described above.

The last strategy considers that previous models, although inaccurate at the sub-millimeter per year level, can still be useful to correct the largest bias and will improve the determination of the Euler pole. We follow the three strategies and evaluate their impact on the determined Euler pole.

In the following, we evaluate the quality of the Euler pole inversion using two criterions. The weighted-root-mean-square defined as:

$$WRMS = \sqrt{\frac{\sum_{i=1}^{n}\left(\frac{r_{e_i}^2}{\sigma_{e_i}^2}+\frac{r_{n_i}^2}{\sigma_{n_i}^2}\right)}{\sum_{i=1}^{n}\left(\frac{1}{\sigma_{e_i}^2}+\frac{1}{\sigma_{n_i}^2}\right)}} \tag{3.1}$$

The wrms is the weighted average of velocity residuals and hence a number indicating the level of the plate rigidity. Both global and regional tectonic plate kinematics studies show that wrms is the order of 0.2-0.5 mm/yr for plates (e.g. Altamimi et al. (2017), Nocquet (2012)), a value also found for South America in this study (0.15 mm/yr).

Sigma 0 ($\sigma_0 = V_s^T C d^{-1} V_s / dof$), called reduced chi-square or posterior variance factor indicates the average agreement between the obtained residuals and the uncertainty associated to the data. A value of σ_0 close to one indicates an overall agreement between the rigid plate hypothesis and the observed residuals given the data uncertainty. A value significantly larger than 1 indicates either some plate internal deformation larger than the velocity uncertainty, or underestimated uncertainties in the data or a combination of both (Nocquet et al. 2001). Proper handling of velocity uncertainties usually leads to σ_0 close to 1 for most plates (e.g. Sella et al. (2002), Prawirodirdjo and Bock (2004)) or here 1.1 found for the South America pole.

3.4.1 Euler pole from geodesy only

Here we use the subset of the best determined sites [ISPA, ILSG, GLPS, SCEC, MALO] to estimate the Euler pole. The associated velocity uncertainties are the one reported in the Table 3.1 derived from the time series noise analysis.

This first calculation provides an Euler pole at (NZROT50: lon. -91.57°E, lat. 56.25°N, ω=0.591°/Myr). While similar to Kendrick et al. (2003) (-94.4°E, 61.0°N, 0.57°/Myr), it predicts up to 3.5 mm/yr faster convergence rate in Chile. The wrms for this calculation is 0.90 mm/yr. This result is already good, indicating an overall agreement at the order of 1 mm/yr between the areas sampled by the GPS data. In the details, this number is about twice the usual value reported for most tectonic plates (e.g. Altamimi et al. (2017)). A σ_0 of 2.9 also suggests either a non-perfect rigidity or underestimated uncertainties by a factor $\sim$3. The largest residuals are found for Malpelo Island (2 mm/yr southeastwards) and the North component of GLPS (1.5 mm/yr northwards).

Removing GLPS from the calculation provides a pole at (NZROT40: lon. -90.41°E, lat. 57.01°N, ω=0.590°/Myr), but with lower residuals (wrms=0.60 mm/yr) and σ_0 =2.0. Although

not perfect, this calculation offers the advantage of a good sampling of the plate with sites in Easter Island, Salas y Gomez, the Galapagos and Malpelo, reasonable statistics with all residuals are below 1 mm/yr. As detailed previously, there are several reasons to consider GLPS as an outlier: the analysis of GLPS time series described in section 3.3.2 shows that the north component might be biased by $\sim$1 mm/yr and departs from SCEC certainly less impacted by volcano deformation and which agrees with the others sites. The impact of removing GLPS on the Nazca/South America convergence prediction is small (<0.3 mm/yr) compared to including all sites.

As an alternative, we remove MALO from the previous calculation. The obtained pole is located at (NZROT30: lon. -91.41°E, lat. 55.30°N, ω=0.593), with wrms=0.33 mm/yr and σ_0=1.3. However, the degrees of freedom is only 3, making the statics indicators less significant. In that case, MALO has a residual of 2.3 mm/yr SE.

Now keeping MALO and considering both Galapagos sites as outliers, we find a pole at (NZROT31:lon. -89.67°E, lat. 58.23°N and ω=0.59°/Myr), and wrms=0.35 mm/yr, σ_0=1.3. In that calculation, SCEC has residuals of 1.9 mm/yr mainly northward.

So small residuals, similar to the ones obtained for the major tectonic plates are obtained by considering either Galapagos sites or Malpelo as outliers. The lack of redundancy prevents to decide which sites from Galapagos or Malpelo might be an outlier.

3.4.2 Tectonic and volcanic deformation as additional uncertainties

The analysis presented in section 3.3 provides some first-order information for the magnitude and direction of tectonic/volcanic deformation, which contributes to adding noise to the GPS velocities in their ability to represent the rigid motion of the Nazca plate. In order to account for this effect, here, we simply add a variance based on our model to the variance estimated from our geodetic noise analysis.

In section 3.3.1, we find a possible bias of 1.1 mm/yr and 0.7 mm/yr on the East component of velocity for ISPA and ILSG induced by magma injection at the spreading center delimiting the Nazca/Pacific plate boundary. We therefore add this amount as additional uncertainty on the velocity East component now becoming 1.13 ($\sqrt{0.28^2+1.1^2}$) for ISPA and 0.87 ($\sqrt{0.51^2+0.7^2}$) for ILSG.

We saw in section 3.3.2 that GLPS north component is likely biased by $\sim$1 mm/yr. We therefore add an uncertainty of 1.25 mm/yr to GLPS north velocity (1.29 mm/yr). Because the active volcano centers are located west to northwest of GLPS and SCEC, we add another 0.5 mm/yr on the East component of GLPS and both component of SCEC.

Finally, MALO is potential impacted by (1) elastic effect of the Panama transform fault (2) the earthquake cycle along the subduction located ∼300 km. The latter has two opposite effects, one being the elastic effect induced by locking along the megathrust, the other being the viscoelastic relaxation coming from past large earthquakes, the closest being the Mw 8.2 1979 southern Colombia earthquake. Interestingly, for all Euler pole calculation, MALO residual velocity has an almost constant direction of N140°E, pointing towards northernmost Ecuador-southern Colombia where the Mw 8.2 1979 earthquake broke a 230 km long segment of the megathrust Kanamori and McNally (1982). Based on this, we choose to add a 1 mm/yr uncertainty on both north and east component.

This approach provides an Euler pole at (NZROT51: long. -90.93°E, lat. 56.19°N, ω=0.588), with wrms = 0.57 mm/yr and σ_0=1.1, suggesting that the uncertainties added to the geodetic noise are appropriate. This approach offers the advantage of providing better estimates of uncertainty of the Nazca kinematics and hence on the convergence rate along the South America subduction zone.

3.4.3 Tectonic and volcanic deformation as a priori correction to data

As a last test, we use the analysis described in section 3.3 to correct the geodetic velocity from tectonic/volcanic deformation. We further make the assumption that these models are correct at the 0.5 mm/yr, that is quadratically added to the geodetic uncertainties.

ISPA east velocity is reduced from 64.8±0.3 to 63.7±0.6 mm/yr and ILSG from 64.0±0.5 to 63.3±0.7 mm/yr to account for elastic strain from the opening at the East Pacific Rise. GLPS is corrected from 2.3±0.3 to 1.0±0.6 mm/yr. SCEC is not changed but 0.5 mm/yr is quadratically added to the geodetic uncertainties. MALO is corrected from -1.5 mm/yr motion in the north N120°E to account for possible viscoelastic following the Mw 8.2 1979 Colombia earthquake, here with a 1 mm/yr uncertainty.

Using this procedure, the Euler pole found is lon. -90.80°E, lat. 56.48°N, ω=0.583°/Myr (NZROT52). The wrms is 0.39 mm/yr now similar to other plates and σ_0=0.8 suggesting that the 0.5 mm/yr of additional uncertainty was pessimistic.

We acknowledge that this procedure is speculative, but at least it illustrates that the sense of the velocity residuals noted in the purely geodetic calculations is in agreement with the direction and magnitude of known tectonic processes.

Table 3.2 – Summary of the Euler pole estimates using different subset of sites. σ_0: posterior variance factor. First number at the solution names is the number of sites used in the Euler pole estimate.

Solution	Lon	Lat	ω	χ^2	σ_0	WRMS	Associated Error Ellipse			$\sigma\omega$
	°E	°N	°/My			mm/yr	Semi-Major	Semi-minor	Azimut	
NZROT30	-91.41	55.30	0.593	4.9	1.3	0.33	0.66	0.20	-41.0	0.003
NZROT31	-89.67	58.23	0.590	5.1	1.3	0.35	0.60	0.20	-36.3	0.002
NZROT40	-90.41	57.01	0.590	20.9	2.0	0.60	0.50	0.18	-24.2	0.002
NZROT50	-91.57	56.25	0.591	60.8	2.9	0.90	0.46	0.15	-11.1	0.002
NZROT51	**-90.93**	**56.19**	**0.588**	8.1	1.1	0.57	0.96	0.22	-53.3	0.006
NZROT52	-90.80	56.48	0.583	5.0	0.8	0.39	0.73	0.20	-38.8	0.004

3.5 DISCUSSION

3.5.1 Preferred Pole

The three approaches described in section 3.4 lead to 6 different estimates for the Nazca/South America Euler pole (Table 3.2). We first evaluate how different they are, by calculating their predicted values at different locations of the Nazca plate boundary. For each of the six Euler poles described in the previous section, Figure 3.12 shows the predicted motion for the Nazca plate with respect to the adjacent plate. For the Antarctic and Pacific plates, we use the ITRF2014 plate model from Altamimi et al. (2017), the MORVEL Euler pole for the Cocos plate (DeMets et al. 2010). We calculate the velocity uncertainty by propagating the plate rotation variance-covariance matrix to the location of the model prediction, using the equation (3.5) in the Appendix. The plate rotation variance-covariance matrix were first rescaled by σ_0, except for the model obtained using a priori tectonic corrections, which had $\sigma_0 < 1$.

Figure 3.12 first shows that the maximum difference among the different model predictions is 1.5 mm/yr at the 95% confidence level. Figure 3.12 also indicates that the NZROT51 pole, derived using all the geodetic data but accounting for tectonic/volcanic uncertainty, provides an average value of all Nazca Euler pole predictions. Furthermore, its 95% level confidence region encompasses all the other Euler pole predictions, except NZROT40 and NZROT31, whose predictions would fall inside the 97% confidence level region.

Therefore, we propose the NZROT51 solution as our preferred Euler pole and associated uncertainty to describe the current Nazca plate motion.

3.5.2 San Felix

We did not include campaign results published by Kendrick et al. (2003) for San Felix (FLIX) and Robinson Crusoe (RBSN) islands in our calculations, because different ITRF and a different realization of the South America plate fixed frame were used. The analysis shown for EISL also indicates that velocities estimated using data collected in the 90's might have 1-2 mm/yr differences compared to velocity determined using post-2000 data. It is, however, informative to check our

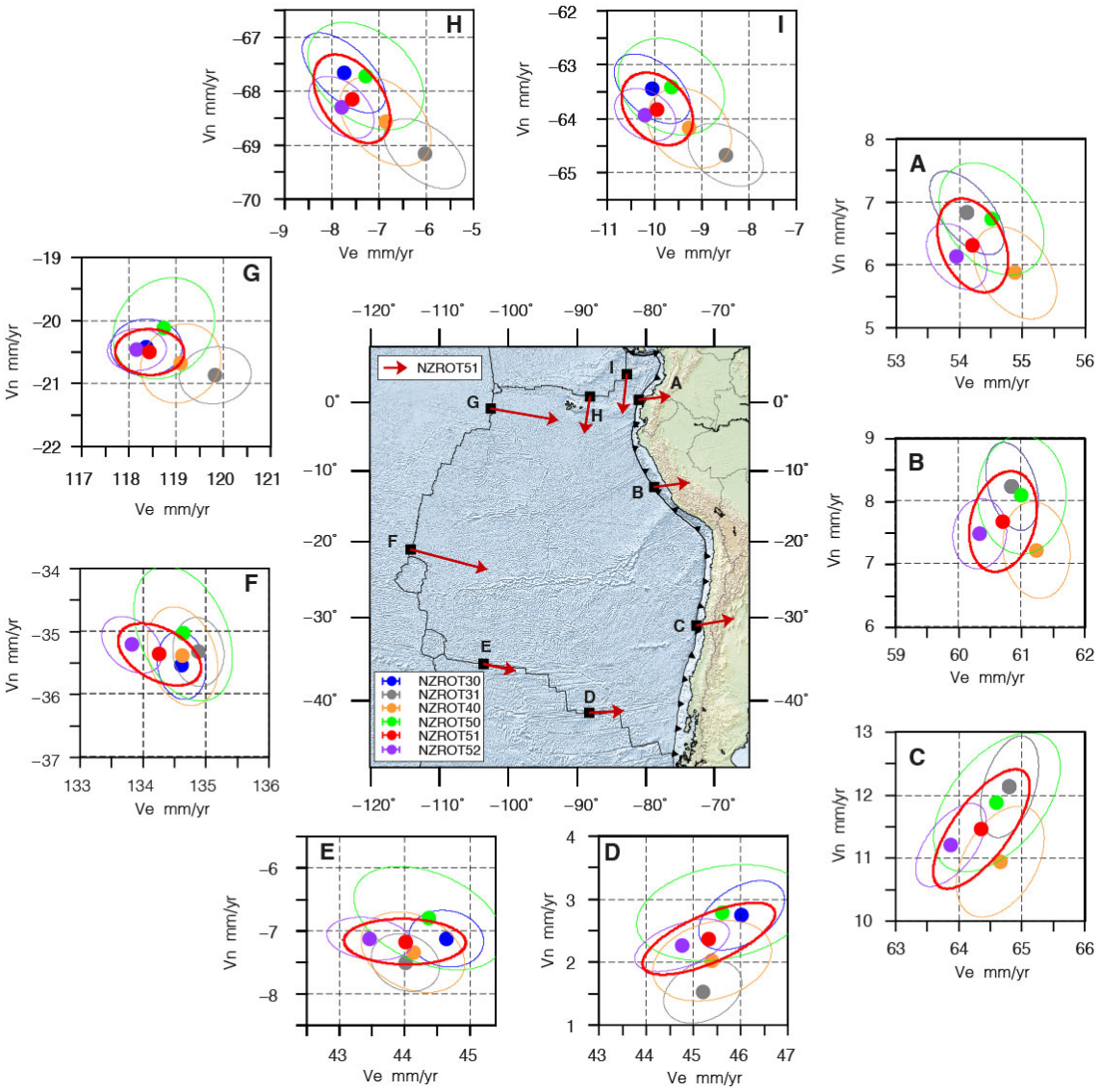

Figure 3.12 – Predicted velocities from the 6 Nazca Euler poles summarized in table 3.2. The map shows the selected locations along the Nazca plate boundary indicated by the black square labeled from A to I. Red arrows show the velocity predicted by model NZROT51 for the Nazca plate with respect to the adjacent plate. The sub-plots A to I show the prediction for the different Euler poles, together with their error ellipse at the 95% confidence level region.

results against the published values and make some predictions to be compared to future estimates. San Felix island is located ∼800 km from the Chilean trench, in front of a segment ruptured by a great earthquake a century ago (Ruiz and Madariaga 2018). No tectonic deformation is suspected in that area, making San Felix an ideal site to determine the rigid motion of the Nazca plate.

Our preferred solution prediction at FLIX is 64.5 ± 0.5 mm/yr and 6.9 ± 0.5 mm/yr for the East and North components respectively. This prediction is 1.6 ± 0.4 mm/yr faster than the observed velocity estimated by Kendrick et al. (2003). We believe that this difference is consistent with a more realistic uncertainty than the one reported (0.2 mm/yr for both components) in Kendrick et al. (2003).

We further evaluate the improvement expected from adding a well-defined velocity at the 0.5 mm/yr at San Felix Island. The availability of new measurements at San Felix would significantly improve the spatial sampling of the Nazca plate and would allow a precise test of potential internal deformation with respect to Salas y Gomez/Easter Islands. As an exercise adding a fictive measurement at San Felix, we find that the formal variance for the rotation rate for the Nazca plate would be decreased by 50% and the uncertainty in the convergence along the Chilean trench would be improved by ∼35% (0.5 mm/yr vs. 0.8 mm/yr for our solution). Therefore, continuous GNSS measurements at San Felix appear as a priority to improve the Nazca current plate kinematics description.

3.5.3 Convergence along the Andean margin

Figure 3.13 shows the magnitude and direction for the convergence of the Nazca plate with respect to South America all along the trench from Colombia to Chile for previously published Euler poles and our preferred solution. Our model predicts ∼51 mm/yr of convergence in northern Colombia, increasing to ∼58 mm/yr at the convex bend of the trench at latitude 5°S. The convergence rate along the Peru trench increases from ∼58 mm/yr in northern Peru to 64 mm/yr in its southern part. Aside the model from Angermann et al. (1999), the difference among model predictions is less than 2 mm/yr for the northern Andes. Differences increases in southern Peru and are the largest along the Chilean trench where our model predicts a maximum convergence rate of 65.5 mm/yr at latitude ∼30°S in Chile, falling in the middle of the fastest model from Vigny et al. (2009) at 68 mm/yr and the slowest model of Kendrick et al. (2003) at 63 mm/yr. The predicted convergence azimuths are usually similar within 5° for all models, but our model prediction is systematically rotated by a few degrees clockwise with respect to the other models. Overall, our model is close to Altamimi et al. (2017), but with ∼1 mm/yr slower convergence in front of Chile. Furthermore, the obliquity of the predicted convergence vectors along the whole trench axis (figure 3.13:C) appears consistent with the lateral motion found for continental slivers along the Andean margin (Brooks et al. 2003, Métois et al. 2013, Nocquet et al. 2014, Wang et al. 2007).

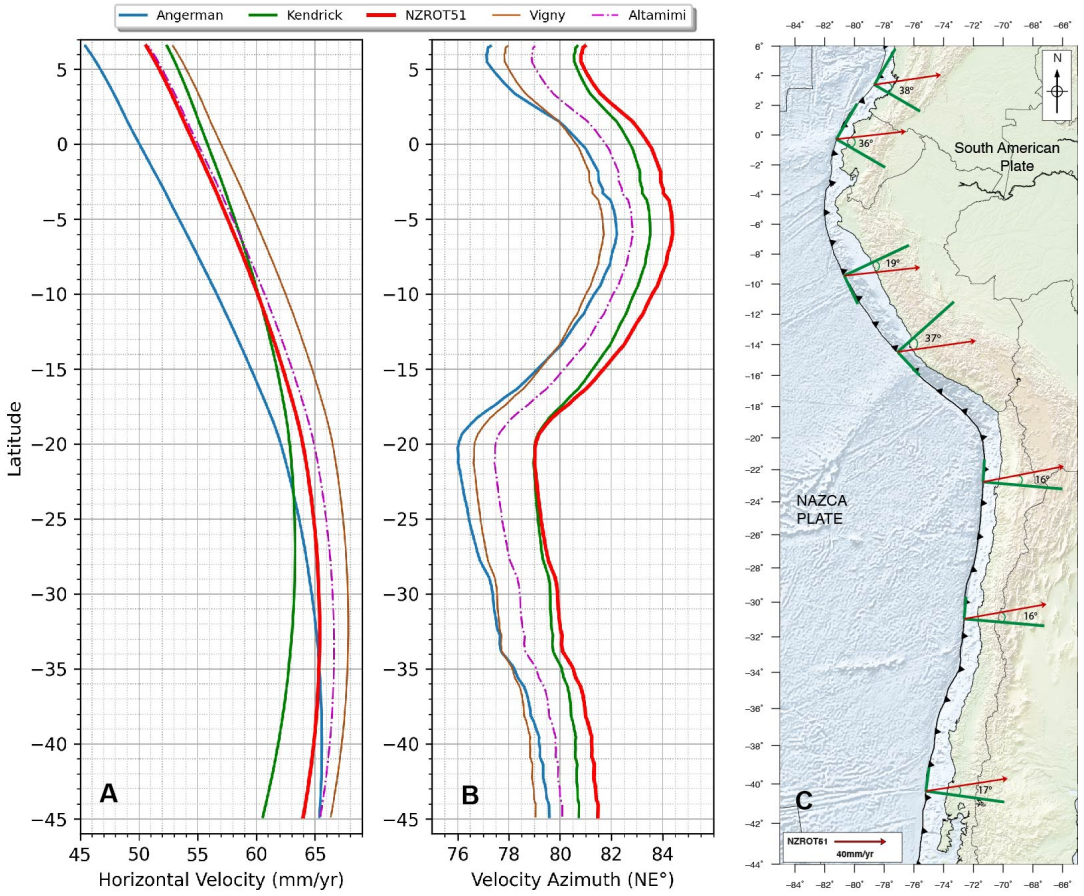

Figure 3.13 – A) Predicted velocity norm and **B)** predicted directions along the NAZCA/SOAM plate boundary according to our preferred model NZROT51, Angermann et al. (1999), Kendrick et al. (2003), Vigny et al. (2009), and Altamimi et al. (2017). **C)** Convergence obliquity predicted by model NZROT51. Green lines indicate parallel and normal trench components of the Nazca/SOAM convergence vectors (red arrows).

3.5.4 Comparison to geological models

The progressive slowdown of Nazca eastward motion has been well-documented from both geological and geodetic results (DeMets et al. 2010, Norabuena et al. 1999). Among the best evidence, DeMets et al. (2010) show the decrease of opening rates along the Antarctic/Nazca spreading centers from 57–58 mm/yr in NUVEL-1A, which average motion since 3.16 Myr, to 50-52 mm/yr for MORVEL (average motion since 0.78 Ma). Combining our preferred pole with the one from Altamimi et al. (2017) for the Antarctic plate, we find an Euler pole at -92.038°E 39.246°N 0.414 deg/Myr for the current Nazca/Antarctic plate, predicting opening rates at 44-46 mm/yr. Such values confirm the ongoing deceleration of opening rate along that plate boundary. We can further test whether our geodetic estimates agree with a constant deceleration rate. For that, we can notice that for a linear function, the average rate over a given period is the value of the function at the middle time of the period. Thus, the deceleration rate is $a = 2(V_{nuvel1A} - V_{morvel})/(3.16 - 0.78)$ and the present-day velocity=$V_{morvel} - 0.78a/2$. At longitude 89-99°W, west of the Valdavia transform fault, MORVEL opening rates are 50 ± 1 mm/yr against 56 ± 1 mm/yr for NUVEL1A, leading to a deceleration rate of 5 mm/Myr and a prediction

of present-day of 46 mm/yr, in perfect agreement with the geodetic prediction (45.3±1 mm/yr). At longitude 78-82°W, East of the Valdavia transform fault, MORVEL opening rates are 52 ± 1 mm/yr against 57-58 ±1 mm/yr for NUVEL1A, leading to a present-day opening rate of ∼46 mm/yr, also in perfect agreement with our geodetic prediction of 45.2±0.7 mm/yr.

Our pole is therefore consistent with a constant and consistent deceleration of opening rates along the Nazca/Antartic for 3.16 Ma. As for the MORVEL model, combining the Euler pole from Altamimi et al. (2017) for the Antarctic and Pacific plates with our pole for the Nazca pole, a plate circuit closure test shows insignificant residual (∼1 mm/yr) supporting the plate rigidity hypothesis.

On the northern part of the Nazca plate, our analysis does not support the hypothesis of the independent Malpelo microplate proposed by Zhang et al. (2017). Indeed, Zhang et al. (2017) relative motion between the Nazca plate and Malpelo microplate is expected to be 5-6 mm/yr while Malpelo Island shows a residual velocity always less than 1.5 mm/yr in all Nazca Euler estimations.

We test whether our new solution can improve the misfit of the Pacific/Cocos/Nazca plate circuit closure or provide clues to explain it. Using MORVEL Cocos/Pacific pole together with the geodetic poles for the Pacific plate from Altamimi et al. (2017) and our pole for the Nazca plate, we obtain a linear velocity of non-closure by 9.7 ± 2.1 mm/yr (evaluated at location: -102.0°E, 2.3°N) at the 95 percent confidence level for the Pacific/Cocos/Nazca plate circuit, which is 30% and 17% better than MORVEL and Zhang et al. (2017) estimates.

Our solution includes the site ISCO located on the Cocos Island. ISCO horizontal velocity is (Ve=54.35, and Vn=64.25 mm/yr) in the South American reference frame and (Ve=3.7 and Vn=61.8 mm/yr) with respect to the Nazca plate using our solution. At the ISCO location, MORVEL prediction for the Cocos plate motion in a Nazca fixed frame is (Ve=-1.8, and Vn=59.0 mm/yr). Thus, there is a clear discrepancy of ∼6 mm/yr mainly on the east component between MORVEL prediction and the only available geodetic observation of Cocos/Nazca plates relative motion. Interestingly, we also note that this discrepancy would be reduced by applying a decrease of the East component of the Nazca plate similar to the one observed in its southern part. Noting the potentially biased Cocos kinematics in MORVEL, DeMets et al. (2010) propose an alternative Euler pole called PVEL for the Cocos/North America and Cocos/Caribbean plates. Using their values for the Cocos/North America pole, together with Altamimi et al. (2017) for the North America/South America kinematics and our Nazca/South America poles, the predicted velocity for PVEL at ISCO relative to Nazca is (Ve=9.9, and Vn=68.4 mm/yr).

3.6 CONCLUSIONS

Despite the reduced number of available continuous GPS observations within the plate, our study has allowed us to better constrain the kinematics of the Nazca plate by reducing the uncertainties of previous pole estimates. Our best estimate for the Nazca plate Euler pole includes 5 sites spatially

sampling the entire plate.

Analysis of potential volcanic and tectonic deformation show that ILSG in Salas y Gomez Island and SCEC in the easternmost island of the Galapagos archipelago are the most stable sites within the plate. Easter Island, Santa Cruz Island in the Galapagos, and Malpelo Island offshore Colombia probably undergo deformation at the 1-2 mm/yr level. Robinson Crusoe Island undergoes viscoelastic effects of the large earthquakes along the Chile subduction zone, still biasing velocity estimates at 4-5 mm/yr. In the absence of absolute sea-floor geodesy measurements, confirmation or re-evaluation of the Nazca present-day kinematics is expected to come as a reliable velocity estimate will become available at San Felix Island located ∼800 km from the Chile trench.

New GPS measurements at Malpelo Island do not support the existence of an independent Malpelo microplate in the northernmost part of the Nazca plate. On the contrary, our analysis supports a single plate with possible internal deformation of the order of 0.6 mm/yr, providing residuals similar to other large tectonic plates when correcting velocities from geophysical models. This indicates a very small, if any, contribution of thermal contraction of the oceanic lithosphere previously proposed (Kumar and Gordon 2009). The misfit of the Pacific/Cocos/Nazca plate circuit closure appears to be reduced but not solved by our Nazca pole. However, the good agreement of geodetic velocity with the plate rigidity assumption for a large area of the Nazca plate sampled by geodetic velocity points makes unlikely internal deformation or fragmentation of the Nazca plate as a potential explanation. A combination of fast slowdown of the Nazca plate and bias in the Cocos plate kinematics appears more probable explanation to the Cocos-Pacific-Nazca plate circuit non-closure issue.

3.7 ACKNOWLEDGMENTS

This research was supported by the Secretaría Nacional de Educación Superior, Ciencia y Tecnología (SENESCYT-Ecuador) in the frame of P. Jarrin's doctoral fellowship (grant number:IFTH-DFN-2018-0096/092-2017). We acknowledge support from the Institut de Recherche pour le development and Agence Nationale de la Recherche in the frame of IRD/ANR-S5 AAP CE31 project. We thank the Colombian Geological Survey, the Centro Sismológico Nacional of Chile, Unavco, the Instituto Geofísico of Ecuador and the Instituto Geográfrico Militar of Ecuador for providing valuable geodetic data. Most figures were compiled using the Generic Mapping Tools (GMT) software.

3.8 APPENDIX

The fundamental equation used to estimate an Euler pole located in the rigid part of the plate p is expressed by the relation :

$$v_{(M)} = \dot{\omega}_p \times r_{OM} \tag{3.2}$$

Where v is the horizontal velocity vector of a M point on the Earth's surface within the plate p, r_{OM} is the vector joining the center of the earth in the point M, and $\dot{\omega}_p$ is the Euler pole. If we have a velocity field v_i with $i \in [1, n]$ and taking into account that geodetic observations provide 3D velocities in geocentric Cartesian coordinates, $\dot{\omega}_p$ is computed by the condition (Nocquet 2002, Nocquet et al. 2001):

$$\sum_{i=1}^{n} \left\| \dot{\omega} \times r_{OM} - v^i \right\| \ \textit{is minimum} \tag{3.3}$$

Where $v^i = \begin{bmatrix} v_x^i & v_y^i & v_z^i \end{bmatrix}^t$ and $r_{OM} = \begin{bmatrix} x^i & y^i & z^i \end{bmatrix}^t$. Expanding the cross product of equation 3.2 and rewrite it as a linear equation:

$$\begin{bmatrix} 0 & z^i & -y^i \\ -z^i & 0 & x^i \\ y^i & -x^i & 0 \end{bmatrix} \begin{bmatrix} \dot{\omega}_x \\ \dot{\omega}_y \\ \dot{\omega}_z \end{bmatrix} = \begin{bmatrix} v_x^i \\ v_y^i \\ v_z^i \end{bmatrix} \tag{3.4}$$

As the model of a rigid rotation only predicts horizontal velocities $\begin{bmatrix} v_e^i & v_n^i \end{bmatrix}^t$. we therefore modify equation 3.4 using a rotation matrix H^i (restricted to its 2 first lines) in order to convert it from geocentric Cartesian coordinates to local coordinates.

$$H^i A^i \omega^i = H^i v^i \tag{3.5}$$

The variance-covariance matrix for the predicted velocity is obtained using the law of variance propagation as $C_{v_{en}}^i = H C_{v_{xyz}}^i H^t$. Finally, equation 3.5 is expressed in the linear system format and solved using least-squares estimation with the weight matrix $C_{v_{en}}^i$.

3.9 REFERENCES

- Adamek, S., Frohlich, C. & Pennington, W.D. (1988) Seismicity of the Caribbean-Nazca Boundary: Constraints on microplate tectonics of the Panama region. Journal of Geophysical Research: Solid Earth, 93, 2053–2075. doi:10.1029/JB093iB03p02053

- Altamimi, Z., Métivier, L. & Collilieux, X. (2012) ITRF2008 plate motion model. Journal of Geophysical Research: Solid Earth, 117, John Wiley & Sons, Ltd. doi:10.1029/2011JB008930

- Altamimi, Z., Métivier, L., Rebischung, P., Rouby, H. & Collilieux, X. (2017) ITRF2014 plate motion model. Geophys J Int, 209, 1906–1912. doi:10.1093/gji/ggx136

- Alvarado, A., Ruiz, M., Mothes, P., Yepes, H., Segovia, M., Vaca, M., Ramos, C., et al. (2018) Seismic, Volcanic, and Geodetic Networks in Ecuador: Building Capacity for Monitoring and Research. Seismological Research Letters, 89, 432–439. doi:10.1785/0220170229

- Amelung, F., Jónsson, S., Zebker, H. & Segall, P. (2000) Widespread uplift and trapdoor faulting on Galápagos volcanoes observed with radar interferometry. Nature, 407, 993–996.

- Angermann, D., Klotz, J. & Reigber, C. (1999) Space-geodetic estimation of the nazca-south america euler vector. Earth and Planetary Science Letters, 171, 329–334. doi:https://doi.org/10.1016/S0012-821X(99)00173-9

- Árnadóttir, T., Lund, B., Jiang, W., Geirsson, H., Björnsson, H., Einarsson, P. & Sigurdsson, T. (2009) Glacial rebound and plate spreading: results from the first countrywide GPS observations in Iceland. Geophysical Journal International, 177, 691–716, John Wiley & Sons, Ltd. doi:10.1111/j.1365-246X.2008.04059.x

- Báez, J.C., Leyton, F., Troncoso, C., Campo, F. del, Bevis, M., Vigny, C., Moreno, M., et al. (2018) The Chilean GNSS Network: Current Status and Progress toward Early Warning Applications. Seismological Research Letters, 89, 1546–1554. doi:10.1785/0220180011

- Bagnardi, M. & Amelung, F. (2012) Space-geodetic evidence for multiple magma reservoirs and subvolcanic lateral intrusions at Fernandina Volcano, Galápagos Islands. Journal of Geophysical Research: Solid Earth, 117. doi:10.1029/2012JB009465

- Baker, M.S. (2012) Investigating the Dynamics of Basaltic Volcano Magmatic Systems with Space Geodesy, 1320 S Dixie Hwy, Coral Gables, FL 33146, U.S.: University of Miami. Retrieved from $https://scholarlyrepository.miami.edu/oa_dissertations/917$

- Behn, M.D. & Ito, G. (2008) Magmatic and tectonic extension at mid-ocean ridges: 1. Controls on fault characteristics. Geochemistry, Geophysics, Geosystems, 9, John Wiley & Sons, Ltd. doi:10.1029/2008GC001965

- Bevis, M. & Brown, A. (2014) Trajectory models and reference frames for crustal motion geodesy. Journal of Geodesy, 88, 283–311. doi:10.1007/s00190-013-0685-5

- Bird, P. (2003) An updated digital model of plate boundaries. Geochemistry, Geophysics, Geosystems, 4, John Wiley & Sons, Ltd. doi:10.1029/2001GC000252

- Blewitt, G., Hammond, W. & Kreemer, C. (2018) Harnessing the GPS Data Explosion for Interdisciplinary Science. Eos, 99. doi:10.1029/2018EO104623

- Blewitt, G. & Lavallée, D. (2002) Effect of annual signals on geodetic velocity. Journal of Geophysical Research: Solid Earth, 107, ETG 9-1-ETG 9-11. doi:10.1029/2001JB000570

- Boehm, J., Werl, B. & Schuh, H. (2006) Troposphere mapping functions for GPS and very long baseline interferometry from European Centre for Medium-Range Weather Forecasts operational analysis data. Journal of Geophysical Research: Solid Earth, 111. doi:10.1029/2005JB003629

- Bos, M. S., Fernandes, R.M.S., Williams, S.D.P. & Bastos, L. (2013) Fast error analysis of continuous GNSS observations with missing data. Journal of Geodesy, 87, 351–360. doi:10.1007/s00190-012-0605-0

- Bos, Machiel S. & Fernandes, R.M.S. (2015) Investigation of Random Walk Noise in GNSS Time-series. AGU Fall Meeting Abstracts, pp. G13A-0990, Presented at the 2015 AGU Fall Meeting, AGU. Retrieved from https://agu.confex.com/agu/fm15/meetingapp.cgi/Paper/73901

- Brooks, B.A., Bevis, M., Smalley Jr., R., Kendrick, E., Manceda, R., Lauría, E., Maturana, R., et al. (2003) Crustal motion in the Southern Andes (26°–36°S): Do the Andes behave like a microplate? Geochemistry, Geophysics, Geosystems, 4, John Wiley & Sons, Ltd. doi:10.1029/2003GC000505

- Chadwick, W.W., Jr., Geist, D.J., Jónsson, S., Poland, M., Johnson, D.J. & Meertens, C.M. (2006) A volcano bursting at the seams: Inflation, faulting, and eruption at Sierra Negra volcano, Galápagos. Geology, 34, 1025–1028. doi:10.1130/G22826A.1

- DeMets, C., Gordon, R.G. & Argus, D.F. (2010) Geologically current plate motions. Geophysical Journal International, 181, 1–80. doi:10.1111/j.1365-246X.2009.04491.x

- DeMets, C., Gordon, R.G., Argus, D.F. & Stein, S. (1994) Effect of recent revisions to the geomagnetic reversal time scale on estimates of current plate motions. Geophysical Research Letters. Retrieved from https://agupubs.onlinelibrary.wiley.com/doi/abs/10.1029/94GL02118

- Di Giacomo, D., Bondár, I., Storchak, D.A., Engdahl, E.R., Bormann, P. & Harris, J. (2015) ISC-GEM: Global Instrumental Earthquake Catalogue (1900–2009), III. Re-computed MS and mb, proxy MW, final magnitude composition and completeness assessment. Physics of the Earth and Planetary Interiors, 239, 33–47. doi:10.1016/j.pepi.2014.06.005

- Dow, J.M., Neilan, R.E. & Rizos, C. (2009) The International GNSS Service in a changing landscape of Global Navigation Satellite Systems. Journal of Geodesy, 83, 191–198. doi:10.1007/s00190-008-0300-3

- Ekström, G., Nettles, M. & Dziewoński, A.M. (2012) The global CMT project 2004–2010: Centroid-moment tensors for 13,017 earthquakes. Physics of the Earth and Planetary Interiors, 200–201, 1–9. doi:10.1016/j.pepi.2012.04.002

- Engdahl, E.R., Di Giacomo, D., Sakarya, B., Gkarlaouni, C.G., Harris, J. & Storchak, D.A. (2020) ISC-EHB 1964–2016, an Improved Data Set for Studies of Earth Structure and Global Seismicity. Earth and Space Science, 7, e2019EA000897, John Wiley & Sons, Ltd. doi:10.1029/2019EA000897

- Engeln, J.F. & Stein, S. (1984) Tectonics of the Easter plate. Earth and Planetary Science Letters, 68, 259–270. doi:10.1016/0012-821X(84)90158-4

- Galetto, F., Bagnardi, M., Acocella, V. & Hooper, A. (2019) Noneruptive Unrest at the Caldera of Alcedo Volcano (Galápagos Islands) Revealed by InSAR Data and Geodetic Modeling. Journal of Geophysical Research: Solid Earth. doi:10.1029/2018JB017103

- Geist, D.J., Harpp, K.S., Naumann, T.R., Poland, M., Chadwick, W.W., Hall, M. & Rader, E. (2008) The 2005 eruption of Sierra Negra volcano, Galápagos, Ecuador. Bulletin of Volcanology, 70, 655–673. doi:10.1007/s00445-007-0160-3

- Griffiths, J. (2019) Combined orbits and clocks from IGS second reprocessing. Journal of Geodesy, 93, 177–195. doi:10.1007/s00190-018-1149-8

- Herring, T.A., Floyd, M.A., King, R.W. & McClusky, S.C. (2015) Global Kalman filter VLBI and GPS analysis program Release 10.6, p. 95, MIT.

- Herring, T.A., King, R.W., Floyd, M.A. & McClusky, S.C. (2018) GPS Analysis at MIT Release 10.7 (No. Release 10.7), MIT.

- Johnston, G., Riddell, A. & Hausler, G. (2017) The International GNSS Service. In Teunissen, Peter J.G., & Montenbruck, O. (Eds.). in IGS, 1st ed., pp. 967–982, Cham, Switzerland: Springer International Publishing. Retrieved from http://kb.igs.org/hc/en-us/articles/360018811151

- Kanamori, H. & McNally, K.C. (1982) Variable rupture mode of the subduction zone along the Ecuador-Colombia coast. Bulletin of the Seismological Society of America, 72, 1241–1253.
- Kendrick, E., Bevis, M., Smalley, R., Brooks, B., Vargas, R.B., Lauriá, E. & Fortes, L.P.S. (2003) The Nazca–South America Euler vector and its rate of change. Journal of South American Earth Sciences, 16, 125–131. doi:https://doi.org/10.1016/S0895-9811(03)00028-2
- Khazaradze, G., Wang, K., Klotz, J., Hu, Y. & He, J. (2002) Prolonged post-seismic deformation of the 1960 great Chile earthquake and implications for mantle rheology. Geophysical Research Letters, 29, 7–1, John Wiley & Sons, Ltd. doi:10.1029/2002GL015986
- Klein, E., Fleitout, L., Vigny, C. & Garaud, J.D. (2016) Afterslip and viscoelastic relaxation model inferred from the large-scale post-seismic deformation following the 2010 Mw 8.8 Maule earthquake (Chile). Geophysical Journal International, 205, 1455–1472. doi:10.1093/gji/ggw086
- Kobayashi, D., LaFemina, P., Geirsson, H., Chichaco, E., Abrego, A.A., Mora, H. & Camacho, E. (2014) Kinematics of the western Caribbean: Collision of the Cocos Ridge and upper plate deformation. Geochemistry, Geophysics, Geosystems, 15, 1671–1683. doi:10.1002/2014GC005234
- Kruse, S.E., Liu, Z.J., Naar, D.F. & Duncan, R.A. (1997) Effective elastic thickness of the lithosphere along the Easter Seamount Chain. Journal of Geophysical Research: Solid Earth, 102, 27305–27317, John Wiley & Sons, Ltd. doi:10.1029/97JB02158
- Kumar, R.R. & Gordon, R.G. (2009) Horizontal thermal contraction of oceanic lithosphere: The ultimate limit to the rigid plate approximation. Journal of Geophysical Research: Solid Earth, 114, John Wiley & Sons, Ltd. doi:10.1029/2007JB005473
- Liu, Z. (1996) The Origin and Evolution of the Easter Seamount Chain, University of South Florida. Retrieved from https://books.google.fr/books?id=w8kPAQAAIAAJ
- Lonsdale, P. (2005) Creation of the Cocos and Nazca plates by fission of the Farallon plate. Tectonophysics, 404, 237–264. doi:10.1016/j.tecto.2005.05.011
- Lonsdale, P. & Klitgord, K.D. (1978) Structure and tectonic history of the eastern Panama Basin. GSA Bulletin, 89, 981–999. doi:10.1130/0016-7606(1978)89<981:SATHOT>2.0.CO;2
- Lyard, F., Lefevre, F., Letellier, T. & Francis, O. (2006) Modelling the global ocean tides: modern insights from FES2004. Ocean Dynamics, 56, 394–415. doi:10.1007/s10236-006-0086-x
- Marcaillou, B., Charvis, P. & Collot, J.-Y. (2006) Structure of the Malpelo Ridge (Colombia) from seismic and gravity modelling. Marine Geophysical Researches, 27, 289–300. doi:10.1007/s11001-006-9009-y
- Mccaffrey, R. (2002) Crustal Block Rotations and Plate Coupling. in Plate Boundary Zones, pp. 101–122, American Geophysical Union (AGU). doi:https://doi.org/10.1029/GD030p0101
- McCarthy, D. (1996) IERS Conventions (1996), Technical Note 21., Observatory of Paris: IERS. Retrieved from https://www.iers.org/IERS/EN/Publications/TechnicalNotes/tn21.html
- Meade, B. J. & Hager, B. (2005) Block models of crustal motion in southern California constrained by GPS measurements. Journal of Geophysical Research, 110.

- Meade, Brendan J. (2007) Algorithms for the calculation of exact displacements, strains, and stresses for triangular dislocation elements in a uniform elastic half space. Computers & Geosciences, 33, 1064–1075. doi:10.1016/j.cageo.2006.12.003

- Métois, M., Socquet, A., Vigny, C., Carrizo, D., Peyrat, S., Delorme, A., Maureira, E., et al. (2013) Revisiting the North Chile seismic gap segmentation using GPS-derived interseismic coupling. Geophysical Journal International, 194, 1283–1294. doi:10.1093/gji/ggt183

- Mishra, J.K. & Gordon, R.G. (2016) The rigid-plate and shrinking-plate hypotheses: Implications for the azimuths of transform faults. Tectonics, 35, 1827–1842, John Wiley & Sons, Ltd. doi:10.1002/2015TC003968

- Mooney, W. (2015) Crust and Lithospheric Structure - Global Crustal Structure. in Treatise on Geophysics, Vol. 1, pp. 339–372, Elsevier B.V.

- Mora-Páez, H., Kellogg, J.N., Freymueller, J.T., Mencin, D., Fernandes, R.M.S., Diederix, H., LaFemina, P., et al. (2019) Crustal deformation in the northern Andes – A new GPS velocity field. Journal of South American Earth Sciences, 89, 76–91. doi:https://doi.org/10.1016/j.jsames.2018.11.002

- Mora-Páez, H., Peláez-Gaviria, J., Diederix, H., Bohórquez-Orozco, O., Cardona-Piedrahita, L., Corchuelo-Cuervo, Y., Ramírez-Cadena, J., et al. (2018) Space Geodesy Infrastructure in Colombia for Geodynamics Research. Seismological Research Letters, 89, 446–451. doi:10.1785/0220170185

- Mothes, P.A., Nocquet, J.-M. & Jarrín, P. (2013) Continuous GPS Network Operating Throughout Ecuador. Eos, Transactions American Geophysical Union, 94, 229–231. doi:10.1002/2013EO260002

- Nocquet, Jean-Mathieu. (2012) Present-day kinematics of the Mediterranean: A comprehensive overview of GPS results. Tectonophysics, 579, 220–242. doi:https://doi.org/10.1016/j.tecto.2012.03.037

- Nocquet, J-M. (2002) Mesure de la déformation crustale en Europe occidentale par géodésie spatiale.

- Nocquet, J-M., Calais, E., Altamimi, Z., Sillard, P. & Boucher, C. (2001) Intraplate deformation in western Europe deduced from an analysis of the International Terrestrial Reference Frame 1997 (ITRF97) velocity field. Journal of Geophysical Research: Solid Earth, 106, 11239–11257. doi:10.1029/2000JB900410

- Nocquet, J-M., Jarrin, P., Vallée, M., Mothes, P.A., Grandin, R., Rolandone, F., Delouis, B., et al. (2016) Supercycle at the Ecuadorian subduction zone revealed after the 2016 Pedernales earthquake. Nature Geoscience, 10, 145. doi:10.1038/ngeo2864

- Nocquet, J-M., Villegas-Lanza, J.C., Chlieh, M., Mothes, P.A., Rolandone, F., Jarrin, P., Cisneros, D., et al. (2014) Motion of continental slivers and creeping subduction in the northern Andes. Nature Geoscience, 7, 287–291. doi:10.1038/ngeo2099

- Norabuena, E.O., Dixon, T.H., Stein, S. & Harrison, C.G.A. (1999) Decelerating Nazca-South America and Nazca-Pacific Plate motions. Geophysical Research Letters, 26, 3405–3408. doi:10.1029/1999GL005394

- Pennington, W.D. (1981) Subduction of the Eastern Panama Basin and seismotectonics of northwestern South America. Journal of Geophysical Research: Solid Earth, 86, 10753–10770. doi:10.1029/JB086iB11p10753

- Perfit, M.R. & Chadwick Jr., W.W. (1998) Magmatism at Mid-Ocean Ridges: Constraints from Volcanological and Geochemical Investigations. in Faulting and Magmatism at Mid-Ocean Ridges, pp. 59–115, American Geophysical Union (AGU). doi:10.1029/GM106p0059

- Piñón, D.A., Gómez, D.D., Smalley, R., Jr., Cimbaro, S.R., Lauría, E.A. & Bevis, M.G. (2018) The History, State, and Future of the Argentine Continuous Satellite Monitoring Network and Its Contributions to Geodesy in Latin America. Seismological Research Letters, 89, 475–482. doi:10.1785/0220170162

- Prawirodirdjo, L. & Bock, Y. (2004) Instantaneous global plate motion model from 12 years of continuous GPS observations. Journal of Geophysical Research: Solid Earth, 109, John Wiley & Sons, Ltd. doi:10.1029/2003JB002944

- Rebischung, P., Altamimi, Z., Ray, J. & Garayt, B. (2016) The IGS contribution to ITRF2014. Journal of Geodesy, 90, 611–630. doi:10.1007/s00190-016-0897-6

- Rodrigo, C., Diaz, J. & Gonzalez-Fernandez, A. (2014) Origin of the Easter Submarine Alignment: morphology and structural lineaments. Latin american journal of aquatic research, 42, 857–870, scielocl. Retrieved from https://scielo.conicyt.cl/scielo.php

- Ruiz, S. & Madariaga, R. (2018) Historical and recent large megathrust earthquakes in Chile. Tectonophysics, 733, 37–56. doi:10.1016/j.tecto.2018.01.015

- Sella, G.F., Dixon, T.H. & Mao, A. (2002) REVEL: A model for Recent plate velocities from space geodesy. Journal of Geophysical Research: Solid Earth, 107, ETG 11-1, John Wiley & Sons, Ltd. doi:10.1029/2000JB000033

- Suito, H. & Freymueller, J. (2009) A viscoelastic and afterslip postseismic deformation model for the 1964 Alaska earthquake. Journal of Geophysical Research, 114. doi:10.1029/2008JB005954

- Trenkamp, R., Kellogg, J.N., Freymueller, J.T. & Mora, H.P. (2002) Wide plate margin deformation, southern Central America and northwestern South America, CASA GPS observations. Journal of South American Earth Sciences, 15, 157–171. doi:https://doi.org/10.1016/S0895-9811(02)00018-4

- UNAVCO. (2004) Project Highlights 2004 - Easter Island IGS Station Install and Maintenance. Retrieved from https://www.unavco.org/highlights/2004/easterisland2.html

- UNAVCO Community. (2008) COCONet GPS Network: Station CN00 and 45 Others, UNAVCO, Inc. doi:10.7283/T5WM1BRG

- Vezzoli, L. & Acocella, V. (2009) Easter Island, SE Pacific: An end-member type of hotspot volcanism. GSA Bulletin, 121, 869–886. doi:10.1130/B26470.1

- Vigny, C., Socquet, A., Peyrat, S., Ruegg, J.-C., Métois, M., Madariaga, R., Morvan, S., et al. (2011) The 2010 Mw 8.8 Maule Megathrust Earthquake of Central Chile, Monitored by GPS. Science, 332, 1417. doi:10.1126/science.1204132

- Vigny, Christophe, Rudloff, A., Ruegg, J.-C., Madariaga, R., Campos, J. & Alvarez, M. (2009) Upper plate deformation measured by GPS in the Coquimbo Gap, Chile. Physics of the Earth and Planetary Interiors, 175, 86–95. doi:https://doi.org/10.1016/j.pepi.2008.02.013

- Wang, K., Hu, Y., Bevis, M., Kendrick, E., Smalley Jr., R., Vargas, R.B. & Lauría, E. (2007) Crustal motion in the zone of the 1960 Chile earthquake: Detangling earthquake-cycle deformation and forearc-sliver translation. Geochemistry, Geophysics, Geosystems, 8. doi:10.1029/2007GC001721

- White, S.M., Trenkamp, R. & Kellogg, J.N. (2003) Recent crustal deformation and the earthquake cycle along the Ecuador–Colombia subduction zone. Earth and Planetary Science Letters, 216, 231–242. doi:10.1016/S0012-821X(03)00535-1

- Williams, S.D.P. (2008) CATS: GPS coordinate time series analysis software. GPS Solutions, 12, 147–153. doi:10.1007/s10291-007-0086-4

- Ye, L., Kanamori, H., Avouac, J.-P., Li, L., Cheung, K.F. & Lay, T. (2016) The 16 April 2016, MW7.8 (MS7.5) Ecuador earthquake: A quasi-repeat of the 1942 MS7.5 earthquake and partial re-rupture of the 1906 MS8.6 Colombia–Ecuador earthquake. Earth and Planetary Science Letters, 454, 248–258. doi:https://doi.org/10.1016/j.epsl.2016.09.006

- Zhang, T., Gordon, R.G., Mishra, J.K. & Wang, C. (2017) The Malpelo Plate Hypothesis and implications for nonclosure of the Cocos-Nazca-Pacific plate motion circuit. Geophysical Research Letters, 44, 8213–8218. doi:10.1002/2017GL073704

3.10 SUPPORTING INFORMATION

Supporting Information for Uncertainties in the Present–day kinematics of the Nazca plate from GPS observations

P. Jarrin[1*], J.-M. Nocquet[2,3], F. Rolandone[1], H. Mora-Páez[4], P. Mothes[5], D. Cisneros[6]

[1] Sorbonne Université, Institut des Sciences de la Terre Paris, ISTeP, UMR 7193, F-75005 Paris, France.

E-mail: paul.jarrin@sorbonne-universite.fr

[2] Université Côte d'Azur, IRD, CNRS, Observatoire de la Côte d'Azur, Géoazur, 06560 Valbonne, France

[3] Institut de Physique du Globe de Paris, Université de Paris, Paris, France

[4] Colombian Geological Survey, Space Geodesy Research Group, Bogotá, Colombia

[5] Escuela Politécnica Nacional Instituto Geofísico, Ladrón de Guevara E11-253 Apartado 2759 Quito, Ecuador

[6] Instituto Geográfico Militar de Ecuador IGM-EC, Sector El Dorado, 2435 Quito, Ecuador.

This file includes:

- Table 3.3 - 3.6
- Figure 3.14 - 3.15

Table 3.3 – GPS Velocities expressed in the ITRF2014 reference frame. This subset of 17 sites are used to estimate the South American pole. Longitude and Latitude in decimal degrees. Ve and Vn are east and north components of velocity in mm/yr. SVe, SVn are the associated uncertainties of Ve and Vn to 95% confidence level in mm/yr

Site	Lon.	Lat.	Ve	Vn	SVe	SVn
ACP1	-79.950	9.371	16.33	12.00	0.16	0.10
ACP6	-79.408	9.238	17.03	12.10	0.13	0.15
ANTC	-71.532	-37.339	15.82	10.37	0.13	0.04
ARCA	-70.759	7.084	-4.76	11.28	0.17	0.07
AREQ	-71.493	-16.466	12.54	14.58	0.60	0.41
ASC1	-14.412	-7.951	-5.27	11.16	0.40	0.20
BOGT	-74.081	4.640	-0.23	14.79	0.14	0.28
BRAZ	-47.878	-15.947	-3.76	12.57	0.11	0.07
BUE1	-58.519	-34.574	-0.57	11.80	0.35	0.42
CFAG	-68.233	-31.602	6.66	12.11	0.05	0.12
CHPG	-45.002	-22.682	-3.61	12.57	0.29	0.15
CHPI	-44.985	-22.687	-3.80	12.58	0.11	0.10
CN28	-79.034	8.625	17.99	13.85	0.16	0.18
CONT	-73.025	-36.843	33.55	20.84	0.11	0.10
COPO	-70.338	-27.385	21.51	19.02	0.36	0.20
CORD	-64.470	-31.528	0.60	12.42	0.34	0.14
COYQ	-71.892	-45.514	0.97	9.35	0.08	0.08
FALK	-57.874	-51.694	0.00	13.23	0.10	0.11
GAMB	-134.965	-23.130	-66.99	31.90	0.47	0.44
GOUG	-9.881	-40.349	21.32	18.55	0.14	0.13
GRE0	-61.640	12.222	13.44	15.24	0.22	0.16
IQQE	-70.132	-20.274	23.27	16.67	0.35	0.13
IQTS	-73.275	-3.767	-3.66	10.91	0.25	0.10
IQUI	-73.269	-3.767	-3.85	10.93	0.27	0.30
ISCO	-87.056	5.544	49.27	73.46	0.42	0.38
KOU1	-52.806	5.252	-4.25	12.87	0.27	0.48
LHCL	-65.595	-38.003	0.02	10.58	0.06	0.09
LMMF	-60.996	14.595	12.75	15.69	0.08	0.07
MPLA	-57.531	-38.036	-0.37	12.09	0.08	0.30
NEIA	-47.925	-25.020	-3.18	12.77	0.15	0.13
PARA	-49.231	-25.448	-2.98	12.50	0.22	0.27
POVE	-63.896	-8.709	-3.60	12.14	0.11	0.06
PUIN	-67.903	3.851	-4.75	11.78	0.20	0.34
RECF	-34.952	-8.051	-4.66	12.77	0.44	0.46
RIO2	-67.751	-53.785	3.63	11.90	0.14	0.08
RIOP	-78.651	-1.651	2.07	8.58	0.19	0.15
SALU	-44.212	-2.593	-4.32	12.94	0.35	0.18
SAN0	-81.716	12.580	12.12	6.75	0.26	0.17
SANT	-70.669	-33.150	21.15	16.71	0.37	0.22
SAVO	-38.432	-12.939	-4.34	12.85	0.10	0.11
SCRZ	-63.160	-17.797	-1.95	12.15	0.43	0.28
STHL	-5.667	-15.943	23.90	18.45	0.43	0.35
TEFE	-64.721	-3.349	-4.17	11.77	0.11	0.23
TGCV	-22.983	16.755	19.15	16.11	0.07	0.09
TUCU	-65.230	-26.843	2.34	10.38	0.09	0.08
UFPR	-49.231	-25.448	-3.46	12.95	0.22	0.22
UNSA	-65.408	-24.727	5.21	11.70	0.20	0.15
VALP	-71.626	-33.027	27.51	21.80	0.32	0.18
VDPR	-73.248	10.436	7.83	14.69	0.39	0.38

Table 3.4 – Estimated South American pole with its associated variance-covariance matrix. R_ve and R_vn are east and north velocity residuals in mm/yr. S_ve and S_vn are formal errors of R_vE and R_vn. RN_ve and RN_vn are normalized residuals.

```
ROTATION RATE VECTOR
Wx (rad/yr): -1.3718E-09 +- 1.0414E-11
Wy (rad/yr): -1.4564E-09 +-  1.501E-11
Wz (rad/yr): -6.6597E-10 +- 7.2744E-12

ASSOCIATED VARIANCE-COVARIANCE MATRIX (rad/yr)**2
        Wx          Wy            Wz
---------------------------------------
Wx | 1.0846E-22  -1.332E-22  -3.4946E-23
Wy |              2.2531E-22  5.209E-23
Wz |                           5.2916E-23
---------------------------------------

EULER POLE :
longitude (dec. degree)    : -133.29
latitude  (dec. degree)    : -18.41
angular velocity (deg/Myr ):  0.121
ASSOCIATED ERROR ELLIPSE
semi major axis            :  0.47
semi minor axis            :  0.17
azimuth of semi major axis : -32.6
std(angular velocity)      : 0.000

STATISTICS
Number of sites     =         17
Chi**2              =       40.8
Reduced Chi**2      =        1.1
Deg. of freedom     =         31
A post. var. factor =        1.1

RESIDUALS
site         R_ve       R_vn       S_ve       S_vn      RN_ve      RN_vn
-------------------------------------------------------------------------
ARCA         0.17      -0.04       0.17       0.07       1.02      -0.59
ASC1        -0.22      -0.02       0.40       0.20      -0.54      -0.09
BRAZ         0.04      -0.15       0.11       0.07       0.40      -2.11
CHPG         0.16      -0.18       0.29       0.15       0.55      -1.15
CHPI        -0.02      -0.17       0.11       0.10      -0.20      -1.74
IQTS         0.16      -0.14       0.25       0.10       0.65      -1.43
IQUI        -0.03      -0.13       0.27       0.30      -0.09      -0.42
KOU1         0.17       0.28       0.27       0.48       0.62       0.59
NEIA         0.24       0.06       0.15       0.13       1.58       0.45
PARA         0.29      -0.18       0.22       0.27       1.35      -0.68
POVE        -0.08       0.20       0.11       0.06      -0.74       3.36
PUIN        -0.16       0.18       0.20       0.34      -0.79       0.53
RECF        -0.19       0.15       0.44       0.46      -0.43       0.32
SALU        -0.09       0.18       0.35       0.18      -0.24       1.00
SAVO         0.04       0.14       0.10       0.11       0.40       1.25
TEFE        -0.20      -0.11       0.11       0.23      -1.81      -0.49
UFPR        -0.19       0.26       0.22       0.22      -0.86       1.17
-------------------------------------------------------------------------
rms =       0.16 mm/yr    wrms =       0.15 mm/yr
```

Table 3.5 – Noise amplitudes and spectral indices estimated by CATS at EISL and ISPA sites. k: spectral index. WH: White noise in mm. According to k values, flicker noise is the dominant model in the power-law process (PL), which is expressed in $mm/yr^{1/4}$.

Site	**Component**	**k**	**Noise Amplitudes**	
			WH	**PL**
EISL	North	-0.7	1.4 ± 0.1	4.0 ± 0.2
	East	-0.8	1.8 ± 0.1	6.6 ± 0.3
ISPA	North	-0.8	1.0 ± 0.1	3.7 ± 0.2
	East	-1.0	1.4 ± 0.1	4.6 ± 0.2

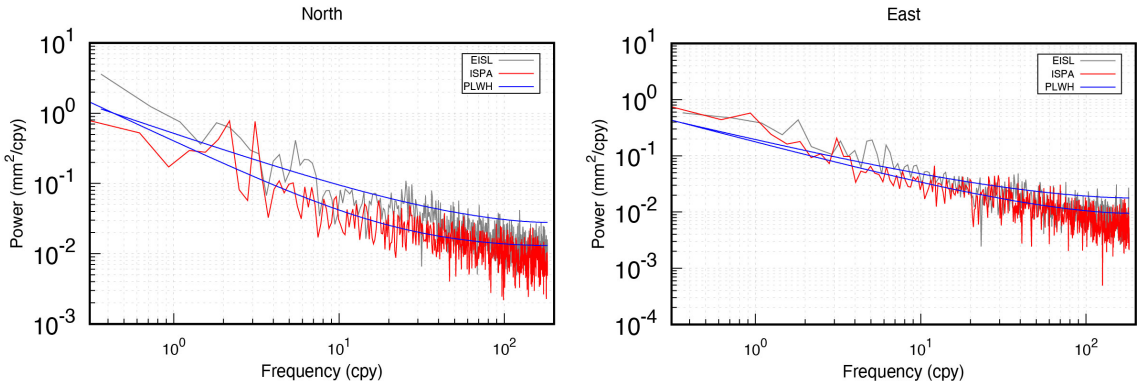

Figure 3.14 – Power spectral densities (PSDs) from the EISL and ISPA residual time series. Blue solid lines are the fitted power-law plus white noise model

Table 3.6 – Best Nazca plate rotation pole (NZROT51) with the associated variance-covariance matrix. R_ve and R_vn are east and north velocity residuals in mm/yr. S_ve and S_vn are formal errors of R_ve and R_vn. RN_ve and RN_vn are normalized residuals.

```
ROTATION RATE VECTOR
Wx (rad/yr): -9.2515E-11 +- 5.6928E-11
Wy (rad/yr): -5.7094E-09 +- 1.8327E-10
Wz (rad/yr):  8.5271E-09 +-  5.954E-11
ASSOCIATED VARIANCE-COVARIANCE MATRIX (rad/yr)**2
        Wx           Wy            Wz
---------------------------------------
Wx | 3.2408E-21  7.4627E-21  8.8266E-22
Wy |             3.359E-20   3.7443E-21
Wz |                         3.5451E-21
---------------------------------------

RESIDUALS
----------
site         R_ve       R_vn       S_ve       S_vn      RN_ve      RN_vn
-------------------------------------------------------------------------
GLPS        -0.45       1.90       0.64       1.29      -0.71       1.48
ILSG        -0.34      -0.43       0.87       0.41      -0.40      -1.04
ISPA         0.70       0.20       1.13       0.38       0.62       0.52
MALO         1.34      -1.30       1.07       1.07       1.25      -1.21
SCEC        -0.05       0.47       0.59       0.65      -0.08       0.72
-------------------------------------------------------------------------
rms =       0.91 mm/yr    wrms =       0.57 mm/yr
```

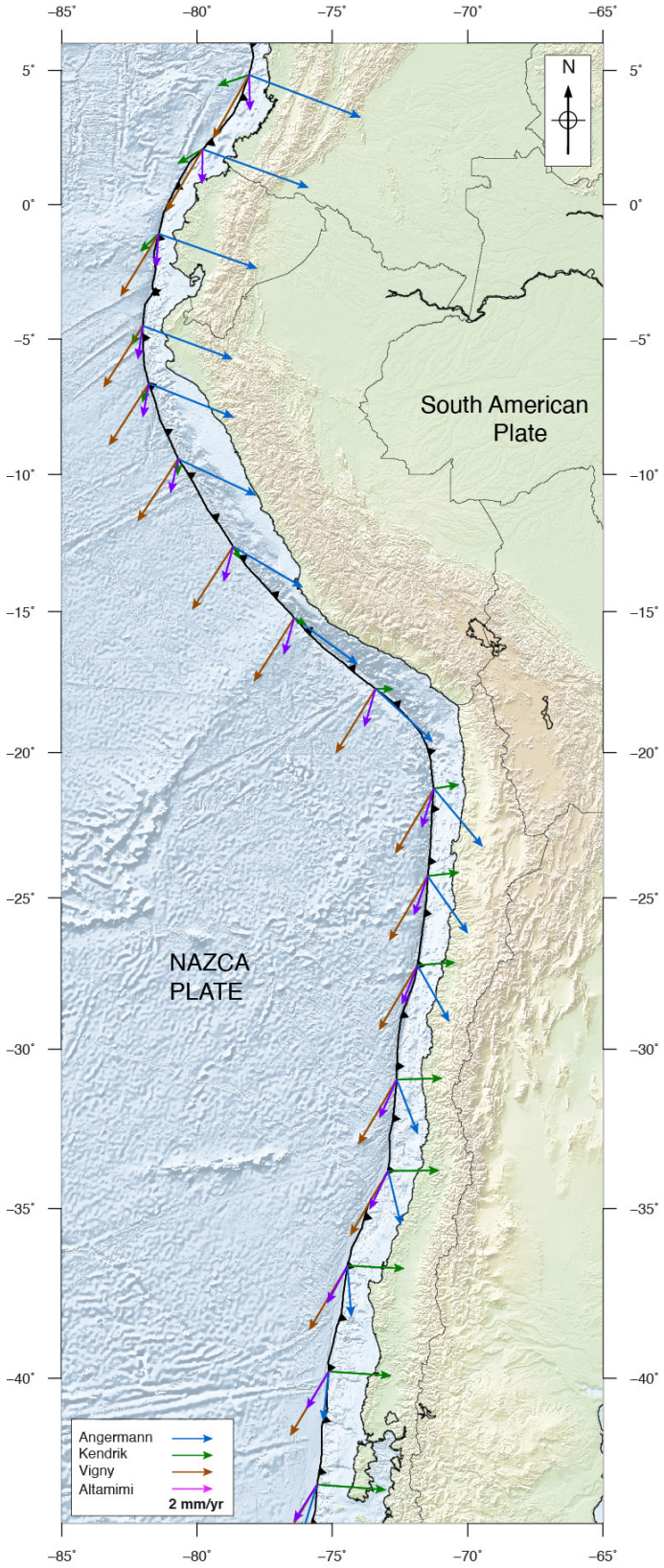

Figure 3.15 – Differences of velocity prediction from Angermann et al. (1999), Kendrick et al. (2003), Vigny et al. (2009), and Altamimi et al. (2017) with respect to NZROT51 prediction every 3° along the Nazca/SOAM plate boundary.

CHAPTER 4

Continental Block motion in the Northern Andes from GPS measurements

In this chapter, I aim at defining a kinematic model at the scale of the Northern Andes. The objective is two fold.

The first objective is to test whether the whole GPS data set can be fitted by a single model, consistent at the regional scale of the Northern Andes, explaining most of the documented patterns of the active continental deformation. Among the outcomes from this study, slip rates along the major faults provide new constraints on the seismic hazard for ongoing projects like the South American Risk Assessment (SARA) project.

The second objective is to improve the determination of the interseismic coupling distribution along the Nazca/South America subduction interface.

The used approach is to build an elastic block model. Although this approach simultaneously solves for the interseismic coupling (ISC) at the subduction interfaces and block rotations, this chapter presents only the results for the continental part. Chapter 5 describes the results obtained for the Interseismic coupling.

The software used for this part is pyeblock from the PYACS package. The core pyeblock code has been developped by Jean-Mathieu Nocquet. During this study, I participated to the evolution of the code and performed benchmarks against existent packages like blocks (Meade and Loveless 2009).

Continental Block motion in the Northern Andes from GPS measurements

Abstract
The North Andean Sliver (NAS) is a continental domain squeezed between the Nazca, Caribbean, and South American plates. Several attempts have been performed to characterize the NAS motion using geodetic measurements. Most of them have estimated the NAS kinematics as a single rigid block moving towards the north-northeast at 8-10 mm/yr based on partial GPS data sets. Although the NAS boundaries hosts the largest earthquakes in the northern Andes, geological and seismotectonic data also indicates internal deformation, across secondary fault systems, resulting from the interaction of several tectonic blocks. Here, we present an updated and most extensive interseismic horizontal velocity field derived from continuous and episodic GPS data from 1994 to 2019.9 that encompasses the whole North Andean Sliver and neighboring regions. We then develop a kinematic elastic block model in order to simultaneously estimate rigid block rotations and consistent slip rates at crustal faults. Our model is not constrained by prior information derived from geological slip rates or creeping faults. Results of our model indicate that the NAS kinematics is well described by the rotation of 6 tectonic blocks, showing increasing eastward motion from south to north. The Eastern boundary of the sliver is defined by a right-lateral transpressive system accommodating 5 to 17 mm/yr of motion. Deformation within the NAS occurs along several secondary fault systems at 2-4 mm/yr. Slow reverse motion across the Eastern Subandean belt at 2-4 mm/yr delimit the Subandean domain in Ecuador and north-central Peru. We propose a new boundary for the Panama/NAS suture zone where arc-Continental collision is accommodated at 6 and 15 mm/yr across the Uramita fault and Eastern Panama deformed zone respectively. A portion of strain from this collision is also transferred towards the northeast throughout the San Jacinto fold belt and extends as far as longitude ∼75°W. Slip rates estimates for these fault systems thus provide new insights for seismic hazard assessment. In addition, the Caribbean/SOAM relative motion confirms slow active subduction at ∼4.5 mm/yr along the South Caribbean Deformed Belt offshore northern Colombia and relatively uniform 2 mm/yr offshore northern Venezuela. Oblique convergence along the Ecuadorian and Colombian trench axis at ∼47.5 and ∼44.5 mm/yr with respect to the motion of NAS is consistent with a subduction interface rapidly accumulating elastic strain.

Key words: Elastic model, Euler pole estimate, block model, Satellite geodesy, Plate motion: North Andean sliver.

4.1 INTRODUCTION

The North Andean Sliver (hereinafter NAS) is a ∼2200 km long and 300 to 1000 km wide continental domain lying at the northwestern leading edge of the South American plate (SOAM). The NAS comprises the Andean Cordillera and its margin in Ecuador north of the Gulf of Guayaquil, Colombia and western Venezuela (figure 4.1). Large megathrust earthquakes frequently occur along its western boundary where the oceanic Nazca plate subducts beneath the

South America continent. The NAS also hosts numerous crustal earthquakes, among the largest documented in the Andes, sometimes occurring close to populated areas (Beauval et al. 2010; 2013).

Along the Ecuador-Colombian Pacific margin, convergence of the oceanic Nazca plate beneath the South American continental plate occurs at a rate ranging from 56 to 52 mm/yr towards ∼N83°E, and is 30-40° oblique to the trench perpendicular direction (Nocquet et al. 2014, Yepes et al. 2016, Jarrin et al. (submitted)). As observed in many ocean-continent subduction settings (e.g. McCaffrey (1992)), oblique convergence induces long-term shear stress, which results in a translation motion of a continental upper plate sliver, individualized from the rest of the overriding plate. The translation motion occurs in the same sense as the trench parallel component of the convergence and cause partitioning of the plate convergence vector into reverse slip at the subduction interface and trench parallel strike-slip crustal faulting accommodating part or all of the trench parallel component. Such partitioning appears to occur along the whole ∼6000 km length of the Nazca/SOAM plate boundary (Nocquet et al. 2014). Indeed, aside the Northern Andes, 5-6 mm/yr southeastward motion is observed throughout Peru for the Inca sliver (Nocquet et al. 2014, Villegas-Lanza et al. 2016b), and in Chile south of latitude ∼38°S where the Liquiñe-Ofqui right-lateral strike slip fault zone delimits the Chiloe sliver moving northward at ∼6 mm/yr with respect to SOAM (Melnick et al. 2009, Moreno et al. 2008, Wang et al. 2007).

In the northern Andes, regional analysis of focal mechanism solutions, seismicity distribution and active tectonics studies suggest that the lateral motion of the NAS is accommodated throughout several fault systems running along the Eastern Andean Cordillera and merging with the subduction in the Gulf of Guayaquil (Alvarado et al. 2016, Audemard et al. 2008, Audemard 2009, Egbue and Kellogg 2010, Ego et al. 1995, Pennington 1981, Tibaldi et al. 2007, Velandia et al. 2005). GPS survey mode measurements performed during the 90s in Central America and northern South America provided first-order constraints about the regional continental deformation in Ecuador and Colombia (Freymueller et al. 1993, Trenkamp et al. 2002, White et al. 2003). Trenkamp et al. (2002) quantified the northeastward escape of the NAS as a single rigid block moving at ∼6±2 mm/yr to the northeast. Analysis of 4 years of a GPS network extending from central Peru to northern Ecuador provided an updated horizontal velocity field at the regional scale (Nocquet et al. 2014). In order to determine the NAS motion, Nocquet et al. (2014) noted that elastic strain induced by interseismic locking at the megathrust is negligible in Ecuador south of the Carnegie ridge and north of the Gulf of Guayaquil. Then, they found that these velocities are consistent at the 1 mm/yr level with velocities in southern and central Colombia ∼300 km away from the trench, allowing to estimate an Euler pole at longitude -83.4°E, latitude 15.21°N, 0.29 deg/Myr, predicting northeastward (N70°±10E) 8.5±1 mm/yr motion with respect to South America. Their kinematic model for the NAS implies only ∼20% of partitioning. More recently, Mora-Páez et al. (2019) provide an augmented spatial sampling of the NAS than Nocquet et al. (2014) by including additional velocities at GPS sites north of latitude 4°N. Their proposed Euler pole (longitude -185.2°E, latitude 58.6°N, 0.07 deg/Myr) predicts 8.6 mm/yr towards N60°E. Despite their large difference in location, both Euler poles predict similar velocities at latitude 2-4°N. However,

differences reaching 5 mm/yr in northern Colombia show better predictions for Mora-Páez et al. (2019) model. Significant discrepancies are also observed with results from Symithe et al. (2015) and Pérez et al. (2018), which were estimated from kinematic models at the northernmost part of the sliver in northern Colombia and Venezuela. Such differences among published models probably arise from different areas sampled by the individual data sets and suggest that the NAS kinematics is not well described using the assumption of a single idealized rigid block.

Active crustal deformation occurring within the sliver is indeed confirmed by tectonic studies and both recent and historical seismicity. Active tectonic studies usually agree on recognizing the eastern boundary of the NAS as successive right-lateral transpressional fault systems along the eastern Andes (Alvarado et al. 2016, Audemard 2009, Eguez et al. 2003, Paris et al. 2000, Taboada et al. 2000). From south to north, this fault system includes the Gulf of Guyaquil in Ecuador, cuts through the Andean Cordillera at latitude ∼2°S and then run along the eastern flank of the Andes north up to Venezuela. This major boundary hosts most of the large crustal earthquakes documented in the northern Andes. However, few large crustal earthquakes as the 1868 Mw ∼7.2 Ibarra earthquake, the 1766 Mw 6.5 Cali earthquake, and the 1885 Mw ∼ 6.4 El Tambo earthquake have happened well inside the NAS (Beauval et al. 2010, Dimaté et al. 2005, SGC 2021, Yepes et al. 2016). Focal mechanisms (Figure 4.1) also attest for regular Mw>5 occurring on active faults within the NAS (Ekström et al. 2012, Vaca et al. 2019, Yepes et al. 2016). How much of the deformation is taken up by these faults, knowing whether they are significantly less active than the one delimiting the eastern boundary of the NAS remains largely unknown.

Understanding and modeling the current motion and internal deformation of the NAS requires to define the kinematics conditions acting along its edges. Aside the oblique convergence of the Nazca plate described above, there are at least two additional boundaries to account for: (1) In northwestern Colombia, crustal earthquakes, neotectonic studies, and previous geodetic results point out the collision of Panama block against the NAS at ∼1 cm/yr. The ongoing collision that started ∼15 Myr ago induces a broad deformation in northwestern Colombia (Kellogg et al. 2019, Kobayashi et al. 2014, Mora-Páez et al. 2019, Taboada et al. 2000, Trenkamp et al. 2002). (2) Northeast of Panama block, the kinematic boundary acting along the northern edge of the NAS is provided by the eastward motion of the Caribbean plate, at 17-18 mm/yr (Symithe et al. 2015) with respect to South America. The plate boundary is made of an accretionary prism offshore western Venezuela and Colombia referred as the "South Caribbean Deformed Belt" (SCDB) (Kroehler et al. 2011), overriding a low angle subduction (Bernal-Olaya et al. 2015, Hilst and Mann 1994, Kellogg and Bonini 1982, Kellogg et al. 2019, Lizarazo et al. 2021, Mora et al. 2017, Mora-Páez et al. 2019, Syracuse et al. 2016, Taboada et al. 2000). The subduction appears to be atypical with the absence of a developped magmatic arc and with no large megathrust earthquake documented. Both the SCDB and the subduction interface are expected to accommodated shortening between the NAS and the Caribbean plate. Recent elastic block models from Symithe et al. (2015) and Pérez et al. (2018) estimate a Caribbean/NAS convergence at 5-9 mm/yr offshore northern Colombia. However, these models neither include the Panama block nor the possible contribution of locking

of the Nazca subduction, possibly resulting in a biased estimate.

To date, a model that accurately describes Present-day kinematics of the NAS based on geodetic observations is not available. This study presents an updated extensive interseismic horizontal velocity field derived from continuous and episodic GPS measurements encompassing the North Andean Sliver and neighboring regions. This velocity field benefits from longer time series than available for previous studies and integrates new GPS sites in Ecuador, Colombia, Panama, and Peru. Using the velocity field as input, we then build a kinematic elastic block model that simultaneously solves for rigid block rotations and spatially variable coupling at the subduction interfaces, providing crustal fault slip rates consistent with the derived kinematics. The interseismic coupling (ISC) results at the Nazca/SOAM subduction interface are not presented in this paper, but they will be discussed separately in a forthcoming article. Our model is not constrained using prior information on geologic slip rates or focal mechanisms, but we use this information to validate our model. We finally discuss our results in terms of seismic hazards and the geodynamics governing the region.

4.2 ACTIVE TECTONIC SETTING

Here, we summarize the active seismo-tectonic information that is then used to build the geometry of our models described in section 4.5. Figure 4.1 outlines the major active plate boundaries and tectonic features along the North Andean Sliver compiled from Audemard (1996), Taboada et al. (2000), and Alvarado et al. (2016), together with focal mechanisms solutions from Ekström et al. (2012), Vaca et al. (2019), and SGC (2020a).

4.2.1 North Andean Sliver (NAS) eastern boundary

The eastern boundary marks the transition between actively deforming areas to the undeforming stable South America. The East-West trending El Pillar strike-slip fault in Venezuela accommodates most of the relative motion between the Carribean and South America plates. It prolongates to the west by the San Sebastian fault, marking the eastern limit between the NAS and South America. The westernmost extension of the San Sebastian fault merges with the NW-SE trending Boconó fault (BF), a predominantly right-lateral ∼500 km long fault system, also showing significant compression. The Boconó fault (BF) appears to be the most active structure running along the Merida or Venezuelan Andes. Two large earthquakes with magnitudes Mw ∼7.5 occurred in 1610 and 1894, probably rupturing the central portion of the fault and impacting the Merida and Barquisimeto cities (Audemard et al. 2008, Schubert 1982).

South of the Boconó fault, historical crustal earthquakes with M > 7 as the 1785 and 1827 M 7.1 Cundinamarca and Altamira earthquakes (Dimaté et al. 2005, SGC 2021) indicate the Eastern Frontal Fault System (EFFS) and the Afiladores-Sibundoy fault (ASF) as the primary active faults in Colombia (Acosta et al. 2007, Paris et al. 2000, Tibaldi et al. 2007). Several focal mechanism solutions (figure 4.1) support a transition from transpression across the Eastern Frontal

Fault System to pure right-lateral along the Afiladores-Sibundoy fault, that continues southward throughout the Chingual-Cosanga-Pallatanga-Puna (CCPP) fault system in Ecuador (Alvarado et al. 2016, Yepes et al. 2016). The latter two segments of CCPP fault called Pallatanga and Puna delimit the southern boundary between the NAS and the Inca sliver that encompasses the Andean Cordillera and its margin throughout Peru (Nocquet et al. 2014, Villegas-Lanza et al. 2016b).

In general, the CCPP fault is a transpressive right-lateral system. However, the Puna segment exhibits some portions of normal faulting on secondary faults defining a pull-apart structure in the the Gulf of Guayaquil (Alvarado et al. 2016, Eguez et al. 2003, Tibaldi et al. 2007). Active deformation has been evidenced along the Chingual-Cosanga-Pallatanga-Puna fault system (CCPP) in the last 500 years. This ∼800 km long structure hosted large crustal earthquakes as the 1797 Mw ∼7.6 earthquake which destroyed city of Riobamba, and the 1987 Mw ∼7.1 Reventador earthquake which caused 1000 deaths (Alvarado et al. 2016, Beauval et al. 2018; 2010).

In most regions along the Andes, fold-and-thrust belts have developed over tens or even hundreds of kilometers east of the Cordillera, referred as the sub-andean domain (Baby et al. 1997, Brooks et al. 2011, Bès de Berc et al. 2005, Weiss et al. 2016). However, no sub-andean domain is documented north of latitude 4°N . In Ecuador and Peru, active seismic exploration profiles reveal the presence of active thrust overlying a shallow (<10km) continuous flat decollement as far as 600 km from the trench and 300 km from the eastern flank of Andean Cordillera (Baby et al. 1997). Active deformation within the sub-andean domain is further witnessed by Mw ∼6 earthquakes in the Amazonia basin and for well developed morphology in the Eastern Subandean belt (ESB), like the Napo-Cutucu fault and Macas fault system (MFS). The latter fault hosted the Mw 7.0 1995 earthquake (See Figure 4.1) (Legrand et al. 2005).

4.2.2 Colombia

In northern Colombia, the main active structures are the Oca-Ancon (OAF) and the Santa-Martha Bucaramaga (SMB) fault systems. The east-west trending Oca-Ancon prolongates to the west the San Sebastian fault. It exhibits right-lateral strike-slip motion with reverse motion documented along the Oca segment (Audemard 1996). Crustal shallow earthquakes with Mw < ∼5 characterizes this ∼600 km long structure (figure 4.1 and 4.3) (Engdahl et al. 2020). However, evidence of Holocene activity with M ∼7 earthquakes is suggested by paleoseismological studies (Audemard 1996). It interstects the SSE-NNW Santa-Martha Bucaramanga fault at longitude 74°W. Although seismicity has been low for decades along the Santa-Martha Bucaramanga fault (Engdahl et al. 2020, Vargas 2019), paleoseismology studies suggest that several earthquakes occurred on the Bucaramanga segment since the Quaternary (Diederix et al. 2020). Both the Oca-Ancon and Santa Marta-Bucaramanga faults delimit the Bonaire and Maracaibo blocks (figure 4.1), accommodating the differential motion of the northernmost part of the NAS with the Caribbean plate and probably the Panama block (Audemard 2014; 2009, Symithe et al. 2015).

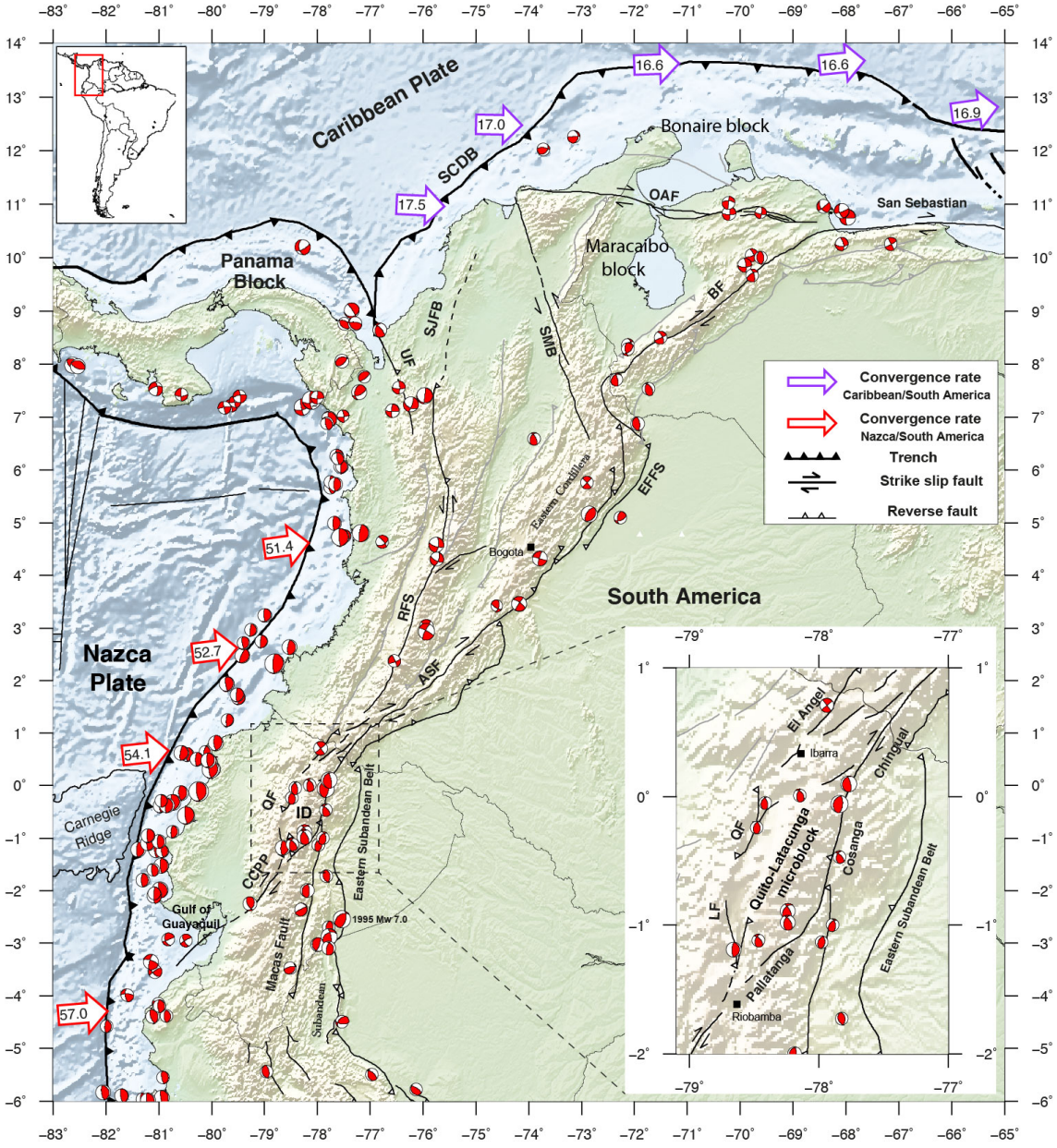

Figure 4.1 – Seismotectonic map of the North Andean Sliver. Thick black lines show major active plate boundaries and tectonic features summarized from Taboada et al. (2000), Audemard and Audemard (2002), and Alvarado et al. (2016). Shallow (<40 km depth) focal mechanisms solutions are Mw>5 from Ekström et al. (2012), Vaca et al. (2019), and SGC (2020b). Thin gray lines show crustal faults. Red and Violet arrows show the Nazca/SOAM and Caribbean/SOAM convergence velocities (in mm/yr) from Jarrin et al. submitted and Symithe et al. (2015) respectively. CCPP: Chingual-Cosanga-Pallatanga-Puna fault system. QF: Quito Fault, LF: Latacunga fault. ID: InterAndean Depression. RFS: Romeral Fault System, ASF: Afiladores-Sibundoy Fault. UF: Uramita Fault. SMB: Santa-Martha Bucaramanga Fault. OAF: Oca-Ancon Fault. BF: Boconó Fault. EFFS: Eastern Frontal Fault System. SJFB: San Jacinto Fold Belt. SCDB: South Caribbean Deformed Belt.

In south-central Colombia (latitudes 1°N - ∼7°N), the Romeral fault system (RFS) is the main structure running along the western slope of the central Cordillera. Geometrical complexities arise southward of latitude ∼ 4°N where the fault changes from left-lateral strike-slip motion to right-lateral with a reverse component (Ego et al. 1995, Paris et al. 2000, Taboada et al. 2000). Such behavior is also observed by the focal mechanism solutions displayed in figure 4.1. Active faulting for this structure is evidenced by earthquakes of Mw ∼ 6.0 that affected several departments in the Cauca river valley, like the 1994 Mw 6.8 Paéz earthquake and the 1999 Mw 6.1 Armenia earthquake which caused 921 deaths (SGC 2021).

4.2.3 Ecuador

Aside the main Chingual-Cosanga-Pallatanga-Puna fault system (CCPP) delimiting the eastern boundary of the NAS, major active faults have been recognized within the Interandean Depression in central Ecuador like the Latacunga fault (LF) and the Quito Fault (QF). Active deformation in the Quito fault is evidenced throughout several Mw > 5 shallow damaging earthquakes since the last decades along its different fault segments (inset of figure 4.1). The Quito fault is a blind reverse fault, dipping west that includes minor dextral strike-slip faulting and extending along ∼60 km (Alvarado et al. 2016; 2014). Further north, the Otavalo-El Angel fault is considered as being the northernmost extension of the Quito fault. It hosted the 1868 Mw ∼7.2 earthquake that destroyed the Ibarra city (Beauval et al. 2010). Therefore, the Quito-Latacunga and the Cosanga faults are proposed as the eastern and western boundaries of the Quito-Latacunga microblock, as a result of a progressive narrowing restraining bends (Alvarado et al. 2016).

In southern Ecuador (southward of latitude 4°S), the Macas fault (MF) appears following the eastern flank of the Andean Cordillera, extending to northern Peru merging with the transpressive Marañon fault system. The Marañon fault is a transpressional left-lateral strike-slip structure that follows the boundary between Western and Eastern cordilleras and probably extends further south in central Peru along the Chontal Fault System (Villegas-Lanza et al. 2016b). No large historical earthquake has been reported for the Marañon fault. However, seismic activity is witnessed by Mw 4-5 shallow earthquakes for the last decades (Ekström et al. 2012, Engdahl et al. 2020).

4.3 GPS DATA ANALYSIS

We use data from several regional continuous and episodic stations from a collaborative project between the French National Research Institute for Sustainable Development (IRD), the Geophysical Institute (IG-EPN) (Alvarado et al. 2018, Mothes et al. 2013), the Militar Geographical Institute (IGM) of Ecuador and the Geophysical Institute of Peru (IGP). We integrate data of 10 cGPS sites from the GeoRED Project (Geodesia: Red de Estudios de Deformación) in Colombia, which is run by the Space Geodesy Research Group from the Colombian Geological Survey (SGC:Mora-Páez et al. (2018)). We also include 180 cGPS sites from the National Geographical Institute of Peru (IGN), the Agustin Codazi Geographical Institute (IGAC) of Colombia, the

Tommi Guardia Geographical Institute (IGNTG) of Panama, Argentine Network for Continuous Satellite Monitoring (Piñón et al. 2018), the Low-Latitude Ionosphere Sensor Network (LISN: Valladares and Chau (2012)), COCONet Project (Community 2008), and regional stations from the global network of the International GNSS Service for Geodynamics (IGS, Dow et al. (2009)).

In addition, we integrate the GPS survey-mode data already used by Nocquet et al. (2014) but benefitting from one to three additional epochs of measurement in Ecuador and Peru. The final data set includes 416 sites covering the 1994 – 2019.9 period, among which 140 are located within the NAS.

Continuous and episodic GPS data were homogeneously analyzed using the GAMIT/GLOBK software release 10.71 (Herring et al. 2015; 2018), applying the methodology described in (Jarrin et al. submitted) to derive time series expressed in the international reference frame ITRF2014 (Altamimi et al. 2016) through its weekly updated realization from the IGS (Rebischung et al. 2016). We select cGPS benefitting from at least three years of observations to mitigate the impact of seasonal variations (Blewitt and Lavallée 2002). For the final velocity field, we select 83 campaign sites with at least four periods of measurements spanning at least 4 years. Daily position time series are visually inspected in order to identify offsets induced by earthquakes or antenna changes. We remove specific time windows showing non-linear evolution caused by post-seismic deformation after the 2016 Pedernales Mw 7.8 earthquake in Ecuador (Mothes et al. 2018, Rolandone et al. 2018), as well as during slow slip events occurring at the Ecuador-northern Peru subduction interface (Segovia et al. 2015, Vaca et al. 2018, Vallée et al. 2013, Villegas-Lanza et al. 2016a). We also remove obvious outliers for which velocity departs a few mm/yr from nearby sites. We then apply Bevis and Brown (2014) formulation to simultaneously estimate velocities, annual and semi-annual terms, and offsets. For cGPS time series, realistic velocity uncertainties are derived using the white and power-law noise combination by applying the maximum likelihood estimator implemented in the CATS software (Williams 2008). To estimate noise properties for campaign data with too few measurements, we add (quadratically) a colored noise contribution taken from the median value of surrounding cGPS sites to the uncertainty obtained using classical least-square (white noise).

Velocity uncertainties for cGPS sites are of the order of $\sim$0.3 mm/yr at the 1-sigma confidence level. For episodic GPS sites, velocity uncertainties are between 0.3 and 1.1 mm/yr at the 1-sigma confidence level for 10-15 years of observation.

In order to derive the most comprehensive velocity field at the scale of the North Andean Sliver, we combine our velocity field with the most recent published velocity field solutions from Mora-Páez et al. (2019) and Pérez et al. (2018) in a single consistent reference frame using common sites between solutions and applying the methodology proposed by Nocquet (2012). It is worth noting that Pérez et al. (2018) solution is mostly derived from episodic GPS measurements in Venezuela, resulting in a significant number of velocities with uncertainties exceeding 3 mm/yr.

In some cases, several ones have no coherent sense of motion with respect to the overall tectonic motion. Therefore, velocities with uncertainties greater than 1.5 mm/yr and velocities showing opposite motion to nearby cGPS sites were rejected. We keep the most recent estimate in the case of significative velocity discrepancies at common sites between solutions. Applying these criteria, our combination shows a weighted root mean square (wrms) of 0.8 mm/yr, indicating a good agreement between our solution with Mora-Páez et al. (2019) and Pérez et al. (2018) solutions. Finally, the resulting velocity field is expressed with respect to the stable part of the South American plate applying the Euler pole from Jarrin et al. submitted, which shows a wrms of 0.15 mm/yr. Velocities are listed in table 4.4 in the Supporting information.

Compared to previous studies, our velocity field provides a better spatial sampling of the NAS, with an average inter-site distance of 100-200 km in Colombia and ∼35 km in Ecuador. It also includes more sites within the Amazon basin allowing us to test how far deformation spreads inside the South America plate east of the Andes. Many Slow Slip Events (SSE) have been documented all along the Ecuadorian coast and northern Peru (Rolandone et al. 2018, Segovia et al. 2015, Vaca et al. 2019, Vallée et al. 2013, Villegas-Lanza et al. 2016a), with recurrence time of a few (2-3) years only at certain locations. Compared with the Nocquet et al. (2014) solution, (eventually used in Chlieh et al. (2014), Villegas-Lanza et al. (2016b) and Mora-Páez et al. (2019)), our updated solution is more robust to potential biases induced by undetected SSE because: (1) several survey sites from Nocquet et al. (2014) have been progressively equipped with cGPS from 2011 onwards, allowing better detection of SSEs, (2) the survey sites used in our study have additional epochs of measurements. Only sGPS with at least 4 epochs of measurements with linear behavior are kept, and (3) cGPS have longer time series against the ∼3 years available in 2013 for most sites. A possible influence of transient motion is further suggested by comparing our solution with respect to Nocquet et al. (2014) velocity field. The median bias (median of the differences) is less than 0.5 mm/yr for sites located in the Amazonia and the Andean Cordillera, but is 1.3 mm/yr westward for sites located in the coastal region of Ecuador. The westward bias exceeds 3 mm/yr in southern coastal Ecuador. Search for potential transients during the 2009-2013 period is left for future studies, but we note that the area where significant bias is found corresponds to the one impacted by the 2015 deep SSE described in Rolandone et al. (2018). Using the data selection criteria described above, our new velocity field for Ecuador can be considered as reflecting the steady interseismic regime between SSEs.

4.4 MAIN PATTERNS OF THE VELOCITY FIELD

The obtained regional velocity field with respect to Stable South America (SOAM) (Figure 4.2) shows several large-scale patterns that we briefly describe. Across the Gulf of Guayaquil (latitude ∼3°S) and across the Puna-Pallatanga fault, a clear velocity direction change occurs from N70°E to N130°E, highlighting the boundary between the NAS and the Inca Sliver (Nocquet et al. 2014, Villegas-Lanza et al. 2016b). With respect to the Nazca/SOAM convergence direction (N83°E), the velocity field is rotated by 10° counter-clockwise rotation in the southern part of the NAS and

40° clockwise in Peru. While this rotation is coherent with the change of convergence obliquity induced by the change of the trench strike from the northern Andes to Peru, it is interesting to note that the direction change of onland GPS is shifted by ∼200 km north of the convergence obliquity change, which occurs at latitude 5°S. As noted in Nocquet et al. (2014) and Villegas-Lanza et al. (2016b), little if any elastic strain induced by locking at the megathrust occurs in that area.

Within the Peruvian Andes, velocities at latitude 6°S (LMAS, MOYB, YRMG, Figure 4.2) depart from the overall 4-5 mm/yr southeastward constant motion within the Inca sliver to 2-3 mm/yr eastward dominant motion. These velocities therefore witness internal deformation of the Inca sliver and induce ∼2 mm/yr of shortening accommodated through folding and thrusting in the Subandean domain (Villegas-Lanza et al. 2016b).

In central and northern Ecuador (latitudes 2°S - 1°N), velocities rapidly decrease from 20-25 mm/yr at the coastline down to 6-7 mm/yr at ∼180 km inland in the eastern Cordillera. This systematic decrease defines a velocity gradient that reflects significant locking taking place at the megathrust interface (Chlieh et al. 2014, Gombert et al. 2018, Jarrin et al. 2016, Nocquet et al. 2016, Nocquet et al. 2014). East of the Chingual-Cosanga faults, the direction of velocities within the subandean domain is similar to those observed in the subandean domain of northern Peru (figure 4.13 in the supplementary information), suggesting ∼2 mm/yr of shortening accommodated across the Easter Subandean Belt.

Along the Pacific coast of Colombia, the few available cGPS sites (TUCO, GUAP, BUGT, latitude 2-4°N) are located at almost the same distance from the trench, so that any change in their velocity magnitude can be used as a proxy of lateral change of interseismic coupling at the megathrust. GUAP and BUGT show velocity magnitude 35% and 45% lower than for TUCO, indicating that interseismic coupling decreases from south to north. To illustrate this point, insets A and B in Figure 4.2 show two profiles perpendicular to the trench and a best fit two-dimensional back-slip model prediction (Savage 1983) for a ∼20° constant dipping with homogeneous locking from the surface down to 40 km depth. Both profiles show low-velocity gradients (3 mm/yr), consistent with ∼50% partial interseismic coupling at the subduction interface. Such low velocity gradients contrast with the higher velocity of 18 mm/yr and ∼10 mm/yr gradient observed in southern Colombia and northern Ecuador at similar distances from the trench.

The overall velocity field within the NAS shows a progressive counter-clockwise rotation from latitude 0° in Ecuador to latitude 5.5°N in Colombia and then a clockwise rotation from latitude 5.5°N to latitude 12°N. This pattern demonstrates that neither the Euler pole from Nocquet et al. (2014) predicting a progressive counter-clockwise rotation to the north nor the Euler pole from Mora-Páez et al. (2019) predicting a progressive clockwise rotation to the north can correctly describe the kinematics of the NAS (see figure 4.5). Indeed, fitting such a pattern requires either at least two blocks and/or internal deformation within the sliver.

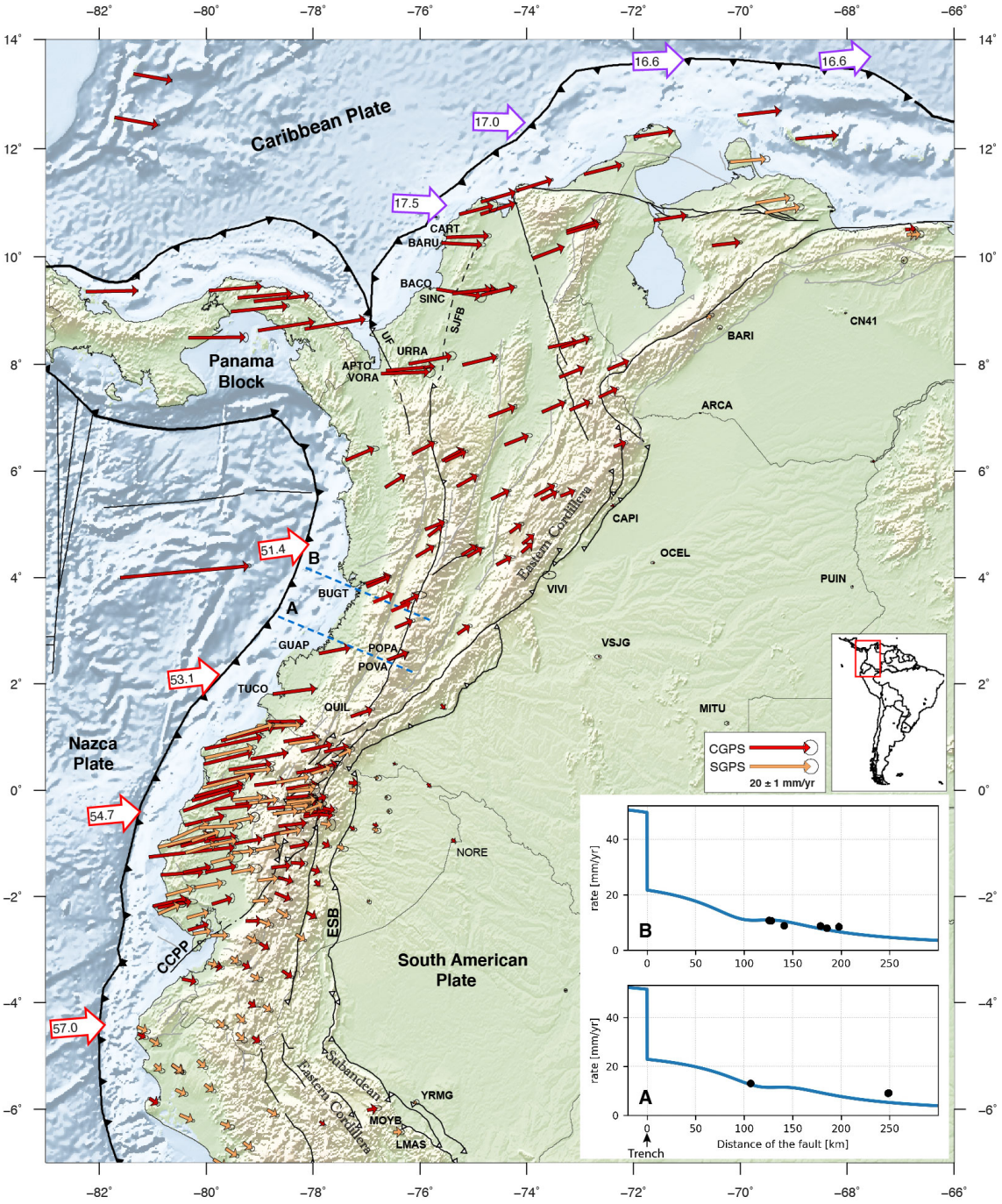

Figure 4.2 – Horizontal velocity field in the North Andean Sliver (NAS) relative to stable South America (SOAM). Red and orange arrows are continuous and campaign site velocities respectively. Ellipses are 95% confidence level. UF: Uramita Fault. SJFB: San Jacinto Fold Belt. CCPP: Chingual-Cosanga-Pallatanga-Puna fault system. ESB: Eastern Subandean Belt. Red and Violet arrows show the convergence margins are the estimated NAZCA/SOAM and Caribbean/SOAM relative motions from Jarrin et al. submitted and Symithe et al. (2015). Inset figures (A and B) are 2-dimensional forward elastic models perpendicular to the trench for the two profiles shown by dotted line in Colombia. The blue curves are the model predicted velocities whereas black points are observed velocities.

Where available, GPS sites located east of the Andean Cordillera indicate different levels of deformation. In Peru at latitude 6°S, site YRMG shows negligible residual velocity (∼1.5 mm/yr) in a SOAM fixed frame, indicating that all shortening is accommodated across the westernmost part of the subandean domain there. On the contrary, velocities at latitude 0.5°S show systematic eastward 1-2 mm/yr residuals velocities, as far as NORE located ∼250 km east of the Andean Cordillera foothills in Ecuador. In Colombia, sites VIVI, OCEL, VSJG surrounding latitude 4°N appear to be part of stable SOAM. Together with the very small residuals at CAPI (latitude ∼5.3°N), all of them indicate very little deformation east of the Eastern Cordillera. A similar observation is made east of the Boconó fault in Venezuela, where GPS sites (ARCA, BARI, and CN41) appear to be part of the stable SOAM (∼0.5 mm/yr). Thus, the existence of an actively deforming sub-andean domain appears restricted to Peru and Ecuador.

8 cGPS velocities in Panama show a 22-24 mm/yr eastward motion for the Panama block with respect to SOAM. The magnitude and direction of VORA and APTO velocities (located in the Atrato region, in Colombia, Figure 4.2) suggest that those sites also belong to the Panama block. Close to the Uramita fault and San Jacinto fold belt, 5 GPS sites (SINC, CORO, BACO, BARU, and CART) are moving at 17-18 mm/yr with the same orientation as the observed velocities within Panama, while velocities northward of latitude 10.5°N experience a slight counterclockwise rotation with respect to the direction of the Caribbean/SOAM motion. Therefore, the velocity field in northernmost Colombia and western Venezuela appears to undergo the effects of the Panama block collision and the Caribbean plate subduction in addition to the NAS translation (Mora-Páez et al. 2019, Trenkamp et al. 2002).

4.5 MODEL SETUP

4.5.1 Modelling Approach

We model the velocity field expressed in the South America fixed reference frame by assuming that the horizontal velocity at any GPS site is the result of a rotation of a rigid block hosting the site and an elastic contribution induced by locking at faults. Such approach called "elastic block modelling" has been implemented by Mccaffrey (2002) and Meade and Hager (2005), Meade and Loveless (2009). We developed our own implementation of this problem. Our appraoch follows the linear implementation described in Meade and Loveless (2009) with two minor differences: (1) the matrix relating the unit slip at faults to the surface displacement is made using the artefact-free formulation of Kikkhoo et al. (2015) instead of the Meade (2007) for triangular dislocation elements (2) Meade and Loveless (2009) use Laplacian-like regularization constraints for solving for spatially variable slip-deficit at subduction interface. We use instead a regularization constraint through a decreasing exponential model variance-covariance matrix that simultaneously imposes some level of smoothness and minimizes the departure from a prior model m_0, as in Radiguet et al. (2011) and Nocquet et al. (2014). This approach offers two advantages: (1) it allows an exact calculation in the case of variable mesh size (2) it enables to explore a range of model allowed by the data by varying

the prior model from null coupling (fully creeping) to fully coupled interface. This approach is useful to test whether deep coupling induces a trade-off with the estimated rotation of blocks and to provide the interval of the moment deficit accumulating at the megathrust.

4.5.2 Subduction Interface Geometry

The slab2.0 Nazca/SOAM subduction interface (Hayes 2018) is discretized into 21771 triangular dislocations elements of 8km long edges down to 80km depth. For the La Plata area in central Ecuador (latitude 0.2S° - 3.5°S), we modified the slab2.0 contours by including contours derived from marine seismic profiles and hypocentral solutions of micro-seismicity (Collot et al. 2017, Font et al. 2019, Segovia et al. 2018). Our triangular grid therefore extends south as far as latitude ∼13°S in order to re-evaluate the motion of the Inca sliver in northern and central Peru. For the Caribbean/SOAM subduction interface westward of longitude 73°W, the geometry is derived from hypocentral solutions from global and local earthquake catalogs between 1970 and 2019 (Engdahl et al. 2020, SGC 2020b). Revisiting the shallow seismicity distribution along AA' and BB' cross-sections shown in figure 4.3, we define a subduction interface with an average dip of 11° down to ∼40 km depth. We discretize this subduction interface into Rectangular Dislocation Elements of ∼25x20 km edge lengths with a constant dip of 11°. Eastward of longitude 73°W, the Caribbean/SOAM subduction interface is discretized using 100x60 km rectangular dislocations dipping at 13° down to 30 km (Pérez et al. 2018, Schmitz et al. 2008). We use dipping fault planes at 20° and 15° for the western and eastern portions of the North Panama Deformed Belt (NPDB) (Kobayashi et al. 2014). The South Panama Deformed Belt (SPDB) is constrained as single vertical faults locked down to 13 km based on the average of hypocentres depth provided by the ISC reviewed earthquake catalog (Engdahl et al. 2020).

4.5.3 Crustal Fault Geometry

Crustal block boundaries are rectangular fault planes with constant dip, assumed to be locked from the surface down to a prescribed depth. Fault parameters are assigned from published information derived from geological or focal mechanisms where available. In the case of no published information, we use vertical faults locked to 15 km depth. When GPS data is sparse, we adopt use regularization parameters constraining the coupling to be similar among adjacent fault segments (Elliott et al. 2010). Iterative inversions were run to adjust fault parameters that provide the lowest velocity residuals (observed minus modeled). All crustal fault parameters are available in the Supplementary Information.

4.5.4 Neighbouring plate and block motion

In all inversions, we fix the relative motion of the Caribbean/SOAM to their values published by Symithe et al. (2015) and to the values of Jarrin et al. submitted for the NAZCA/SOAM relative motion. Both Euler poles were carefully determined from both plate scale studies and our data set is not expected to provide any additional contribution. For the PANAMA/SOAM and INCA/SOAM relative motions, we use the values from Kobayashi et al. (2014) and Villegas-Lanza et al. (2016b)

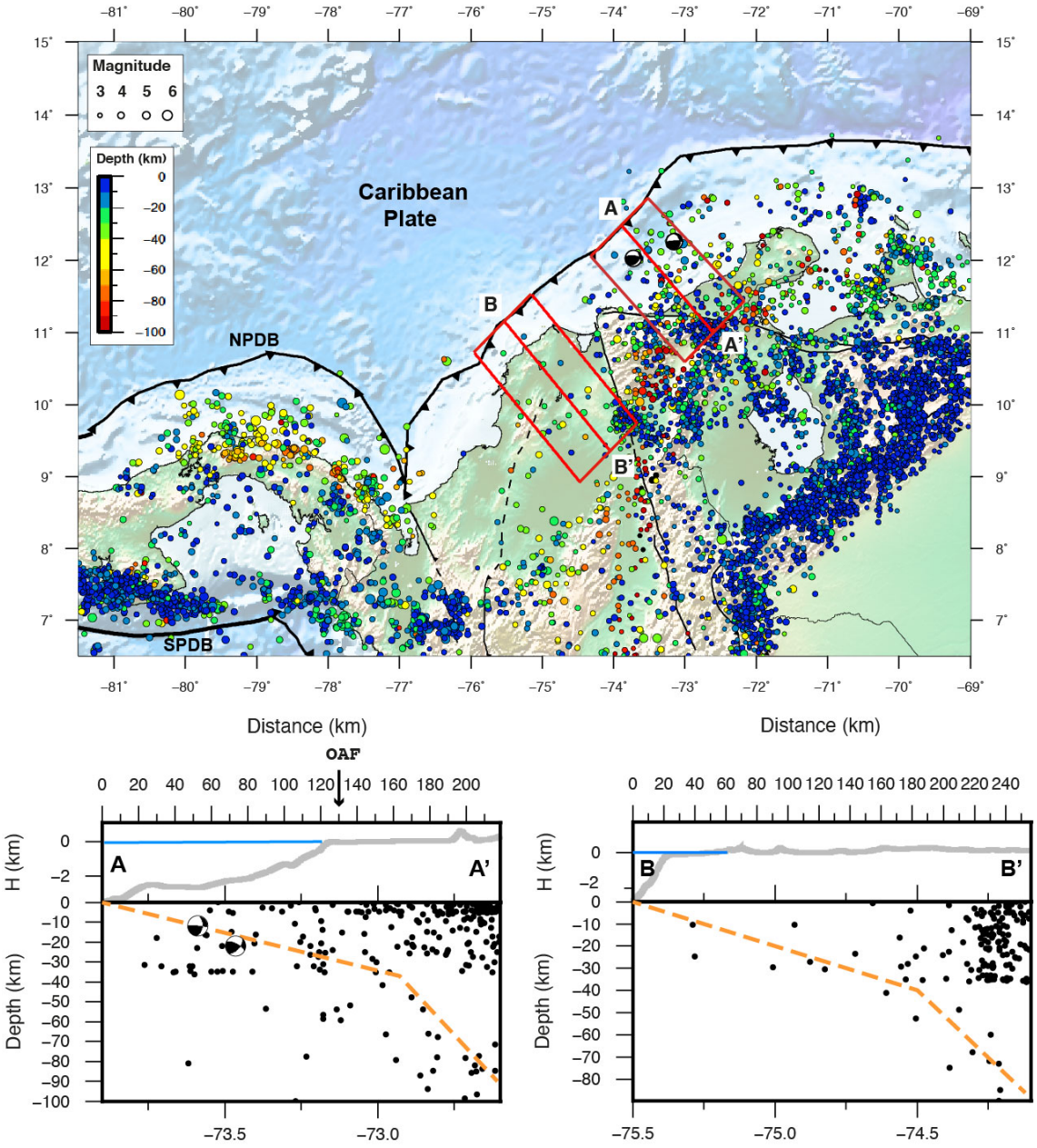

Figure 4.3 – Earthquake focal mechanisms and seismicity distribution on the northwestern edge of South America from 1970 to 2019, at depth < 100 km and Mw < 6.0 (Engdahl et al. 2020, SGC 2020a;b). Red rectangles show the location and width of the cross-sections AA' and BB'.NPDF and SPDF: North and South Panama Deformed Belts. Bottom: Earthquake hypocenter along cross-sections AA' and BB'. Grey and Blue curves indicate sea surface and topography along cross-sections, and dashed oranges lines are our proposed dip angle for the Caribbean plate subduction interface. OAF:Oca-Ancon fault.

as prior. However, their values are re-estimated in the inversion. We make this choice because our data set includes sites at those two block boundaries that might require adjustment to the previously published values.

4.5.5 Block model geometry and model selection

Defining the geometry of a block model remains, at least partly, a subjective choice. We choose to move from the simplest model consisting of a single NAS block and progressively increase the complexity by introducing step-by-step faults delimiting new blocks. For that, we use the available information about mapped fault traces from active tectonic studies, seismicity distribution and focal mechanisms indicating the sense of relative motion between blocks, and velocity gradients observed in the GPS data. In order to assess whether additional complexity is required by the data, we use the classical F_{ratio} test (equation 4.3). A F_{ratio} test quantifies whether the decrease of chi-square (χ^2), defined as the weighted quadratic sum of model residuals obtained when adding one or several blocks, is statistically significant (e.g. Stein and Gordon (1984), Nocquet et al. (2001)). Available Holocene slip rates for faults and slip vectors from focal mechanisms were not included in our inversions. They are used for a posterior validation of our best model described in section 4.6. Figure 4.4 shows our selection of the most relevant geometries.

4.5.6 Results for increasing complex models

Model A (Figure 4.4A) considers the North Andean Sliver (NAS) as a single block outlined by large-scale tectonic plate boundaries with the Nazca, South America, and Caribbean plates, and the Panama block (Alvarado et al. 2016, Audemard et al. 2000, Bird 2003, Machare et al. 2003, Taboada et al. 2000). North of latitude ~7.0°N, the Panama block collides with the NAS producing a relatively broad deformation zone (Kellogg and Vega 1995, Mora-Páez et al. 2019, Pennington 1981, Trenkamp et al. 2002). As a first attempt, we define the Panama/NAS boundary following the trend of shallow seismicity clusters (see Figure 4.3) as far as the southernmost extension of the Uramita fault southward of VORA and APTO GPS sites (see Figure 4.2). Both sites show velocities similar to the overall Panama block motion. At the southern tip of the NAS, we follow the Peruvian Forearc (PF) boundary proposed by Villegas-Lanza et al. (2016b) along the Marañon river in Peru, but choose to prolongate it in the subandean domain along the Macas reverse fault system (MFS), merging to the Cosanga fault, instead of cutting the Andean Cordillera in southern Ecuador (Figure 4.1). This choice is grounded in the well-documented compressive Macas fault (Legrand et al. 2005) and the absence of known large active faults or crustal seismicity in the western Cordillera in southern Ecuador.

As expected from the description of the general pattern of the velocity field, Model A cannot satisfactorily fit the data. Despite a relatively low average residuals (wrms=1.92 mm/yr), larger velocity residuals are observed in several areas of the sliver, especially in northwestern Colombia and Venezuela, reaching up to ~7 mm/y (velocity residuals available in figure 4.16 of

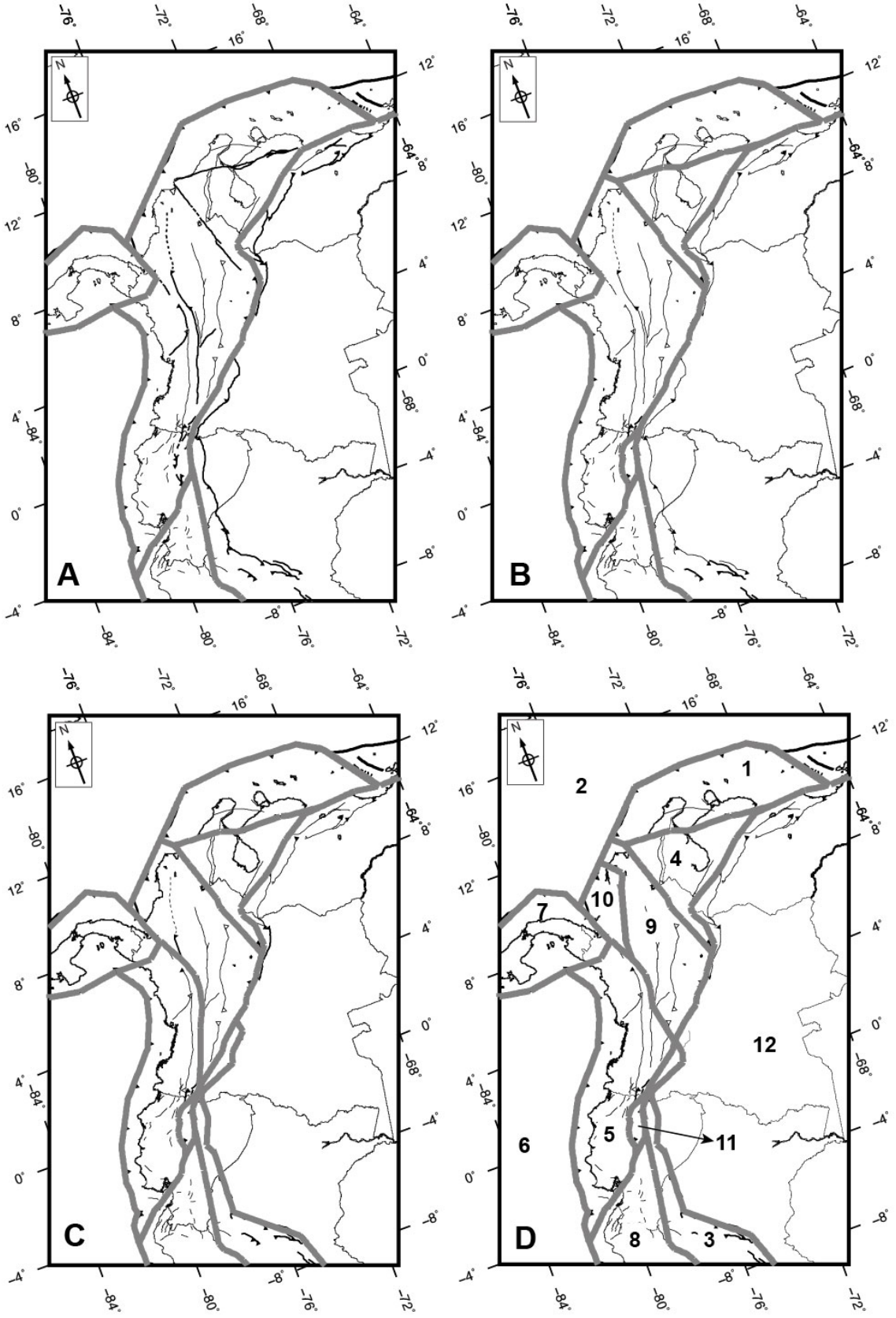

Figure 4.4 – Block and fault geometry for model A-D. Thick gray lines are block boundaries. Thin black lines are major active faults. Block names shown by numbers: (1) BONA (Bonaire), (2) CARI (Caribbean), (3) EPSUB (Subandean), (4) MARA (Maracaibo), (5) NAW (North Andean West), (6) NAZCA (Nazca), (7) PANA (Panama), (8) PFW (Peruvian Forearc West), (9) ROME (Romeral), (10) SANJ (San Jacinto), (11) UIOL (Quito-Latacunga), (12) SOAM (South America).

the supplementary information). In northern Colombia, clusters of shallow seismicity are observed along the Oca-Ancon and Santa Martha-Bucaramaga fault systems (Figure 4.3), and geological studies concluded that these two fault systems delimit an independent Maracaibo block (Audemard 2014; 2009). Adding the Oca-Ancon fault allows us to delimit an independent Bonaire block between the Maracaibo block and the Caribbean Plate (Figure 4.1). A second area of obvious misfit is the Interandean Depression in Ecuador, where ∼3 mm/yr of very localized east-west shortening (Mariniere et al. 2019) suggests the existence of an additional block outlined by the Latacunga, Quito, and El Angel faults (Alvarado et al. 2016) (Figure 4.1).

Our model B therefore includes these 3 additional blocks to model A. Model B (Figure 4.4B) shows significant fit improvement (χ^2=2965.2 and variance reduction of 99.17%). The F_{ratio} test with respect to model A is positive at the 99% confidence level (table 4.1). However, remaining 3 to 7 mm/yr velocity misfits are observed at the south of Santa Martha Bucaramanga fault (SMB) on several sites surrounding the Panama/Colombia boundary and the Eastern Frontal fault system (velocity residuals available in figure 4.16 of the supplementary information). Similarly, 2-3 mm/yr of residuals persists within the Subandean region of Ecuador and northern Peru. In addition, model B predicts ∼6 mm/yr of opening along the Puna and the southernmost extension of Pallatanga fault segments, at odd with the dominant strike-slip faulting inferred by geological studies (Alvarado et al. 2016, Baize et al. 2020; 2015).

In an attempt to solve these problems, we note that GPS velocities suggest ∼2 mm/yr of shortening accommodated throughout the Romeral fault system in central Colombia. Furthermore, active faulting along this ∼1000 km long structure is confirmed by the 1999 and 1994 shallow earthquakes (section 4.2) (Ekström et al. 2012, Taboada et al. 2000). To define a new block, we merge the Romeral fault to the north at the southernmost extension of the Uramita fault and southward with the Algercidas-Sibundoy fault. For the subandean region of Ecuador and northern Peru, the velocity field suggests 2-3 mm/yr of shortening accommodated by the Eastern Subandean Belt (Figure 4.2). Focal mechanisms also confirms active reverse faulting in that area (Figure 4.1). Therefore, we define the EPSUB block in order to model the Subandean zone following the Eastern Subandean Belt boundary from southernmost part of the Andean Cordillera in Colombia to northern Peru.

Including these new blocks into model C (Figure 4.4C), velocity residuals improve at ∼1 mm/yr within the Subandean and at several sites close to the Eastern Front Fault system (velocity residuals available in figure 4.16 of the supplementary information). Model C variance reduction is 99.45%, and the improvement of chi-square decrease is significant well above the 99% (χ^2 decrease = 1542.5). The unrealistic opening along the Puna-Pallatanga faults is now reduced to ∼2 mm/yr, making this fault system predominantly right-lateral strike-slip in agreement with tectonic studies. However, we find two remaining issues for model C: (1) large velocity residuals (4-5 mm/yr) are still observed at several GPS sites (BACO, BARU, CART, CORO, SINC, and URRA: fig. 4.2) close to the Panama/Colombia border (Figure 4.16 in the supplementary information),

requiring additional complexity in that area, (2) model C predicts 6-7 mm/yr of shortening along the southernmost extension of the Romeral fault between latitudes ∼1°N and ∼4°N, at odd with the geological study from Paris et al. (2000), which proposed a low slip rate of the order of 1 mm/yr.

In order to improve the fit to GPS data close to the Panama/Colombia boundary, we follow the proposition from several studies in which the San Jacinto fold belt (SJFB) is the northward prolongation of the Romeral fault merging with the westernmost extension of the Oca-Ancon fault surrounding the Santa-Martha city (latitude ∼11°N). However, the absence of surface fault traces and low seismicity makes it difficult to image its northernmost extension (Cediel et al. 2003, Kellogg et al. 2019, Mora et al. 2017, Taboada et al. 2000). By contrast, GPS sites (BQLA, VPOL, and CN37: Figure 4.16 in the supplementary information) at latitudes 10.6°N-11°N have velocities consistent with sites located in central Colombia east of the Romeral fault. We therefore propose a boundary merging the northernmost extension of SJFB with the Caribbean plate boundary at latitude ∼10.5°N, hence defining a new San Jacinto (SANJ) block (Figure 4.4:D). On the other hand, the low slip rate proposed by Paris et al. (2000) for the southern segments of Romeral fault suggests that it accommodates only a fraction of the deformation within the Andean Cordillera in southern Colombia. Furthermore, two sites POPA and POVA show velocity consistent with the kinematics of the westernmost block in Ecuador and Colombia (Figure 4.2 and Figure 4.16 in the supplementary information). Both observations suggest that some deformation should also take place east of the southern Romeral fault, but the scarce GPS data in that part of Colombia prevents us to determine an even first-order location for that boundary. In our model D, this is technically achieved by attributing sites west and east of the Romeral fault to two different blocks without accounting for elastic strain for that part of the boundary separating them. Finally, the geometry for our final model is shown in Figure 4.4D.

Table 4.1 – Statistics for each model geometry and F_{ratio} test among selected models M1 and M2 with a M1 model with less blocks than M2 model. NB: Number of blocks per model according to M2 column. DOF: Degree of freedom. R: Variance reduction estimated in percentage (equation 4.2). 1-P is the probability of data for supporting additional blocks. WRMS: weighted-root-mean-square estimated for all sites within the NAS in mm/yr. σ_0: Reduced χ^2

M1	M2	χ^2-A	χ^2-B	NB	DOF-A	DOF-B	WRMS	σ_0	R	F_{ratio}	1-P (%)
	A		4124.0	6		616	1.92	6.69	99.03		
A	B	4124.0	2965.2	9	616	607	1.61	4.88	99.17	26.4	99.99
B	C	2965.2	1542.5	11	607	601	1.41	2.57	99.45	92.4	99.99
C	D	1542.5	1199.2	12	601	598	0.95	2.01	99.60	57.1	99.99

4.6 BEST FIT MODEL DESCRIPTION, UNCERTAINTY & VALIDATION

4.6.1 Best Fit model geometry summary

Our best fit model includes 9 blocks outside the SOAM, NAZCA and Caribbean plates that define kinematic boundary conditions at the edges of the model. The Panama block and Inca sliver are treated as intermediate boundary conditions, taking previously published Euler poles from Kobayashi et al. (2014) and Villegas-Lanza et al. (2016b), but allowing changes in their geometry and small adjustment to their published values. For the Panama block, our pole is now at (lon: -83.07°E, lat: 50.11°N, 0.300 °/Myr), almost identical to Kobayashi et al. (2014) (lon: -88.358°E, lat: 43.447°N, 0.364 °/Myr) but predicting 1.5 mm/yr slower velocity. Another difference with Kobayashi et al. (2014) is that we do not find the need for an additional Choco block south of the Panama/Colombia border. Instead we find that an intermediate San Jacinto (SANJ) block is required to explain GPS velocities north of the Uramita fault (Figure 4.4). Our new estimate for the Inca sliver is close to Villegas-Lanza et al. (2016b), but sites located in the southern Ecuador Cordillera indicates a different boundary delimiting the Peruvian forearc sliver.

The kinematics within the NAS can be modeled by the rotation of 6 blocks, accommodating their relative motion across major faults or active structures identified by previous active tectonics studies. Two block boundaries appear to be required by the geodetic data, despite a lack of seismological or geological observational evidence for their activity: a ∼150 km segment at the northern tip of the San Jacinto Fold Belt in northern Colombia and a ∼200km segment south of latitude 4°N in southern Colombia. Both are indicated by dotted lines in Figures 4.6 to 4.12.

An additional complexity to previous models is also observed south of latitude 2°N, where compressional deformation occurs within the Subandean domain, possibly penetrating the SOAM plate over a few hundred kilometers in Ecuador and northern Peru.

4.6.2 Euler poles and comparison with previous results

Table 4.2 summarizes the Euler poles with respect to South America and the associated uncertainties for our preferred model. Figure 4.5 and Figure 4.15 in the supplementary information show predicted velocities for selected sites from Euler poles reported in table 4.2. The smallest blocks (UIOL and SANJ) within the NAS have the largest uncertainties, which is directly related to their size and the reduced coverage of GPS sites within them.

Predicted velocities within the North Andean Sliver (NAS) indicate that the BONA block is the fastest. Its Euler pole predicts constant velocity at 17.5 mm/yr toward N83.5°±1.5E, similar to 17.5 mm/yr towards N87.5°±2.5 predicted by the Caribbean/SOAM relative motion along the northernmost boundary of the NAS surrounding the Southern Caribbean Belt. By contrast, the Pole

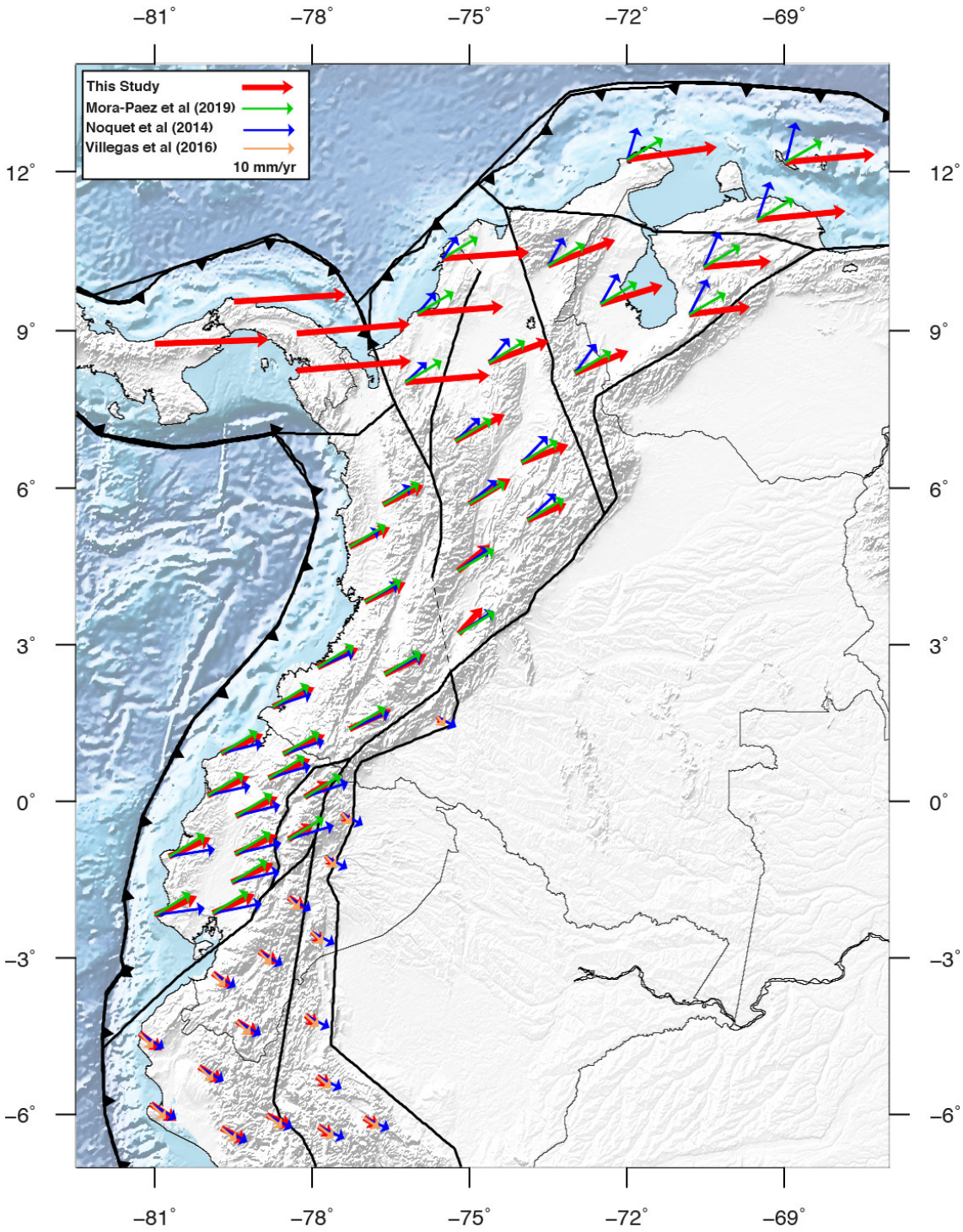

Figure 4.5 – Predicted block velocities for selected coordinates within the North Andean Sliver and Inca sliver with respect to South American plate reported by this study, Mora-Páez et al. (2019), Nocquet et al. (2014), and Villegas-Lanza et al. (2016b)

.

Table 4.2 – Euler Poles estimates from model D with respect to the South American plate. Smajor and Sminor are the semi-major and semi-minor axes of error ellipse at the 95% confidence level. Az: Azimuth in decimal degrees. NS: Number of GPS sites used in the Pole estimates. N: Number of block shown in figure 4.4D

N	Block/Plate	Name	Lon	Lat	Rate	Associated Error Ellipse			NS	WRMS
			°E	°N	°/My	Smajor	Sminor	Az		mm/yr
1	Bonaire	BONA	116.12	39.49	0.200±0.006	2.29	0.06	-30.3	6	0.71
2	Caribbean	CARI[a]	-73.87	50.58	0.247					
3	Subandean	EPSUB	-69.49	5.94	0.124±0.006	0.64	0.15	-143.0	18	1.69
4	Maracaibo	MARA	110.34	-0.01	0.662+0.009	0.12	0.01	-76.0	11	0.50
5	North Andean West	NAW	-136.08	61.50	0.082±0.002	4.92	0.23	-102.8	88	0.83
6	Nazca	NAZCA[b]	-90.93	56.19	0.588±0.006	0.96	0.22	-53.3	5	0.57
7	Panama	PANA	-83.07	50.11	0.300±0.004	0.61	0.04	22.6	10	1.09
8	Peruvian Forearc West	PFW	-73.57	5.53	0.219+0.005	0.28	0.09	-96.0	66	0.64
9	Romeral	ROME	108.45	0.09	0.713±0.005	0.05	0.01	-92.9	27	1.30
10	San Jacinto	SANJ	109.11	44.22	0.186+0.057	22.44	0.10	-21.7	6	1.21
11	Quito-Latacunga	UIOL	-91.16	18.86	0.127±0.081	15.15	0.35	139.0	18	1.22

[a] Value estimated from Symithe et al. (2015)

[b] Value estimated from Jarrin et al. (submitted)

of the UIOL block predicts the lowest velocities throughout the NAS at 5.5 mm/yr toward N57±1°E.

The MARA block undergoes fast clockwise rotations. Velocity azimuths increase from west to east by 15° (N70°-85°E) and velocity magnitudes increase from 10.6 mm/yr at latitude 8°N to 13 mm/yr at latitude ∼10°N (figure 4.5 and figure 4.15 in the supplementary information). Within the SANJ block, predicted velocity are 16.7±0.2 mm/yr towards azimuths (N85.5°±0.5E), almost the same direction as the Panama block (22 mm/yr toward N86°E), hence suggesting a predominant control of the Panama collision in that part of the NAS. Along the NAW block, our model prediction is 8.8±0.1 mm/yr toward N65°±1E, consistent with the average predicted rigid motion from simple models reported by Mora-Páez et al. (2019) (8.0 mm/yr toward N59°E) and Nocquet et al. (2014) (8.5±1 mm/yr toward N70°±10E). Despite this agreement, we find discrepancies in the predicted rigid motion from Nocquet et al. (2014) in central-southern Ecuador (latitudes 3°S - 0.5°N) at 1.5-2.0 mm/yr in the east and north velocity components, and ∼1 and 0.4 mm/yr in the east and north velocity components with respect to the prediction from Mora-Páez et al. (2019). We also observe velocity discrepancies at ∼1 mm/yr from both predictions in southern Colombia. Two elements might explain these discrepancies (1) the elastic contribution on site velocities induced from the locking on the subduction interface and the locking of the crustal faults, (2) velocity estimates impacted by SSEs discussed in section 4.3.

Our model estimates at ∼0.5 mm/yr the elastic contribution induced by the CCPP fault (Puna-Pallatanga faults) for velocities used in the Nocquet et al. (2014) model in southern Ecuador (latitudes 1.8°S-2.5°S). By contrast, locking along the subduction interface induces ∼2 mm/yr on the east component of these site velocities, suggesting that it is the primary source of the discrepancy found with previous models.

Regarding the Inca sliver, our predicted velocities for the western part of the Inca sliver (PFW block) in southern Ecuador and northern Peru are quite similar both in magnitude (5.0±0.4

mm/yr) and azimuths (N125°±0.5E) as those proposed by Villegas-Lanza et al. (2016b) (4.7±0.3 mm/yr toward N125°±0.5E). The PFW pole predicts velocities (for the east component) ∼0.5 mm/yr faster than Villegas-Lanza et al. (2016b) pole (lon: -73.66°E, lat: 4.26°N, 0.215). Such slight/negligible difference for the east component of velocity prediction might arise from the spatial length sampled by the Euler Poles for the Inca sliver. We estimated the kinematic of the Inca sliver as far as 13°S while Villegas-Lanza et al. (2016b) encompass an Inca Sliver south up to ∼19°S. Detailed analysis between both poles for the region of PFW block is left for future studies.

4.6.3 Model fit and uncertainties

Our preferred model (fig. 4.4D) shows statistics significantly better (table 4.1) than simpler models including a smaller number of blocks (model A-C in fig. 4.4). A single non-deforming North Andean Sliver (NAS) block (model A in fig. 4.4) is unable to correctly explain the direction change observed from south to north within the NAS and results in velocity systematic residuals up to 7 mm/yr at several locations. For our preferred model, the data variance reduction is 99.6%, the wrms is 0.95 mm/yr and the reduced χ^2 = 2.01 showing a good agreement between the average model residuals and data uncertainties. The spatial distribution of velocity residuals does not indicate any systematic pattern or area suffering obvious mismodelling (figure 4.6), and the histogram of velocity residuals follows a normal distribution in which most of them are lower than 1.0 mm/yr (see figure 4.6:B). Compared to simpler models, the F_{ratio} test shows significance above the 99% confidence level, suggesting an appropriate division of blocks (table 4.1).

Although our model provides an average fit of ∼1 mm/yr to the observed GNSS velocities, residuals exceeding 2 mm/yr are found for several GPS sites (BASO, BACO, DAR2, VORA, CASI, figure 4.6 and figure 4.16 in the supplementary information). All these sites (except BASO) are located within a broad deformation zone caused by the collision between the Panama block and the NAS. There, deformation might be more diffuse, involving additional secondary faults not accounted for in our model (Duque-Caro 1990, Paris et al. 2000, Taboada et al. 2000).

Assessing the uncertainty and validating a kinematic model is difficult, because the choice of the boundaries is somehow subjective. There is however a minimum of information that can be provided, and we detailed it below. Since our approach uses a linear formulation for the forward model, the posterior variance-covariance matrix provides formal estimates of the uncertainties. The full variance-covariance matrix is provided as Supplementary Data (table 4.6). Various elements of the variance-covariance matrix are useful to look at. First, the full sub-variance-covariance matrix includes information about the precision of each pole. Using the propagation law of covariance, an ellipse error can be provided for the predicted motion at the centroid of each block. Figure 4.7 shows that each block has a kinematics formally determined at the ∼0.3 mm/yr to 95% confidence level.

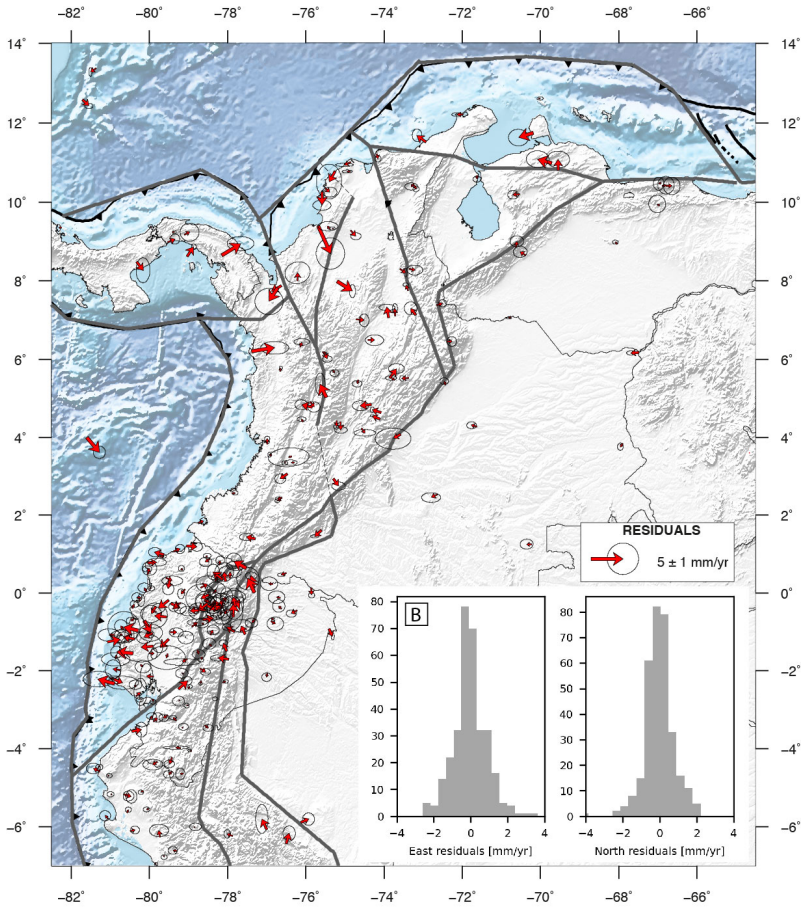

Figure 4.6 – Velocity residuals (observed - modeled) from model 4. Thick gray lines are block boundaries. B) Histograms for East and North velocity residuals.

Locking along the subduction interface induces a gradient to the velocity field. Possible high coupling at depth might also generate a low-velocity gradient, similar to a translation that could bias the estimates of block rotations. To assess this potential impacts, we predict the motion at several sites within the North Andean West (NAW) block (fig. 4.4D) using Euler pole estimates from a range of interseismic coupling (ISC) models allowed by the GPS data. This exploration of ISC models is performed by varying parameters that control the smoothness of the solution (Dc) and the weight given to smoothing and damping (σ_m) with respect to a priori model m_0. A detailed discussion of the ISC models and methods is provided in chapter 5.

Figure 4.8A display the L-curve showing χ^2 values with respect to σ_m constraint for the dip-slip component with a priori model m_0=0 (null coupling). The best ISC model if found for σ_m=20 mm/yr. However, ISC models with a σ_m between 5 and 35 mm/yr are also possible. Predicted velocity magnitudes (fig. 4.8B) show negligible discrepancies (for example: 0.1 mm/yr southward of latitude 2°N for the ISC model with σ_m=5) for ISC models with σ_m values of 5, 20, and 35 mm/yr. Slight variations in predicted azimuths that does not exceed 1° (fig. 4.8C) are observed for the ISC model with a σ_m=5 mm/yr southward of latitude 2°N, where the coupling distribution is high (∼80%). The same test of velocity predictions was performed for the UOIL and ROME blocks, and provided similar results. In conclusion, we find negligible biases in the block

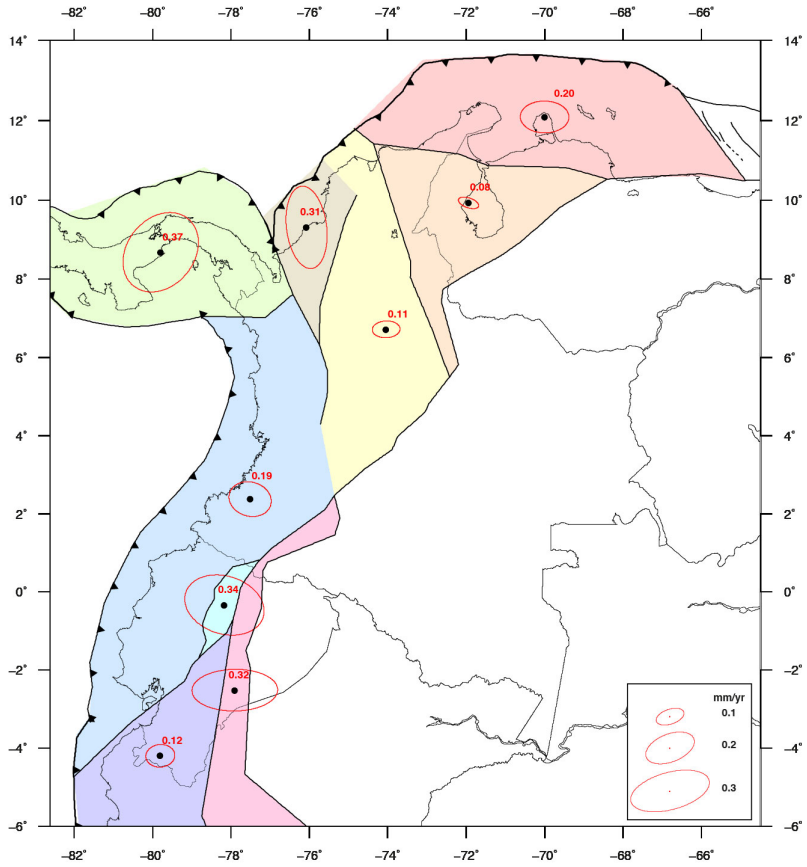

Figure 4.7 – Predicted uncertainty at the centroid of each block for the best model. Ellipses show 95% of confidence.

rotations coming from the trade-off between interseismic coupling and block rotations, attesting to Euler poles' stability for the different block forming the NAS.

Another validation consists in comparing some predictions from our model with independent data. Comparison for the direction of relative motion as inferred from focal mechanisms is presented in the next paragraph. A critical comparison of tectonic regime and geologically derived slip rates is discussed in detail in section 4.9.

4.6.4 Comparison to earthquake slip vectors

Where available, earthquake slip vectors provide information, independent from geodesy, about the relative motion of blocks surrounding a fault. Earthquake slip vectors can therefore be used to validate or point out problems in our model.

We use focal mechanism solutions from global (Ekström et al. 2012, Trabant et al. 2012) and local (SGC 2020a, Vaca et al. 2019) catalogs for the NAS and neighboring regions. As these catalogs have solutions of different quality, we exclude solutions with Mw < 5.0 and at depths greater than 30 km for crustal faults. We also exclude solutions with fault planes and slip vectors non-consistent with fault directions. Applying these criteria, we compiled 91 focal mechanism

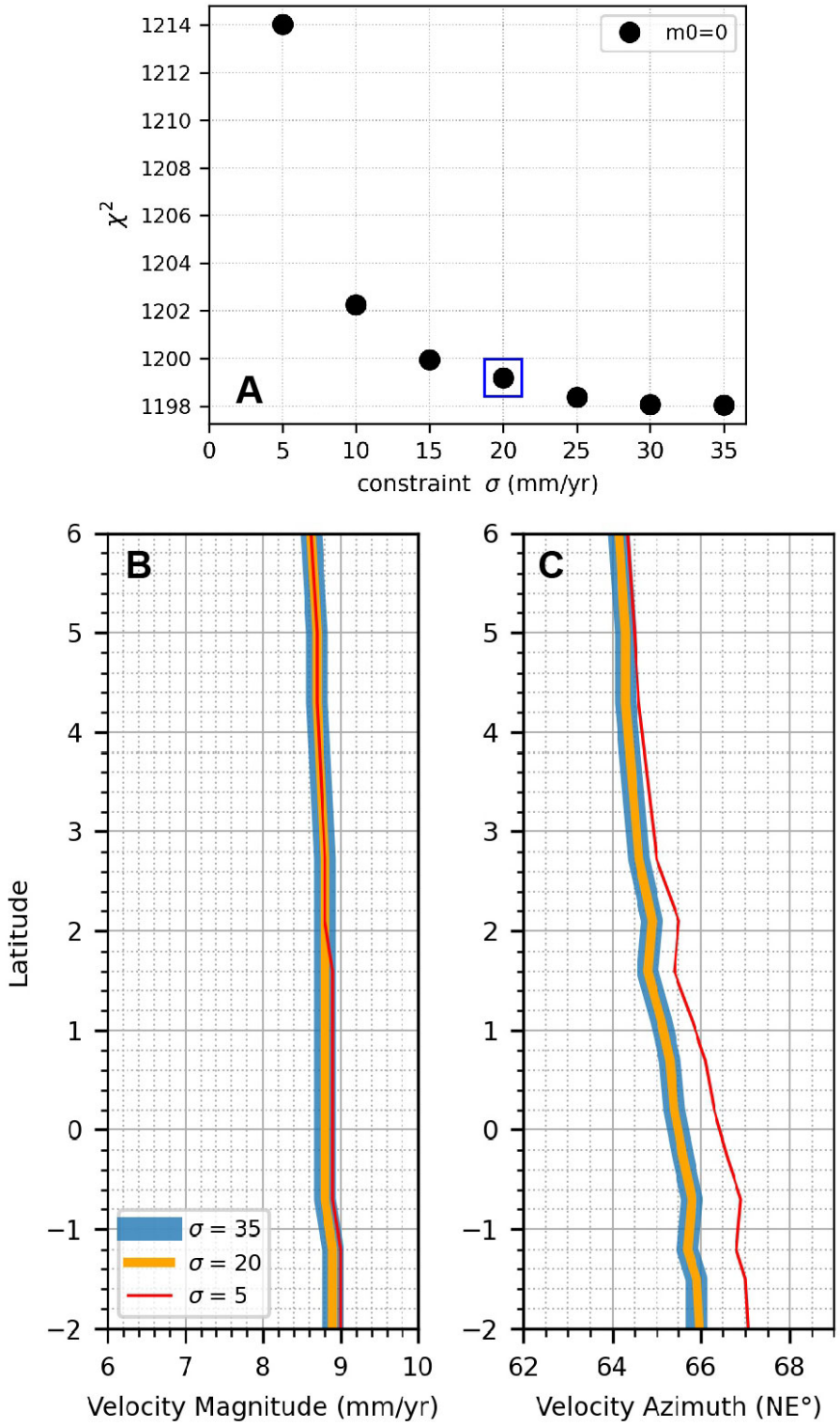

Figure 4.8 – Stability of Euler pole estimates as a function of the exploration of ISC models. A) χ_2 as a function of the imposed σ_m constraints for disp-slip component with a priori model m_0=0, *Dc*=30 km and regularization parameters for the slike-slip component fixed (refer to section 5.3 in chapter 5). Blue square is the best model for an ISC model with σ_m=20 mm/yr. B) Predicted velocity magnitude at several sites within the North Andean West (NAW) block using Euler pole estimates for ISC models with σ_m values of 5, 20 and 35 mm/yr. Predicted velocities range from 76.2°W at latitude 2.3°S to 76.6°W at latitude 6°N. C) Same as B but for predicted velocity azimuths.

solutions (listed in table 4.7 in the supplementary information). Surface projection of earthquake slip vectors is then compared to the direction of relative motion predicted by our model for pairs of blocks. Figure 4.9 shows relative block directions inferred from focal mechanism solution and from our best fit model (model D).

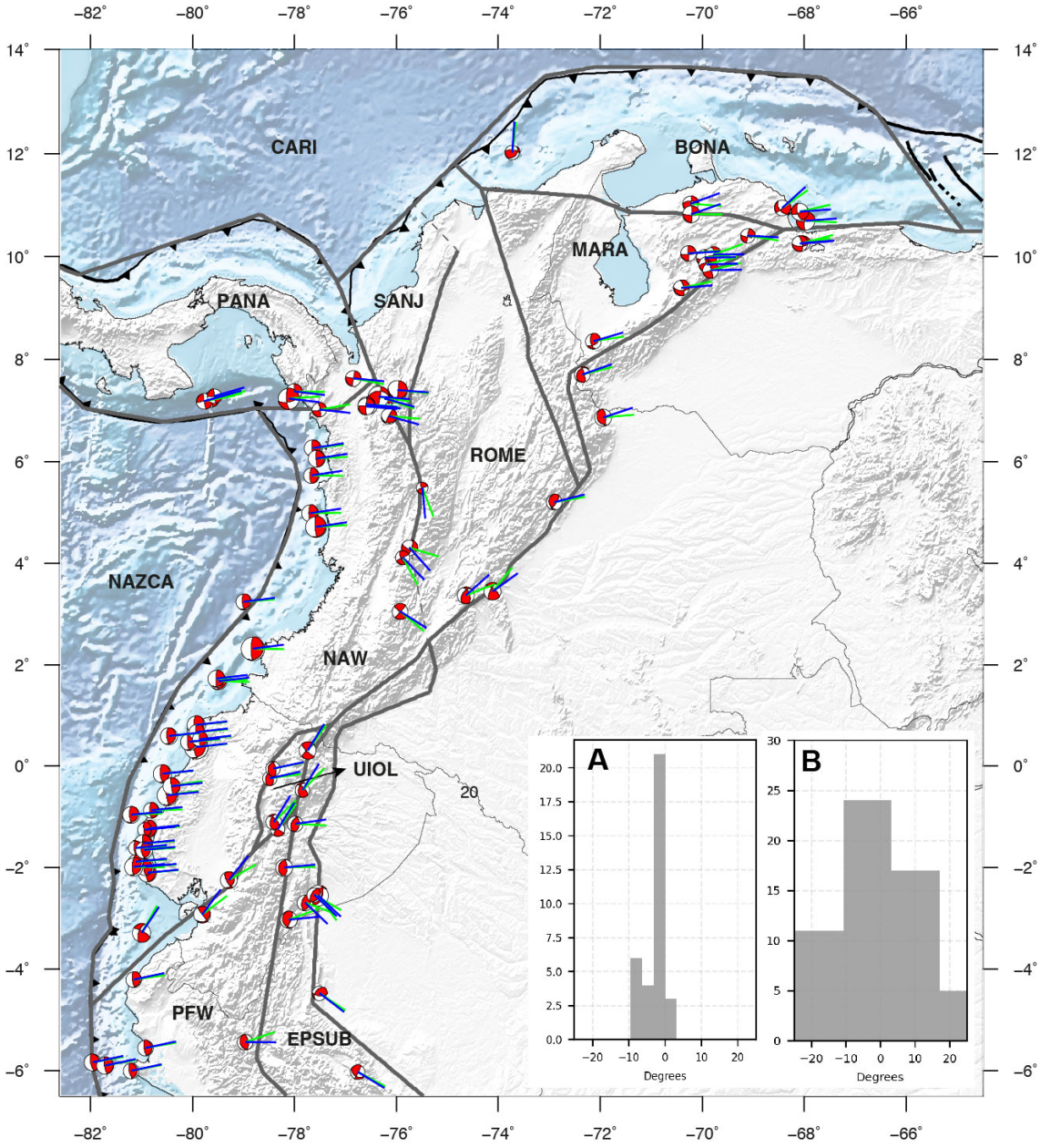

Figure 4.9 – Comparison between earthquake slip vector direction and relative motion at block boundaries from our best model. Green lines at focal mechanism solutions are the earthquake slip vector projection on the surface, while blue lines depict the relative direction between pair of blocks. Histograms quantify the difference between earthquake slip vector direction and the relative direction from our model for (**A**) the subduction zone (NAZCA/NAW and NAZCA/PFW) and (**B**) Crustal faults. Histograms plotted at bins = 4. See Table 4.2 for the blocks full names.

In general, we note a good consistency between earthquake slip vectors and the predicted relative motion predicted by our model. Statistical analysis of focal mechanism solutions

worldwide suggests that uncertainties ∼15° in the axial orientation of tensor solutions must be considered (Frohlich and Davis 1999). Comparison of relative motion direction show a negligible bias of -0.1° and a standard deviation of 12° for the crustal fault (inset B within figure 4.9). This indicates a very good agreement between the geodetic model prediction and focal mechanisms. At the Ecuador-Colombia and northern Peru subduction zones, earthquake slip vector directions agree within ∼2.5° (bias=-2.8° and standard deviation of 3.1) to the predicted NAZCA/NAW and NAZCA/PFW relative motions (inset A within figure 4.9), validating our model estimates for the trench parallel motion. Furthermore, given the complex block geometry surrounding the Panama/NAS boundary (PANA/SANJ/NAW/CARI blocks), only 2 of the 8 available earthquake slip vectors differ more than 6° with respect to our model prediction. This good agreement therefore supports our proposed geometry for that part of the NAS.

In the northern part of the sliver, we notice discrepancies of ∼20° between the BONA/MARA relative motion and the slip vector for the only two available Mw 5.7 and 5.4 earthquakes at the Oca-Ancon fault at longitude ∼70°W. For these focal mechanisms, the nodal planes appear to be slightly oblique to the average fault strike (N84°E: (Paris et al. 2000)), suggesting that these earthquakes occurred on secondary faults and do not describe correctly the motion in that region.

4.7 COMPARISON WITH ACTIVE TECTONICS RESULTS WITHIN THE NORTH ANDEAN SLIVER

In this section, we compare the prediction of our best kinematic block model with results from active tectonic studies, in terms of faulting and when available, to Quaternary or Holocene fault slip rates. Figure 4.10 summarizes the slip rate predicted from our prefered model together with geological slip rates available from the literature. Slip rates per component (strike-slip and dip-slip) are available in figure 4.15 in the supplementary information.

4.7.1 Eastern boundary of the NAS

Along the southernmost boundary of the NAS, our best fit model estimates right-lateral slip rate at 7.6 ± 0.1 mm/yr along the Puna fault and along the southern section of Pallatanga fault, resulting from the relative motion between the NAS and Peruvian Forearc West block (PFW). These estimates are in agreement within the range of 5.8-8 mm/yr proposed by Dumont et al. (2005) from river channel offsets at Puna island since the mid-Holocene (5-6 Kyr). In addition to the predominantly strike-slip motion, our model also predicts uniform fault-normal opening rates across the Puna and southern Pallatanga faults at 2.2 ± 0.2 mm/yr. From the thickness of sediment deposit in the Gulf of Guayaquil since 5.3 My, Lavenu et al. (1995) estimated an opening rate normal to the Puna fault of 2.4 ± 1.1 mm/yr consistent with our model prediction. Available seismic reflection profiles offshore the Gulf of Guayaquil have also identified normal faulting

delimiting subsiding basins Witt et al. (2006).

The northern segment of Pallatanga fault delimits the boundary between the Peruvian Forearc West and the Quito-Latacunga block, whose motion is slower than the western NAS. Slip rates along that section are therefore expected to be slower than for the southern Pallatanga and Puna faults. Our estimate is right-lateral slip rate at 4.8 ± 0.1 mm/yr. Baize et al. (2020) summarize slip rates estimates along a 90 km long segment of the Pallatanga fault from the Rumipamba section (lon. 78.9°E, lat. 1.8°S) to the Pisayambo section (lon. 78.3°E, lat. 1.1°S) from offsets and dating of morphological markers and lava flow. Their proposed slip rates range from 2 to 6 mm/yr compatible with our model prediction. However in the details, their new Holocene slip rate estimates for the Rumipamba section is 2 mm/yr slower than previous estimates of 2.9 - 4.6 mm/yr proposed by Winter et al. (1993) and Baize et al. (2015). At this location, our estimate is ∼7 mm/yr if we consider that this fault segment is part of the NAW/PFW boundary and 5 mm/yr if it is part of the UIOL/PFW (Quito-Latacunga/Peruvian Forearc west) boundary. Igualata volcano Holocene lava flow offsets (lon. -78.3, lat. -1.5) indicate slip rates of 4-6 mm/yr in agreement with our estimates. In addition, Baize et al. (2020) also propose slip rates of 3-4 mm/yr for the northernmost Pisayambo segment that would be 1-2 mm/yr slower than our model prediction. In summary, our model predictions agree with the upper range of Holocene estimates in that area.

The Cosanga and Chingual faults define the boundary between the Subandean domain and the Quito-Latacunga block from latitude 1°S to 1°N. Our model predicts right-lateral strike-slip rates at 5.5 ± 0.1 and 5.9 ± 0.1 along the Cosanga and Chingual fault systems respectively, with a minor reverse component of 2.0 ± 0.2 mm/yr for the Cosanga fault vanishing along the Chingual fault. Geological estimates for the Cosanga fault are not available. However, average slip rates (7 ± 3 mm/yr) estimated from volcanic deposits dated at 37 and 8.6 kyr from the Soche volcano at the southwestern section of the Chingual fault (Ego et al. 1995) are consistent with our model prediction.

Dominant right-lateral motion at 8.7 mm/yr along the Algercidas-Sibundoy fault agrees with late Pleistocene-Holocene rates (7.7 – 11.9 mm/yr) based on geomorphological studies (Tibaldi et al. 2007). Further north, our model finds a transition from dominant rigth-lateral strike-slip motion to transpression along the Guaycaramo fault. We estimate right-lateral strike-slip rates decreasing from 6.2 mm/yr at latitude ∼3°N to 5.8 mm/yr at latitude ∼6°N, while reverse slip rates increase from 2.1 mm/yr to 4.7 mm/y. These values are compatible with the upper bounds of average Quaternary rates (3 ± 2 mm/yr) from landforms and offsets of alluvial terraces (Paris et al. 2000). In Venezuela, our best model predicts 10 ± 0.5 mm/yr of right-lateral motion along the Boconó fault separating the Maracaibo block from stable SOAM. Our estimate agree with average Holocene slip rate of 9.5 ± 0.5 mm/yr estimated in the central section of the fault at Mesa del Caballo and the Pleistocene slip rate 5-11 mm/yr in the Yarucuy valley based on paleoseismological studies (Audemard et al. 2008, Audemard and Audemard 2002, Pousse-Beltran et al. 2017). In addition to strike-slip motion, our model predicts shortening across the Boconó fault ranging from 2.5 to 5 mm/yr at their southern and central sections, increasing up to ∼7.0

mm/yr at their northernmost section. Fast and dominant right-lateral strike-slip motion occurs along the San Sebastian (17 mm/yr) and El Pilar faults (18 mm/yr), supporting the interpretation that both systems accommodate almost all of the Caribbean/SOAM relative motion (18 mm/yr).

In summary, we find good agreements between present-day fault slip rates and Pleistocene-Holocene slip rates for almost all faults along the eastern boundary of the NAS. At the large scale, our model finds that the eastern boundary of the North Andean Sliver is a dominant right lateral transpressive fault system with increasing slip rate from south to north. The relative magnitude of the strike-slip and shortening component changes with the changes of the strike of the fault (figure 4.15:C in the supplementary information).

4.7.2 Deformation within the Interandean Depression in Ecuador

The existence of the Quito-Latacunga (UIOL) block outlined by the foothills of Western Cordilleras and the Cosanga-chingual faults in central Ecuador is required to explain decreasing geological slip rates observed from the Puna to Pallatanga faults. The western boundary for this block is defined by several westward dipping thrust faults at Latacunga, Quito, and the surface trace of the El Angel fault systems (Alvarado et al. 2016; 2014, Lavenu et al. 1995). Seismic activity recorded by instrumental networks since the 90s shows recurrent Mw ∼5 earthquakes (ex: 1990 Mw 5.3, 2014 Mw 5.1) along the Latacunga and Quito faults (Alvarado et al. 2014, Ekström et al. 2012, Vaca et al. 2019), but larger earthquakes are documented along whole fault length in the past centuries (1868 Mw ∼7.3 Ibarra, 1587 Mw ∼6.4 Guayallabamba, and 1757 Mw ∼6.2 Latacunga earthquakes (Beauval et al. 2010; 2013).

South of Quito, the relative motion between the NAW and UIOL blocks predicts shortening at 3.3 ± 0.1 mm/yr at the latitude of Latacunga city (∼0.9°S), which can be compared to several geological estimates. Lavenu et al. (1995) proposed a shortening rate of 1.4 ± 0.3 mm/yr constrained either by outcrops surrounding the Latacunga fault since the Late Plio-Quaternary or 2 ± 1 mm/yr for the shortening integrated across the Interandean Depression based on the difference of Quaternary slip rates among the Pallatanga and Chingual faults (Ego et al. 1995). Lavenu et al. (1995) further indicate that these values could be considered as a lower bound. More recently, Baize et al. (2020) used InSAR data in the interandean depression and proposed horizontal shortening rates of 2-2.4 mm/yr. These values are 1 mm/yr smaller that the prediction from our model.

Although there is no geological slip rate estimate available for the Quito fault, detailed GNSS studies complemented by InSAR results proposed a range of 3 to 5 mm/yr for East-West shortening rate (Alvarado et al. 2014, Mariniere et al. 2019). Mariniere et al. (2019) further found that very shallow locking is required to explain the sharp gradient across the Quito fault observed in both GNSS and InSAR data. Although our block model has a lower spatial resolution around Quito than Mariniere et al. (2019), it offers the advantage to integrate the GNSS measurements into a larger scale. Our model predicts 2.5 ± 0.2 mm/y of E-W shortening at across the southern section

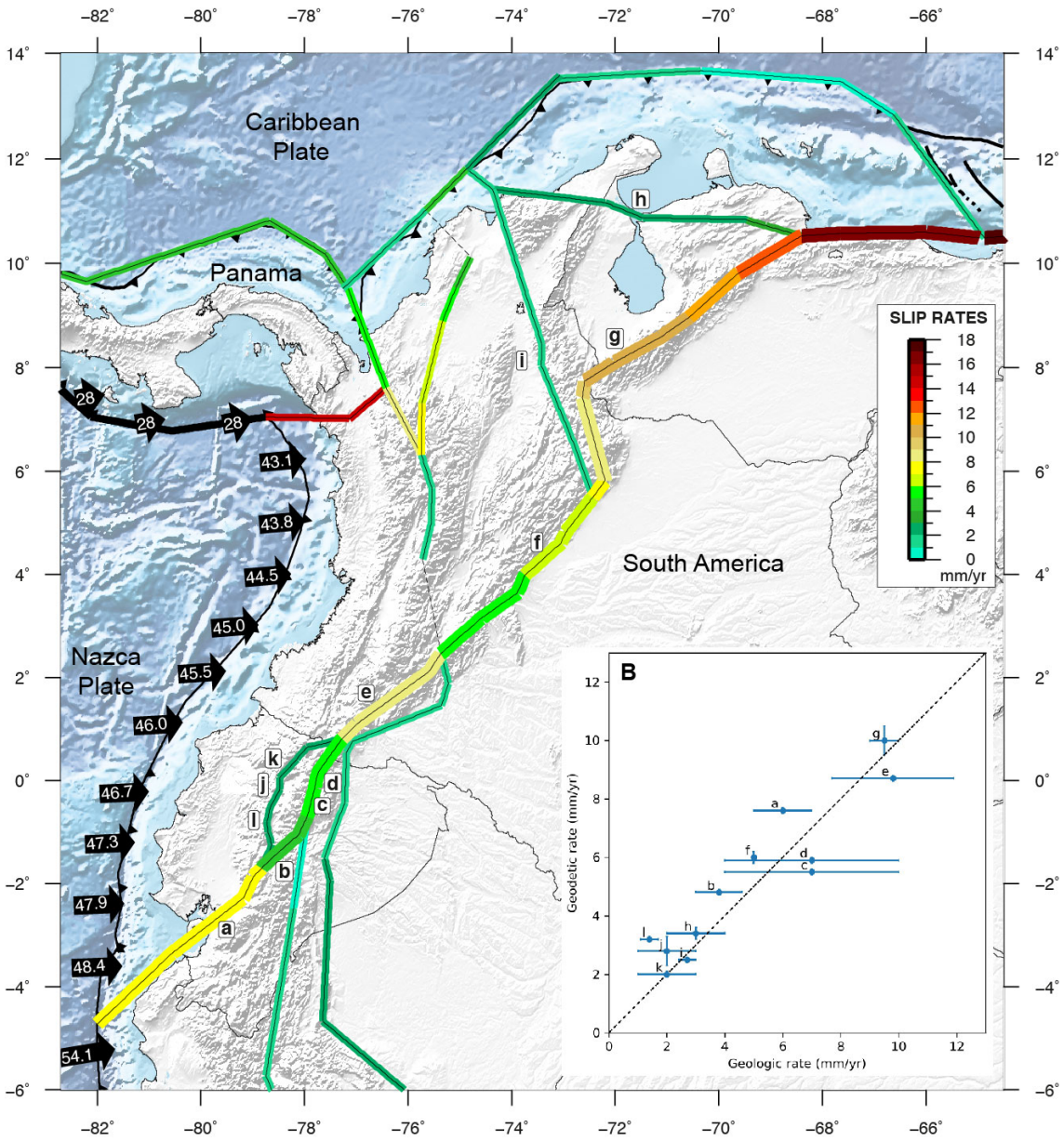

Figure 4.10 – Slip rates (norm) at block boundaries estimated for model D. Thick color line is the eastern boundary of the NAS. B) Comparison between geological (from literature) and geodetic slip rates (this study) according to the slip discussed in the text. Geological slip rates are plotted as average values from their range of rates. Fault systems: Puna (a), Pallatanga (b), Cosanga (c), Chingual (d), Algercidas-Sibundoy (e), Eastern Frontal Fault System (f), Boconó (g), Oca-Ancon (h), Santa Marta-Bucaramanga (i), Quito (j), El Angel (k), Latacunga (l).

of the Quito fault but with 2.2 ± 0.1 mm/yr of right-lateral strike-slip motion, changing to 3.3 ± 0.1 mm/y and 0.8 ± 0.1 mm/y respectively on its northern section. Our model finds an average coupling coefficient not higher than 50% for the Quito fault. Thus, our block model is in good agreement with the result from Mariniere et al. (2019), and provides a narrower range of relative motion across the fault (2.3-3.4 mm/yr).

Further north, 2.1 ± 0.2 mm/yr of shortening are found across the El Angel fault with 2.9 ± 0.1 mm/yr of right-lateral motion, but no geological data are available there for a comparison.

4.7.3 Southernmost extension of the Romeral fault system

The Romeral fault system is a complex and continuous structure, inherited from sequences of oceanic accretions since the Cretaceous (Cediel et al. 2003, Suter et al. 2008, Taboada et al. 2000). It consists in several parallel faults running along the western foothills of Central Cordillera. The southernmost extension of this fault system is thought to be connected to the northernmost extension of the El Angel fault in Ecuador (Paris et al. 2000, Suter et al. 2008, Taboada et al. 2000). By considering this geometry in model C (figure 4.4:C), we find unrealistic 6.5 ± 1.5 mm/yr reverse slip rates between latitudes 4°N and ∼0.7°N. Such a model neither agrees with slip rate predictions for the northern section of the Romeral fault (normal reverse slip at 1± 0.5 mm/yr latitudes 4°N - 6°N) nor its southernmost extension at the El Angel fault (∼2.0 mm/yr reverse slip). In addition, model C also predicts 4-6 mm/yr of shortening across the Algercidas-Sibundoy fault, which disagrees with a predominantly strike-slip motion inferred from geological mapping, landforms, and aerial images (Tibaldi et al. 2007, Velandia et al. 2005). Thus, we conclude that the lack of geodetic observations together with the block geometry of model C is not able to constrain the motion in southern Colombia adequately.

An alternative block geometry is provided by our best model (figure 4.4:D). Within this configuration, we find left-lateral motion at 1.6 ± 0.1 mm/yr with normal compressive slip at 1 ± 0.6 mm/yr across the Romeral fault between latitudes 4°N and 6°N (figure 4.10 and figure 4.15 in the supplementary information). Long-term slip rates remain largely unknown for the Romeral fault. Only Paris et al. (2000) suggest Quaternary rates of ∼1 mm/yr for the Paraiso and Piendamó sections (latitude ∼3°N -5°N) based on geomorphic analysis, but lacking from precise dating. Therefore, the southern Romeral fault possibly accommodates only a fraction of the North Andean West/Romeral (NAW/ROME) relative motion. The scarce geodetic data available in that part of Colombia prevents us to better define a boundary, which also may consist of several faults. Understanding the deformation in southern Colombia is left for future studies.

4.7.4 Subandean deformation

The Subandean domain is characterized by low-angle thrust ramps rising as fold and thrust belts of sedimentary rocks, east of the Eastern Cordillera in Ecuador and Peru (Alvarado et al. 2016, Baby et al. 2018, Bès de Berc et al. 2005, Calderón et al. 2013, Eude et al. 2015, Suárez et al.

1983, Villegas-Lanza et al. 2016b). In our model, the kinematics of this domain is described by the motion of an idealized over-simplified rigid Subandean (EPSUB) block. Across the Eastern Subandean Belt (ESB), E-W shortening occurs at 1.9 ± 0.2 mm/yr with 1.2 ± 0.2 mm/yr of left-lateral motion in northern Ecuador surrounding the Napo region (net slip = 2 ± 0.2 mm/yr) (see figure 4.10 and figure 4.15 in the supplementary information). Shortening across the ESB increases to 2.4 ± 0.1 mm/yr with left-lateral strike-slip motion to 1.5 ± 0.3 mm/yr (net slip = 3 ± 0.2 mm/yr) south of the Puyo and Pastaza regions (latitude 2°S-4°S). Although not statistically significant, this increase in slip rates (∼1 mm/yr) is consistent with a faster and more active deformation in southern Ecuador sub-andean domain compared to that observed at latitude 0°. Within the Subandean, the western boundary of the EPSUB is well constrained by the Macas fault in Southern Ecuador. Our best model estimate also dominant E-W shortening across this structure at 1.5 ± 0.4 mm/yr, providing a posterior reason to select that fault as the eastern limit of the Inca sliver in southern Ecuador.

In northern Peru, the Marañon fault system accommodates 2.3 ± 0.2 mm/yr from the convergence (reverse slip at 2.0 ± 0.3 and left-lateral strike-slip at 1.0 ± 0.3 mm/yr). Interestingly, the Eastern Subandean Belt surrounding the Yurimaguas region (latitudes 5°S-7°S) moves at 3.1 ± 0.1 mm/yr with dominant left-lateral motion (reverse slip of 0.6 ± 0.2 mm/yr) (figure 4.10 and figure 4.15 in the supplementary information). Between latitudes 5°S-7°S, the strike of the Eastern Subandean Belt along ∼360 km length is N130°E and perpendicular to the average strike (N40°E) along the Puna and Pallatanga faults. Therefore, the sense of motion of the Eastern Subandean Belt is well compatible with the normal opening at the southwestern boundary of the NAS.

Our results suggest that the Eastern Subandean Belt (ESB) in Ecuador and Northern Peru is the easternmost boundary of the Inca sliver accommodating 5% - 7% of the NAZCA/SOAM convergence.

4.8 RELATIVE MOTION AT THE NAS BOUNDARIES

4.8.1 Nazca subduction

Our new NAZCA/SOAM convergence estimates benefit from an improved determination of the Nazca plate kinematics (Jarrin et al. submitted). Consequently, the new prediction of the Nazca/North Andean West (Nazca/NAW) convergence rates along the Ecuador-Colombia trench axis is more accurate. Our model predicts convergence rates from 49 mm/yr at latitude ∼4°S to 46.0 mm/yr at latitude ∼1.5°S in Ecuador (average rate of 47.5 mm/yr). In south-central Colombia, rates decrease from 45.5 mm/yr at latitude ∼2°N to 43.1 mm/yr at latitude ∼6.0°N (average rate of 44.3 mm/yr) (figure 4.10).

The predicted Nazca/NAW trench-parallel motion increases from 4.2 mm/yr at latitude ∼3.5°S to 6.3 mm/yr at latitude ∼6°N, while the trench-normal motion decrease from 48.3 mm/yr

to 42.6 mm/yr at the same latitudes. Compared to Nocquet et al. (2014) model, we find that the predicted velocities from Nocquet et al. (2014) are 2-3 mm/yr faster for the trench-normal motion and 0.5-1.5 mm/yr faster for the trench-parallel motion. These discrepancies arise from (1) the Euler pole used by Nocquet et al. (2014) for the Nazca plate is ∼1 mm/yr faster than the pole used by our model (detailed discussion available in Jarrin et al. submitted) and (2) the NAS kinematics from Nocquet et al. (2014) predicts constant trench-parallel motion at 6 mm/yr.

In northern Peru, we estimate constant Nazca/Peruvian Forearc West (Nazca/PFW) convergence rates at 54.2 ±0.1 mm/yr between latitudes 5°S and 8°S. These predicted convergence rates are consistent within ∼0.6 mm/yr from the values reported by Villegas-Lanza et al. (2016b). Our additional data and analysis therefore confirms the view of a sliver made of two separated blocks, namely the Peruvian Forearc West (PFW) and the Subandean (EPSUB), whose boundary is the Marañon fault.

Our model further confirms that trench-parallel component motion reverses at the latitude ∼5°S, with righ-lateral strike-slip motion along the North Andean Sliver and left-lateral strike-slip along the Peruvian sliver.

4.8.2 Caribbean subduction

Tomography results and plate reconstruction support active subduction of the Caribbean plate beneath the northern Andes since 75 million years. Seismic reflection profiles also image underthrusting of Caribbean crust, below the northern NAS, consisting of a deformed accretionary prism. Whether active subduction occurs is central for both understanding the geodynamics in the northern Andes and seismic hazard assessment. Geodetic models support active subduction beneath northern Colombia but differs on the convergence rate and the part of the relative motion taken up by deformation within the SCDB.

Symithe et al. (2015) modeled the northern part of the NAS as 3 blocks similar to our model C. Their model predicts convergence rate of 9 mm/yr decreasing eastward to zero at the longitude 68^oW and predicting increasing extension up to 5 mm/yr at the junction with the El Pillar fault.

Oppositely, Lizarazo et al. (2021) propose that the northern NAS is made of a single Macondo block with an undefined southern boundary at latitude 7.5°N. In this view, convergence rate occurs at 7 mm/yr. However, modelling the few GPS data available requires significant coupling to occur down to 20 km depth in addition to inelastic deformation within the SCDB.

Our best model includes 4 blocks required to correctly describe the GPS velocity field in the northern part of the NAS. The pattern of relative motion along the Caribean plate boundary is similar to Symithe et al. (2015), showing a transition from active subduction (figure 4.11) in the western part to opening in the easternmost part (figure 4.12). In the details, there are a

few differences: in the westernmost part of the plate boundary, we find that the convergence is accommodated partly along the subduction interface (3 mm/yr) but also by shortening across the San Jacinto Fold Belt (4-5 mm/yr). This is required to improve the fit for the velocity at BACO, BARU, CART and consistent with a mechanically weak, deforming accretionary prism. Our subduction rate is thefore much slower than Symithe et al. (2015) (9 mm/yr) or Lizarazo et al. (2021) (7 mm/yr). Along the subduction interface, oppositely to Lizarazo et al. (2021), we do not find the need for significant interseismic coupling along the Caribbean subduction interface, that was left as a free parameter in our model (figure 4.11). Relative motion is also found to be slower than previous estimates offshore Venezuela with a maximum convergence rate of 2 mm/yr against 4 mm/yr for Symithe et al. (2015) at longitude 72^{o}W and 2 mm/yr of oblique opening against 5 mm/yr for Symithe et al. (2015) at the eastern end of the Bonnaire block (figure 4.12).

In our model, the northern NAS shows a complex deformation pattern accommodating the 17 mm/yr of motion of the Caribbean plate with respect to South America. In short, slip along the subduction interface accounts for at most 30% of the relative motion in the western part to 0% in the eastern part. Another 30% is taken up along at eastern NAS boundary along the Eastern Frontal Fault System and the Bocono fault. The remaining part occurs through a combination of shortening along the San Jacinto Fold Belt and shear and rapid rotation around the Maracaibo block.

4.8.3 Panama block Collision

The collision of the Panama block against the NAS produces an area of active and distributed deformation (Mora-Páez et al. 2019, Trenkamp et al. 2002). Two shallow Mw 6.6 and Mw 7.1 earthquakes occurred in 1992 in the Mutata region, with focal mechanism solutions compatible with a compressive regime (Ekström et al. 2012, Mora-Páez et al. 2019). In our model, the Panama/NAS boundary were defined from the location of clusters of shallow seismicity, sharp gradient found in GPS velocities, and neotectonic information. We name this boundary as the East Panama Deformed Zone (EPDZ) (figure 4.11). Along the East Panama Deformed Zone, right lateral strike slip decreases from 15 mm/yr at longitude 77°W to down 10 mm/yr at longitude 76.4°W, whereas compression increases from 1 to 11 mm/yr at the same longitude. The Uramita fault (the easternmost Panama/NAS boundary) accommodates dominant compression at 5.7 ± 0.4 mm/yr and 1.5 ± 0.1 mm/yr of left-lateral motion (figure 4.11 and figure 4.15 in the supplementary information). Together with the shortening at the San Jacinto fold belt described in the previous paragraph, the EPDZ defines a broad deforming zone accommodating the eastward motion of the Panama and Caribbean. This area experienced 6 earthquakes with magnitude between 6.3 and 7.3 since 1976 (figure 4.1). That part of the NAS appears to be among the most active both in terms of deformation with 1 cm/yr accommodated over 100 km, slip rate and occurrence of relatively large crustal earthquakes.

To the south of the East Panama deformed zone, the impact of the collision appears to end on the Romeral fault close to the Medellín city (latitude ∼6.5°N). Slip rates along the Romeral fault

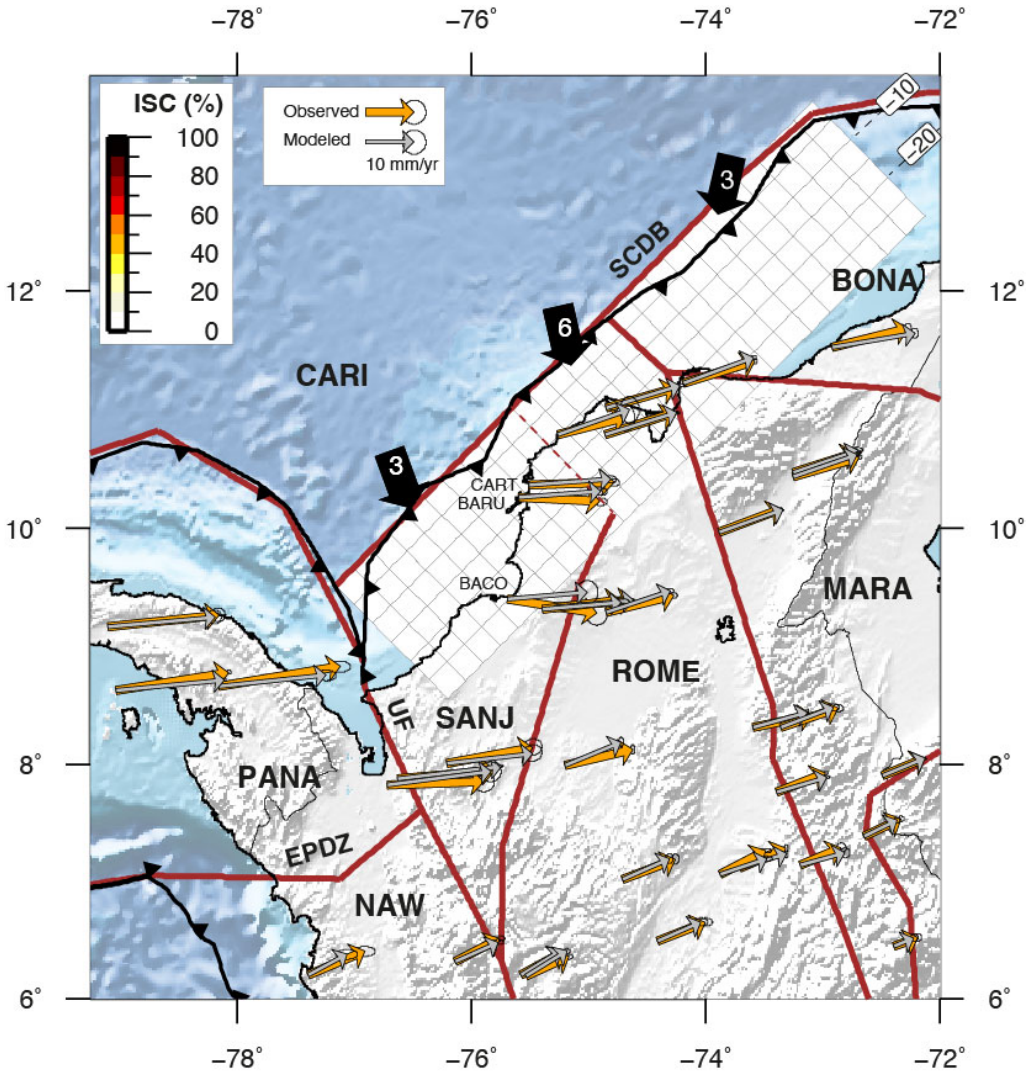

Figure 4.11 – Interseismic coupling and relative motion between blocks estimated by model 4 at the northwestern edge of the NAS. Black arrows depict the predicted convergence rates between pair of blocks: Caribbean/San Jacinto (CARI/SANJ), Caribbean/Romeral (CARI/ROME), Caribbean/ Bonaire (CARI/BONA). Number within the black arrows in mm/yr. MARA: Maracaibo block. NAW: North Andean West block. PANA: Panama block. SCDB: South Caribbean Deformed Belt. EPDZ: East Panama Deformed Zone. UF: Uramita fault.

abruptly decrease from 8 mm/yr at the north of latitude 6°N down to 2 mm/yr south of latitude 6°N. Such decrease is indeed observed in the drastic reduction of velocities (∼9 mm/yr) at the latitude 6°N with respect to velocities near the collision zone (figure 4.11).

Despite the reduced number of GPS observations surrounding the Panama/NAS boundary, our model allows us to capture the main signal of the deformation produced by the collision. Better densification of geodetic measurements is required in the future for separating contributions from the Caribbean subduction and the Panama collision on the San Jacinto fold belt.

4.9 DISCUSSION

4.9.1 Implication for seismic hazard in the northern Andes

Our model highlight many crustal fault systems potentially accumulating significant elastic strain to be released by future earthquakes surrounding large cities. Our model provides some first order assessment of the seismic potential along major faults. We focus on the most relevant active fault systems where rupture areas of the historical and past shallow crustal earthquakes (Mw $\geq$ 7.0 and depth < 20 km) occurred. We assume that the slip rate deficit (product of interseismic coupling and the predicted slip rate) is steady through time and homogeneously distributed along the whole fault plane where earthquakes are presumed to occur. Using the slip rates from our model, we estimate the moment rate deficit (M0) considering a rigidity module of 3.1×10^{10} Pa.

In Ecuador, the northern section of Pallatanga fault near Riobamba city hosted the most destructive historical crustal earthquake (the Mw 7.6 1797) in Ecuador (Beauval et al. 2010). Predicted slip rates from our model are consistent with those proposed by long-term geological estimates, whose rates are the lowest with respect to the other fault segments along the whole Eastern boundary of the North Andean Sliver. With a yearly slip deficit of 5.3 mm/yr, we find a moment rate deficit of 1.73×10^{17} N.m.yr^{-1} that is equivalent to a single Mw 7.6 earthquake every ∼1600 years. That estimate falls within the time interval proposed by Baize et al. (2015) from plaeo-seismology studies. The Cosanga fault has ruptured during the Mw 7.0 1987 Salado-Reventador earthquake, which impacted several cities within the Interandean Drepession and Subandean region (Alvarado et al. 2016, Beauval et al. 2010). We find a moment rate accumulation of 0.585×10^{17} N.m.yr^{-1} with a recurrence time of earthquakes of ∼607 years for a similar magnitude of 7.0. Tibaldi et al. (2007) and Diederix et al. (2021) suggest that the Algeciras-Sibundoy fault system can generate earthquakes with moment magnitudes ∼7.0. The last major documented historical earthquake (1827) associated with this fault had a Mw 7.1, which mainly affected towns in the Huila department (SGC 2021). For this fault, we estimate a moment rate deficit of 11.4×10^{17} N.m.yr^{-1}, that could produce a Mw 7.1 earthquake every 50 years, if all fault sections break at once. However, an alternative estimate of seismic potential is obtained by considering individual rupture of fault segments. In this case, the 1827 earthquake is related to the activity of Acevedo section (Central section of the Algeciras-Sibundoy fault) (Velandia et al. 2005).

Therefore, we estimate 4.85×10^{17} N.m.yr^{-1} to be accumulated during ~110 years, which would be the most likely seismic potential.

The 1967 Mw 7.0 earthquake is one of the most important earthquakes in central Colombia that impacted several towns of Colombia, including Bogota city (SGC 2021). Given the moment magnitude and its proposed epicenter (Dimaté et al. 2005), the Eastern Frontal Fault System (EFFS) central section surrounding Bogota city is the most likely system able to generate it. Thus, we estimate a moment rate deficit of 3.96×10^{17} N.m.yr^{-1} with a recurrence time of 90 years to recover ~1.2 m of estimated slip (according Wells and Coppersmith (1994) relationship) during the 1785 earthquake. Within northwestern Colombia surrounding Murindo city, we find a moment rate deficit at 5.27×10^{17} N.m.yr^{-1} for the fault section connecting the Uramita and Romeral systems (latitude ~6.2°N-7°N). At this rate, it would take only ~95 years to produce a Mw 7.1 earthquake as the one that occurred in 1992 (Ekström et al. 2012, Mora-Páez et al. 2019).

Three historical earthquakes with Mw $\geq$ 7.1 occurred surrounding the junction of the Bocono and San Sebastian faults (Choy et al. 2010, Colón et al. 2015, Pérez et al. 2018). One of them (Mw ~7.7) impacted a large region of North-central Venezuela in 1900, in which the eastern section of the San Sebastian fault was broken (Choy et al. 2010). In our model, the San Sebastian fault accumulates a moment rate deficit of 15.2×10^{17} N.m.yr^{-1}. This value suggests that ~260 years are expected to recover the same moment magnitude. Table 4.3 summarizes fault parameters used in the earthquake recurrence time and moment rate deficit estimates.

Table 4.3 – Fault parameters used in the estimated moment rate deficit derived from this study. ISC: Interseismic coupling. RT: Recurrence time

Fault/Section	**Slip rate** mm/yr	**ISC** %	**Width** km	**Length** km	**M_0** $\times 10^{17}$N.m.yr^{-1}	**RT** years	**Mw**
Central Algercidas-Sibundoy	8.7	100	15	120	4.05	~110	7.1
Cosanga	5.9	50*	10	64	0.585	~607	7.0
Murindo	8.8	100	12	161	5.27	~95	7.1
Northern Pallatanga	5.3	100	15	70	1.73	~1600	7.6
San Sebastian	17.0	100	11	263	15.2	~260	7.7
Central EFFS	6.7	100	15	127	3.96	~90	7.1

* ISC value fixed for our best model. At this value, velocity residuals are the smallest for GPS sites on either side of the fault.

4.9.2 Continental deformation in the northern Andes

The North Andean Sliver (NAS) is deforming through its fragmentation into several blocks, whose relative motion is accommodated by crustal faults over the whole extension of the sliver (~2000 km length). The fast and oblique subduction of the Nazca plate beneath South America controls the overall deformation regime. Trench-normal motion induces elastic strain accumulation at the megathrust interface and within the upper plate through crustal faults, while trench-parallel motion is accommodated by right-lateral slip producing the lateral translation-like motion of the sliver. In addition, the Caribbean/South American convergence is accommodated offshore

across the Southern Caribbean Deformed Belt and onshore faults on the Oca-Ancon, Santa Marta-Bucaramanga, and San Jacinto Fold Belt. The last one also accommodates some motion of the Panama collision.

Further East, in northern Venezuela, deformation occurs along the San Sebastian-El Pilar faults. Both fault systems are moving at almost the same rate as the Caribbean motion. However, a fraction of the Caribbean/SOAM relative motion is also transferred at the easternmost extensions of the Oca-Ancon and Boconó fault systems. Both the Nazca subduction and the arrival of the Carnegie ridge in the Ecuadorian trench since ∼2 Myr are interpreted as the mechanisms responsible for the N-NE escape of the NAS (Egbue and Kellogg 2010, Gutscher et al. 1999, Kellogg and Mohriak 2001, Pennington 1981, Trenkamp et al. 2002). However, the observed deformation pattern northward of latitude ∼7°N suggests the Panama collision or the Caribbean motion also contributes to an "increase" of eastward motion (Audemard 2014; 2009, Egbue and Kellogg 2010).

Within the NAS two patterns of deformation are observed: (1) localized deformation along several secondary fault systems accumulating slip rates at 2-4 mm/yr (The Oca-Ancon, Santa-Martha Bucaramanga, Romeral, Latacunga-Quito-El Angel fault systems) and (2) distributed deformation broadening as far as hundreds of kilometers surrounding the Panama-northeastern Colombia suture zone (Uramita fault and Eastern Panama deformed zone).

Outside the NAS, the East Deformed Belt (Subandean region) accommodates 2-3 mm/yr of the Nazca/SOAM convergence. However, the convergence also appears to control a pattern of distributed deformation as far as ∼220 km east of the Andean Cordillera within Ecuadorian Amazonia. The velocity field in this region shows velocities at ∼2 mm/yr, pointing out east-southeastward (figure 4.12 and figure 4.2). Future coverage of continuous geodetic observations is required to better constrain the width of the subandean domain and to delimit where its easternmost front reaches the stable part of South America in this region.

4.10 CONCLUSIONS

Our study provides the first regional kinematic model for the North Andean Sliver (NAS) and neighboring regions simultaneously solving for the effects of rigid block rotations and elastic strain accumulation at faults. We propose a block model built with 12 blocks that explains well more than 80% of the observed interseismic velocity field by fragmenting the sliver into 6 blocks that rotate with respect to South America. Our results also confirm that the Panama block is colliding against the NW Colombia as a single rigid block based on the available GPS observations within Panama. The kinematic of the Inca sliver in north-central Peru (as far as 14°S of latitude) is consistent with the motion of two rigid blocks accommodating deformation across known Quaternary fault systems.

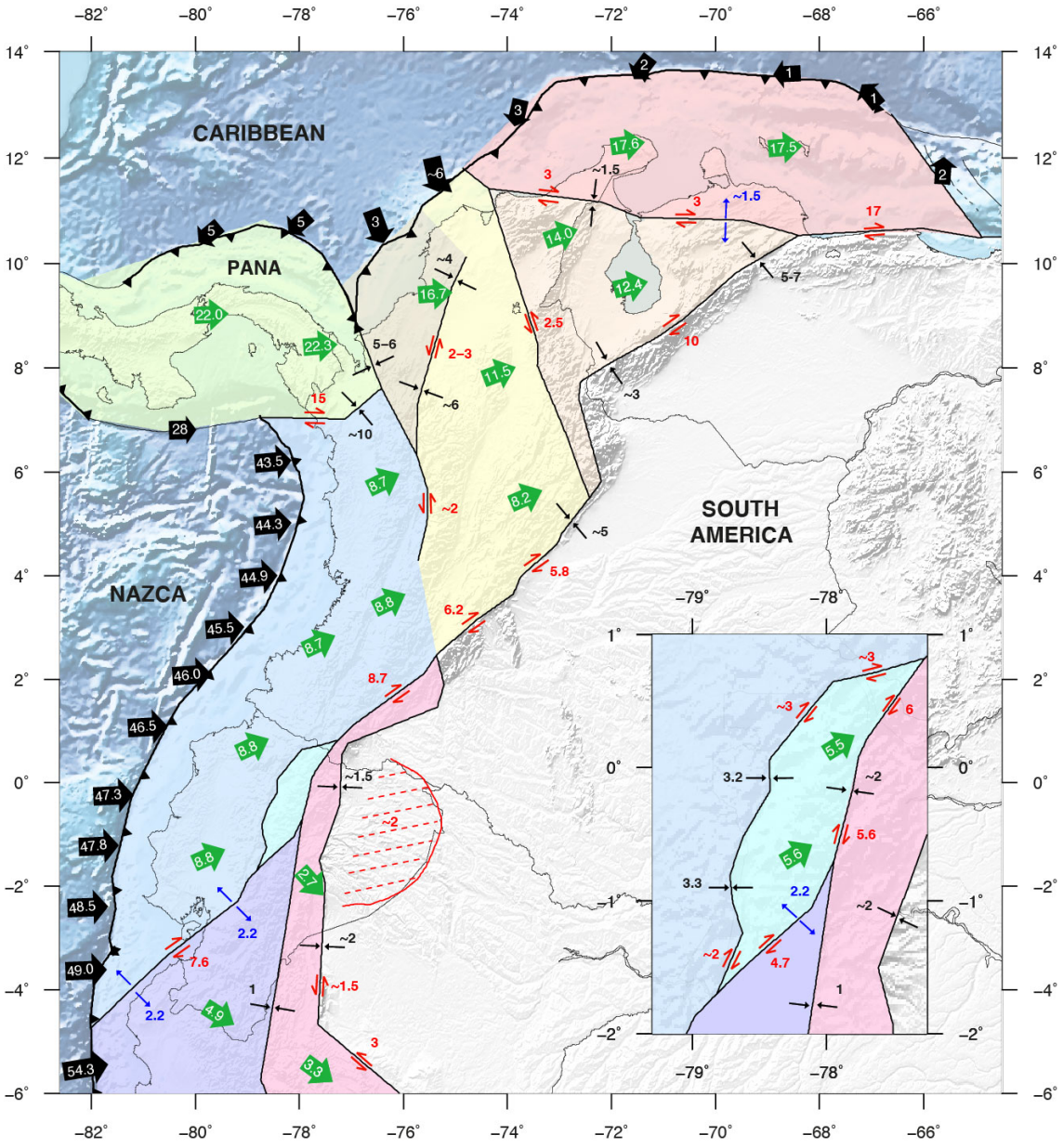

Figure 4.12 – Kinematic model for the North Andean Sliver showing the obtained main results from this study. Numbers within or next to the colored arrows are in mm/yr and depict slip rate estimates on block-bounding faults (across fault systems). Green arrows indicate the block motion with respect to South America. Red dashed area shows a possible region accommodating deformation in the order of ∼2 mm/yr

We confirm that the Eastern boundary of the NAS is the major intraplate transpressive fault system accommodating 5-17 mm/yr of motion. Localized internal deformation on mapped active faults as the Oca-Ancon, Santa Martha-Bucarmanga, Romeral, and the Latacunga-Quito-El Angel fault systems at 2-4 mm/yr is compatible with geological estimates. These fault systems delimit tectonic blocks whose rotations are kinematically consistent. The Subandean domain is bounded to the west by the Eastern Subandean Belt, which is characterized by slow reverse slip increasing southward from 2 mm/yr in Ecuador to 4 mm/yr in Peru and induces deformation penetrating

inside the Amazonia basin.

Slight motion along the Southern Caribbean Deformed belt at ∼4.5 mm/yr offshore northern Colombia decreasing eastward to 2 mm/yr offshore northern Venezuela is consistent with low angle subduction interface without significant interseismic coupling. The Nazca plate subducts beneath the NAS at ∼47.5 mm/yr in Ecuador and ∼44.5 mm/yr in south-central Colombia. The North Andean West (NAW) block is moving at 8.8 ± 0.1 mm/yr towards N65°±1E with respect to South America. The fast collision of the Panama block at 22 mm/yr produces a broad region of distributed deformation. Consequently, a portion of the strain from this collision is transferred northeastward within the sliver across the San Jacinto fold belt and inland as far as latitude ∼75°W.

The good agreements between present-day slip rate estimates from our kinematic elastic block model and long-term geological estimates on available fault systems suggest that the GPS velocity field accurately captures the NAS motion since the Quaternary. Consequently, our model provides a high-quality image of the interseismic deformation as an input for future seismic hazard evaluations on a regional scale. Finally, scarce geodetic observations in some regions where major historical earthquakes have occurred (ex: along the coastline of south-central Colombia, region of Panama collision, Subandean domain) require future densification of continuous or campaign GPS measurements.

4.11 ACKNOWLEDGMENTS

This research was supported by the Secretaría Nacional de Educación Superior, Ciencia y Tecnología (SENESCYT-Ecuador) in the frame of P. Jarrin's doctoral fellowship (grant number:IFTH-DFN-2018-0096/092-2017). We acknowledge support from the Institut de Recherche pour le development and Agence Nationale de la Recherche in the frame of IRD/ANR-S5 AAP CE31 project.

4.12 APPENDIX

Equation 4.1 is used to quantify the goodness of fit from residual values in terms of χ^2. V_{obs} and V_{mod} are the observed and modeled velocities respectively, σ is the standard error assigned to the observed velocities and n is the number of observations.

$$\chi^2 = \sum_{i=1}^{n} \frac{(Vobs_i - Vmod_i)^2}{\sigma_i^2} \tag{4.1}$$

We use the Variance reduction R to assess the accuracy increase of the model based on the block geometry evolution (Bougrine et al. 2019):

$$R = 1 - \frac{\sum_{i=1}^{n} (Vobs_i - Vmod_i)^2}{\sum_{i=1}^{n} (Vobs_i)^2} \tag{4.2}$$

The F_{ratio} test (Nocquet et al. 2001, Stein and Gordon 1984) is used to compare how well two models derived from least squares estimations fit the data according to their degree of freedom.

$\chi^2_{p_1}$ and $\chi^2_{p_2}$ are the chi-square statistics from the two models with p_1 and p_2 degrees of freedom respectively

$$F = \frac{\left(x^2_{p_1} - x^2_{p_2}\right) / (p_1 - p_2)}{x^2_{p_2} / p_2} \tag{4.3}$$

The empirical value of F is compared to the expected value from a Fischer-Snedecor distribution with p_1, p_2 degrees of freedom at a given confidence level.

4.13 REFERENCES

- Acosta, J., Velandia, F., Osorio, J., Lonergan, L. & Mora, H. (2007) Strike-slip deformation within the Colombian Andes. in Deformation of the Continental Crust: The Legacy of Mike Coward eds. Ries, A.C., Butler, R.W.H. & Graham, R.H., Vol. 272, p. 0, Geological Society of London. doi:10.1144/GSL.SP.2007.272.01.16

- Altamimi, Z., Rebischung, P., Métivier, L. & Collilieux, X. (2016) ITRF2014: A new release of the International Terrestrial Reference Frame modeling nonlinear station motions. Journal of Geophysical Research: Solid Earth, 121, 6109–6131. doi:10.1002/2016JB013098

- Alvarado, A., Audin, L., Nocquet, J.M., Jaillard, E., Mothes, P., Jarrín, P., Segovia, M., et al. (2016) Partitioning of oblique convergence in the Northern Andes subduction zone: Migration history and the present-day boundary of the North Andean Sliver in Ecuador. Tectonics, 35, 1048–1065. doi:10.1002/2016TC004117

- Alvarado, A., Audin, L., Nocquet, J.M., Lagreulet, S., Segovia, M., Font, Y., Lamarque, G., et al. (2014) Active tectonics in Quito, Ecuador, assessed by geomorphological studies, GPS data, and crustal seismicity. Tectonics, 33, 67–83, John Wiley & Sons, Ltd. doi:10.1002/2012TC003224

- Alvarado, A., Ruiz, M., Mothes, P., Yepes, H., Segovia, M., Vaca, M., Ramos, C., et al. (2018) Seismic, Volcanic, and Geodetic Networks in Ecuador: Building Capacity for Monitoring and Research. Seismological Research Letters, 89, 432–439. doi:10.1785/0220170229

- Audemard, Felipe & Audemard, F. (2002) Structure of the Mérida Andes, Venezuela: relations with the South America–Caribbean geodynamic interaction. Tectonophysics, 345, 1–26. doi:https://doi.org/10.1016/S0040-1951(01)00218-9

- Audemard, Franck. (1996) Paleoseismicity studies on the Oca-Ancón fault system, northwestern Venezuela. Tectonophysics, 259, 67–80. doi:10.1016/0040-1951(95)00144-1

- Audemard, Franck. (2009) Key issues on the post-Mesozoic Southern Caribbean Plate boundary. in The Origin and Evolution of the Caribbean Plate, Geological Society of London. doi:10.1144/SP328.23

- Audemard, Franck. (2014) Active block tectonics in and around the Caribbean: A Review. in The Northeastern Limit of the South American Plate - Lithospheric Structures from Surface to the Mantle, pp. 29–77, Editorial Innovación Tecnológica. Retrieved from https://www.academia.edu/22801718

- Audemard, Franck, Ollarves, R., Bechtold, M., Díaz, G., Beck, C., Carrillo, E., Pantosti, D., et al. (2008) Trench investigation on the main strand of the Boconó fault in its central section, at Mesa del Caballo, Mérida Andes, Venezuela. Tectonophysics, 459, 38–53. doi:10.1016/j.tecto.2007.08.020

- Audemard, Frank, Machette, M., Cox, J., Dart, R. & Haller, K. (2000) Open-File Report (Open-File Report). Open-File Report.

- Baby, P., Rochat, P., Mascle, G. & Hérail, G. (1997) Neogene shortening contribution to crustal thickening in the back arc of the Central Andes. Geology, 25, 883–886. doi:10.1130/0091-7613(1997)025<0883:NSCTCT>2.3.CO;2

- Baize, S., Audin, L., Winter, T., Alvarado, A., Moreno, L.P., Taipe, M., Reyes, P., et al. (2015) Paleoseismology and tectonic geomorphology of the Pallatanga fault (Central Ecuador), a major structure of the South-American crust. Geomorphology, 237, 14–28. doi:https://doi.org/10.1016/j.geomorph.2014.02.030

- Baize, S., Audin, L., Alvarado, A., Jomard, H., Bablon, M., Champenois, J., Espin, P., et al. (2020) Active Tectonics and Earthquake Geology Along the Pallatanga Fault, Central Andes of Ecuador. Frontiers in Earth Science, 8, 193. doi:10.3389/feart.2020.00193

- Baby, P., Calderón, Y., Brusset, S., Roddaz, M., Brichau, S., Eude, A., Calves, G., et al. (2018) Chapter 4: The Peruvian Sub-Andean Foreland Basin System: Structural Overview, Geochronologic Constraints, and Unexplored Plays. AAPG, 91–119, AAPG Special Volumes. doi:10.1306/13622118M1173767

- Beauval, C., Marinière, J., Yepes, H., Audin, L., Nocquet, J. -M., Alvarado, A., Baize, S., et al. (2018) A New Seismic Hazard Model for Ecuador. Bulletin of the Seismological Society of America, 108, 1443–1464. doi:10.1785/0120170259

- Beauval, C., Yepes, H., Bakun, W.H., Egred, J., Alvarado, A. & Singaucho, J.-C. (2010) Locations and magnitudes of historical earthquakes in the Sierra of Ecuador (1587–1996). Geophysical Journal International, 181, 1613–1633. doi:10.1111/j.1365-246X.2010.04569.x

- Bernal-Olaya, R., Mann, P. & Vargas, C.A. (2015) Earthquake, Tomographic, Seismic Reflection, and Gravity Evidence for a Shallowly Dipping Subduction Zone beneath the Caribbean Margin of Northwestern Colombia. in Petroleum Geology and Potential of the Colombian Caribbean Margin eds. Bartolini, C. & Mann, P., Vol. 108, p. 0, American Association of Petroleum Geologists. doi:10.1306/13531939M1083642

- Bès de Berc, S., Soula, J.C., Baby, P., Souris, M., Christophoul, F. & Rosero, J. (2005) Geomorphic evidence of active deformation and uplift in a modern continental wedge-top–foredeep transition: Example of the eastern Ecuadorian Andes. Tectonophysics, 399, 351–380. doi:10.1016/j.tecto.2004.12.030

- Bevis, M. & Brown, A. (2014) Trajectory models and reference frames for crustal motion geodesy. Journal of Geodesy, 88, 283–311. doi:10.1007/s00190-013-0685-5

- Bird, P. (2003) An updated digital model of plate boundaries. Geochemistry, Geophysics, Geosystems, 4, John Wiley & Sons, Ltd. doi:10.1029/2001GC000252

- Boschman, L.M., Hinsbergen, D.J.J. van, Torsvik, T.H., Spakman, W. & Pindell, J.L. (2014) Kinematic reconstruction of the Caribbean region since the Early Jurassic. Earth-Science Reviews, 138, 102–136. doi:10.1016/j.earscirev.2014.08.007

- Bougrine, A., Yelles-Chaouche, A.K. & Calais, E. (2019) Active deformation in Algeria from continuous GPS measurements. Geophysical Journal International, 217, 572–588. doi:10.1093/gji/ggz035

- Brooks, B.A., Bevis, M., Whipple, K., Ramon Arrowsmith, J., Foster, J., Zapata, T., Kendrick, E., et al. (2011) Orogenic-wedge deformation and potential for great earthquakes in the central Andean backarc. Nature Geoscience, 4, 380–383. doi:10.1038/ngeo1143

- Calderón, Y., Baby, P., Hurtado, C., Bolaños, R. & Bandach, A. (2013) PRE CRETACEOUS FOLD AND THRUST BELTS IN THE MARANON BASIN. INGEPET (GEO-EX-YC-15-N), 4.

- Cediel, F., Shaw, R.P. & Cáceres, C. (2003) Tectonic Assembly of the Northern Andean Block. in The Circum-Gulf of Mexico and the Caribbean: Hydrocarbon Habitats, Basin Formation and Plate Tectonics, American Association of Petroleum Geologists. doi:10.1306/M79877C37

- Chlieh, M., Mothes, P.A., Nocquet, J.-M., Jarrin, P., Charvis, P., Cisneros, D., Font, Y., et al. (2014) Distribution of discrete seismic asperities and aseismic slip along the Ecuadorian megathrust. Earth and Planetary Science Letters, 400, 292–301. doi:10.1016/j.epsl.2014.05.027

- Choy, J.E., Palme, C., Guada, C., Morandi, M. & Klarica, S. (2010) Macroseismic Interpretation of the 1812 Earthquakes in Venezuela Using Intensity Uncertainties and A Priori Fault-Strike Information. Bulletin of the Seismological Society of America, 100, 241–255. doi:10.1785/0120080345

- Collot, J.-Y., Sanclemente, E., Nocquet, J.-M., Leprêtre, A., Ribodetti, A., Jarrin, P., Chlieh, M., et al. (2017) Subducted oceanic relief locks the shallow megathrust in central Ecuador. Journal of Geophysical Research: Solid Earth, 122, 3286–3305. doi:10.1002/2016JB013849

- Colón, S., Audemard, F.A., Beck, C., Avila, J., Padrón, C., De Batist, M., Paolini, M., et al. (2015) The 1900 Mw 7.6 earthquake offshore north–central Venezuela: Is La Tortuga or San Sebastián the source fault? Marine and Petroleum Geology, 67, 498–511. doi:10.1016/j.marpetgeo.2015.06.005

- Diederix, H., Bohórquez-Orozco, O., Gómez-Hurtado, E., Idárraga-García, J., Rendón-Rivera, A., Audemard, F. & Mora-Páez, H. (2021) Paleoseismologic trenching confirms recent Holocene activity of the major Algeciras fault system in southern Colombia. Journal of South American Earth Sciences, 109, 103263. doi:10.1016/j.jsames.2021.103263

- Diederix, Hans, Bohórquez, O.P., Mora-Paez, H., Peláez-Gaviria, J.-R., Cardona-Piedrahita, L., Corchuelo-Cuervo, Y., Ramírez-Cadena, J., et al. (2020) Quaternary Activity of the Bucaramanga Fault n the Departments of Santander and Cesar. Gómez, J. & Pinilla–Pachon The Geology of Colombia, Capter 13, Volume 4 Quaternary, 453–477. doi:10.32685/pub.esp.38.2019.13

- Dimaté, C., Rivera, L. & Cisternas, A. (2005) Re-visiting large historical earthquakes in the Colombian Eastern Cordillera. Journal of Seismology, 9, 1–22. doi:10.1007/s10950-005-1413-2

- Dow, J.M., Neilan, R.E. & Rizos, C. (2009) The International GNSS Service in a changing landscape of Global Navigation Satellite Systems. Journal of Geodesy, 83, 191–198. doi:10.1007/s00190-008-0300-3

- Dumont, J.F., Santana, E., Vilema, W., Pedoja, K., Ordóñez, M., Cruz, M., Jiménez, N., et al. (2005) Morphological and microtectonic analysis of Quaternary deformation from Puná and Santa Clara Islands, Gulf of Guayaquil, Ecuador (South America). Tectonophysics, 399, 331–350. doi:10.1016/j.tecto.2004.12.029

- Duque-Caro, H. (1990) The choco block in the northwestern corner of South America: Structural, tectonostratigraphic, and paleogeographic implications. Journal of South American Earth Sciences, 3, 71–84. doi:10.1016/0895-9811(90)90019-W

- Egbue, O. & Kellogg, J. (2010) Pleistocene to Present North Andean “escape”. Tectonophysics, 489, 248–257. doi:10.1016/j.tecto.2010.04.021

- Ego, F., Sébrier, M. & Yepes, H. (1995) Is the Cauca-Patia and Romeral Fault System left or right lateral Geophysical Research Letters, 22, 33–36, John Wiley & Sons, Ltd. doi:10.1029/94GL02837

- Eguez, A., Alvarado, A., Yepes, H. de J.M., Machette, M.N., Costa, C. & Dart, R.L. (2003) Database and map of Quaternary faults and folds of Ecuador and its offshore regions (Report No. 2003–289). Open-File Report, p. 289, U.S. Geological Survey (USGS).

- Ekström, G., Nettles, M. & Dziewoński, A.M. (2012) The global CMT project 2004–2010: Centroid-moment tensors for 13,017 earthquakes. Physics of the Earth and Planetary Interiors, 200–201, 1–9. doi:10.1016/j.pepi.2012.04.002

- Elliott, J.L., Larsen, C.F., Freymueller, J.T. & Motyka, R.J. (2010) Tectonic block motion and glacial isostatic adjustment in southeast Alaska and adjacent Canada constrained by GPS measurements. Journal of Geophysical Research: Solid Earth, 115, John Wiley & Sons, Ltd. doi:10.1029/2009JB007139

- Engdahl, E.R., Di Giacomo, D., Sakarya, B., Gkarlaouni, C.G., Harris, J. & Storchak, D.A. (2020) ISC-EHB 1964–2016, an Improved Data Set for Studies of Earth Structure and Global Seismicity. Earth and Space Science, 7, e2019EA000897, John Wiley & Sons, Ltd. doi:10.1029/2019EA000897

- Eude, A., Roddaz, M., Brichau, S., Brusset, S., Calderon, Y., Baby, P. & Soula, J.-C. (2015) Controls on timing of exhumation and deformation in the northern Peruvian eastern Andean wedge as inferred from low-temperature thermochronology and balanced cross section. Tectonics, 34, 715–730, John Wiley & Sons, Ltd. doi:10.1002/2014TC003641

- Font, Y., Barros-Lopez, J.G., Hernandez, M.J., Collot, J.-Y., Alvarado, A., Michaud, F. & Marcaillou, B. (2019) Slab curvature in Ecuador and plate interface geometry. Retrieved from https://hal.archives-ouvertes.fr/hal-02527198

- Freymueller, J.T., Kellogg, J.N. & Vega, V. (1993) Plate Motions in the north Andean region. Journal of Geophysical Research: Solid Earth, 98, 21853–21863. doi:10.1029/93JB00520

- Frohlich, C. & Davis, S.D. (1999) How well constrained are well-constrained T, B, and P axes in moment tensor catalogs Journal of Geophysical Research: Solid Earth, 104, 4901–4910, John Wiley & Sons, Ltd. doi:10.1029/1998JB900071

- Gombert, B., Duputel, Z., Jolivet, R., Rivera, L., Simons, M., Jiang, J., Liang, C., et al. (2018) A stochastic view on the strain budget of the Ecuador-Columbia subduction zone. EGU General Assembly Conference Abstracts EGU General Assembly Conference Abstracts, p. 13759.

- grand, D., Baby, P., Bondoux, F., Dorbath, C., Bès de Berc, S. & Rivadeneira, M. (2005) The 1999–2000 seismic experiment of Macas swarm (Ecuador) in relation with rift inversion in Subandean foothills. Tectonophysics, 395, 67–80. doi:10.1016/j.tecto.2004.09.008

- Gutscher, M.-A., Malavieille, J., Lallemand, S. & Collot, J.-Y. (1999) Tectonic segmentation of the North Andean margin: impact of the Carnegie Ridge collision. Earth and Planetary Science Letters, 168, 255–270. doi:10.1016/S0012-821X(99)00060-6

- Hayes, G. (2018) Slab2 - A Comprehensive Subduction Zone Geometry Model, U.S. Geological Survey. doi:10.5066/F7PV6JNV

- Herring, T.A., Floyd, M.A., King, R.W. & McClusky, S.C. (2015) Global Kalman filter VLBI and GPS analysis program.

- Herring, T.A., King, R.W., Floyd, M.A. & McClusky, S.C. (2018) GPS Analysis at MIT Release 10.7 (No. Release 10.7), MIT.

- Hilst, R. van der & Mann, P. (1994) Tectonic implications of tomographic images of subducted lithosphere beneath northwestern South America. Geology, 22, 451–454. doi:10.1130/0091-7613(1994)022<0451:TIOTIO>2.3.CO;2

- Idárraga-García, J. & Romero, J. (2010) Neotectonic study of the Santa Marta Fault System, Western foothills of the Sierra Nevada de Santa Marta, Colombia. Journal of South American Earth Sciences, 29, 849–860. doi:https://doi.org/10.1016/j.jsames.2009.11.004

- Jarrin, P.A., Nocquet, J.M., Rolandone, F. & Mothes, P.A. (2016) Interseismic velocity field and coupling along the Ecuador Subduction interface in relation to the 2016 Pedernales Earthquake. AGU Fall Meeting Abstracts, Vol. 2016, pp. T51E-2978.

- Jiménez, G., Speranza, F., Faccenna, C., Bayona, G. & Mora, A. (2015) Magnetic stratigraphy of the Bucaramanga alluvial fan: Evidence for a $\leq$ 3 mm/yr slip rate for the Bucaramanga-Santa Marta Fault, Colombia. Journal of South American Earth Sciences, 57, 12–22. doi:10.1016/j.jsames.2014.11.001

- Jouanne, F., Audemard, F.A., Beck, C., Welden, A.V., Ollarves, R. & Reinoza, C. (2011) Present-day deformation along the El Pilar Fault in eastern Venezuela: Evidence of creep along a major transform boundary. Journal of Geodynamics, 51, 398–410. doi:https://doi.org/10.1016/j.jog.2010.11.003

- Kellogg, J. N. & Bonini, W.E. (1982) Subduction of the Caribbean Plate and basement uplifts in the overriding South American Plate. Tectonics, 1, 251–276. doi:10.1029/TC001i003p00251

- Kellogg, J. N. & Mohriak, W.U. (2001) The Tectonic and Geological Environment of Coastal South America. in Coastal Marine Ecosystems of Latin America eds. Seeliger, U. & Kjerfve, B., pp. 1–16, Berlin, Heidelberg: Springer Berlin Heidelberg. doi:10.1007/978-3-662-04482-7_1

- Kellogg, James N., Camelio, G.B.F. & Mora-Páez, H. (2019) Chapter 4 - Cenozoic tectonic evolution of the North Andes with constraints from volcanic ages, seismic reflection, and satellite geodesy. in Andean Tectonics eds. Horton, B.K. & Folguera, A., pp. 69–102, Elsevier. doi:10.1016/B978-0-12-816009-1.00006-X

- Kellogg, James N. & Vega, V. (1995) Tectonic development of Panama, Costa Rica, and the Colombian Andes: Constraints from Global Positioning System geodetic studies and gravity. in Geological Society of America Special Papers, Vol. 295, pp. 75–90, Geological Society of America. doi:10.1130/SPE295-p75

- Kobayashi, D., LaFemina, P., Geirsson, H., Chichaco, E., Abrego, A.A., Mora, H. & Camacho, E. (2014) Kinematics of the western Caribbean: Collision of the Cocos Ridge and upper plate deformation. Geochemistry, Geophysics, Geosystems, 15, 1671–1683. doi:10.1002/2014GC005234

- Kroehler, M.E., Mann, P., Escalona, A. & Christeson, Gail.L. (2011) Late Cretaceous-Miocene diachronous onset of back thrusting along the South Caribbean deformed belt and its importance for understanding processes of arc collision and crustal growth. Tectonics, 30. doi:10.1029/2011TC002918

- Ladd, J.W., Truchan, M., Talwani, M., Stoffa, P.L., Buhl, P., Houtz, R., Maufiret, A., et al. (1984) Seismic reflection profiles across the southern margin of the Caribbean. in The Caribbean-South American Plate Boundary and Regional Tectonics eds. Bonini, W.E., Hargraves, R.B. & Shagam, R., Vol. 162, p. 0, Geological Society of America. doi:10.1130/MEM162-p153

- Lavenu, A., Winter, T. & Dávila, F. (1995) A Pliocene–Quaternary compressional basin in the Interandean Depression, Central Ecuador. Geophysical Journal International, 121, 279–300. doi:10.1111/j.1365-246X.1995.tb03527.x

- Lizarazo, S.C., Sagiya, T. & Mora-Páez, H. (2021) Interplate coupling along the Caribbean coast of Colombia and its implications for seismic/tsunami hazards. Journal of South American Earth Sciences, 110, 103332. doi:10.1016/j.jsames.2021.103332

- McCaffrey, R. (1992) Oblique plate convergence, slip vectors, and forearc deformation. Journal of Geophysical Research: Solid Earth, 97, 8905–8915, John Wiley & Sons, Ltd. doi:10.1029/92JB00483

- Machare, J., Fenton, C.H., Machette, M.N., Lavenu, A., Costa, C. & Dart, R.L. (2003) Database and Map of Quaternary Faults and Folds in Peru and its Offshore Region (Report No. 2003–451). Open-File Report, Version 1.1. doi:10.3133/ofr03451

- Mariniere, J., Nocquet, J.-M., Beauval, C., Champenois, J., Audin, L., Alvarado, A., Baize, S., et al. (2019) Geodetic evidence for shallow creep along the Quito fault, Ecuador. Geophysical Journal International, 220, 2039–2055. doi:10.1093/gji/ggz564

- Melnick, D., Bookhagen, B., Strecker, M.R. & Echtler, H.P. (2009) Segmentation of megathrust rupture zones from fore-arc deformation patterns over hundreds to millions of years, Arauco peninsula, Chile. Journal of Geophysical Research: Solid Earth, 114, John Wiley & Sons, Ltd. doi:10.1029/2008JB005788

- Mora, J.A., Oncken, O., Le Breton, E., Ibánez-Mejia, M., Faccenna, C., Veloza, G., Vélez, V., et al. (2017) Linking Late Cretaceous to Eocene Tectonostratigraphy of the San Jacinto Fold Belt of NW Colombia With Caribbean Plateau Collision and Flat Subduction. Tectonics, 36, 2599–2629, John Wiley & Sons, Ltd. doi:10.1002/2017TC004612

- Morales Rivera, A.M., Amelung, F., Mothes, P., Hong, S.-H., Nocquet, J.-M. & Jarrin, P. (2017) Ground deformation before the 2015 eruptions of Cotopaxi volcano detected by InSAR. Geophysical Research Letters, 44, 6607–6615, John Wiley & Sons, Ltd. doi:10.1002/2017GL073720

- Mora-Páez, H., Kellogg, J.N., Freymueller, J.T., Mencin, D., Fernandes, R.M.S., Diederix, H., LaFemina, P., et al. (2019) Crustal deformation in the northern Andes – A new GPS velocity field. Journal of South American Earth Sciences, 89, 76–91. doi:https://doi.org/10.1016/j.jsames.2018.11.002

- Mora-Páez, H., Mencin, D.J., Molnar, P., Diederix, H., Cardona-Piedrahita, L., Peláez-Gaviria, J.-R. & Corchuelo-Cuervo, Y. (2016) GPS velocities and the construction of the Eastern Cordillera of the Colombian Andes. Geophysical Research Letters, 43, 8407–8416. doi:10.1002/2016GL069795

- Mora-Páez, H., Peláez-Gaviria, J., Diederix, H., Bohórquez-Orozco, O., Cardona-Piedrahita, L., Corchuelo-Cuervo, Y., Ramírez-Cadena, J., et al. (2018) Space Geodesy Infrastructure in Colombia for Geodynamics Research. Seismological Research Letters, 89, 446–451. doi:10.1785/0220170185

- Moreno, M.S., Klotz, J., Melnick, D., Echtler, H. & Bataille, K. (2008) Active faulting and heterogeneous deformation across a megathrust segment boundary from GPS data, south central Chile (36–39°S). Geochemistry, Geophysics, Geosystems, 9, John Wiley & Sons, Ltd. doi:10.1029/2008GC002198

- Mothes, P.A., Nocquet, J.-M. & Jarrín, P. (2013) Continuous GPS Network Operating Throughout Ecuador. Eos, Transactions American Geophysical Union, 94, 229–231. doi:10.1002/2013EO260002

- Mothes, P.A., Rolandone, F., Nocquet, J., Jarrin, P.A., Alvarado, A.P., Ruiz, M.C., Cisneros, D., et al. (2018) Monitoring the Earthquake Cycle in the Northern Andes from the Ecuadorian cGPS Network. Seismological Research Letters, 89, 534–541. doi:10.1785/0220170243

- Nocquet, Jean-Mathieu. (2012) Present-day kinematics of the Mediterranean: A comprehensive overview of GPS results. Tectonophysics, 579, 220–242. doi:https://doi.org/10.1016/j.tecto.2012.03.037

- Nocquet, J-M., Calais, E., Altamimi, Z., Sillard, P. & Boucher, C. (2001) Intraplate deformation in western Europe deduced from an analysis of the International Terrestrial Reference Frame 1997 (ITRF97) velocity field. Journal of Geophysical Research: Solid Earth, 106, 11239–11257. doi:10.1029/2000JB900410

- Nocquet, J-M., Jarrin, P., Vallée, M., Mothes, P.A., Grandin, R., Rolandone, F., Delouis, B., et al. (2016) Supercycle at the Ecuadorian subduction zone revealed after the 2016 Pedernales earthquake. Nature Geoscience, 10, 145. doi:10.1038/ngeo2864

- Nocquet, J-M., Villegas-Lanza, J.C., Chlieh, M., Mothes, P.A., Rolandone, F., Jarrin, P., Cisneros, D., et al. (2014) Motion of continental slivers and creeping subduction in the northern Andes. Nature Geoscience, 7, 287–291. doi:10.1038/ngeo2099

- Paris, G., Machette, M.N., Dart, R.L. & Haller, K.M. (2000) Map and database of Quaternary faults and folds in Colombia and its offshore regions (Report No. 2000–284). Open-File Report, U.S. Geological Survey (USGS). doi:10.3133/ofr00284

- Pennington, W.D. (1981) Subduction of the Eastern Panama Basin and seismotectonics of northwestern South America. Journal of Geophysical Research: Solid Earth, 86, 10753–10770. doi:10.1029/JB086iB11p10753

- Pérez, O.J., Wesnousky, S.G., De La Rosa, R., Márquez, J., Uzcátegui, R., Quintero, C., Liberal, L., et al. (2018) On the interaction of the North Andes plate with the Caribbean and South American plates in northwestern South America from GPS geodesy and seismic data. Geophysical Journal International, 214, 1986–2001. doi:10.1093/gji/ggy230

- Piñón, D.A., Gómez, D.D., Smalley, R., Jr., Cimbaro, S.R., Lauría, E.A. & Bevis, M.G. (2018) The History, State, and Future of the Argentine Continuous Satellite Monitoring Network and Its Contributions to Geodesy in Latin America. Seismological Research Letters, 89, 475–482. doi:10.1785/0220170162

- Pousse-Beltran, L., Vassallo, R., Audemard, F., Jouanne, F., Carcaillet, J., Pathier, E. & Volat, M. (2017) Pleistocene slip rates on the Boconó fault along the North Andean Block plate boundary, Venezuela. Tectonics, 36, 1207–1231, John Wiley & Sons, Ltd. doi:10.1002/2016TC004305

- Rebischung, P., Altamimi, Z., Ray, J. & Garayt, B. (2016) The IGS contribution to ITRF2014. Journal of Geodesy, 90, 611–630. doi:10.1007/s00190-016-0897-6

- Rolandone, F., Nocquet, J.-M., Mothes, P., Jarrin, P., Vallée, M., Cubas, N., Hernandez, S., et al. (2018) Areas prone to slow slip events impede earthquake rupture propagation and promote afterslip. Science Advances, 4, eaao6596. doi:10.1126/sciadv.aao6596

- Savage, J. (1983) A Dislocation Model of Strain Accumulation and Release at a Subduction Zone. Journal of Geophysical Research, 88, 4984–4996. doi:10.1029/JB088iB06p04984

- Schmitz, M., Avila, J., Bezada, M., Vieira, E., Yáñez, M., Levander, A., Zelt, C.A., et al. (2008) Crustal thickness variations in Venezuela from deep seismic observations. Tectonophysics, 459, 14–26. doi:https://doi.org/10.1016/j.tecto.2007.11.072

- Schubert, C. (1982) Neotectonics of Boconó fault, Western Venezuela. Elsevier Scientific Publishing Company, Vol. 85, pp. 205–220, Tectonophysics.

- Segall, P. (2010) Earthquake and Volcano Deformation, ilustrada ed., Princeton University Press, 2010. Retrieved from https://press.princeton.edu/books/hardcover/9780691133027/earthquake-and-volcano-deformation

- Segovia, M., Font, Y., Regnier, M.M., Charvis, P., Nocquet, J.M., Galve, A., Hello, Y., et al. (2015) Intense Microseismicity Associated with a SSE at La Plata Island in the Central Subduction Zone of Ecuador. AGU Fall Meeting Abstracts, Vol. 2015, pp. S31A-2736.

- Segovia, Mónica, Font, Y., Régnier, M., Charvis, P., Galve, A., Nocquet, J.-M., Jarrín, P., et al. (2018) Seismicity Distribution Near a Subducting Seamount in the Central Ecuadorian Subduction Zone, Space-Time Relation to a Slow-Slip Event. Tectonics, 37, 2106–2123. doi:10.1029/2017TC004771

- SGC. (2020) Catálogo Mecanismo Focal y Tensor Momento (Internet research No. 2020), Servicio Geológico Colombiano. Retrieved from $http://bdrsnc.sgc.gov.co/sismologia1/sismologia/focal_seiscomp\_3/index.html$

- SGC. (2021) Sismicidad Histórica de Colombia (Internet research No. 2021), Servicio Geológico Colombiano. Retrieved from $http://sish.sgc.gov.co/visor$

- SGC, S. (2020) Catálogo de Sismicidad (Internet research No. 2020), Servicio Geológico Colombiano. Retrieved from $http://bdrsnc.sgc.gov.co/paginas1/catalogo/index.php$

- Syracuse, E.M., Maceira, M., Prieto, G.A., Zhang, H. & Ammon, C.J. (2016) Multiple plates subducting beneath Colombia, as illuminated by seismicity and velocity from the joint inversion of seismic and gravity data. Earth and Planetary Science Letters, 444, 139–149. doi:10.1016/j.epsl.2016.03.050

- Soulas, J.P., Egüez, A., Yepes, H. & Perez, H. (1991) Tectónica activa y riesgo sismico en los Andes ecuatorianos y el extremo sur de Colombia. Bol. Geol. Ecuat., 2, 3–11.

- Stein, S. & Gordon, R.G. (1984) Statistical tests of additional plate boundaries from plate motion inversions. Earth and Planetary Science Letters, 69, 401–412. doi:10.1016/0012-821X(84)90198-5

- Suárez, G., Molnar, P. & Burchfiel, B.C. (1983) Seismicity, fault plane solutions, depth of faulting, and active tectonics of the Andes of Peru, Ecuador, and southern Colombia. Journal of Geophysical Research: Solid Earth, 88, 10403–10428, John Wiley & Sons, Ltd. doi:10.1029/JB088iB12p10403

- Suter, F., Sartori, M., Neuwerth, R. & Gorin, G. (2008) Structural imprints at the front of the Chocó-Panamá indenter: Field data from the North Cauca Valley Basin, Central Colombia. Tectonophysics, 460, 134–157. doi:https://doi.org/10.1016/j.tecto.2008.07.015

- Symithe, S., Calais, E., Chabalier, J.B. de, Robertson, R. & Higgins, M. (2015) Current block motions and strain accumulation on active faults in the Caribbean. Journal of Geophysical Research: Solid Earth, 120, 3748–3774. doi:10.1002/2014JB011779

- Taboada, A., Rivera, L.A., Fuenzalida, A., Cisternas, A., Philip, H., Bijwaard, H., Olaya, J., et al. (2000) Geodynamics of the northern Andes: Subductions and intracontinental deformation (Colombia). Tectonics, 19, 787–813. doi:10.1029/2000TC900004

- Tibaldi, A., Rovida, A. & Corazzato, C. (2007) Late Quaternary kinematics, slip-rate and segmentation of a major Cordillera-parallel transcurrent fault: The Cayambe-Afiladores-Sibundoy system, NW South America. Journal of Structural Geology, 29, 664–680. doi:$https://doi.org/10.1016/j.jsg.2006.11.008$

- Toto, E.A. & Kellogg, J.N. (1992) Structure of the Sinu-San Jacinto fold belt — an active accretionary prism in northern Colombia. Journal of South American Earth Sciences, 5, 211–222. doi:10.1016/0895-9811(92)90039-2

- Trenkamp, R., Kellogg, J.N., Freymueller, J.T. & Mora, H.P. (2002) Wide plate margin deformation, southern Central America and northwestern South America, CASA GPS observations. Journal of South American Earth Sciences, 15, 157–171. doi:$https://doi.org/10.1016/S0895-9811(02)00018-4$

- UNAVCO Community. (2008) COCONet GPS Network: Station CN00 and 45 Others, UNAVCO, Inc. doi:10.7283/T5WM1BRG

- Vaca, S., Vallée, M., Nocquet, J.-M. & Alvarado, A. (2019) Active deformation in Ecuador enlightened by a new waveform-based catalog of earthquake focal mechanisms. Journal of South American Earth Sciences, 93, 449–461. doi:https://doi.org/10.1016/j.jsames.2019.05.017

- Vaca, S., Vallée, M., Nocquet, J.-M., Battaglia, J. & Régnier, M. (2018) Recurrent slow slip events as a barrier to the northward rupture propagation of the 2016 Pedernales earthquake (Central Ecuador). Tectonophysics, 724–725, 80–92. doi:10.1016/j.tecto.2017.12.012

- Valladares, C.E. & Chau, J.L. (2012) The Low-Latitude Ionosphere Sensor Network: Initial results. Radio Science, 47, John Wiley & Sons, Ltd. doi:10.1029/2011RS004978

- Vallée, M., Nocquet, J.-M., Battaglia, J., Font, Y., Segovia, M., Régnier, M., Mothes, P., et al. (2013) Intense interface seismicity triggered by a shallow slow slip event in the Central Ecuador subduction zone. Journal of Geophysical Research: Solid Earth, 118, 2965–2981, John Wiley & Sons, Ltd. doi:10.1002/jgrb.50216

- Vargas, C.A. (2019) Subduction Geometries in Northwestern South America (No. 58), p. 58, Bogotá: Servicio Geológico Colombiano. doi:10.32685/pub.esp.38.2019.11

- Velandia, F., Acosta, J., Terraza, R. & Villegas, H. (2005) The current tectonic motion of the Northern Andes along the Algeciras Fault System in SW Colombia. Tectonophysics, 399, 313–329. doi:10.1016/j.tecto.2004.12.028

- Veloza, G., Taylor, M., Mora, A. & Gosse, J. (2015) Active mountain building along the eastern Colombian Subandes: A folding history from deformed terraces across the Tame anticline, Llanos Basin. GSA Bulletin, 127, 1155–1173. doi:10.1130/B31168.1

- Villegas-Lanza, J.C., Chlieh, M., Cavalié, O., Tavera, H., Baby, P., Chire-Chira, J. & Nocquet, J.-M. (2016) Active tectonics of Peru: Heterogeneous interseismic coupling along the Nazca megathrust, rigid motion of the Peruvian Sliver, and Subandean shortening accommodation. Journal of Geophysical Research: Solid Earth, 121, 7371–7394. doi:10.1002/2016JB013080

- Villegas-Lanza, J.C., Nocquet, J.-M., Rolandone, F., Vallée, M., Tavera, H., Bondoux, F., Tran, T., et al. (2016) A mixed seismic–aseismic stress release episode in the Andean subduction zone. Nature Geoscience, 9, 150–154. doi:10.1038/ngeo2620

- Wang, K., Hu, Y., Bevis, M., Kendrick, E., Smalley Jr., R., Vargas, R.B. & Lauría, E. (2007) Crustal motion in the zone of the 1960 Chile earthquake: Detangling earthquake-cycle deformation and forearc-sliver translation. Geochemistry, Geophysics, Geosystems, 8. doi:10.1029/2007GC001721

- Wells, D.L. & Coppersmith, K.J. (1994) New empirical relationships among magnitude, rupture length, rupture width, rupture area, and surface displacement. Bulletin of the Seismological Society of America, 84, 974–1002.

- Weiss, J.R., Brooks, B.A., Foster, J.H., Bevis, M., Echalar, A., Caccamise, D., Heck, J., et al. (2016) Isolating active orogenic wedge deformation in the southern Subandes of Bolivia. Journal of Geophysical Research: Solid Earth, 121, 6192–6218, John Wiley & Sons, Ltd. doi:10.1002/2016JB013145

- Williams, S.D.P. (2008) CATS: GPS coordinate time series analysis software. GPS Solutions, 12, 147–153. doi:10.1007/s10291-007-0086-4

- Winter, T., Avouac, J.-P. & Lavenu, A. (1993) Late Quaternary kinematics of the Pallatanga strike-slip fault (Central Ecuador) from topographic measurements of displaced morphological features. Geophysical Journal International, 115, 905–920. doi:10.1111/j.1365-246X.1993.tb01500.x

- Witt, C., Bourgois, J., Michaud, F., Ordoñez, M., Jiménez, N., & Sosson, M. (2006). Development of the Gulf of Guayaquil (Ecuador) during the Quaternary as an effect of the North Andean block tectonic escape. Tectonics, 25(3). https://doi.org/10.1029/2004TC001723

- Yepes, H., Audin, L., Alvarado, A., Beauval, C., Aguilar, J., Font, Y. & Cotton, F. (2016) A new view for the geodynamics of Ecuador: Implication in seismogenic source definition and seismic hazard assessment. Tectonics, 35, 1249–1279, John Wiley & Sons, Ltd. doi:10.1002/2015TC003941

4.14 SUPPORTING INFORMATION

Supporting Information for Block motions and active faulting define a new Kinematic model for the North Andean Sliver constrained by GPS measurements

This file includes:

- Figure 4.13-4.16
- Table 4.4-4.5

4.14.1 Data Set

We present the interseismic velocity field for the North Andean Sliver and neighboring regions used in the kinematic model from the main article.

Table 4.4 – Velocity field with respect to South American plate. Longitude and Latitude in decimal degrees. Ve and Vn are east and north components of velocity in mm/yr. SVe, SVn are the associated uncertainties of Ve and Vn to 95% confidence level (mm/yr).

Site	Lon.	Lat.	Ve	Vn	SVe	SVn
01AQ	-78.4980	-0.1470	11.56	1.20	0.30	0.27
05PC	-75.8640	0.1170	1.38	-1.24	0.20	0.18
06LR	-77.3106	-0.6885	1.90	-1.20	0.40	0.30
3009	-79.6265	0.9890	19.11	5.44	0.40	0.30
ABMF	-61.5275	16.2623	16.00	3.43	0.18	0.12
ABPD	-74.0990	4.4770	4.42	3.84	0.15	0.07
ACP1	-79.9500	9.3700	21.85	1.72	0.14	0.10
ACP6	-79.4100	9.2400	22.33	1.84	0.11	0.12
AGCA	-73.5950	8.3150	12.18	2.52	0.10	0.28
AGIP	-77.8520	-0.6220	4.61	-0.70	0.60	1.00
AHUA	-77.5500	-1.0610	3.00	-1.04	0.70	0.40
ALBE	-73.3890	7.7610	10.08	3.96	0.18	0.12
ALPA	-72.9200	11.5300	15.61	3.91	0.31	0.40
ALTB	-78.5450	0.9130	14.20	2.38	0.25	0.16
AM01	-77.8730	-6.2350	2.14	-1.50	0.20	0.27
AMAL	-79.4270	-4.5810	3.10	-2.79	0.33	0.24
AMUA	-70.1880	11.7530	14.82	1.24	0.63	0.53
ANCH	-76.8700	3.5350	8.13	3.47	0.12	0.15
ANCO	-80.8947	-2.3296	9.03	3.87	0.94	0.50
APTO	-76.6320	7.8780	19.93	1.71	0.14	0.15
APU1	-79.7240	-6.2630	4.18	-1.65	0.61	0.39
ARCA	-70.7590	7.0840	0.19	-0.03	0.17	0.07
ARJF	-78.8330	-33.6290	70.00	6.40	0.48	0.57
ARSH	-79.0980	0.0960	12.96	1.72	0.22	0.32
ASC1	-14.4121	-7.9512	-0.21	-0.02	0.40	0.20
AU14	-76.8870	-0.7300	2.33	-0.79	0.53	0.43
AUCA	-76.8800	-0.6400	1.98	-0.70	0.11	0.11
AYAX	-80.7570	-1.9890	11.18	2.97	0.50	0.60
BACO	-75.6900	9.4000	18.40	-2.90	0.90	1.00
BAEZ	-77.8900	-0.4600	5.70	-0.40	0.30	0.20

Site	Lon.	Lat.	Ve	Vn	SVe	SVn
BAHI	-80.3980	-0.6590	16.34	3.90	0.31	0.22
BALZ	-79.9090	-1.3670	9.80	2.52	1.37	0.93
BAME	-74.5700	4.2400	6.24	3.25	0.70	0.21
BAPA	-74.6600	5.4700	7.39	3.66	0.31	0.21
BARB	-59.6091	13.0879	17.61	2.71	3.81	0.40
BARI	-70.3810	8.6570	0.01	0.56	0.44	0.36
BARU	-75.5900	10.2600	16.79	-0.82	0.58	0.32
BASO	-77.3900	6.2000	11.63	4.92	0.90	0.41
BAYO	-81.0660	-5.7990	3.56	-2.32	0.35	0.33
BEJA	-73.8760	7.0610	9.36	4.87	0.51	0.20
BERR	-74.4100	6.4930	9.95	3.90	0.58	0.34
BOAV	-60.6950	2.8340	0.20	-0.99	0.20	0.18
BOBG	-73.3600	8.3100	11.79	4.00	0.51	0.31
BOGT	-74.0800	4.6400	4.64	3.80	0.13	0.17
BOSC	-73.8860	9.9670	12.85	4.83	0.09	0.09
BQLA	-74.8500	11.0200	14.14	4.11	0.58	0.10
BRAZ	-47.8780	-15.9480	0.05	-0.15	0.11	0.07
BUEN	-77.0100	3.8820	10.18	3.50	0.10	0.09
BUGT	-76.9900	3.8300	9.72	4.24	0.17	0.17
CABP	-80.4290	-0.3860	21.20	7.28	0.28	0.22
CAJA	-79.2370	-2.7530	4.04	-2.19	0.38	0.31
CALI	-76.5330	3.3760	8.06	3.50	0.19	0.14
CANO	-67.4820	6.1850	-1.02	-0.08	0.28	0.13
CAPI	-72.4300	5.3500	1.53	0.24	0.27	0.21
CART	-75.5040	10.3640	17.52	0.57	0.46	0.32
CAS2	-66.9600	9.9260	0.67	0.31	0.54	0.56
CASI	-75.2000	7.9890	14.00	3.30	0.20	0.42
CASX	-78.4800	-0.0370	11.08	1.13	0.97	0.89
CBLA	-79.3050	-6.6250	3.69	-2.55	0.30	0.24
CCAN	-76.3000	3.3600	7.60	3.70	0.41	0.17
CCHO	-80.9620	-5.1660	2.88	-2.59	0.23	0.17
CCNE	-78.3120	0.3200	12.20	1.97	0.40	0.25
CHEP	-79.1040	9.1710	22.84	2.39	0.60	0.58
CHOR	-80.0730	0.0440	19.57	5.09	0.40	0.30
CHPG	-45.0020	-22.6820	0.17	-0.17	0.29	0.15
CHPI	-44.9850	-22.6870	-0.02	-0.17	0.11	0.10
CHUL	-80.1580	-5.0920	3.24	-2.86	0.17	0.14
CHUR	-69.5410	10.8180	14.44	2.39	0.72	0.54
CHZO	-78.7760	-1.4670	8.90	0.30	0.40	0.30
CIA1	-76.3600	3.5100	7.57	3.60	1.30	0.60
CN19	-70.0500	12.6100	17.70	1.98	0.20	0.10
CN20	-82.2560	9.3510	21.45	0.45	0.13	0.22
CN28	-79.0300	8.6300	23.29	3.65	0.16	0.17
CN33	-80.3300	8.4900	23.59	0.24	0.45	0.80
CN35	-81.3629	13.3755	15.78	-2.78	0.11	0.28
CN37	-75.2600	10.7900	13.89	3.54	0.81	1.12
CN38	-71.9900	12.2200	16.36	2.46	0.31	0.11
CN39	-70.5240	10.2060	11.58	1.36	0.34	0.28
CN40	-68.9600	12.1800	17.36	1.58	0.11	0.10
CN41	-68.0410	8.9430	0.30	0.31	0.20	0.12
CN45	-60.9383	10.8371	17.64	1.00	0.25	0.23
CN46	-61.4270	12.4868	17.99	2.33	0.51	0.21
CN47	-60.9405	13.7108	18.25	3.90	0.46	0.12
CN49	-63.6183	15.6672	16.27	2.23	0.45	0.47

Site	Lon.	Lat.	Ve	Vn	SVe	SVn
CNJO	-76.8450	0.2380	1.57	-0.25	0.54	0.43
COCH	-79.2570	-2.4660	6.52	0.10	0.27	0.26
COEC	-77.7900	0.7200	10.13	2.24	0.60	0.29
COLI	-80.0120	-1.5480	12.72	2.63	0.21	0.35
CORA	-79.0790	-1.1380	10.22	1.94	0.50	0.40
CORO	-75.2900	9.3300	16.00	1.51	0.16	0.10
CRCS	-66.9130	10.5030	4.43	0.20	0.34	0.42
CRUZ	-72.6721	-7.6112	0.47	-0.01	0.20	0.20
CSEC	-80.7280	-1.0530	17.94	4.98	0.66	0.40
CUCU	-72.4880	7.8980	8.73	3.63	0.08	0.06
CUEC	-79.0020	-2.8830	3.69	-2.34	0.17	0.15
CULA	-78.6960	0.1440	13.78	2.50	0.70	0.52
CUM3	-64.1950	10.4290	4.17	2.40	0.46	0.57
CUYC	-78.8550	-6.0120	3.98	-2.39	0.38	0.24
DAR2	-78.1540	8.6580	25.08	4.15	0.86	0.45
DESV	-79.9240	-1.0400	10.74	1.99	0.50	0.40
DOMI	-61.3891	15.3062	17.97	3.47	0.44	0.32
ECEC	-79.4520	-0.2720	15.07	1.67	0.39	0.34
ELCH	-77.8060	-0.3340	3.80	-1.50	0.80	0.40
ESMR	-79.7200	0.9300	21.80	5.57	0.20	0.12
ETEN	-79.8580	-6.9470	5.04	-3.06	0.12	0.10
FLFR	-79.8430	-0.3570	15.65	1.76	0.67	0.54
FLOR	-75.6050	1.6200	1.60	-2.00	0.27	0.10
FQNE	-73.7350	5.4670	6.70	3.30	0.35	0.15
GALA	-90.3040	-0.7420	55.20	1.50	0.53	0.45
GGPA	-78.5937	-0.1804	12.75	1.24	0.90	0.70
GLPS	-90.3030	-0.7430	54.40	2.30	0.40	0.31
GMTE	-78.7080	-1.9350	6.40	-2.70	0.33	0.21
GONZ	-79.4310	-4.2260	3.22	-3.24	0.33	0.24
GOYA	-69.7080	10.9950	14.16	2.20	0.72	0.54
GPH1	-79.9110	-2.7370	6.88	0.04	0.19	0.15
GRE0	-61.6405	12.2218	18.43	3.13	0.22	0.16
GUAP	-77.8900	2.5700	12.90	2.50	0.20	0.14
GYEC	-79.8920	-2.1490	8.30	2.50	0.40	0.80
GZEC	-78.5810	-3.4010	4.00	-2.65	0.34	0.22
HENO	-76.6490	-0.1320	1.15	-0.17	0.53	0.40
HONA	-79.1600	-3.4770	3.66	-1.86	0.32	0.22
HSPR	-78.8500	-0.3520	11.89	1.31	0.31	0.21
IBAG	-75.2150	4.4280	6.28	3.96	0.18	0.15
IGMV	-78.4940	-0.2150	11.28	1.47	0.60	0.50
IGN1	-79.5360	8.9850	23.30	2.30	0.31	0.32
IGNA	-78.7520	-0.4510	10.23	1.25	0.60	0.32
ILHE	-39.1720	-14.7970	0.77	-0.70	0.40	0.31
ILSG	-105.3618	-26.4729	64.00	-9.50	0.51	0.41
INR1	-75.8970	4.9090	8.13	3.23	0.40	0.33
IQTS	-73.2750	-3.7670	0.09	-0.12	0.25	0.10
IQUI	-73.2687	-3.7673	-0.03	-0.12	0.27	0.30
ISCO	-87.0558	5.5443	54.34	64.25	0.42	0.38
ISPA	-109.3444	-27.1249	64.80	-11.30	0.28	0.38
ISPT	-81.0740	-1.2620	35.35	4.08	0.29	0.28
JAM1	-80.2650	-0.2020	21.08	5.82	0.24	0.40
KOU1	-52.8060	5.2520	-0.16	0.47	0.27	0.48
KOUR	-52.8060	5.2520	-0.29	0.48	0.15	0.12
LCOL	-79.2040	-0.2500	11.87	1.59	0.32	0.30
LETA	-69.9430	-4.2140	-0.99	0.22	0.24	0.12
LGCB	-79.5750	0.3820	17.50	2.60	0.67	0.31

Site	Lon.	Lat.	Ve	Vn	SVe	SVn
LIMO	-76.6205	-0.4033	1.17	0.09	0.40	0.40
LITA	-78.2190	0.7260	12.70	2.95	0.28	0.26
LITS	-78.4480	0.8700	12.90	1.81	0.40	0.30
LJEC	-79.1990	-3.9880	2.81	-2.03	0.83	0.10
LMAS	-76.4990	-6.4380	3.56	0.20	0.39	0.48
LMMF	-60.9962	14.5948	17.83	3.53	0.08	0.07
LPIU	-80.6390	-5.1700	4.12	-2.93	0.35	0.32
LUMB	-77.3280	0.1370	3.76	-0.23	0.37	0.23
LUMD	-77.3220	0.0080	3.04	0.02	0.72	0.72
MA00	-71.6240	10.6740	13.67	2.13	0.26	0.19
MACH	-79.9680	-3.2560	4.01	-0.91	0.32	0.21
MAEC	-78.1180	-2.3050	3.88	-2.28	0.17	0.11
MALO	-81.6061	4.0032	53.10	4.60	0.39	0.40
MANT	-80.6710	-0.9370	15.66	6.86	0.40	0.40
MD01	-69.1780	-12.5942	1.14	0.32	0.41	0.26
MECE	-73.7100	7.1100	9.60	4.18	0.17	0.31
MEDE	-75.5790	6.1990	8.85	4.83	0.10	0.07
MEND	-78.3200	-2.7170	3.77	-2.49	0.17	0.12
MERC	-79.5079	-0.1876	12.72	1.34	0.40	0.31
MIGU	-79.0390	-1.7030	8.30	1.00	1.17	0.21
MINA	-80.2790	-0.9630	11.50	4.00	1.02	1.00
MIRA	-78.5090	-0.2700	9.80	-0.09	0.60	0.52
MITU	-70.2300	1.2600	-0.45	0.02	0.41	0.32
MOCA	-79.5090	-1.1870	8.86	0.91	0.44	0.30
MOMP	-80.0470	0.4920	20.10	5.00	0.47	0.44
MONT	-76.9810	-2.0670	0.93	-0.98	0.31	0.27
MORA	-80.0220	-5.5440	3.52	-2.62	0.21	0.16
MOYB	-77.0020	-6.0680	2.20	0.01	0.40	0.93
MRO2	-80.3410	-2.6450	8.50	2.49	0.41	0.88
MSL1	-80.8990	-1.0730	21.20	5.30	0.70	0.40
MUIS	-80.0240	0.6050	20.14	4.49	0.30	0.20
MZAL	-75.4700	5.0300	6.33	7.06	0.31	0.70
NARI	-79.5360	-3.1410	3.04	-2.40	0.31	0.23
NAUS	-60.0550	-3.0230	-0.90	-0.89	1.25	1.04
NEIA	-47.9250	-25.0200	0.24	0.06	0.15	0.13
NEVA	-75.2930	2.9370	4.99	3.43	0.44	0.26
NORE	-75.4010	-0.9190	1.44	-1.36	0.10	0.23
OCEL	-71.6200	4.2700	-0.40	0.28	0.31	0.22
OLIM	-80.1285	-0.7112	16.00	0.94	0.73	0.54
OREC	-79.8960	-3.3010	4.46	-0.96	0.34	0.30
PAL1	-73.1900	7.1400	8.45	3.57	0.41	0.41
PAMP	-72.6480	7.3840	7.70	3.63	0.25	0.23
PARA	-49.2310	-25.4480	0.06	0.09	0.22	0.27
PARI	-56.7560	-2.6400	1.13	0.26	1.34	1.07
PASI	-76.5000	0.5100	1.15	-0.45	0.25	0.10
PBLR	-79.1600	0.5820	15.17	2.68	0.20	0.20
PDEC	-79.1310	-4.6480	3.15	-2.24	0.30	0.36
PDNS	-79.9910	0.1110	19.59	4.24	0.20	0.16
PI01	-80.6280	-5.1800	4.52	-2.93	0.35	0.43
PI03	-81.2690	-4.5870	2.97	-1.58	0.45	0.34
PJEC	-80.4250	-1.5520	11.46	2.30	0.38	0.38
PLHA	-78.5020	0.0220	12.77	2.00	0.26	0.18
PLOB	-81.2890	-4.4530	4.21	-1.99	0.23	0.18
POPA	-76.6100	2.4500	8.54	3.30	0.15	0.10
POSO	-80.2430	-2.7100	7.54	1.32	0.22	0.17
POVA	-76.6140	2.4490	8.53	3.00	0.16	0.11

Site	Lon.	Lat.	Ve	Vn	SVe	SVn
POVE	-63.8963	-8.7093	-0.08	0.20	0.11	0.06
PPRT	-80.2160	-0.1250	20.04	5.39	0.32	0.30
PREC	-77.9630	-1.7080	2.10	-2.20	0.52	0.20
PROG	-80.3650	-2.4110	8.90	2.48	0.41	0.30
PTEC	-80.4750	-1.0580	14.64	4.11	0.30	0.43
PTGL	-80.0300	0.7820	23.57	4.97	0.61	0.25
PTPO	-79.6280	-6.7400	4.63	-3.10	0.20	0.15
PUEB	-79.5310	-1.5590	9.80	1.80	1.20	0.76
PUIN	-67.9000	3.8500	-0.12	-0.50	0.19	0.23
PUYO	-78.0250	-1.4920	3.56	-1.06	0.27	0.20
QLTA	-78.9180	-0.8710	11.38	2.58	0.63	0.22
QNDE	-79.4755	0.3275	15.41	1.60	0.36	0.38
QUEM	-78.4970	-0.2370	12.19	1.46	0.28	0.24
QUIB	-76.6470	5.6950	8.17	5.13	0.10	0.10
QUIL	-77.2900	1.3900	8.80	3.00	0.45	0.23
QVEC	-79.4700	-1.0120	11.40	2.00	0.45	0.29
RECF	-34.9510	-8.0510	-0.18	0.14	0.44	0.46
RIOP	-78.6500	-1.6500	6.10	-1.70	0.18	0.14
RVRD	-79.3850	1.0680	19.50	3.10	0.30	0.30
SABA	-80.2230	-1.8410	11.84	2.10	0.50	0.40
SABU	-74.1870	11.2250	14.70	4.53	0.20	0.21
SALU	-44.2120	-2.5940	-0.07	0.18	0.35	0.18
SAN0	-81.7157	12.5805	17.98	-3.24	0.26	0.17
SAVO	-38.4320	-12.9390	0.05	0.14	0.10	0.11
SBEN	-77.8730	-0.5750	4.20	-2.71	0.70	1.10
SCEC	-89.6149	-0.9020	54.90	1.30	0.32	0.42
SCH1	-80.4910	-6.1120	5.39	-2.33	0.28	0.25
SCH2	-80.5750	-5.6350	4.17	-1.88	0.20	0.17
SEEC	-80.9040	-2.2200	13.90	2.60	1.00	0.42
SEL1	-75.5300	6.1900	8.89	4.07	0.31	0.21
SEVG	-80.0340	-0.9740	13.06	2.23	0.25	0.23
SIEC	-79.3150	-3.2750	3.06	-1.63	0.23	0.13
SINC	-75.3880	9.3160	16.00	1.90	0.64	0.29
SLGO	-80.8490	-1.6000	17.43	1.21	0.91	0.43
SNLR	-78.8500	1.2900	15.57	0.26	0.17	0.15
SNSN	-75.3080	5.7150	8.26	4.57	0.28	0.22
SOZO	-79.7920	-4.3340	3.00	-2.83	0.64	0.34
SRAM	-79.5607	-0.6100	10.37	2.21	0.80	0.80
SRNW	-56.9920	5.9450	0.13	-0.27	0.23	0.22
SROQ	-76.2240	-0.4540	0.44	-0.72	0.33	0.23
STAA	-80.3870	-1.1830	12.69	3.83	0.40	0.30
STOD	-70.6300	8.8600	2.03	1.27	0.44	0.35
SUNW	-81.0550	-4.6930	3.89	-2.26	0.18	0.15
SVGB	-61.2503	13.2746	17.11	2.04	0.29	0.08
TEFE	-64.7210	-3.3490	-0.18	-0.10	0.11	0.23
TEN1	-77.8160	-0.9900	3.00	-1.72	0.28	0.20
TICU	-69.9400	-4.1900	-0.57	-0.71	0.32	0.32
TOLA	-79.0450	1.2100	17.92	0.23	0.36	0.28
TONE	-76.1400	6.3200	9.12	4.75	0.51	0.21
TORR	-79.1320	-2.0860	6.94	0.35	0.40	0.30
TOTO	-78.6730	-2.2570	4.60	-2.90	0.11	0.09
TU01	-80.4520	-3.5570	5.70	-1.19	0.38	0.47
TUCO	-78.7500	1.8100	17.90	2.30	0.23	0.20
TUNA	-73.3640	5.5310	5.94	2.34	0.15	0.18
UC01	-74.5310	-8.3840	1.19	0.23	0.60	0.41
UEPP	-51.4090	-22.1200	0.21	0.33	0.09	0.10

Site	Lon.	Lat.	Ve	Vn	SVe	SVn
UFPR	-49.2310	-25.4484	-0.19	0.26	0.22	0.22
URRA	-76.2100	8.0100	17.73	3.26	0.80	0.70
USB0	-66.7920	10.4090	3.79	0.30	0.53	0.56
USB1	-66.8830	10.4110	3.49	0.41	0.53	0.56
UWAS	-72.3900	6.4500	4.95	1.78	0.31	0.31
VALL	-73.2520	10.4740	12.98	4.15	0.41	0.23
VBUV	-73.8600	5.5300	8.48	4.56	0.51	0.31
VDPR	-73.2500	10.4400	13.68	3.98	0.19	0.19
VIVI	-73.5840	4.0750	0.13	-0.51	1.14	0.67
VMAG	-74.8500	9.2900	13.96	3.47	0.33	0.22
VORA	-76.7200	7.8200	19.98	0.70	0.90	0.84
VOTU	-74.7100	7.0200	10.97	4.17	0.31	0.41
VPIJ	-75.1100	4.4000	6.26	3.52	0.41	0.21
VPOL	-74.8600	10.7900	14.32	4.53	0.33	0.10
VROS	-74.3200	4.8500	4.81	3.52	0.51	0.31
VSJG	-72.6400	2.5300	-0.49	-0.39	0.61	0.31
VSJP	-75.8400	4.7800	5.72	4.41	0.41	0.31
VZCY	-78.4120	-1.3640	5.81	-0.44	0.43	0.35
YRMG	-76.1300	-5.8970	1.60	0.65	0.38	0.40
ZAMO	-78.9320	-4.0550	3.30	-2.09	0.12	0.10
ZARZ	-76.0680	4.3970	7.40	4.34	0.29	0.14
ZHUD	-79.0060	-2.4610	4.86	-1.85	0.15	0.11

4.14.2 Fault Geometry

Fault parameters are defined from neotectonics studies, patterns of seismicity distribution, and velocity gradients derived from the horizontal velocity field. Here, we present locking depths, dip values, and the interseismic coupling factor for the fault segments in the continental side constrained by our best model. As fault segments are rectangular fault planes with constant dips stuck to a given depth in the downdip direction, there could be possible discrepancies in the dip value with respect to those proposed by geological studies. However, our estimates represent the average dip because continental faults are usually steeper on the surface than at depth.

For the case of the Cosanga and Uramita fault systems, we performed simple two-dimensional forward models using the back-slip approach in a homogeneous elastic half-space (Savage 1983, Segall 2010). We project horizontal velocities in the vicinity of Cosanga and Uramita fault systems across two profiles roughly perpendicular to the average strike of each fault (fig 4.13). Within the Interandean Depression in Central Ecuador, several studies found negligible elastic strain contributions from the Quito fault system over far-field site velocities (ANTN, ASEC, PAPA, PINT, SALF, and CUYU: figure 4.13A) located eastward one (Alvarado et al. 2014, Mariniere et al. 2019). However small elastic strain contributions from the locking at the subduction interface are expected, but they would not be higher than 1 mm/yr (Nocquet et al. 2016). On the other hand, far-field velocities on either side of the Cosanga fault (figure 4.13:A) indicate an east-west shortening of $\sim$6 mm/yr. We, therefore, modeled the Cosanga profile dipping west with pure reverse slip and found 51° of dip locked down 8 km as average values (figure 4.13:C). This dip value is consistent with the average dip (mainshock and aftershocks) from the 1987 Cosanga earthquake (Ekström et al. 2012) and the 2014 Mw 5.0 earthquake (Vaca et al. 2019). Furthermore,

despite having three geodetic velocities on the Uramita profile, their predictions occur at average dip values of 11° locked down 10 km (figure 4.13:D).

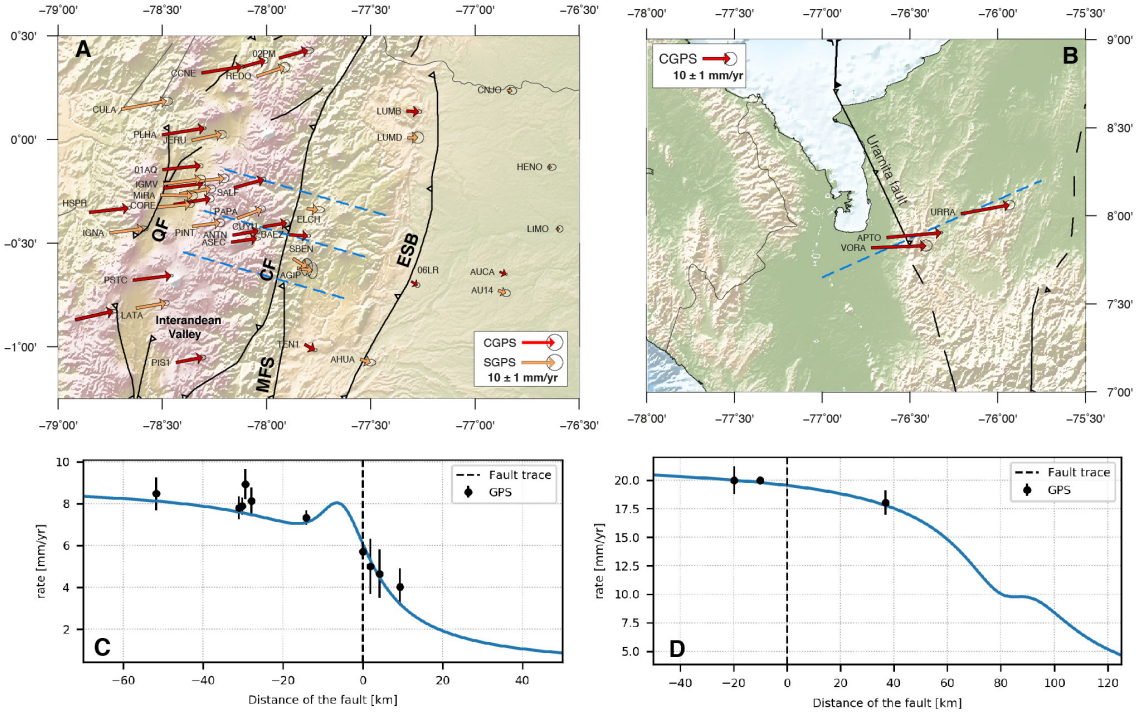

Figure 4.13 – Horizontal velocity field with respect to South America in the vicinity of: **A**) Quito (QF), Cosanga (CF), Eastern Suabandean belt (ESB), and Macas (MFS) faults. **B**) Uramita fault. Error ellipses show 95% confidence level. Blue solid lines are perpendicular profiles to the average strike of the Cosanga and Uramita faults. **C**) and **D**) are horizontal velocity predictions using 2-D synthetic elastic models at the Cosanga and Urramita faults respectively.

Analysis of geodetic and InSAR data suggest 30° of dip with locking depths at 10 km as average fault parameters for the Quito fault (Mariniere et al. 2019), and modeling of the Yanayacu flexure proposes dipping values of ∼60° for the Latacunga fault (Fiorini and Tibaldi 2012). Two Mw $\geq$ 5.3 earthquake focal mechanisms suggest faulting in vertical planes (dip ∼83°) with right-lateral motion along the Puna fault (Vaca et al. 2019). Tibaldi et al. (2007) and Velandia et al. (2005) found dominant transcurrent motion in nearly vertical fault planes on the Chingual and Algercidas-Sibundoy fault systems based on field observations of Holocene deposits and landforms. On the contrary, the Eastern Frontal Fault System (EEFF) exhibits west-dipping reverse motion at ∼30° with a right-lateral component extending from latitude 3°N to ∼7.5°N (Paris et al. 2000). Two Mw $\geq$ 5.4 focal mechanism solutions (1995 and 2015 earthquakes) show nodal planes with average dips ∼83° for the Boconó fault. Similarly, the September 2009 Mw 6.4 and July 1997 Mw 6.9 earthquakes show nodal planes with dips ∼83° for the San Sebastian and El Pilar faults (Ekström et al. 2012, Trabant et al. 2012). Therefore, these fault systems indicate a major right-lateral motion with faulting in vertical fault planes.

For the right-lateral OCA-Ancon fault system, Paris et al. (2000) and Audemard et al. (2000) suggest in general faulting in vertical and sub-vertical planes, which is confirmed by nodal planes derived from the 1999 Mw 5.4 and 5.7 focal mechanisms (dips of 83° and 90° respectively) (Ekström et al. 2012). Although low shallow seismic activity characterizes the Santa-Martha Bucaramanga fault, its neotectonics suggest faulting in subvertical planes in the Bucaramanga segment (Paris et al. 2000). Therefore, it is acceptable that this system has similar fault parameters to those defined for the OCA-Ancon fault because both systems outline the same tectonic block.

We adopt vertical fault planes for the south and central sections of the San Jacinto fold belt based on the 1977 Mw 6.5 focal mechanisms solution (dip 89°) Trabant et al. (2012), changing to 30°E for its northernmost section (value found by our best model). The Romeral fault sections between latitudes 5°N and 6°N has similar dip values to those defined by the southernmost extension of the San Jacinto fold belt, whereas the section between ∼4.2N° and 5°N is fixed to 80°E for our best model. The last one is compatible with the focal mechanism solution (dip ∼70°) from the 1999 Mw 6.1 Armenia earthquake (Ekström et al. 2012).

Table 4.5 – Parameters for Continental faults constrained by the best model described in the main article. N: number of fault section.

N	Fault Segment	Locking depth km	Dip deg.	Coupling Coefficient
1	Algercidas-Sibundoy	14	90	1.0
2	Boconó south	11	90	0.5
3	Boconó north	12	90	1.0
4	Chingual	14	90	1.0
5	Cosanga	8	51W	0.5
6	Easternn Frontal Fault System	15	30W	1.0
7	East Panama Deformed Zone	12	80E	1.0
8	Eastern Subandean Belt	3	35W	1.0
9	El Angel	10	80W	0.5
10	El Pilar	12	90	1.0
11	Latacunga	9	60W	1.0
12	Quito north	10	30W	0.5
13	Quito south	10	30W	0.5
14	Macas	7	35W	1.0
15	Oca-Ancon west	5	90	1.0
16	Oca-Ancon central	8	90	1.0
17	Oca-Ancon east	0.1	90	1.0
18	Pallatanga	15	90	1.0
19	Puna	15	90	1.0
20	Romeral section 1	10	90	1.0
21	Romeral section 2	10	80	1.0
22	San Jacinto Fold Belt north	4	30E	0.9
23	San Jacinto Fold Belt south-central	5	90	1.0
24	San Sebastian	12	90	1.0
25	Santa-Martha Bucaramanga west	5	90	1.0
26	Santa-Martha Bucaramanga central	8	90	1.0
27	Santa-martha Bucaramanga south	0.5	80	1.0
28	Uramita	10	11E	0.8

At a regional scale, fold and thrust belts are observed in subandean zones, attributed to dipping thrust ramps (Alvarado et al. 2016, Audemard et al. 2000, Bès de Berc et al. 2005). GPS data is sparse within these zones, but hypocentral solutions from the ISC reviewed catalog (Engdahl et al. 2020) and earthquake focal mechanism solutions from the Global Centroid Moment Tensor catalog Ekström et al. (2012) suggest average values of 35°±15W and 10±6 km as a dip and locking depths respectively. Finally, these values are constrained by our best model at 35° and 3 km for the Eastern Subandean Belt (ESB) and for the Macas fault at 35° and 7 km. The Eastern Panama Deformed Zone and the Angel faults are also constrained by the model in agreement with neighboring faults. Table 4.5 summarizes fault geometry parameters described above, whose spatial location is shown in figure 4.14.

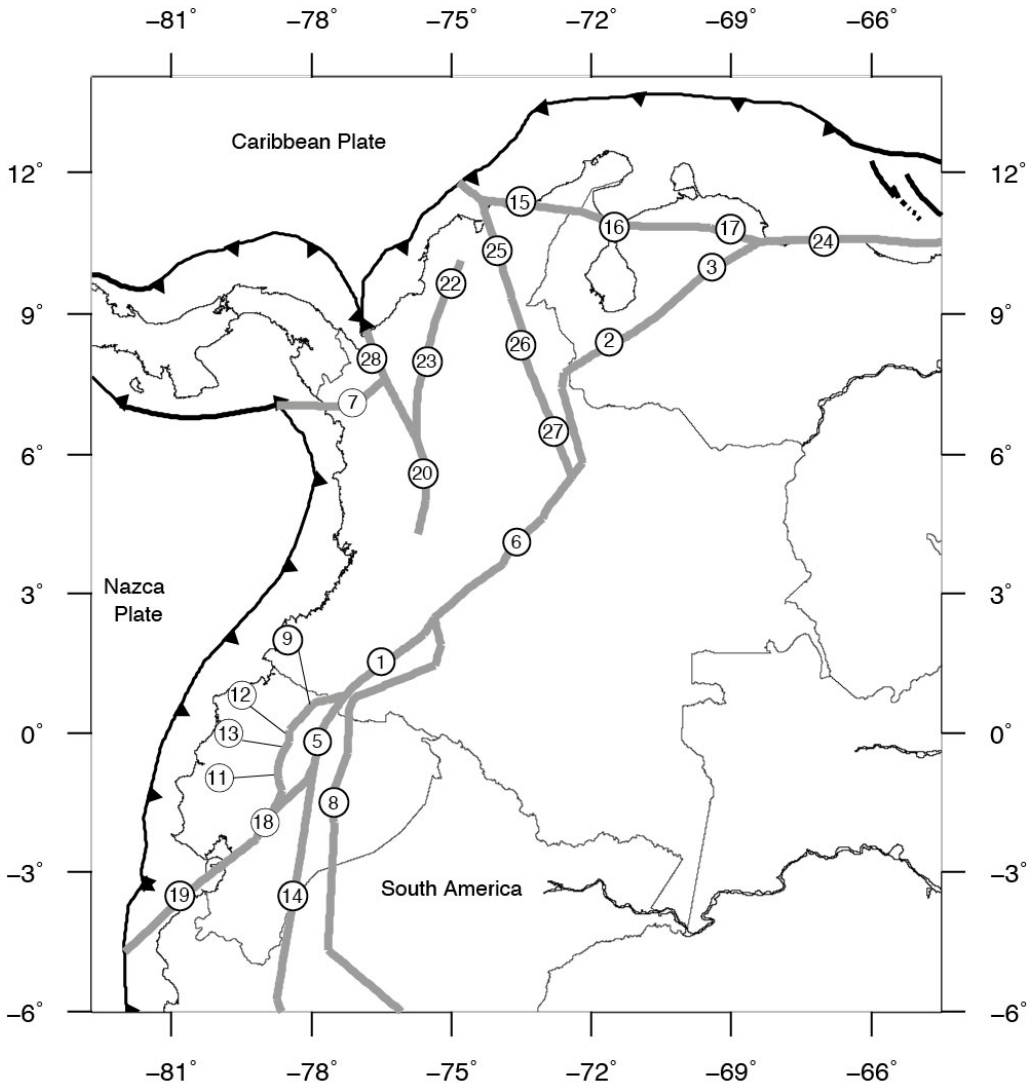

Figure 4.14 – Spatial location of fault parameters from table 2. The number inside the circle corresponds to the fault sections according to the first column of Table 4.5

4.14.3 Slip rates per component

Net slip rates at bounding blocks are estimated into strike slip (fault parallel) and dip slip (fault normal) components from the best fit model results. Figure 4.15 shows slip rates per component following the convention of hanging wall block with respect to footwall block. Therefore, Strike-slip rates with right-lateral motion are depicted as negative values (figure 4.15:A), while Dip slip rates (figure 4.15:B) on dipping faults or vertical faults (tensile) as positive values for compression.

Figure 4.15:C shows the fault motion predominance depicted by a color scale with RL-R: right-lateral reverse (compression), RL-N: right-lateral normal (opening), RL: right-lateral. Similar acronymous for left lateral (LL-R, LL-N, LL). Figure 4.15:D shows block rigid motion prediction at selected locations.

4.14.4 Velocity Residuals per model

Figure 4.16 shows the velocity residuals decrease according to the most relevant block model geometries discussed in the main article (from model A to D).

4.14.5 Variance Co-varinace Matrices

We provides variance co-variance values for Euler poles estimates from the best fit model described in the main article. The main elements of the matrix diagonal are W_{xx}, W_{yy}, W_{zz}. Table 4.6 summarizes values for reconstructing the full variance covariance (VCV) matrix per pole following:

$$VCV_{name} = \begin{bmatrix} W_{xx} & W_{xy} & W_{xz} \\ W_{xy} & W_{yy} & W_{yz} \\ W_{xz} & W_{yz} & W_{zz} \end{bmatrix}$$

Table 4.6 – Variance co-variance matrix of Euler Poles estimated from our best fit model (model D)

Block/Plate	Name	W_{xx}	W_{yy}	W_{zz}	W_{xy}	W_{yz}	W_{xz}
		x $10^{-21}(rad/yr)^2$					
Bonaire	BONA	3.5273	26.512	1.4214	-9.6514	-6.0744	2.2126
Subandean	EPSUB	0.51822	10.1120	0.12116	-2.2515	0.77532	-0.17089
Maracaibo	MARA	2.0501	20.9220	0.51761	-6.5382	-3.2411	1.0141
North Andean West	NAW	0.9355	15.639	0.10783	-3.7607	-0.98915	0.23731
Nazca	NAZCA	3.2408	33.59	3.5451	7.4627	3.7443	0.88266
Panama	PANA	0.25377	6.8059	0.18856	-1.2787	-1.0965	0.20281
Peruvian Forarc West	PFW	0.28998	6.4964	0.11462	-1.2854	0.59807	-0.1184
Romeral	ROME	0.51771	6.8003	0.11033	-1.8694	-0.81944	0.225
San Jacinto	SANJ	173.61	2528.4	73.01	-662.48	-429.29	112.48
Quito-Latacunga	UIOL	96.642	2268.8	0.29064	-467.97	11.378	-2.3038

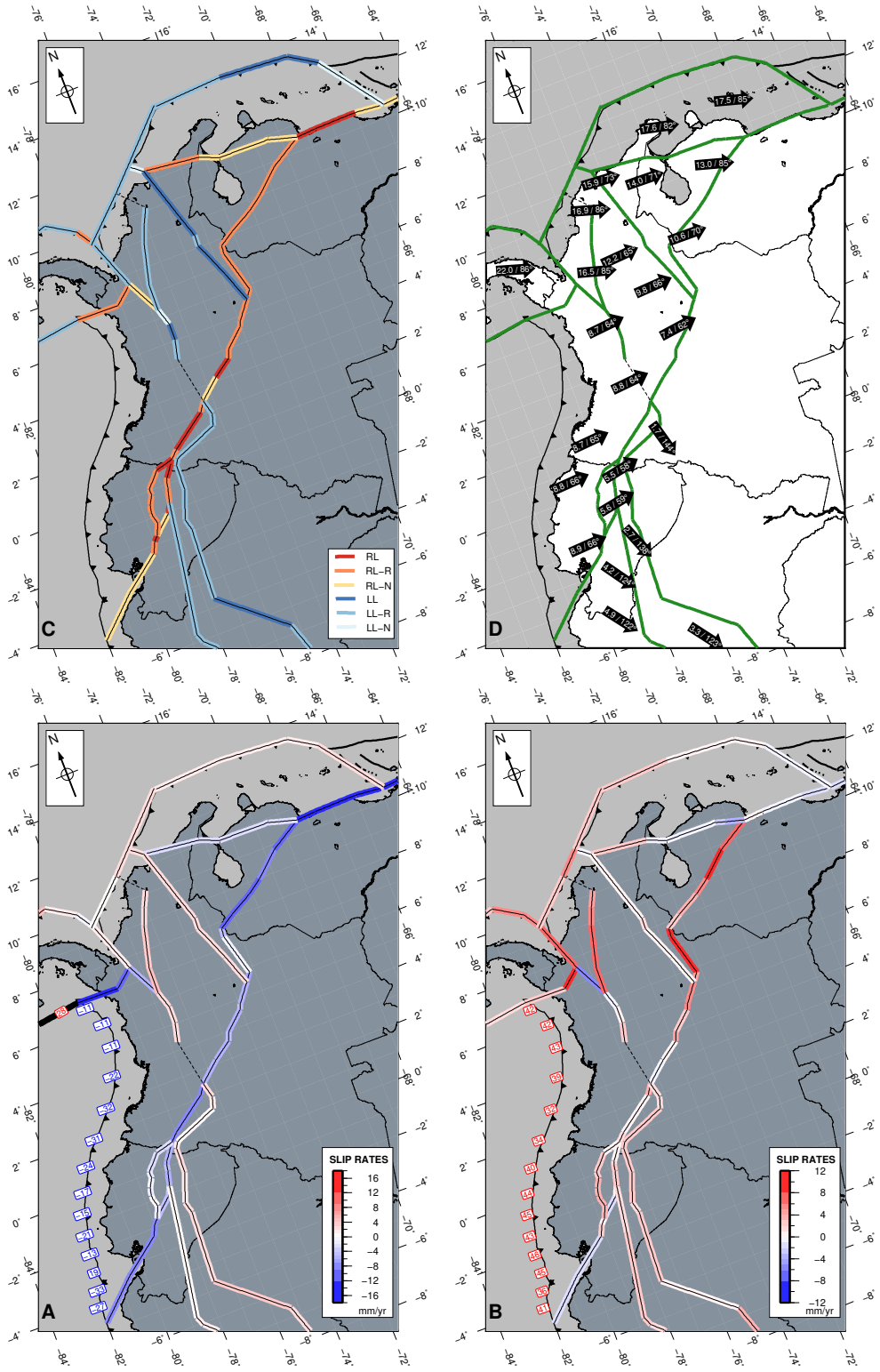

Figure 4.15 – Slip rates per component from the best fit model. A) Strike slip rates. B) Dip slip rates. C) fault motion predominance. D) Block rigid motion at selected locations

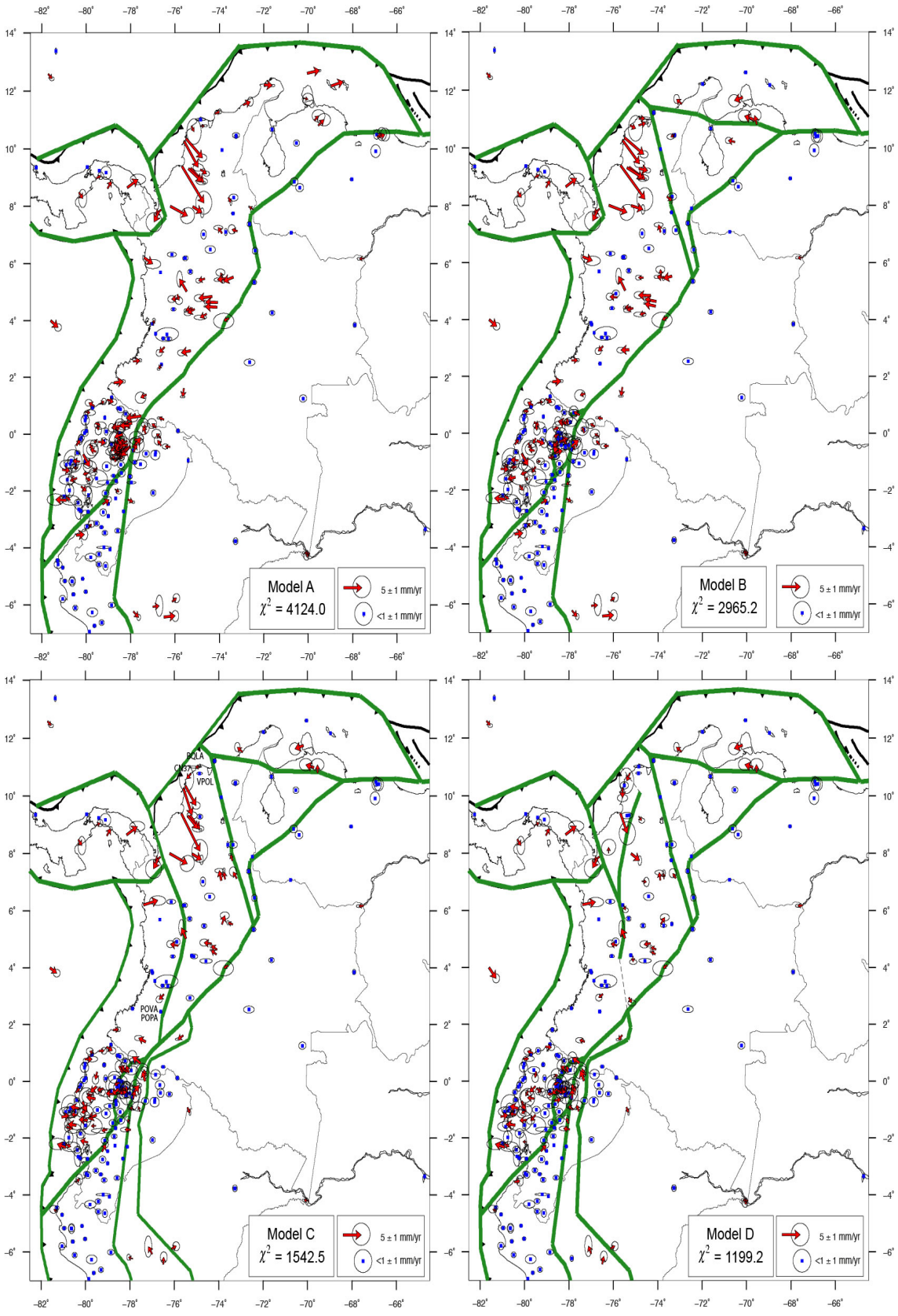

Figure 4.16 – Velocity residuals for the most relevant block geometries discussed in the main article

4.14.6 Earthquake Slip Vector

Here, we summarize focal mechanisms solutions used in the main article.

Table 4.7 – Focal mechanisms solution used for comparing earthquake slip vector and relative block motion at block boundaries in the main article. Longitud and Latitud in decimal degrees. Depth in kilometers.

Lon.	Lat.	Depth	Strike	Dip	Rake	Mw	Date
-78.480	-0.240	12.0	197	44	109	5.1	20140812
-78.416	-0.051	5.0	198	33	115	5.1	20140812
-79.280	-2.251	8.0	22	38	135	5.6	20140325
-80.990	-3.290	24.0	201	61	163	6.4	20050521
-79.800	-2.930	25.0	48	17	175	5.6	20171118
-77.980	-1.140	18.0	204	46	105	5.2	20091009
-78.190	-2.000	16.0	199	26	109	5.6	19840428
-78.960	-5.440	25.0	351	59	95	5.3	19850726
-78.100	-3.030	15.0	20	73	104	5.7	19951007
-77.530	-2.550	25.0	18	57	68	7.0	19951003
-77.790	-2.700	25.0	190	55	84	5.3	19901125
-77.500	-4.480	12.0	222	42	45	5.1	20200205
-76.750	-6.030	15.0	121	38	4	5.0	20121222
-77.730	0.310	15.0	226	81	-166	6.0	19870306
-77.840	-0.470	20.0	194	43	140	5.0	20141221
-78.320	-1.240	12.0	215	74	-180	5.0	20100326
-78.400	-1.100	12.0	193	50	135	5.2	20040328
-74.110	3.450	19.0	208	67	154	6.0	20191224
-74.630	3.370	30.0	213	51	131	5.6	20161031
-72.890	5.210	33.0	33	72	106	5.2	19950120
-75.490	5.480	3.0	159	79	-2	3.9	20140824
-75.870	4.110	0.0	151	68	-2	4.7	20150918
-76.140	6.890	30.0	92	13	154	5.3	19871111
-76.230	7.240	0.0	118	54	-165	6.2	20160914
-76.840	7.630	15.0	281	90	-180	5.2	19950319
-77.510	7.020	15.0	81	80	-171	4.9	20190524
-78.000	7.370	17.0	91	78	-179	5.4	19990104
-78.110	7.230	15.0	78	67	161	7.3	19760711
-75.970	7.400	15.0	101	17	-175	6.5	19770831
-76.520	7.100	15.0	98	79	-165	5.4	19810427
-76.340	7.270	15.0	270	45	167	7.1	19921018
-76.580	7.120	15.0	92	83	166	5.5	19810825
-76.580	7.080	15.0	273	82	-172	5.7	19860129
-68.420	10.960	15.0	51	85	-39	5.5	19890504
-70.210	10.830	15.0	92	78	-172	5.7	19990330
-72.340	7.710	15.0	226	28	147	5.3	19800502
-69.940	9.980	15.0	88	70	-167	5.7	19951229
-69.910	9.860	15.0	257	74	-175	5.4	19951231
-69.830	9.740	15.0	74	87	-176	5.5	19910817
-69.780	10.050	18.0	75	80	-155	5.3	19840614
-70.400	9.400	25.0	90	60	-156	5.4	20181227
-72.130	8.360	14.0	53	53	138	5.3	20150205
-70.270	10.070	25.0	85	74	179	5.2	20060804
-67.970	10.700	12.0	91	83	163	6.4	20090912
-68.020	10.270	23.0	77	74	-170	4.8	20180427

Lon.	Lat.	Depth	Strike	Dip	Rake	Mw	Date
-68.080	10.260	12.0	90	60	-156	5.4	20181227
-68.080	10.880	15.0	166	62	-168	5.9	19890430
-80.880	-2.100	16.0	353	16	88	6.3	19960805
-80.850	-1.230	12.0	3	18	96	6.0	20050121
-80.930	-1.250	19.0	14	15	111	5.1	20050122
-80.950	-1.530	16.0	6	15	100	6.1	20050124
-81.110	-1.610	26.0	335	20	69	5.1	20050124
-80.800	-0.870	12.0	1	19	92	5.5	20160418
-80.460	0.590	18.0	23	24	116	5.7	19790301
-79.920	0.810	16.0	27	25	120	6.3	19890625
-80.580	-0.150	21.0	22	27	115	6.2	19900902
-80.480	-0.570	26.0	27	15	124	7.1	19980804
-81.200	-0.960	12.0	32	19	123	5.7	20050130
-79.922	0.382	18.0	24	22	118	7.8	20160416
-80.060	0.480	34.0	22	22	115	5.9	20160711
-79.900	0.670	24.0	28	22	121	5.4	20170711
-78.810	2.320	20.0	30	16	118	8.1	19791212
-79.490	1.670	15.0	38	12	126	5.6	20140309
-79.520	1.730	16.0	29	11	116	5.7	20140616
-78.990	3.240	26.0	32	19	125	5.5	19850610
-77.680	4.990	24.0	14	18	104	5.8	19880920
-77.570	4.720	16.0	21	11	114	7.2	20041115
-77.660	5.730	13.0	360	18	89	5.5	20110913
-77.630	6.260	17.0	40	20	134	5.6	19900825
-77.560	6.060	16.0	349	8	82	5.7	19960523
-81.110	-1.890	22.0	354	21	88	5.0	20190331
-80.940	-1.650	31.0	8	31	100	5.8	20050124
-80.920	-1.990	23.0	350	21	85	5.7	20190331
-81.139	-1.982	8.0	28	24	115	6.1	2019033
-80.401	-0.400	8.0	27	8	126	5.8	20160417
-79.847	0.528	4.0	51	18	145	5.4	20160420
-73.720	12.030	11.0	38	40	38	5.0	20190929
-81.950	-5.840	15.0	355	22	95	5.9	19870514
-80.920	-5.550	33.6	171	73	88	5.3	19880402
-81.700	-5.900	13.2	2	14	102	5.8	20090326
-81.200	-6.000	31.2	359	23	99	5.2	20130115
-81.140	-4.210	33.7	20	23	116	5.5	20140803
-78.640	7.140	15.0	266	90	0	5.0	19920208
-79.630	7.220	15.0	350	89	-137	5.2	20000731
-79.560	7.290	12.0	81	86	-6	5.0	20180129

4.14.7 References

- Alvarado, A., Ruiz, M., Mothes, P., Yepes, H., Segovia, M., Vaca, M., Ramos, C., et al. (2018) Seismic, Volcanic, and Geodetic Networks in Ecuador: Building Capacity for Monitoring and Research. Seismological Research Letters, 89, 432–439. doi:10.1785/0220170229

- Audemard, F., Machette, M., Cox, J., Dart, R. & Haller, K. (2000) Open-File Report (Open-File Report). Open-File Report.

- Bès de Berc, S., Soula, J.C., Baby, P., Souris, M., Christophoul, F. & Rosero, J. (2005) Geomorphic evidence of active deformation and uplift in a modern continental wedge-top–foredeep transition: Example of the eastern Ecuadorian Andes. Tectonophysics, 399, 351–380. doi:10.1016/j.tecto.2004.12.030

- Ekström, G., Nettles, M. & Dziewoński, A.M. (2012) The global CMT project 2004–2010: Centroid-moment tensors for 13,017 earthquakes. Physics of the Earth and Planetary Interiors, 200–201, 1–9. doi:10.1016/j.pepi.2012.04.002

- Engdahl, E.R., Di Giacomo, D., Sakarya, B., Gkarlaouni, C.G., Harris, J. & Storchak, D.A. (2020) ISC-EHB 1964–2016, an Improved Data Set for Studies of Earth Structure and Global Seismicity. Earth and Space Science, 7, e2019EA000897, John Wiley & Sons, Ltd. doi:10.1029/2019EA000897

- Fiorini, E. & Tibaldi, A. (2012) Quaternary tectonics in the central Interandean Valley, Ecuador: Fault-propagation folds, transfer faults and the Cotopaxi Volcano. Global and Planetary Change, 90–91, 87–103. doi:10.1016/j.gloplacha.2011.06.002

- Mariniere, J., Nocquet, J.-M., Beauval, C., Champenois, J., Audin, L., Alvarado, A., Baize, S., et al. (2019) Geodetic evidence for shallow creep along the Quito fault, Ecuador. Geophysical Journal International, 220, 2039–2055. doi:10.1093/gji/ggz564

- Paris, G., Machette, M.N., Dart, R.L. & Haller, K.M. (2000) Map and database of Quaternary faults and folds in Colombia and its offshore regions (Report No. 2000–284). Open-File Report, U.S. Geological Survey (USGS). doi:10.3133/ofr00284

- Tibaldi, A., Rovida, A. & Corazzato, C. (2007) Late Quaternary kinematics, slip-rate and segmentation of a major Cordillera-parallel transcurrent fault: The Cayambe-Afiladores-Sibundoy system, NW South America. Journal of Structural Geology, 29, 664–680. doi:$https://doi.org/10.1016/j.jsg.2006.11.008$

- Trabant, C., Hutko, A.R., Bahavar, M., Karstens, R., Ahern, T. & Aster, R. (2012) Data Products at the IRIS DMC: Stepping Stones for Research and Other Applications. Seismological Research Letters, 83, 846–854. doi:10.1785/0220120032

- Vaca, S., Vallée, M., Nocquet, J.-M. & Alvarado, A. (2019) Active deformation in Ecuador enlightened by a new waveform-based catalog of earthquake focal mechanisms. Journal of South American Earth Sciences, 93, 449–461. doi:https://doi.org/10.1016/j.jsames.2019.05.017

- Velandia, F., Acosta, J., Terraza, R. & Villegas, H. (2005) The current tectonic motion of the Northern Andes along the Algeciras Fault System in SW Colombia. Tectonophysics, 399, 313–329. doi:10.1016/j.tecto.2004.12.028

CHAPTER 5

Interseismic Coupling Model along the Ecuador-Colombia Subduction zone

Along subduction zones, the elastic effect of coupling along the subduction interface is most often large enough to induce significant strain rate between GPS sites. In that case, GPS data can be used to solve for the slip deficit accumulating each year at different part of the fault to produce spatially variable interseismic (hereafter referred as ISC) coupling models at the megathrust. Such ISC constitute a reference for several studies of the earthquake cycle and seismic hazard assessment.

Indeed, ISC models provide evidence supporting the current model of a subduction interface made of discrete locked patches embedded in an overall creeping fault. In that view, locked areas are interpreted as velocity-weakening patches that slip seismically during large earthquakes, while low locking areas are interpreted as obeying velocity-strengthening, allowing constant slip and low elastic stress accumulation. Most subduction zones show a spatially heterogeneous pattern of the velocity field, providing a direct evidence supporting the above model. Trench perpendicular velocity gradients at onshore stations allow to quantify the down-dip limit of locked portion of the megathrust. Along strike variations of velocity magnitude and direction witness of along strike variations of the strength of coupling, hence allowing identifying the areas of the fault undergoing more rapid slip deficit accumulation.

Most subduction zones host regular SSEs, providing additional information about the frictional anatomy of the megathrust. Because SSEs were corrected at the step of the time series analysis, ISC models are models of the slip accumulation between large earthquakes but also between large SSEs. Observing the part of slip deficit released through SSEs is important. SSEs indicate areas of the fault that, although being totally or partially locked, behave aseismically. Hence, a more complete description of the fault behaviour comes the simultaneous information of ISC and SSE.

Finally, ISC are often used as additional constraints to calibrate Probabilistic Seismic Hazard Assessment (PSHA) models and guide the probability of future large earthquakes in a given area (ex: Mariniere et al. (2021)).

Several studies have proposed models of interseismic coupling along the Colombia-Ecuador subduction. Trenkamp et al. (2002) and White et al. (2003) first show that, in average, the subduction interface was only partially locked (50%) in Ecuador and possibly even less in Colombia. Nocquet et al. (2014) produced a first large-scale spatially variable ISC model showing that large and great earthquakes in Ecuador and Peru correlate with areas of high-locking, while a large segment from southern Ecuador to central Peru was predominantly creeping at the plate rate. Using the same data set in Ecuador, Chlieh et al. (2014) provided a finer model, and discuss the relationship of highly locked asperities with the areas of past large earthquakes during the XXth century. Availability of new GPS data in Colombia allowed next to extend ISC models further north, along the subduction segment offshore Colombia, with a lower resolution however (Chlieh et al. 2021, Nocquet et al. 2016, Sagiya and Mora-Paez 2020). So far, all these studies made the assumption of a single rigid North Andean Sliver and used residual velocities with respect to the NAS as input data for inversion of ISC models. The previous chapter extensively shows the limitation of this assumption, leading to biases of several millimiters per year, that possibly leak into the slip deficit estimates.

For the first time in the northern Andes, the methodology of the elastic blocks allows to simultaneously solve for rotation of blocks and spatially variable slip deficit along the megathrust. This chapter presents the obtained results. At the time of writing this manuscript, I consider that some additional work is required before submission, which I describe in the last chapter of this thesis.

Interseismic Coupling Model along the Ecuador-Colombia Subduction Zone from 3°S to 5°N

5.1 Introduction

The segment of the Nazca/South America subduction zone in front of Ecuador and Colombia (from latitude 3.5°S to ∼5°N) has experienced large and great megathrust earthquakes, recorded since the end of the XIXth century. The greatest historical event is the 1906 Mw 8.5-8.8 earthquake that ruptured a ∼500km-long segment of the megathrust north of Carnegie ridge (Abe 1979, Kanamori and McNally 1982, Ye et al. 2016). Successive partial ruptures of the previously ruptured segment occurred during the following decades through Mw 7.8-8.2 earthquakes in 1942, 1958, and 1979 (figure 5.1) (Beck and Ruff 1984, Kanamori and McNally 1982, Mendoza and Dewey 1984, Sewnson and Beck 1996). In 2016, the Mw 7.8 earthquake approximately ruptured the same sub-segment previously ruptured by the 1942 Mw 7.8 earthquake (He et al. 2017, Nocquet et al. 2016, Ye et al. 2016). In addition, smaller events with Mw ≥7.0-7.2 occurred (1) at southern edge of the 1906 rupture area in 1898 (Mw 7.0±0.2:SARA project (2021)) and 1998 (Mw 7.1), and (2) north of the 1906 rupture area in 1991 and 2004 at latitude ∼4.5°N, whose focal mechanism solutions agree with subduction thrust events (Global CMT Catalog GCMT:Ekström et al. (2012)).

Along the Colombia-Ecuador margin, the oceanic Nazca plate subducts beneath South America at a rate of 56 to 52 mm/yr towards ∼N83°E, a direction that is oblique to the trench (Nocquet et al. 2014, Yepes et al. 2016, Jarrin et al. submitted). The oblique convergence induces slip partitioning and deformation of the overriding South America continent. According to our best model for the westernmost block of the North Andean Sliver, the slip rate along the megathrust occurs at 47-44 mm/yr in a N87°E direction in central Ecuador and N84.4°E direction in central Colombia (figure 5.1).

5.2 Previous Interseismic Coupling Models

Several studies provided ISC maps of the Ecuador-Colombia subduction interface. Here, we summarize the data and methodology used in previously published studies. The seminal work of Trenkamp et al. (2002) used survey-mode GPS data spanning the 1991-1998 period. Using a 2-dimensional backslip model also accounting for shortening in the back-arc area, they found a preliminary value of 50% for the average locking in northern Ecuador, and no locking required to explain the velocity in central Colombia. White et al. (2003) further showed that low apparent locking in Colombia could be related to the visco-elastic relaxation induced by the 1979 Mw 8.2 earthquake off-shore Colombia. White et al. (2003) also mention the possibility of significant strain accumulation south of the rupture of the great 1906 earthquake. Nocquet et al. (2014) used a combination of survey-mode GPS data spanning the 1994-2009 period and cGPS data for the 2009-2013 period covering Ecuador and Peru down to latitude 10°S. They first estimated the motion of the North Andean Sliver as a single rigid block by selecting sites within areas with no apparent strain in southern Ecuador and Colombia. They used a curved geometry from the

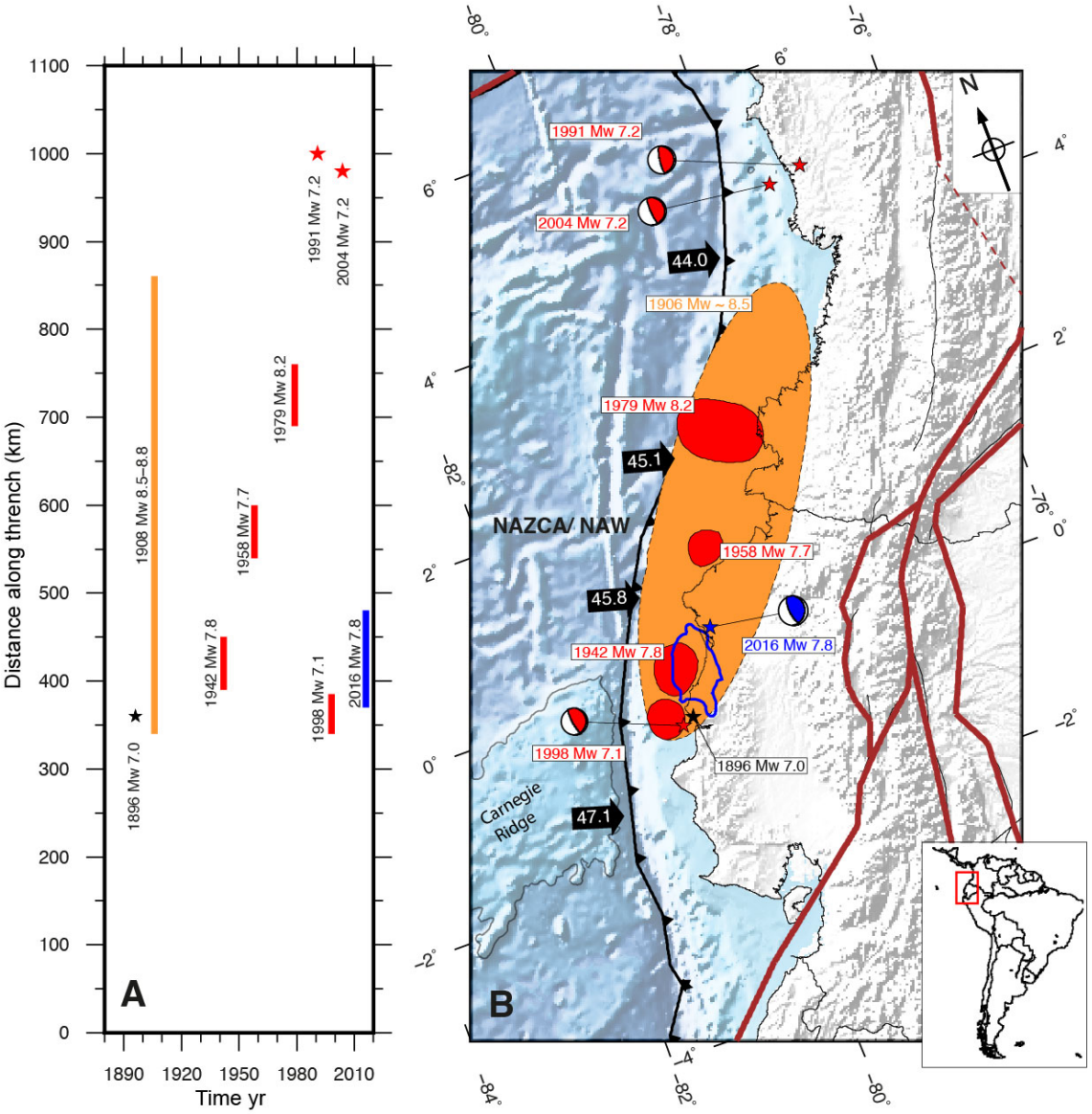

Figure 5.1 – A) Segments ruptured by Mw ≥7.0 earthquakes as a function of time. B) Areas of major moment released for large earthquakes since the 19th century (Beck and Ruff 1984, Chlieh et al. 2014, Kanamori and McNally 1982, Nocquet et al. 2014, Sewnson and Beck 1996). Focal mechanism solutions are from the Global Centroid Moment Tensor catalog (GCMT:Ekström et al. (2012)). Brown lines are the block geometry from Jarrin in prep.

slab1.0 model (Hayes et al. 2012) and an inversion approach based on Tarantola (2005) with no negativity constraints to propose a range of models allowed by the data. The same data set was then used by Chlieh et al. (2014) to perform a similar inversion, but including 1-D elastic model to compute the static Green's function in a simplified geometry model for the subduction interface. Gombert et al. (2018) also used the data set from Nocquet et al. (2014) to perform a Bayesian inversion accounting for error in both the geometry of the plate interface and the Earth's elastic model.

Availability of detailed multichannel seismic reflection lines and wide-angle seismic data collected across the central Ecuador subduction segment allowed to define a new geometry significantly different from the slab1.0 model in central Ecuador (Collot et al. 2017). This new geometry, together with additional survey-mode measurements provided a refined model for central Ecuador in the La Plata area (Collot et al. 2017). Finally, adding a few additional sites along the coast of Colombia, Nocquet et al. (2016) extended Nocquet et al. (2014) models using finer discretization of the megathrust interface. All these models used the residuals velocities with respect to the North Andean Sliver motion estimated in Nocquet et al. (2014). They all show along-strike heterogeneous coupling made of relatively discrete asperities, with high locking confined within the shallowest 35 km of the interface (although a small patch was found by Gombert et al. (2018)). In their details, several differences are found among these models (Figure 5.2). Differences are in the amount of shallow coupling close to the trench and the size of the different asperities. These differences reflect the influence of regularization or simply the choice of the preferred model from the range of explored possible models.

Sagiya and Mora-Paez (2020) used the velocity field from Mora-Páez et al. (2019) to provide the first model extending north in central Colombia. They used baseline rates from Nocquet et al. (2014) and Mora-Páez et al. (2019) as input data for the inversion of the ISC. Their model appears to be smoother than the previous ones, possibly due to the sparser distribution of sites in Colombia that prevents to resolve finer details and imposes their regularization parameters at the entire scale of the model. Finally, Chlieh et al. (2021) used the combined velocity field from Mora-Páez et al. (2019) to perform an inversion up to latitude 4°N. They used the slab2.0 model (Hayes 2018), which is deeper at some places than slab1.0. A consequence of a deeper interface appears to be an increased amount of locking required to explain the GPS data. A drawback of these models is the use of a single rigid North Andean sliver for the whole modeled area (Figure 5.1B and Figure 4.12 in chapter 4).

Here, we present a new ISC model sampling the Ecuador-Colombia subduction zone over ~850 km between latitudes 3.5°S and 5°N. Our new ISC model is derived from a more refined and accurate velocity field. In particular, criteria of at least 4 GPS campaigns and at least 3-years long time series allow a better handling of the numerous SSEs in Ecuador and mitigate their impact on the derived ISC. Solving simultaneously for ISC and for continental block rotations further improves the consistency of our model, and allows us to evaluate the effect of block rotations on the derived locking map.

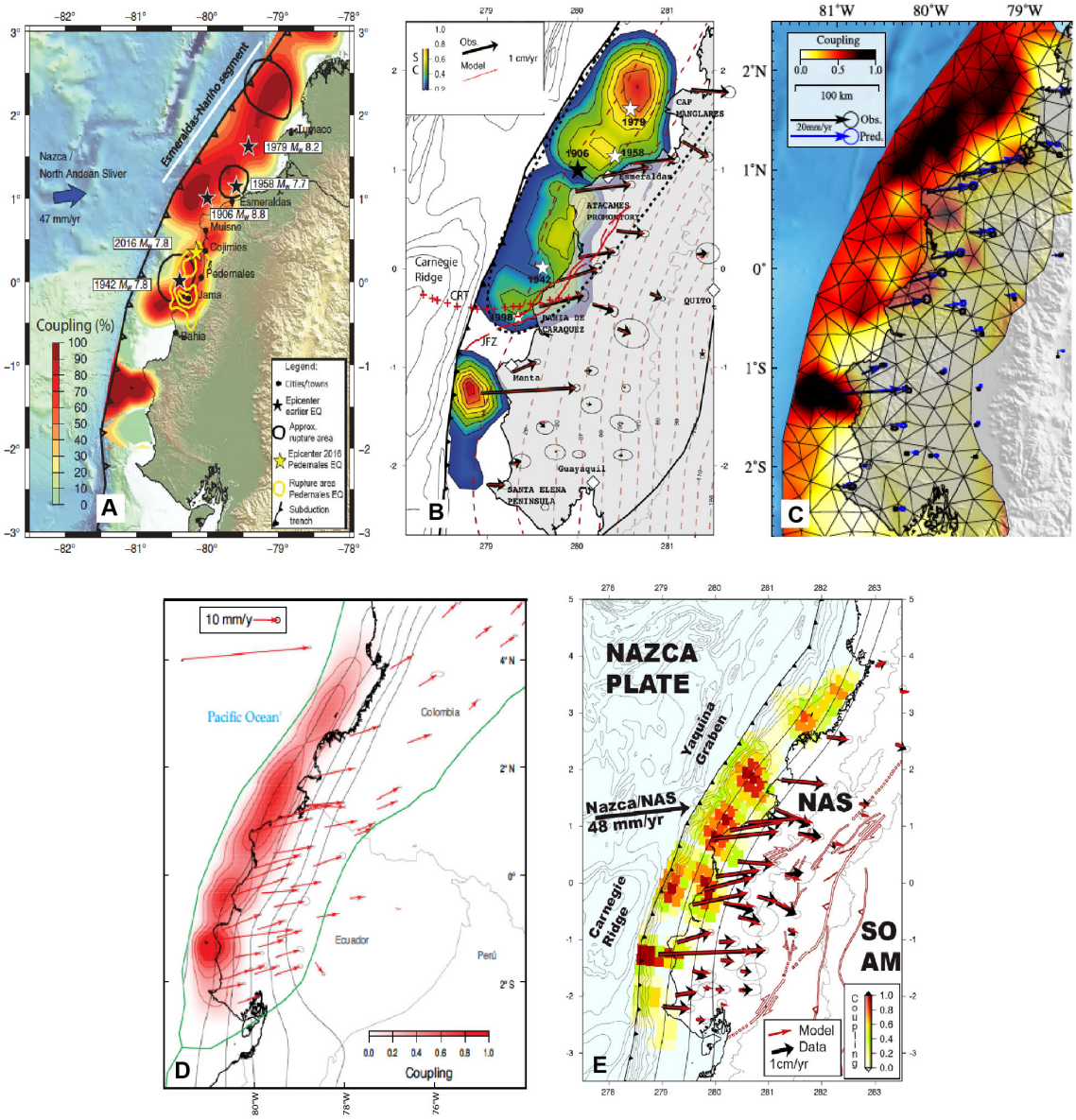

Figure 5.2 – Previous ISC models proposed along the Ecuador-Colombia subduction zone according to: A) Nocquet et al. (2016) model taken from Mothes et al. (2018), B) Chlieh et al. (2014) (average model), and C) Gombert et al. (2018), D) Sagiya and Mora-Paez (2020), and E) Chlieh et al. (2021)

5.3 Methodology

5.3.1 Inversion scheme and regularization constraints

If the vector d of the GPS velocities is expressed in the reference frame of the overriding plate, and in the absence of deformation and/or block rotations, d is the linear sum of slip rate taken in the plate convergence at each every individual subfaults m multiplied by the Green's function:

$$d = Gm \tag{5.1}$$

For inter-seismic modelling, m actually denotes the amount of back-slip (normal slip) (Savage 1983). Because the number of unknown parameters m is much larger than the number of observations, additional constraints are required to solve the inverse problem. We choose an approach where regularization is applied through a model covariance matrix C_m. This approach is grounded in the stochastic approach from Tarantola (2005) for a linear inverse problem with Gaussian prior (see Nocquet (2018) for details). Within this formulation, we minimize the cost function $S(m)$ (equation 5.2):

$$S(m) = \frac{1}{2}\left[(Gm-d)^t C_d^{-1}(Gm-d) + (m-m_0)^t C_m^{-1}(m-m_0)\right] \tag{5.2}$$

Where:

- m: Vector of backslip at each subfault
- m_0: A priori model for the backslip distribution
- d: Vector of horizontal GPS velocities from both components
- G: Green's functions relating the unit slip at each subfault to the horizontal velocities (east and north components).
- C_d and C_m: Covariance matrices for the data (d) and the model (m_0) respectively.

C_d is simply taken as the diagonal matrix of the velocity variance. C_m is chosen as a decreasing exponential matrix that simultaneously introduces correlations between backslip at subfaults pair (i, j) and damping with respect to the prior model m_0:

$$C_m(i,j) = \sigma_m^2 exp\left(-\frac{d(i,j)}{Dc}\right) \tag{5.3}$$

where:

- $d(i,j)$: Distance between centroids of i and j subfaults.
- Dc: Critical distance controlling the slip correlation between subfaults. Dc controls the smoothness of the solution.

- σ_m^2: The inverse of the weight given to smoothing and damping with respect to a priori model m_0.

Within this formulation, if the data does not resolve the slip on a given set of subfaults, their estimated backslip will follow the slip imposed from the a-priori model m_0. The range of models allowed by the data is explored by varying the regularization parameters and m_0 from a null to full coupling prior models.

In the block model, this formulation is modified in several ways. First, we do not know the backslip direction. Thus the vector m now includes a dip-slip and strike-slip component, noted $m_\perp$ and $m_\parallel$ respectively. Regularization constraints are imposed differently according to the components. The strike-slip component is assumed to reflect the slip partitioning induced by the motion of the overriding sliver. Hence, along strike variations certainly occur over large distances if the sliver motion is close to a translation motion. It is also assumed to vary slowly with depth. As a consequence, $Dc_\parallel$ is chosen to be very large and σ_m small. On the contrary, $Dc_\perp$ is chosen to roughly represent the coupling variations expected to be resolved given the spatial distribution of GPS data and $m_\perp$ is expected to be a fraction of the convergence velocity.

A second modification of the simple backslip formulation arises because the slip should be constrained to be close in direction of the relative plate convergence direction. This is applied through an additional pseudo-observation equation relating the backslip to the relative convergence slip predicted from the relative block rotation, also estimated in the inversion. Again, in the linear system, this pseudo-observation is weighted using a covariance matrix having the same shape as C_m. Because the strike of the fault is known, the Dc and σ_m parameters can also be chosen separately, together with different m_0 corresponding to the fraction of the relative motion taken as a prior.

Such formulation allows us to constrain the backslip in the direction of the relative convergence, but does not enforce it strictly. This is useful in subduction setting where slip deficit is expected to accumulate in the plate convergence direction at shallow depth but might vary at depth, especially in the case of laterally curved geometry of the slab at depth.

5.3.2 Resolution analysis

Relative block motion and convergence rate trade-off

As a preliminary test for our ISC models, we first investigate how different regularization parameters impact the convergence rate. Indeed, coupling at depth induces a low surface velocity gradient that mimics a translation-like motion, thus possibly inducing bias in the overriding slip Euler pole estimate. The trade-off between coupling at depth and motion of the sliver might be assessed by plotting the convergence rate estimates as a function of the constraints imposed with respect to the a-priori model m_0.

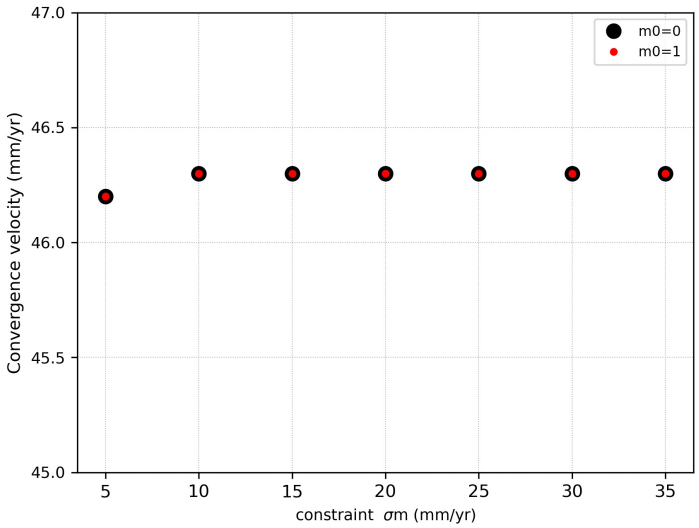

Figure 5.3 – Test of convergence velocity stability by varying σ_m constraint from 5 mm/yr to 35 mm/yr with respecto to a priori models m_0=0 and m_0=1.

Figure 5.3 shows the predicted convergence velocity at (Lon:80.9°W, lat:0.2°N) as a function of sigma variation (from 5mm/yr to 35 mm/yr) with respect to a priori models m_0=0 and m_0=1. *Dc* appears to have a negligible influence. This test shows the estimated convergence rate is not correlated to the amount of coupling, indicating that the distribution of GPS sites above the plate interface is dense enough to resolve both rotation and coupling.

Influence of the regularization on ISC

An additional assessment of the resolution is provided by the influence of the regularization parameters on the obtained ISC map. We compute the coupling variations from the difference between the maximum (model G) and minimum (model A) coupling values according to the variation of σ_m constraint shown in figure 5.6. Figure 5.4 suggests that the coupling variation is lower than 10% throughout the Ecuador-Colombia subduction interface. We observe patches of uncertainty at 4-5% on the rupture areas of the 1958 (Esmeraldas) and 1979 (Tumaco) historical eartquakes, and recent earthquakes (Pedernales: 2016). These patches of low uncertainty confirm that our networks has good resolution to solve shallow coupling close to the coastline and to a less extent also close to the trench. As expected, coupling at 60-80 km depth has relatively high uncertainties ($\sim$9%) northward of latitude $\sim$3°N where our network is not dense.

5.3.3 Preferred Model

Our inversion formulation allows us to explore the range of possible ISC models by varying Dc, σ_m parameters with respect to a priori model (m_0). We plot a L-curve showing the misfit (χ^2) as a function of σ_{ds} (dip-slip component) and σ_{ss} (strike-slip component) constraints for a fixed

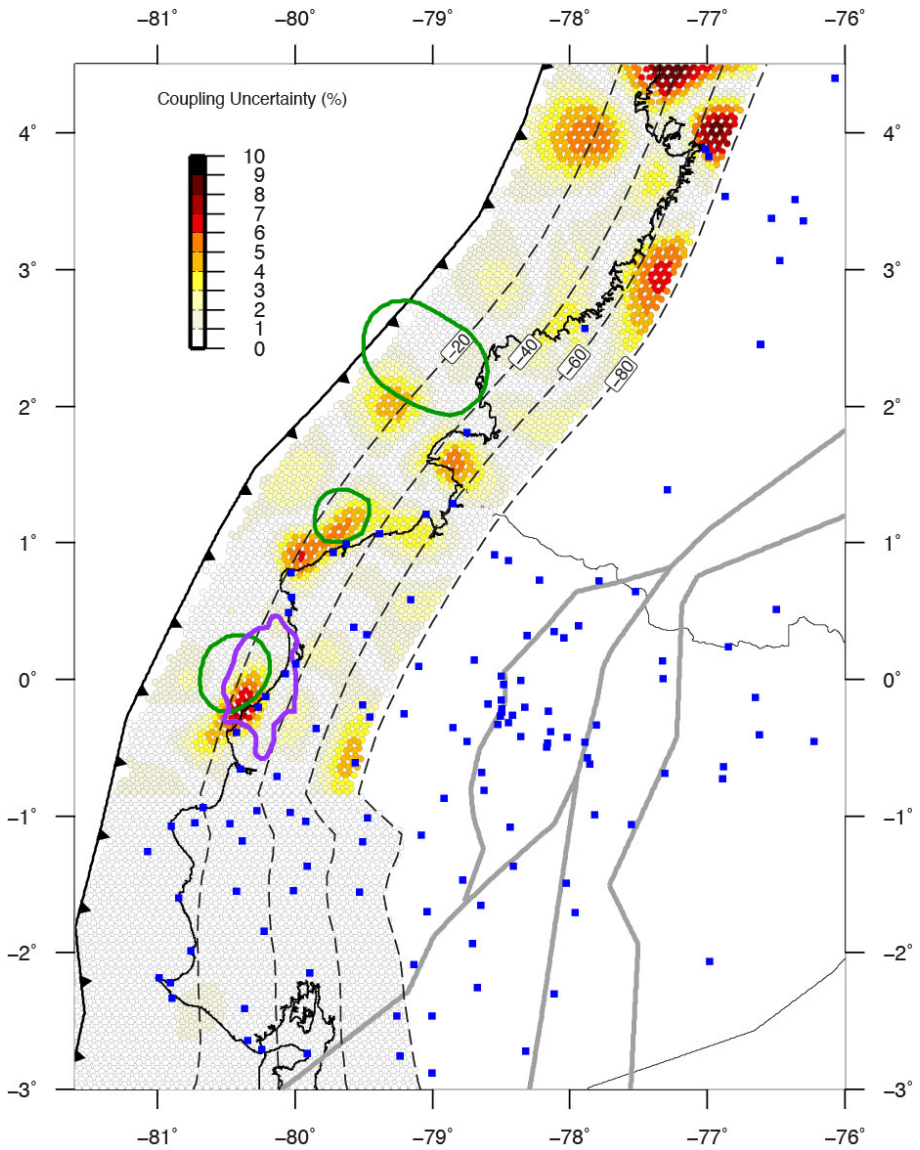

Figure 5.4 – Variation of coupling obtained by changing the regularization parameters between models A and G shown in figure 5.5 and figure 5.6. Green lines are areas of major moment released for 1979, 1958 and 1942 earthquakes (Beck and Ruff 1984, Sewnson and Beck 1996). Violet line is the iso-contour at 1 m for the coseismic slip distribution of the 2016 earthquake (Nocquet et al. 2016). Blue squares are GPS stations.

critical distance (Dc) (figure 5.6).

We select the model D that is located at the inflexion point of the L-curves for σ_{ds}=20 mm/yr and σ_{ss}=0.8 mm/yr. The goodness of fit for the selected model is 1199.2, equivalent to a reduced χ^2 of 2.01. As χ^2 statistics account for the fit of all data (at the scale of the NAS). A more accurate criterium is provided by selecting only residuals within the North Andean West block (NAW) for the χ^2 calculation because of their smaller distance to the subduction interface. In this case, the new χ^2 statistics calculated using 88 sites is 279.7, equivalent to reduced χ^2 of 1.6 showing a good agreement between the residuals and the data uncertainnty.

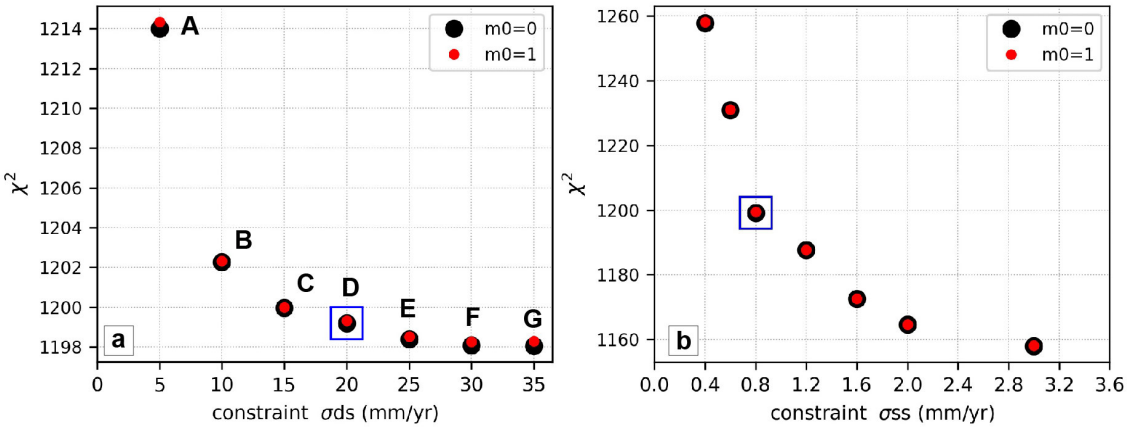

Figure 5.5 – L-curve shows the χ^2 values with respect to σ constraints for a priori models m_{0ss}=m_{0ds} = 0 (null coupling) and m_{0ss}=m_{0ds} = 1 (full coupling). a) L-curve imposing constraints for a dip slip component (σds) between 5mm/yr and 35mm/yr with fixed values for σ_{ss}=0.8 mm/yr, Dc_{ss}=1000km, and Dc_{ds}=30km. b) L-curve imposing constraints for a strike slip component (σss) from 0.4 mm/yr to 3 mm/yr with fixed values for σ_{ds}=20 mm/yr, Dc_{ss}=1000km, and Dc_{ds}=30km

5.4 Alternative Models

Alternative ISC models with σ_{ds} values of 5 and 35 mm/yr are also possible. In both cases, the fit discrepancies are negligibles with respect to the selected ISC model. The Nazca/NAW residuals for a σ_{ds} contraint at 5 mm/yr has a reduced χ^2= 1.68 whereas for σ_{ds}=35 mm/yr has a reduced χ^2= 1.59.

The spatial distribution of interseismic coupling from the range of explored models is quite similar to the one selected as our best fit model (figure 5.6). In general, all models in figure 5.6 show a heterogeneous coupling, including along-strike and along-dip variations. Shallow high coupling at the megathrust interface is restricted to 30-40 km depth in northern Ecuador and to ∼20km at central Ecuador. All models also show null coupling southward of latitude ∼2.5°S and northward of latitude ∼5°N. In conclusion, we found that the coupling distribution from the range of explored models has little variations with respect to the best fit model (±5% of variations).

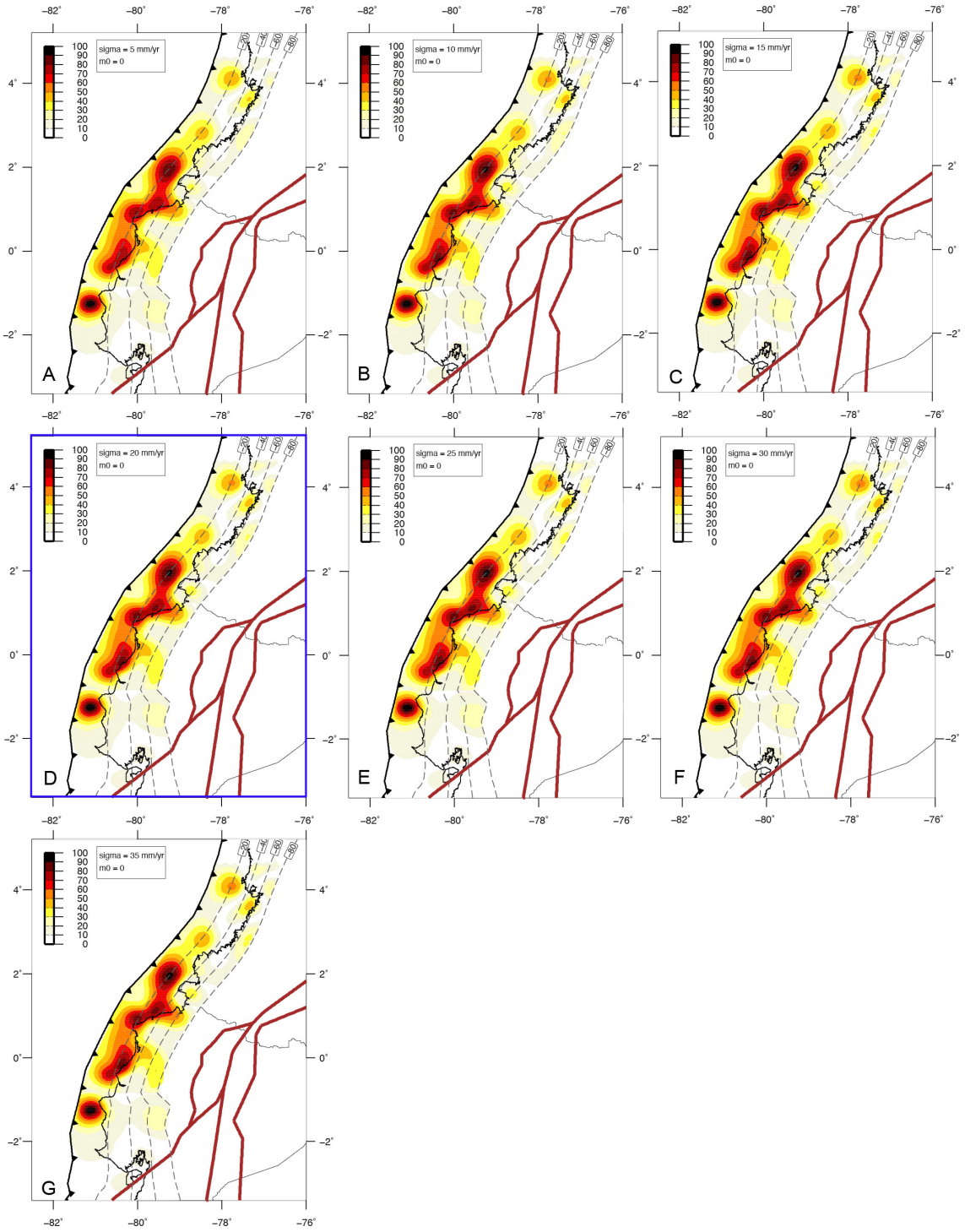

Figure 5.6 – Exploration of interseismic coupling models at the Ecuador-Colombia subduction interface. Figures A-G are interseismic coupling distributions for a priory model m_{0ss}=0, m_{0ds}=0 with respect to constraints: Dc_{ss}=1000 km, Dc_{ds}=30 km, and σ_{ss} = 0.8 mm/yr. σ_{ds} values increasing from 5 mm/yr (figure A) to 35 mm/yr (figure G). Figure marked with blue is the selected model.

5.5 Main Patterns of the Interseismic Coupling from our best fit Model

Figure 5.7 shows an enlarged view of our preferred ISC model along the Ecuador-Colombia subduction zone from latitude 3°S to 5°N. We discuss the main patterns of the coupling distribution in terms of its relationship with seismic and aseismic processes observed at the plate interface. The ISC map defines three major segments with variable coupling. One of them, the central segment encompasses the proposed rupture area of the 1906 earthquake from lat. 0.6°S to lat. 4°N. It is fragmented into areas of relatively high coupling separated by narrow zones of low or partial coupling.

The La Plata Island area that extends from the Salinas Peninsula (latitude ∼2°S) to the Manta Peninsula (latitude ∼1°S) is characterized by a shallow (4-10km) and fully locked patch located below La Plata Island. This isolated patch lies within a ∼1400km long-creeping segment extending from central Ecuador to central Peru (latitude ∼10°S) (Nocquet et al. 2016, Nocquet et al. 2014, Villegas-Lanza et al. 2016b). In the vicinity of La Plata island and after the onset of cGPS observations in ∼2009, three episodic shallow slow slip events (SSEs) with Mw 6.0-6.8 were geodetically detected in 2010, 2013, and 2016 (figure 5.8). All of them were associated with intense or significant microseismicity. (Rolandone et al. 2018, Segovia et al. 2015, Vallée et al. 2013). Aside from these SSEs, several seismic swarms have also been reported in 1977, 1993, 1996, 1998, 2002, 2005 in this region (Font et al. 2013, Holtkamp et al. 2011, Segovia et al. 2018, Vallée et al. 2013). All these episodic events suggest that the La Plata segment periodically releases the stress accumulated in a dominant aseismic mode (Rolandone et al. 2018), which is also consistent with the absence of documented large historical seismic ruptures.

Compared to previous models in the La Plata segment, a second and deep patch of low coupling (20-30%) is found by our model, between 50km and 80km depth. This patch shows a correlations with (1) the spatial distribution of the 2015 deep SSE (slow slip event) that had an equivalent Mw 7.0 (figure 5.8B) (Rolandone et al. 2018), and (2) the southernmost extension of the deep afterslip distribution found for the first 30 days following the 2016 earthquake (figure 5.8A) (Rolandone et al. 2018). Along strike, the northernmost extension of the La Plata segment is made by a narrow strip (∼20km-long) of low coupling (10-20%) extending along the down-dip direction from the trench to 80km depth. This transition zone likely acts as a barrier to seismic ruptures, as observed during the 2016 earthquake seismic rupture. (Nocquet et al. 2016, Rolandone et al. 2018).

From northern Ecuador to southern Colombian, our ISC model identifies three sub-segments that extend along the 1906 earthquake rupture area. The first one, the Bahia-Pedernales sub-segment spreads along the 1942 and 2016 earthquake rupture areas (Mw 7.8). Here, the Bahia-Pedernales segment is defined by a highly locked patch (ISC>70%) confined between 15 and 30km depths. Within this patch, a locked asperity (ISC: 80-90%) of ∼16x20km^2 overlaps most of the region of the maximum coseismic slip (>5 meters) from the 2016 Mw 7.8 earthquake (Gombert et al.

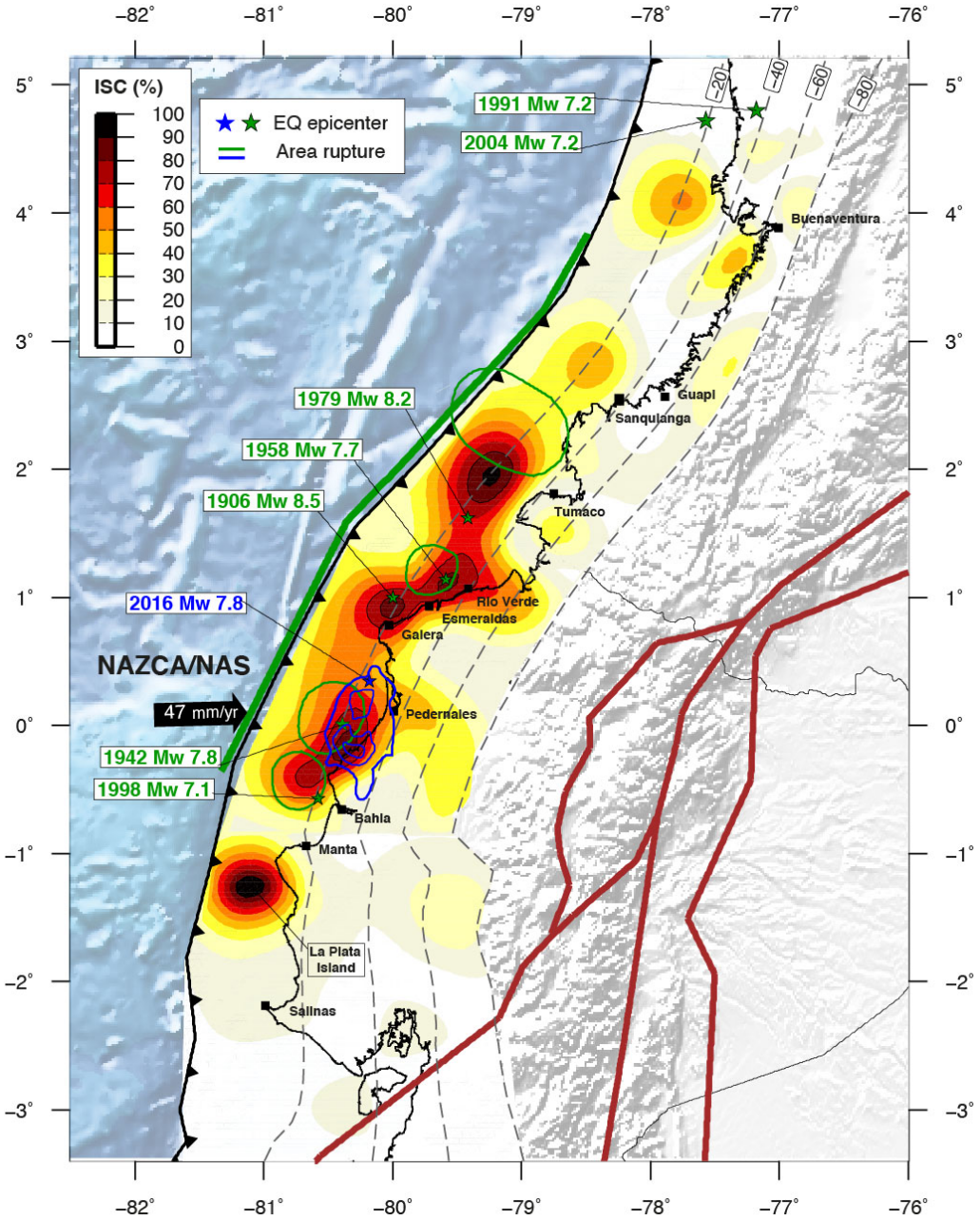

Figure 5.7 – Spatial distribution of Interseimic coupling at the Ecuador-Colombia subduction interface using a priori constraints (σ_{ds} =20mm/yr, $\sigma_{ss} = 0.8mm/yr$, Dc_{ds}=30km, and Dc_{ss}=1000km) with respect to a null coupling model ($m_0 = 0$). Blue lines are iso-contours at 1, 3, and 5 meters for slip rupture from the 2016 Mw 7.8 Pedernales earthquake (Nocquet et al. 2016). Green lines are the proposed area of major moment release for past Mw $\geq$ 7.1 earthquakes with their epicenters depicted as green stars (Beck and Ruff 1984, Kanamori and McNally 1982, Segovia 2001, Sewnson and Beck 1996). The thick green following the trench shows the proposed rupture area for the 1906 earthquake (Kanamori and McNally 1982). Blue star is the epicenters of the 2016 earthquake Nocquet et al. (2016). Green stars at latitude ~4.5°N are epicenters for the 2004 and 1991 Mw 7.2 earthquakes Trabant et al. (2012). Brown lines are the block geometry from Jarrin (in prep).

2018, Nocquet et al. 2016). The southernmost extension of this patch is also a highly coupled area (ISC ∼70%) that correlates with the proposed rupture area of the 1998 Mw 7.1 earthquake (Chlieh et al. 2014, Segovia 2001). Following the shape of the locked Bahia-Pedernales patch, coupling decreases along the down-dip extension from ∼50% (∼40km depth) to ∼20% (80km depth). This deep coupling distribution also shows first-order correlations with the afterslip extension estimated by Rolandone et al. (2018) after 30 days of the 2016 earthquake.

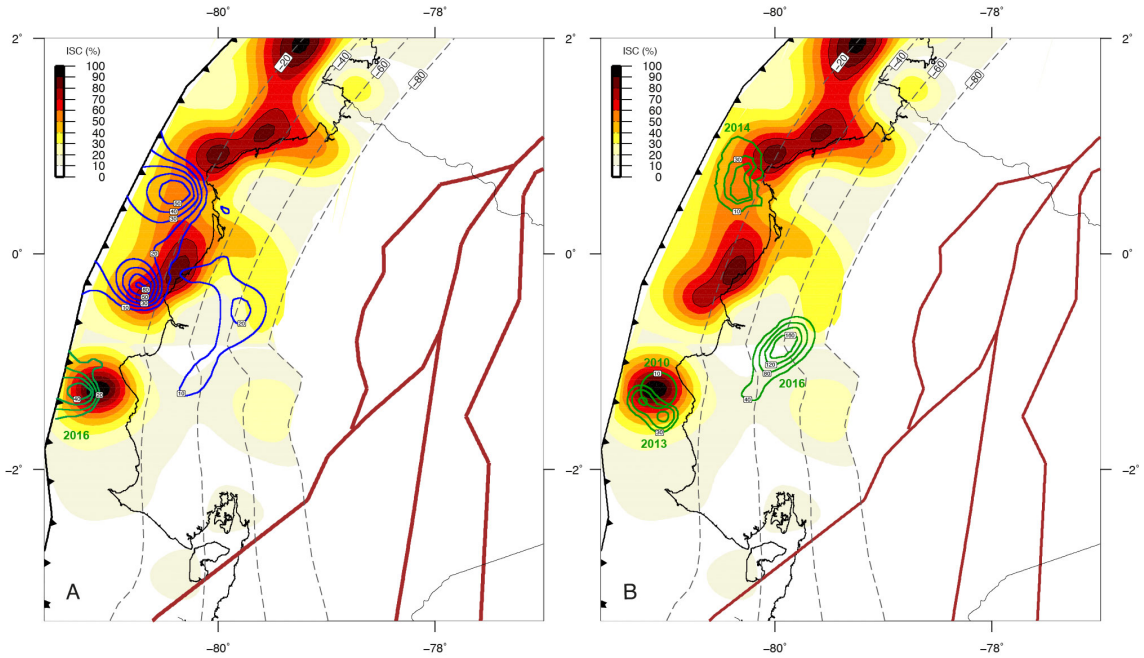

Figure 5.8 – Summary of Slip at the megathrust interface. A) Interseismic coupling from our best model and Afterslip distribution following the first 30 days of the 2016 Mw 7.8 earthquake. Blue lines are iso-contours from the afterslip model whose values are expressed in cm (Rolandone et al. 2018). Green lines are iso-contours (in cm) from the 2016 SSE at the La Plata island (Rolandone et al. 2018). B) Interseismic copling and spatial distribution of Slow Slip Events (SSEs). Green lines are iso-contours from the SSEs expressed in mm (Rolandone et al. 2018, Vaca et al. 2018).

The second sub-segment (Galera-Tumaco) extends from latitude ∼0.7°N to ∼2.5°N. This 200km long sub-segment shows a highly coupled zone (70-90%) between depths of 10km and 40km, in which three locked asperities (ISC>80%) of ∼15x15 km^2 are well identified (figure 5.7 and figure 5.6). High coupling areas on the Galera-Tumaco sub-segment encompass major moment release areas from the 1958 Mw 7.7 and 1979 Mw 8.2 earthquakes (Beck and Ruff 1984, Sewnson and Beck 1996). The northernmost extension of the Galera-Tumaco sub-segment seems bounded by a narrow strip (∼25km-long) of low coupling (∼30%) at the Sanquianga peninsula in southern Colombia, where the major moment release area from the 1979 earthquake ends (Beck and Ruff 1984, Sewnson and Beck 1996). On the contrary, the Galera-Tumaco southernmost extension is defined by a transition zone of low-partial coupling (ISC:30-50%), where two aseismic processes have been observed in the last decade (Figure 5.8: the 2014 slow slip event (Vaca et al. 2018) and the 2016 afterslip process (Rolandone et al. 2018)). Therefore, this transition zone would act as a

barrier separating two high coupling sub-segments that hosted large historical earthquakes.

We identify the last sub-segment (Guapi) along the proposed northernmost extension of the 1906 earthquake ruptured area. The Guapi sub-segment is characterized by a partial coupling patch (∼50%) restricted to depths between 15km and 30km that end at the latitude ∼3.2°N.

Further north, our model estimate a partially locked patch (ISC ∼50%) within the Buenaventura segment at latitude ∼4°N. This patch is restricted at similar depths to those observed on the Guapi segement. Both the Guapi and Buenaventura segments are separated by a zone (∼45 km) of low coupling (10-20%). At the latitude of ∼4.5°N, the interseismic coupling at the megathrust interface vanishes. It is possible that the Buenaventura segment lies within a creeping segment in central Colombia (latitudes 5°-7°N), similar to that observed in southern Ecuador and Northern Peru. Large historical earthquakes are not reported in the Bucaramanga segment. Seismic activity is low and restricted to Mw < 6.0 earthquakes (Ekström et al. 2012, Engdahl et al. 2020, SGC 2020b). However, two earthquakes of Mw 7.2 occurred at its northernmost boundary in 1991 and 2004.

We do not discard some uncertainties in the coupling distribution along the Guapi and Buenaventura segments. Here, cGPS sites are limited (4 sites along coastline and 8 inland:figure 5.4), and the coupling variation explored in section 5.3.2 suggests at least 10% of uncertainty. Additional resolution tests are planned to improve the coupling uncertainty estimate.

Finally, we find some differences in the coupling distribution with respect to previous ISC models. Such differences are observed in the size of locked patches and the amount of shallow coupling close to the trench where the GPS data has low resolution. As mentioned in section 5.2, these differences reflect the influence of regularization or the selection of the preferred model. Our model further suggests partial locking at depth where deep ($\sim 50km$) SSEs have been documented. Our coupling map benefits of a new kinematic model and more refined velocities that were not available in previous studies. Therefore, we expect our ISC model to describe more accurately the interseismic coupling at the plate interface.

5.6 Conclusions

Our ISC model confirms a segmentation of the plate interface based on the coupling variations along-strike. These variations define three main segments (La Plata, Bahia-Guapi, and Buenaventura) separating by narrow zones of low coupling. Additionally, the long-central segment (Bahia-Guapi) is fragmented into three sub-segments, all of them separated by transition zones of partial or low coupling.

The segmentation derived from the ISC model is consistent with the seismotectonic segmentation derived from large historical and recent seismic ruptures, whereas the transition zones show

first-order correlations with zones that behave as barriers to the seismic rupture propagation. Thus, they would act as velocity-strengthening zones that allow slow down or stop large ruptures, but are still ruptured during rare great event like the 1906 earthquake.

CHAPTER 6

Conclusions et Perspectives

La principale contribution de cette thèse est de fournir des modèles cinématiques de référence pour les études tectoniques et les études du cycle sismique dans les Andes du Nord. Je résume les résultats les plus importants obtenus et je propose quelque perspectives de recherche pour l'avenir.

Cinématique de la plaque Nazca

La plaque Nazca est l'une des grandes plaques dont la cinématique est la moins bien déterminée tant sur les temps géologiques (par exemple le modèle MORVEL) que géodésiques. La première difficulté des études géodésiques précédentes pour déterminer la cinématique actuelle de la plaque Nazca vient de l'information fournie uniquement par les mesures GPS sur l'île de Pâques et l'île de Santa Cruz dans l'archipel des Galapagos. Un deuxième problème, soulevé au cours des dernières décennies, est de déterminer si ces mesures GPS ont été perturbées par des processus tectoniques ou volcaniques en raison de leur proximité avec des centres d'expansion océanique ou des complexes volcaniques actifs (comme le volcan Sierra Negra sur l'île d'Isabela aux Galapagos). Dans cette thèse, nous avons utilisé un nouveau jeu de données GPS pour mieux estimer la cinématique actuelle de la plaque Nazca par rapport à l'Amérique du Sud. Les nouvelles vitesses dérivées des observations GPS continues sur les sites de l'île de Salas y Gomez (ILSG) et de l'île de San Cristobal (SCEC) dans l'Archipel des Galapagos, ainsi que les modèles élastiques prédictifs, ont fourni des informations qui montrent que les vitesses sur les sites de l'île de Pâques (ISPA) et l'île de Santa Cruz (GLPS) sont $\sim$1mm/an plus rapides que la vitesse de la plaque Nazca que nous avons estimée. De plus, nos modèles suggèrent également que la vitesse GPS de l'île de Malpelo (MALO) subit une contribution élastique d'environ 1 mm/an à cause du mouvement relatif des plaques Cocos/Nazca.

L'intégration de ces contributions tectoniques et volcaniques, comme incertitudes formelles des vitesses, nous ont permis de trouver un pôle d'Euler qui prend en compte le mouvement de 5 sites et qui supporte l'hypothèse d'une seule plaque Nazca rigide. L'implication, en terme de taux

de convergence, est mineure le long des Andes du Nord et des Andes Centrales par rapport aux estimations précédentes, mais significative pour les Andes Chiliennes. La vitesse prédite par notre pôle aidera à mieux estimer le budget des déficits de glissement et des moments sismiques sur l'interface de subduction de la plaque Nazca dans les études de la deformation inter-sismique.

Déformation dans les Andes du Nord

Les Andes du Nord présentent un processus de déformation complexe résultant du mouvement des plaques tectoniques qui l'entourent. Cette région continentale, longue de $\sim$2200 km en longitude, n'a pas été étudiée avec suffisamment de détails par les études géodésiques précédentes. Cela a conduit à proposer des modèles cinématiques simples, qui décrivent le premier ordre de la déformation observée en surface. Une question soulevée au début de cette thèse était de mieux comprendre comment la déformation continentale est accommodée sur les structures tectoniques actives où l'on observe une grande diversité de la sismicité.

Dans cette thèse, je propose le premier modèle cinématique à l'échelle des Andes du Nord et des régions voisines, basé sur un champ de vitesse GPS horizontale plus étendu et affiné, qui rend compte des observations tectoniques. Le modèle confirme que les mouvement relatifs entre les plaques Nazca/SOAM et Caraïbes/SOAM ne sont pas accommodés par un seul système de failles. Une déformation interne localisée de 2-4 mm/an est accommodée par des failles secondaires actives (les systèmes de failles Oca-Ancon, Santa Martha-Bucarmanga, Romeral et Latacunga-Quito-El Angel). Ces failles limitent des blocs tectoniques et définissent la rotation de plusieurs blocs. Notre modèle a également quantifié les taux d'ouverture entre le NAS et le sliver Inca, en accord avec l'estimation long-terme fournie par les études géologiques. À l'extérieur du NAS, le domaine Subandin accommode un raccourcissement crustal de 2-4 mm/an sur la ceinture Est de chevauchements (Eastern Subandean Belt) le long de l'Equateur et au nord du Pérou, et qui induit une déformation large de plusieurs dizaines de kilomètres vers l'intérieur de l'Amazonie.

Notre modèle confirme l'existence d'une subduction oblique et lente de la plaque Caraïbe sous le NAS le long de la marge nord Colombienne. Cette convergence est accommodée partiellement sur l'interface de subduction (3 mm/an) sans couplage inter-sismique significatif, mais aussi sur les failles à l'intérieur du continent. En ce qui concerne la collision du Panama vers le NAS, notre modèle a quantifié l'ordre de grandeur des mouvements accommodés sur des structures que nous proposons comme nouvelles limites entre ces deux domaines continentaux (la faille de Uramita et l'East Panama Deformed Zone). On observe également que $\sim$1 cm/an de mouvement du bloc Panama est transferé vers l'intérieur de la Colombie et rapidement accommodé sur une distance de 100km vers le nord, à la latitude 6°N.

Finalement, nos résultats fournissent de nouvelles informations pour les études prenant en compte les vitesses des failles crustales dans l'analyse probabilistique de l'aléa sismique (PSHA) à

l'échelle régionale.

Limites du modèle et aspects à améliorer

La construction du modèle de blocs et l'évolution de sa géométrie ont révélé des limitations dans la capacité de nos modèles à résoudre la cinématique sur certaines structures tectoniques. C'est le cas de la partie sud du système de failles de Romeral en Colombie (modèle C). Les vitesses GPS de deux sites dans cette zone de la Colombie suggèrent qu'il y a de la déformation actuelle, mais le manque d'une bonne couverture spatiale des données GPS ne permet pas d'obtenir un premier ordre d'estimation de la déformation dans cette zone. Cependant, les taux de glissement sur la faille de l'Angel au nord de l'Équateur et la partie centrale du système de failles de Romeral (latitude 4°N) suggèrent un ordre de grandeur de 2-3 mm/an, une contribution relativement faible qui n'aura pas d'effets significatifs sur la cinématique globale du modèle.

Par ailleurs, malgré le nombre réduit d'observations GPS autour de la frontière Panama/NAS, notre modèle nous permet de capter le signal principal de la déformation produite par cette collision continentale. Cependant, notre modèle n'est pas capable de séparer les contributions de la subduction de la plaque Caraïbe et de la collision sur la structure de San Jacinto (San Jacinto Fold Belt). De nouvelles observations GPS sont nécessaires pour nous permettre d'évaluer plus précisément cette question.

Notre modèle cinématique permet de bien contraindre la cinématique des failles crustales les plus rapides. Cependant, en dehors de quelques zones bien échantillonnées spatialement, il ne permet pas de contraindre précisément les profondeurs de blocage des failles et plus généralement de bien estimer les taux d'accumulation de moment sur ces failles.

Dans cette étude, mon travail s'est limité à l'aspect cinématique. Néanmoins, le champ de vitesse GPS obtenu et les conditions cinématiques aux limites des Andes du Nord constituent un jeu de données essentiel pour les futures interprétations et modélisations physiques de ces zones, ainsi que pour comprendre son évolution sur les échelles de temps géologiques.

Cycle sismique dans les Andes du Nord

En ce qui concerne la modélisation du couplage inter-sismique, je propose dans ma thèse des modèles estimés simultanément avec la cinématique du Sliver Nord Andin. Les variations latérales du couplage montrent au premier ordre : (1) une corrélation du fort couplage avec les zones de segmentations sismotectoniques dérivées des grandes ruptures sismiques, et (2) une corrélation du couplage faible ou partiel avec des zones de transition où l'on observe la présence d'épisodes de glissements asismiques transitoires (SSE pour Slow Slip Event) récurrents. Ces corrélations dans les zones de transition nous incitent à réfléchir sur la capacité des observations géodésiques à

distinguer entre un couplage long-terme et un couplage court-terme sur l'interface de subduction. Par conséquent, il reste à mener une analyse plus détaillée sur la relation entre glissements asismiques transitoires et couplage.

Une première approche que je propose est d'utiliser les vitesses résiduelles par rapport au mouvement du Sliver Nord Andin et de réaliser une inversion qui permet de prendre en compte les incertitudes, comme les méthodes bayésiennes. Cela nous permettra d'évaluer plus précisément les incertitudes du couplage inter-sismique et la capacité des données à contraindre le couplage peu profond et proche de la fosse. Dans une deuxième étape, le calcul du moment sur l'interface va permettre une réflexion en termes de l'accumulation de contraintes et sa relation avec le risque sismique.

La carte de couplage inter-sismique nous permet également de réfléchir sur le fonctionnement du cycle sismique en Equateur-Colombie. En général, on postule, dans la vision classique du cycle sismique, que la phase inter-sismique est composée d'un état constant de chargement des contraintes pendant de longues périodes de temps. Il existe cependant dans la phase inter-sismique des périodes transitoires où des glissements lents sont observés. Le long de la marge équatorienne, ces deux comportements durant la phase inter-sismique sont identifiés dans les séries temporelles géodésiques, et ont des temporalités différentes. On observe, sur le segment de la Plata, trois SSEs avec des temps de récurrence courts ($\sim$3 ans), tandis que sur le grand segment de Bahia-Tumaco, on observe un SSE en 2014 et peut-être un autre en 2007. Il reste de plus à développer une analyse fine des séries temporelles pour détecter les SSEs de faible magnitude. Notre modèle de couplage montre le couplage statique moyen capturé par les mesures géodésiques, car il est basé sur l'hypothèse que le taux d'accumulation des contraintes sur l'interface est constant avant et après les SSEs. Je propose d'analyser ces variations de vitesse inter-sismique et l'impact des SSEs de manière plus détaillée et plus systématique. Enfin, notre modèle ouvre la perspective d'identifier des glissements lents dans les données de campagnes, en comparant les déplacements observés à ceux prédits par notre modèle, et donc de caractériser des SSEs qui ont eu lieu avant 2008. C'est un travail d'analyse qu'il reste à faire. Pour les raisons discutées précédemment et pour conclure, le travail présenté dans cette thèse constitue un élément important pour les futures études du cycle sismique dans les Andes du Nord.

Bibliography

Abe, K. (1979). Size of great earthquakes of 1837–1974 inferred from tsunami data. *Journal of Geophysical Research: Solid Earth*, 84(B4):1561–1568. Publisher: John Wiley & Sons, Ltd.

Acosta, J., Velandia, F., Osorio, J., Lonergan, L., and Mora, H. (2007). Strike-slip deformation within the Colombian Andes. In Ries, A. C., Butler, R. W. H., and Graham, R. H., editors, *Deformation of the Continental Crust: The Legacy of Mike Coward*, volume 272, page 0. Geological Society of London.

Adamek, S., Frohlich, C., and Pennington, W. D. (1988). Seismicity of the Caribbean-Nazca Boundary: Constraints on microplate tectonics of the Panama region. *Journal of Geophysical Research: Solid Earth*, 93(B3):2053–2075. _eprint: https://agupubs.onlinelibrary.wiley.com/doi/pdf/10.1029/JB093iB03p02053.

Agnew, D. C. (1992). The time-domain behavior of power-law noises. *Geophysical Research Letters*, 19(4):333–336. n/a.

Altamimi, Z., Métivier, L., and Collilieux, X. (2012). Itrf2008 plate motion model. *Journal of Geophysical Research: Solid Earth*, 117(B7).

Altamimi, Z., Métivier, L., Rebischung, P., Rouby, H., and Collilieux, X. (2017). ITRF2014 plate motion model. *Geophysical Journal International*, 209(3):1906–1912.

Altamimi, Z., Rebischung, P., Métivier, L., and Collilieux, X. (2016). Itrf2014: A new release of the international terrestrial reference frame modeling nonlinear station motions. *Journal of Geophysical Research: Solid Earth*, 121(8):6109–6131.

Altamimi, Z., Sillard, P., and Boucher, C. (2002). Itrf2000: A new release of the international terrestrial reference frame for earth science applications. *Journal of Geophysical Research: Solid Earth*, 107(B10):ETG 2–1–ETG 2–19.

Alvarado, A., Audin, L., Nocquet, J. M., Jaillard, E., Mothes, P., Jarrin, P., Segovia, M., Rolandone, F., and Cisneros, D. (2016). Partitioning of oblique convergence in the northern andes subduction zone: Migration history and the present-day boundary of the north andean sliver in ecuador. *Tectonics*, 35(5):1048–1065.

Alvarado, A., Audin, L., Nocquet, J. M., Lagreulet, S., Segovia, M., Font, Y., Lamarque, G., Yepes, H., Mothes, P., Rolandone, F., Jarrín, P., and Quidelleur, X. (2014). Active tectonics in Quito,

Ecuador, assessed by geomorphological studies, GPS data, and crustal seismicity. *Tectonics*, 33(2):67–83. Publisher: John Wiley & Sons, Ltd.

Alvarado, A., Ruiz, M., Mothes, P., Yepes, H., Segovia, M., Vaca, M., Ramos, C., Enríquez, W., Ponce, G., Jarrín, P., Aguilar, J., Acero, W., Vaca, S., Singaucho, J. C., Pacheco, D., and Córdova, A. (2018). Seismic, volcanic, and geodetic networks in ecuador: Building capacity for monitoring and research. *Seismological Research Letters*, 89(2A):432.

Amelung, F., Jónsson, S., Zebker, H., and Segall, P. (2000). Widespread uplift and trapdoor faulting on Galápagos volcanoes observed with radar interferometry. *Nature*, 407:993–996.

Angermann, D., Klotz, J., and Reigber, C. (1999). Space-geodetic estimation of the nazca-south america euler vector. *Earth and Planetary Science Letters*, 171(3):329 – 334.

Argus, D. F., Gordon, R. G., Heflin, M. B., Ma, C., Eanes, R. J., Willis, P., Peltier, W. R., and Owen, S. E. (2010). The angular velocities of the plates and the velocity of Earth's centre from space geodesy. *Geophysical Journal International*, 180(3):913–960.

Árnadóttir, T., Lund, B., Jiang, W., Geirsson, H., Björnsson, H., Einarsson, P., and Sigurdsson, T. (2009). Glacial rebound and plate spreading: results from the first countrywide GPS observations in Iceland. *Geophysical Journal International*, 177(2):691–716. Publisher: John Wiley & Sons, Ltd.

Audemard, F. (2014). Active block tectonics in and around the Caribbean: A Review. In *TheNorth-eastern Limit of the South American Plate - Lithospheric Structures fromSurface to the Mantle*, pages 29–77. Editorial Innovación Tecnológica.

Audemard, F., Machette, M., Cox, J., Dart, R., and Haller, K. (2000). Open-File Report. Open-File Report, U.S. Geological Survey (USGS). Series: Open-File Report.

Audemard, F., Ollarves, R., Bechtold, M., Díaz, G., Beck, C., Carrillo, E., Pantosti, D., and Diederix, H. (2008). Trench investigation on the main strand of the Boconó fault in its central section, at Mesa del Caballo, Mérida Andes, Venezuela. *Tectonophysics*, 459(1):38–53.

Audemard, F. A. (2009). Key issues on the post-Mesozoic Southern Caribbean Plate boundary. In *The Origin and Evolution of the Caribbean Plate*. Geological Society of London.

Audemard, F. A. M. (1996). Paleoseismicity studies on the Oca-Ancón fault system, northwestern Venezuela. *Tectonophysics*, 259(1):67–80.

Audemard, F. E. and Audemard, F. A. (2002). Structure of the Mérida Andes, Venezuela: relations with the South America–Caribbean geodynamic interaction. *Tectonophysics*, 345(1):1 – 26.

Baby, P., Calderón, Y., Brusset, S., Roddaz, M., Brichau, S., Eude, A., Calves, G., Calderón, Y., Quispe, A., Ramirez, L., Bandach, A., Bolaños, R., Hurtado, C., Louterbach, M., and Espurt, N. (2018). Chapter 4: The Peruvian Sub-Andean Foreland Basin System: Structural Overview,

Geochronologic Constraints, and Unexplored Plays. *AAPG*, pages 91–119. Publisher: AAPG Special Volumes.

Baby, P., Rochat, P., Mascle, G., and Hérail, G. (1997). Neogene shortening contribution to crustal thickening in the back arc of the Central Andes. *Geology*, 25(10):883–886.

Bagnardi, M. and Amelung, F. (2012). Space-geodetic evidence for multiple magma reservoirs and subvolcanic lateral intrusions at Fernandina Volcano, Galápagos Islands. *Journal of Geophysical Research: Solid Earth*, 117(B10).

Baize, S., Audin, L., Alvarado, A., Jomard, H., Bablon, M., Champenois, J., Espin, P., Samaniego, P., Quidelleur, X., and Le Pennec, J.-L. (2020). Active Tectonics and Earthquake Geology Along the Pallatanga Fault, Central Andes of Ecuador. *Frontiers in Earth Science*, 8:193.

Baize, S., Audin, L., Winter, T., Alvarado, A., Moreno, L. P., Taipe, M., Reyes, P., Kauffmann, P., and Yepes, H. (2015). Paleoseismology and tectonic geomorphology of the Pallatanga fault (Central Ecuador), a major structure of the South-American crust. *Geomorphology*, 237:14 – 28.

Baker, M. S. (2012). *Investigating the Dynamics of Basaltic Volcano Magmatic Systems with Space Geodesy*. PhD thesis, University of Miami.

Beauval, C., Marinière, J., Yepes, H., Audin, L., Nocquet, J., Alvarado, A., Baize, S., Aguilar, J., Singaucho, J., and Jomard, H. (2018). A New Seismic Hazard Model for Ecuador. *Bulletin of the Seismological Society of America*, 108(3A):1443–1464. _eprint: https://pubs.geoscienceworld.org/bssa/article-pdf/108/3A/1443/4190001/bssa-2017259.1.pdf.

Beauval, C., Yepes, H., Bakun, W. H., Egred, J., Alvarado, A., and Singaucho, J.-C. (2010). Locations and magnitudes of historical earthquakes in the Sierra of Ecuador (1587–1996). *Geophysical Journal International*, 181(3):1613–1633. _eprint: https://onlinelibrary.wiley.com/doi/pdf/10.1111/j.1365-246X.2010.04569.x.

Beauval, C., Yepes, H., Palacios, P., Segovia, M., Alvarado, A., Font, Y., Aguilar, J., Troncoso, L., and Vaca, S. (2013). An Earthquake Catalog for Seismic Hazard Assessment in Ecuador. *Bulletin of the Seismological Society of America*, 103(2A):773–786.

Beck, S. L. and Ruff, L. J. (1984). The rupture process of the Great 1979 Colombia Earthquake: Evidence for the asperity model. *J. Geophys. Res.*, 89(B11):9281.

Behn, M. D. and Ito, G. (2008). Magmatic and tectonic extension at mid-ocean ridges: 1. Controls on fault characteristics. *Geochemistry, Geophysics, Geosystems*, 9(8). Publisher: John Wiley & Sons, Ltd.

Bernal-Olaya, R., Mann, P., and Vargas, C. A. (2015). Earthquake, Tomographic, Seismic Reflection, and Gravity Evidence for a Shallowly Dipping Subduction Zone beneath the Caribbean Margin of Northwestern Colombia. In Bartolini, C. and Mann, P., editors, *Petroleum Geology and Potential of the Colombian Caribbean Margin*, volume 108, page 0. American Association of Petroleum Geologists.

Bevis, M. and Brown, A. (2014). Trajectory models and reference frames for crustal motion geodesy. *Journal of Geodesy*, 88(3):283–311.

Bird, P. (2003). An updated digital model of plate boundaries. *Geochemistry, Geophysics, Geosystems*, 4(3). Publisher: John Wiley & Sons, Ltd.

Blewitt, G., Hammond, W., and Kreemer, C. (2018). Harnessing the GPS Data Explosion for Interdisciplinary Science. *Eos*, 99.

Blewitt, G., Kreemer, C., Hammond, W. C., and Gazeaux, J. (2016). Midas robust trend estimator for accurate gps station velocities without step detection. *Journal of Geophysical Research: Solid Earth*, 121(3):2054–2068.

Blewitt, G. and Lavallée, D. (2002). Effect of annual signals on geodetic velocity. *Journal of Geophysical Research: Solid Earth*, 107(B7):ETG 9–1–ETG 9–11.

Blewitt, G., Lavallée, D., Clarke, P., and Nurutdinov, K. (2002). A new global mode of earth deformation: Seasonal cycle detected. *Science (New York, N.Y.)*, 294:2342–5.

Boehm, J., Werl, B., and Schuh, H. (2006). Troposphere mapping functions for gps and very long baseline interferometry from european centre for medium-range weather forecasts operational analysis data. *Journal of Geophysical Research: Solid Earth*, 111(B2).

Bos, M. S. and Fernandes, R. M. S. (2015). Investigation of Random Walk Noise in GNSS Time-series. In *AGU Fall Meeting Abstracts*, pages G13A–0990. AGU.

Bos, M. S., Fernandes, R. M. S., Williams, S. D. P., and Bastos, L. (2013). Fast error analysis of continuous GNSS observations with missing data. *Journal of Geodesy*, 87(4):351–360.

Bougrine, A., Yelles-Chaouche, A. K., and Calais, E. (2019). Active deformation in Algeria from continuous GPS measurements. *Geophysical Journal International*, 217(1):572–588.

Brooks, B. A., Bevis, M., Smalley Jr., R., Kendrick, E., Manceda, R., Lauría, E., Maturana, R., and Araujo, M. (2003). Crustal motion in the Southern Andes (26°–36°S): Do the Andes behave like a microplate? *Geochemistry, Geophysics, Geosystems*, 4(10). Publisher: John Wiley & Sons, Ltd.

Brooks, B. A., Bevis, M., Whipple, K., Ramon Arrowsmith, J., Foster, J., Zapata, T., Kendrick, E., Minaya, E., Echalar, A., Blanco, M., Euillades, P., Sandoval, M., and Smalley, R. J. (2011). Orogenic-wedge deformation and potential for great earthquakes in the central Andean backarc. *Nature Geoscience*, 4(6):380–383.

Báez, J. C., Leyton, F., Troncoso, C., del Campo, F., Bevis, M., Vigny, C., Moreno, M., Simons, M., Kendrick, E., Parra, H., and Blume, F. (2018). The Chilean GNSS Network: Current Status and Progress toward Early Warning Applications. *Seismological Research Letters*, 89(4):1546–1554. _eprint: https://pubs.geoscienceworld.org/srl/article-pdf/89/4/1546/4228856/srl-2018011.1.pdf.

Bès de Berc, S., Soula, J., Baby, P., Souris, M., Christophoul, F., and Rosero, J. (2005). Geomorphic evidence of active deformation and uplift in a modern continental wedge-top–foredeep transition: Example of the eastern Ecuadorian Andes. *Tectonophysics*, 399(1):351–380.

Calais, E. (1999). Continuous GPS measurements across the Western Alps, 1996–1998. *Geophysical Journal International*, 138(1):221–230.

Calderón, Y., Baby, P., Hurtado, C., Bolaños, R., and Bandach, A. (2013). PRE CRETACEOUS FOLD AND THRUST BELTS IN THE MARANON BASIN. *INGEPET (GEO-EX-YC-15-N)*, page 4.

Cediel, F., Shaw, R. P., and Cáceres, C. (2003). Tectonic Assembly of the Northern Andean Block. In *The Circum-Gulf of Mexico and the Caribbean: Hydrocarbon Habitats, Basin Formation and Plate Tectonics*. American Association of Petroleum Geologists.

Chadwick, Jr., W. W., Geist, D. J., Jónsson, S., Poland, M., Johnson, D. J., and Meertens, C. M. (2006). A volcano bursting at the seams: Inflation, faulting, and eruption at Sierra Negra volcano, Galápagos. *Geology*, 34(12):1025–1028.

Chlieh, M., Beauval, C., Yepes, H., Marinière, J., Saillard, M., and Audin, L. (2021). Seismic and Aseismic Cycle of the Ecuador–Colombia Subduction Zone. *Frontiers in Earth Science*, 9:685.

Chlieh, M., Mothes, P. A., Nocquet, J.-M., Jarrin, P., Charvis, P., Cisneros, D., Font, Y., Collot, J.-Y., Villegas-Lanza, J.-C., Rolandone, F., Vallée, M., Regnier, M., Segovia, M., Martin, X., and Yepes, H. (2014). Distribution of discrete seismic asperities and aseismic slip along the Ecuadorian megathrust. *Earth and Planetary Science Letters*, 400:292 – 301.

Choy, J. E., Palme, C., Guada, C., Morandi, M., and Klarica, S. (2010). Macroseismic Interpretation of the 1812 Earthquakes in Venezuela Using Intensity Uncertainties and A Priori Fault-Strike Information. *Bulletin of the Seismological Society of America*, 100(1):241–255.

Collot, J.-Y., Sanclemente, E., Nocquet, J.-M., Leprêtre, A., Ribodetti, A., Jarrin, P., Chlieh, M., Graindorge, D., and Charvis, P. (2017). Subducted oceanic relief locks the shallow megathrust in central Ecuador. *Journal of Geophysical Research: Solid Earth*, 122(5):3286–3305. Publisher: John Wiley & Sons, Ltd.

Colón, S., Audemard, F., Beck, C., Avila, J., Padrón, C., De Batist, M., Paolini, M., Leal, A., and Van Welden, A. (2015). The 1900 Mw 7.6 earthquake offshore north–central Venezuela: Is La Tortuga or San Sebastián the source fault? *Marine and Petroleum Geology*, 67:498–511.

Community, U. (2008). COCONet GPS Network: Station CN00 and 45 Others. type: dataset.

DeMets, C., Gordon, R. G., and Argus, D. F. (2010). Geologically current plate motions. *Geophysical Journal International*, 181(1):1–80.

DeMets, C., Gordon, R. G., Argus, D. F., and Stein, S. (1990). Current plate motions. *Geophysical Journal International*, 101(2):425–478.

DeMets, C., Gordon, R. G., Argus, D. F., and Stein, S. (1994). Effect of recent revisions to the geomagnetic reversal time scale on estimates of current plate motions. *Geophysical Research Letters*, 21(20):2191–2194.

Di Giacomo, D., Bondár, I., Storchak, D. A., Engdahl, E. R., Bormann, P., and Harris, J. (2015). ISC-GEM: Global Instrumental Earthquake Catalogue (1900–2009), III. Re-computed MS and mb, proxy MW, final magnitude composition and completeness assessment. *Physics of the Earth and Planetary Interiors*, 239:33–47.

Diederix, H., Bohórquez, O. P., Mora-Paez, H., Peláez-Gaviria, J.-R., Cardona-Piedrahita, L., Corchuelo-Cuervo, Y., Ramírez-Cadena, J., and Díaz-Mila, F. (2020). Quaternary Activity of the Bucaramanga Fault in the Departments of Santander and Cesar. *Gómez, J. & Pinilla–Pachon*, Capter 13, Volume 4 Quaternary:453–477.

Diederix, H., Bohórquez-Orozco, O., Gómez-Hurtado, E., Idárraga-García, J., Rendón-Rivera, A., Audemard, F., and Mora-Páez, H. (2021). Paleoseismologic trenching confirms recent Holocene activity of the major Algeciras fault system in southern Colombia. *Journal of South American Earth Sciences*, 109:103263.

Dimaté, C., Rivera, L., and Cisternas, A. (2005). Re-visiting large historical earthquakes in the Colombian Eastern Cordillera. *Journal of Seismology*, 9(1):1–22.

Dong, D., Fang, P., Bock, Y., Cheng, M. K., and Miyazaki, S. (2002). Anatomy of apparent seasonal variations from gps-derived site position time series. *Journal of Geophysical Research: Solid Earth*, 107(B4):ETG 9–1–ETG 9–16.

Dow, J., Neilan, R., and Rizos, C. J. (2009). The international gnss service in a changing landscape of global navigation satellite systems. *Journal of Geodesy*, 83:191–198.

Dumont, J., Santana, E., Vilema, W., Pedoja, K., Ordóñez, M., Cruz, M., Jiménez, N., and Zambrano, I. (2005). Morphological and microtectonic analysis of Quaternary deformation from Puná and Santa Clara Islands, Gulf of Guayaquil, Ecuador (South America). *Andean Geodynamics:*, 399(1):331–350.

Duputel, Z., Jiang, J., Jolivet, R., Simons, M., Rivera, L., Ampuero, J.-P., Riel, B., Owen, S. E., Moore, A. W., Samsonov, S. V., Ortega Culaciati, F., and Minson, S. E. (2015). The iquique earthquake sequence of april 2014: Bayesian modeling accounting for prediction uncertainty. *Geophysical Research Letters*, 42(19):7949–7957.

Duque-Caro, H. (1990). The choco block in the northwestern corner of South America: Structural, tectonostratigraphic, and paleogeographic implications. *Journal of South American Earth Sciences*, 3(1):71–84.

Egbue, O. and Kellogg, J. (2010). Pleistocene to Present North Andean "escape". *Tectonophysics*, 489(1):248–257.

Ego, F., Sébrier, M., and Yepes, H. (1995). Is the Cauca-Patia and Romeral Fault System left or rightlateral? *Geophysical Research Letters*, 22(1):33–36. Publisher: John Wiley & Sons, Ltd.

Eguez, A., Alvarado, A., Yepes, H. d. J. M., Machette, M. N., Costa, C., and Dart, R. L. (2003). Database and map of Quaternary faults and folds of Ecuador and its offshore regions. Report 2003-289, U.S. Geological Survey (USGS).

Ekström, G., Nettles, M., and Dziewoński, A. (2012). The global CMT project 2004–2010: Centroid-moment tensors for 13,017 earthquakes. *Physics of the Earth and Planetary Interiors*, 200-201:1–9.

Elliott, J. L., Larsen, C. F., Freymueller, J. T., and Motyka, R. J. (2010). Tectonic block motion and glacial isostatic adjustment in southeast Alaska and adjacent Canada constrained by GPS measurements. *Journal of Geophysical Research: Solid Earth*, 115(B9). Publisher: John Wiley & Sons, Ltd.

Engdahl, E. R., Di Giacomo, D., Sakarya, B., Gkarlaouni, C. G., Harris, J., and Storchak, D. A. (2020). ISC-EHB 1964–2016, an Improved Data Set for Studies of Earth Structure and Global Seismicity. *Earth and Space Science*, 7(1):e2019EA000897. Publisher: John Wiley & Sons, Ltd.

Engeln, J. F. and Stein, S. (1984). Tectonics of the Easter plate. *Earth and Planetary Science Letters*, 68(2):259–270.

Eude, A., Roddaz, M., Brichau, S., Brusset, S., Calderon, Y., Baby, P., and Soula, J.-C. (2015). Controls on timing of exhumation and deformation in the northern Peruvian eastern Andean wedge as inferred from low-temperature thermochronology and balanced cross section. *Tectonics*, 34(4):715–730. Publisher: John Wiley & Sons, Ltd.

Fiorini, E. and Tibaldi, A. (2012). Quaternary tectonics in the central Interandean Valley, Ecuador: Fault-propagation folds, transfer faults and the Cotopaxi Volcano. *Global and Planetary Change*, 90-91:87–103.

Font, Y., Barros-Lopez, J., Hernandez, M. J., Collot, J.-Y., Alvarado, A., Michaud, F., and Marcaillou, B. (2019). *Slab curvature in Ecuador and plate interface geometry.* Published: 8th International Symposium on Andean Geodynamics (ISAG).

Font, Y., Segovia, M., Vaca, S., and Theunissen, T. (2013). Seismicity patterns along the Ecuadorian subduction zone: new constraints from earthquake location in a 3-D a priori velocity model. *Geophysical Journal International*, 193(1):263–286.

Freymueller, J. T., Kellogg, J. N., and Vega, V. (1993). Plate Motions in the north Andean region. *Journal of Geophysical Research: Solid Earth*, 98(B12):21853–21863.

Frohlich, C. and Davis, S. D. (1999). How well constrained are well-constrained T, B, and P axes in moment tensor catalogs? *Journal of Geophysical Research: Solid Earth*, 104(B3):4901–4910. Publisher: John Wiley & Sons, Ltd.

Galetto, F., Bagnardi, M., Acocella, V., and Hooper, A. (2019). Noneruptive unrest at the caldera of alcedo volcano (Galápagos islands) revealed by insar data and geodetic modeling. *Journal of Geophysical Research: Solid Earth*, 124(4):3365–3381.

Geist, D. J., Harpp, K. S., Naumann, T. R., Poland, M. P., Chadwick, W. W., Hall, M., and Rader, E. (2008). The 2005 eruption of sierra negra volcano, galápagos, ecuador. *Bulletin of Volcanology*, 70:655–673.

Gombert, B., Duputel, Z., Jolivet, R., Rivera, L., Simons, M., Jiang, J., Liang, C., and Fielding, E. (2018). A stochastic view on the strain budget of the Ecuador-Columbia subduction zone. In *EGU General Assembly Conference Abstracts*, EGU General Assembly Conference Abstracts, page 13759.

Griffiths, J. (2019). Combined orbits and clocks from IGS second reprocessing. *Journal of Geodesy*, 93(2):177–195.

Gutscher, M.-A., Malavieille, J., Lallemand, S., and Collot, J.-Y. (1999). Tectonic segmentation of the North Andean margin: impact of the Carnegie Ridge collision. *Earth and Planetary Science Letters*, 168(3):255–270.

Hayes, G. (2018). Slab2 - A Comprehensive Subduction Zone Geometry Model. type: dataset.

Hayes, G. P., Wald, D. J., and Johnson, R. L. (2012). Slab1.0: A three-dimensional model of global subduction zone geometries. *Journal of Geophysical Research: Solid Earth*, 117(B1). Publisher: John Wiley & Sons, Ltd.

He, P., Hetland, E. A., Wang, Q., Ding, K., Wen, Y., and Zou, R. (2017). Coseismic Slip in the 2016 Mw 7.8 Ecuador Earthquake Imaged from Sentinel-1A Radar Interferometry. *Seismological Research Letters*, 88(2A):277–286.

Herring, T. A., Floyd, M. A., King, R. W., and McClusky, S. C. (2015). Global Kalman filter VLBI and GPS analysis program Release 10.6. Technical report, MIT.

Herring, T. A., King, R. W., Floyd, M. A., and McClusky, S. C. (2018). *Introduction Gamit Globk*. MIT, release 10.7 edition.

Hilst, R. v. d. and Mann, P. (1994). Tectonic implications of tomographic images of subducted lithosphere beneath northwestern South America. *Geology*, 22(5):451–454.

Holtkamp, S. G., Pritchard, M. E., and Lohman, R. B. (2011). Earthquake swarms in South America. *Geophysical Journal International*, 187(1):128–146.

Jarrin, P., Nocquet, J. M., Rolandone, F., and Mothes, P. A. (2016). Interseismic velocity field and coupling along the Ecuador Subduction interface in relation to the 2016 Pedernales Earthquake. In *AGU Fall Meeting Abstracts*, volume 2016, pages T51E–2978.

Johnston, G., Riddell, A., and Hausler, G. (2017). The International GNSS Service. In Teunissen, Peter J.G., & Montenbruck, O. (Eds.). In *IGS*, pages 967–982. Springer International Publishing, Cham, Switzerland, 1st edition.

Kanamori, H. and McNally, K. C. (1982). Variable rupture mode of the subduction zone along the Ecuador-Colombia coast. *Bulletin of the Seismological Society of America*, 72(4):1241–1253.

Kellogg, J. N. and Bonini, W. E. (1982). Subduction of the Caribbean Plate and basement uplifts in the overriding South American Plate. *Tectonics*, 1(3):251–276. _eprint: https://agupubs.onlinelibrary.wiley.com/doi/pdf/10.1029/TC001i003p00251.

Kellogg, J. N., Camelio, G. B. F., and Mora-Páez, H. (2019). Chapter 4 - Cenozoic tectonic evolution of the North Andes with constraints from volcanic ages, seismic reflection, and satellite geodesy. In Horton, B. K. and Folguera, A., editors, *Andean Tectonics*, pages 69–102. Elsevier.

Kellogg, J. N. and Mohriak, W. U. (2001). The Tectonic and Geological Environment of Coastal South America. In Seeliger, U. and Kjerfve, B., editors, *Coastal Marine Ecosystems of Latin America*, pages 1–16. Springer Berlin Heidelberg, Berlin, Heidelberg.

Kellogg, J. N. and Vega, V. (1995). Tectonic development of Panama, Costa Rica, and the Colombian Andes: Constraints from Global Positioning System geodetic studies and gravity. In *Geological Society of America Special Papers*, volume 295, pages 75–90. Geological Society of America.

Kendrick, E., Bevis, M., Smalley, R., Brooks, B., Vargas, R. B., Lauría, E., and Fortes, L. P. S. (2003). The nazca-south america euler vector and its rate of change. *Journal of South American Earth Sciences*, 16(2):125 – 131.

Khazaradze, G., Wang, K., Klotz, J., Hu, Y., and He, J. (2002). Prolonged post-seismic deformation of the 1960 great Chile earthquake and implications for mantle rheology. *Geophysical Research Letters*, 29(22):7–1. Num Pages: 7-4 Publisher: John Wiley & Sons, Ltd.

Klein, E., Fleitout, L., Vigny, C., and Garaud, J. (2016). Afterslip and viscoelastic relaxation model inferred from the large-scale post-seismic deformation following the 2010 Mw 8.8 Maule earthquake (Chile). *Geophysical Journal International*, 205(3):1455–1472.

Klein, E., Vigny, C., Fleitout, L., Grandin, R., Jolivet, R., Rivera, E., and Métois, M. (2017). A comprehensive analysis of the illapel 2015 mw8.3 earthquake from gps and insar data. *Earth and Planetary Science Letters*, 469:123 – 134.

Kobayashi, D., LaFemina, P., Geirsson, H., Chichaco, E., Abrego, A. A., Mora, H., and Camacho, E. (2014). Kinematics of the western Caribbean: Collision of the Cocos Ridge and upper plate deformation. *Geochemistry, Geophysics, Geosystems*, 15(5):1671–1683. _eprint: https://agupubs.onlinelibrary.wiley.com/doi/pdf/10.1002/2014GC005234.

Kroehler, M. E., Mann, P., Escalona, A., and Christeson, G. L. (2011). Late Cretaceous-Miocene diachronous onset of back thrusting along the South Caribbean deformed belt and its importance for understanding processes of arc collision and crustal growth. *Tectonics*, 30(6). _eprint: https://agupubs.onlinelibrary.wiley.com/doi/pdf/10.1029/2011TC002918.

Kruse, S. E., Liu, Z. J., Naar, D. F., and Duncan, R. A. (1997). Effective elastic thickness of the lithosphere along the Easter Seamount Chain. *Journal of Geophysical Research: Solid Earth*, 102(B12):27305–27317. Publisher: John Wiley & Sons, Ltd.

Kumar, R. R. and Gordon, R. G. (2009). Horizontal thermal contraction of oceanic lithosphere: The ultimate limit to the rigid plate approximation. *Journal of Geophysical Research: Solid Earth*, 114(B1).

Langbein, J. (2004). Noise in two-color electronic distance meter measurements revisited. *Journal of Geophysical Research: Solid Earth*, 109(B4).

Lavenu, A., Winter, T., and Dávila, F. (1995). A Pliocene–Quaternary compressional basin in the Interandean Depression, Central Ecuador. *Geophysical Journal International*, 121(1):279–300.

Legrand, D., Baby, P., Bondoux, F., Dorbath, C., Bès de Berc, S., and Rivadeneira, M. (2005). The 1999–2000 seismic experiment of Macas swarm (Ecuador) in relation with rift inversion in Subandean foothills. *Tectonophysics*, 395(1):67–80.

Lizarazo, S. C., Sagiya, T., and Mora-Páez, H. (2021). Interplate coupling along the Caribbean coast of Colombia and its implications for seismic/tsunami hazards. *Journal of South American Earth Sciences*, 110:103332.

Lonsdale, P. (2005). Creation of the Cocos and Nazca plates by fission of the Farallon plate. *Tectonophysics*, 404(3):237–264.

Lonsdale, P. and Klitgord, K. D. (1978). Structure and tectonic history of the eastern Panama Basin. *GSA Bulletin*, 89(7):981–999.

Lowrie, W. (2007). *The Earth as a planet*, page 1–42. Cambridge University Press, 2 edition.

Lui, Z. (1996). *The origin and evolution of the Easter seamount chain*. PhD thesis, University of South Florida.

Lyard, F., Lefevre, F., Letellier, T., and Francis, O. (2006). Modelling the global ocean tides: modern insights from FES2004. *Ocean Dynamics*, 56(5):394–415.

Machare, J., Fenton, C. H., Machette, M. N., Lavenu, A., Costa, C., and Dart, R. L. (2003). Database and Map of Quaternary Faults and Folds in Peru and its Offshore Region. Report 2003-451, U.S. Geological Survey (USGS). Edition: Version 1.1.

Mao, A., Harrison, C. G. A., and Dixon, T. H. (1999). Noise in gps coordinate time series. *Journal of Geophysical Research: Solid Earth*, 104(B2):2797–2816.

Marcaillou, B., Charvis, P., and Collot, J.-Y. (2006). Structure of the Malpelo Ridge (Colombia) from seismic and gravity modelling. *Marine Geophysical Researches*, 27(4):289–300.

Mariniere, J., Beauval, C., Nocquet, J., Chlieh, M., and Yepes, H. (2021). Earthquake Recurrence Model for the Colombia–Ecuador Subduction Zone Constrained from Seismic and Geodetic Data, Implication for PSHA. *Bulletin of the Seismological Society of America*, 111(3):1508–1528.

Mariniere, J., Nocquet, J.-M., Beauval, C., Champenois, J., Audin, L., Alvarado, A., Baize, S., and Socquet, A. (2019). Geodetic evidence for shallow creep along the Quito fault, Ecuador. *Geophysical Journal International*, 220(3):2039–2055.

McCaffrey, R. (1992). Oblique plate convergence, slip vectors, and forearc deformation. *Journal of Geophysical Research: Solid Earth*, 97(B6):8905–8915. Publisher: John Wiley & Sons, Ltd.

Mccaffrey, R. (2002). Crustal Block Rotations and Plate Coupling. In *Plate Boundary Zones*, pages 101–122. American Geophysical Union (AGU). _eprint: https://agupubs.onlinelibrary.wiley.com/doi/pdf/10.1029/GD030p0101.

McCarthy, D. (1996). *IERS Conventions (1996)*. IERS, Observatory of Paris, technical note 21 edition.

McCarthy, D. and Petit, G. (2003). *IERS Conventions (2003)*. IERS Conventions, U.S. Naval Observatory Earth Orientation Departement 3450 Massachusetts Avenue, NW Washington, DC USA, technical note 32 edition.

Meade, B. J. (2007). Algorithms for the calculation of exact displacements, strains, and stresses for triangular dislocation elements in a uniform elastic half space. *Computers & Geosciences*, 33(8):1064–1075.

Meade, B. J. and Hager, B. (2005). Block models of crustal motion in southern California constrained by GPS measurements. *Journal of Geophysical Research*, 110.

Meade, B. J. and Loveless, J. P. (2009). Block modeling with connected fault-network geometries and a linear elastic coupling estimator in spherical coordinates. *Bulletin of the Seismological Society of America*, pages 3124–3139.

Melnick, D., Bookhagen, B., Strecker, M. R., and Echtler, H. P. (2009). Segmentation of megathrust rupture zones from fore-arc deformation patterns over hundreds to millions of years, Arauco peninsula, Chile. *Journal of Geophysical Research: Solid Earth*, 114(B1). Publisher: John Wiley & Sons, Ltd.

Mendoza, C. and Dewey, J. W. (1984). Seismicity associated with the great Colombia-Ecuador earthquakes of 1942, 1958, and 1979: Implications for barrier models of earthquake rupture. *Bulletin of the Seismological Society of America*, 74(2):577–593.

Mishra, J. K. and Gordon, R. G. (2016). The rigid-plate and shrinking-plate hypotheses: Implications for the azimuths of transform faults. *Tectonics*, 35(8):1827–1842. Publisher: John Wiley & Sons, Ltd.

Mooney, W. (2015). Crust and Lithospheric Structure - Global Crustal Structure. In *Treatise on Geophysics*, volume 1, pages 339–372. Elsevier B.V.

Mora, J. A., Oncken, O., Le Breton, E., Ibánez-Mejia, M., Faccenna, C., Veloza, G., Vélez, V., de Freitas, M., and Mesa, A. (2017). Linking Late Cretaceous to Eocene Tectonostratigraphy of the San Jacinto Fold Belt of NW Colombia With Caribbean Plateau Collision and Flat Subduction. *Tectonics*, 36(11):2599–2629. Publisher: John Wiley & Sons, Ltd.

Mora-Páez, H., Kellogg, J. N., Freymueller, J. T., Mencin, D., Fernandes, R. M. S., Diederix, H., LaFemina, P., Cardona-Piedrahita, L., Lizarazo, S., Peláez-Gaviria, J.-R., Díaz-Mila, F., Bohórquez-Orozco, O., Giraldo-Londoño, L., and Corchuelo-Cuervo, Y. (2019). Crustal deformation in the northern Andes – A new GPS velocity field. *Journal of South American Earth Sciences*, 89:76 – 91.

Mora-Páez, H., Peláez-Gaviria, J., Diederix, H., Bohórquez-Orozco, O., Cardona-Piedrahita, L., Corchuelo-Cuervo, Y., Ramírez-Cadena, J., and Díaz-Mila, F. (2018). Space Geodesy Infrastructure in Colombia for Geodynamics Research. *Seismological Research Letters*, 89(2A):446–451.

Moreno, M. S., Klotz, J., Melnick, D., Echtler, H., and Bataille, K. (2008). Active faulting and heterogeneous deformation across a megathrust segment boundary from GPS data, south central Chile (36–39°S). *Geochemistry, Geophysics, Geosystems*, 9(12). Publisher: John Wiley & Sons, Ltd.

Mothes, P. A., Nocquet, J.-M., and Jarrín, P. (2013). Continuous GPS Network Operating Throughout Ecuador. *Eos, Transactions American Geophysical Union*, 94(26):229–231. _eprint: https://agupubs.onlinelibrary.wiley.com/doi/pdf/10.1002/2013EO260002.

Mothes, P. A., Rolandone, F., Nocquet, J., Jarrin, P. A., Alvarado, A. P., Ruiz, M. C., Cisneros, D., Páez, H. M., and Segovia, M. (2018). Monitoring the Earthquake Cycle in the Northern Andes from the Ecuadorian cGPS Network. *Seismological Research Letters*, 89(2A):534–541.

Métois, M., Socquet, A., Vigny, C., Carrizo, D., Peyrat, S., Delorme, A., Maureira, E., Valderas-Bermejo, M.-C., and Ortega, I. (2013). Revisiting the North Chile seismic gap segmentation using GPS-derived interseismic coupling. *Geophysical Journal International*, 194(3):1283–1294.

Nocquet, J. M. (2002). *Mésure de la deformation crustale en Europe occidentale par Geodesie spatiale*. PhD thesis, Université de Nice Sophia Antipolis.

Nocquet, J. M. (2011). *Apport de la Geodesie Spatiale á la Connaissance de la Geodynamique en Europe et en Mediterranee. Habilitation á Diriger des Recherches*. PhD thesis, Université de Nice Sophia Antipolis.

Nocquet, J.-M. (2012). Present-day kinematics of the Mediterranean: A comprehensive overview of GPS results. *Tectonophysics*, 579:220 – 242.

Nocquet, J.-M. (2017). Pyacs: un outils pour l'analyse des données géodésiques. In *Observations géodésiques, spatiales et imagerie satellitaire*, Nice-France. Colloque G2.

Nocquet, J.-M. (2018). Stochastic static fault slip inversion from geodetic data with non-negativity and bound constraints. *Geophysical Journal International*, 214(1):366–385.

Nocquet, J.-M., Calais, E., Altamimi, Z., Sillard, P., and Boucher, C. (2001). Intraplate deformation in western europe deduced from an analysis of the international terrestrial reference frame 1997 (itrf97) velocity field. *Journal of Geophysical Research: Solid Earth*, 106(B6):11239–11257.

Nocquet, J.-M., Jarrin, P., Vallée, M., Mothes, P. A., Grandin, R., Rolandone, F., Delouis, B., Yepes, H., Font, Y., Fuentes, D., Regnier, M., Laurendeau, A., Cisneros, D., Hernandez, S., Sladen, A., Singaucho, J.-C., Mora, H., Gomez, J., Montes, L., and Charvis, P. (2016). Supercycle at the ecuadorian subduction zone revealed after the 2016 pedernales earthquake. *Nature Geoscience*, 10:145 EP.

Nocquet, J.-M., Villegas Lanza, J. C., Chlieh, M., Mothes, P. A., Rolandone, F., Jarrin, P., Cisneros, D., Alvarado, A., Audin, L., Bondoux, F., Martin, X., Font, Y., Régnier, M., Vallée, M., Tran, T., Beauval, C., Mendoza, J. M. M., Martinez, W., Tavera, H., and Yepes, H. (2014). Motion of continental slivers and creeping subduction in the northern Andes. *Nature Geoscience*, 7:287–291.

Norabuena, E. O., Dixon, T. H., Stein, S., and Harrison, C. G. A. (1999). Decelerating Nazca-South America and Nazca-Pacific Plate motions. *Geophysical Research Letters*, 26(22):3405–3408.

Paris, G., Machette, M. N., Dart, R. L., and Haller, K. M. (2000). Map and database of Quaternary faults and folds in Colombia and its offshore regions. Report 2000-284, U.S. Geological Survey (USGS).

Pennington, W. D. (1981). Subduction of the Eastern Panama Basin and seismotectonics of northwestern South America. *Journal of Geophysical Research: Solid Earth*, 86(B11):10753–10770. _eprint: https://agupubs.onlinelibrary.wiley.com/doi/pdf/10.1029/JB086iB11p10753.

Perfettini, H., Avouac, J.-P., and Ruegg, J.-C. (2005). Geodetic displacements and aftershocks following the 2001 mw = 8.4 peru earthquake: Implications for the mechanics of the earthquake cycle along subduction zones. *Journal of Geophysical Research: Solid Earth*, 110(B9).

Perfit, M. R. and Chadwick Jr., W. W. (1998). Magmatism at Mid-Ocean Ridges: Constraints from Volcanological and Geochemical Investigations. In *Faulting and Magmatism at Mid-Ocean Ridges*, pages 59–115. American Geophysical Union (AGU). _eprint: https://agupubs.onlinelibrary.wiley.com/doi/pdf/10.1029/GM106p0059.

Piñón, D. A., Gómez, D. D., Smalley, Jr., R., Cimbaro, S. R., Lauría, E. A., and Bevis, M. G. (2018). The History, State, and Future of the Argentine Continuous Satellite Monitoring Network and Its Contributions to Geodesy in Latin America. *Seismological Research Letters*, 89(2A):475–482.

Pousse-Beltran, L., Vassallo, R., Audemard, F., Jouanne, F., Carcaillet, J., Pathier, E., and Volat, M. (2017). Pleistocene slip rates on the Boconó fault along the North Andean Block plate boundary, Venezuela. *Tectonics*, 36(7):1207–1231. Publisher: John Wiley & Sons, Ltd.

Prawirodirdjo, L. and Bock, Y. (2004). Instantaneous global plate motion model from 12 years of continuous GPS observations. *Journal of Geophysical Research: Solid Earth*, 109(B8). Publisher: John Wiley & Sons, Ltd.

Pérez, O. J., Wesnousky, S. G., De La Rosa, R., Márquez, J., Uzcátegui, R., Quintero, C., Liberal, L., Mora-Páez, H., and Szeliga, W. (2018). On the interaction of the North Andes plate with the Caribbean and South American plates in northwestern South America from GPS geodesy and seismic data. *Geophysical Journal International*, 214(3):1986–2001.

Radiguet, M., Cotton, F., Vergnolle, M., Campillo, M., Valette, B., Kostoglodov, V., and Cotte, N. (2011). Spatial and temporal evolution of a long term slow slip event: the 2006 Guerrero Slow Slip Event. *Geophysical Journal International*, 184(2):816–828. Publisher: John Wiley & Sons, Ltd.

Rebischung, P., Altamimi, Z., Ray, J., and Garayt, B. (2016). The igs contribution to itrf2014. *Journal of Geodesy*, 90(7):611–630.

Rebischung, P. and Schmid, R. (2016). Igs14/igs14.atx: a new framework for the igs products. In *Geodesy*. AGU Fall Meeting.

Rodrigo, C., Díaz, J., and González-Fernández, A. (2014). Origin of the Easter Submarine Alignment: morphology and structural lineaments. *Latin american journal of aquatic research*, 42:857 – 870.

Rolandone, F., Nocquet, J.-M., Mothes, P., Jarrin, P., Vallée, M., Cubas, N., Hernandez, S., Plain, M., Vaca, S., and Font, Y. (2018). Areas prone to slow slip events impede earthquake rupture propagation and promote afterslip. *Science Advances*, 4:eaao6596.

Ruiz, S. and Madariaga, R. (2018). Historical and recent large megathrust earthquakes in Chile. *Tectonophysics*, 733:37–56.

Sagiya, T. and Mora-Paez, H. (2020). Interplate Coupling along the Nazca Subduction Zone on the Pacific Coast of Colombia Deduced from GeoRED GPS Observation Data. *Gómez, J. & Pinilla–Pachon*, Chapter 15 Volume 4:499–513.

SARA project, p. (2021). The South American Earthquake Catalogue. Internet research T4-pre1964 CATALOGUE, The South America Risk Assessment (SARA) project.

Savage, J. C. (1983). A dislocation model of strain accumulation and release at a subduction zone. *Journal of Geophysical Research B: Solid Earth*, 88(B6):4984–4996.

Schmitz, M., Avila, J., Bezada, M., Vieira, E., Yáñez, M., Levander, A., Zelt, C. A., Jácome, M. I., and Magnani, M. B. (2008). Crustal thickness variations in Venezuela from deep seismic observations. *Tectonophysics*, 459(1):14 – 26.

Schubert, C. (1982). Neotectonics of Boconó fault, Western Venezuela. In *Elsevier Scientific Publishing Company*, volume 85, pages 205–220. Tectonophysics.

Segall, P. (2010). *Earthquake and Volcano Deformation*. Princeton University Press, 2010, ilustrada edition.

Segovia, M. (2001). *El sismo de Bahía del 4 de agosto de 1998: Caracterización del mecanismo de ruptura y análisis de la sismicidad en la zona costera. Tesis previa a la obtención de titulo de Ingeniera Geologa*. PhD thesis, Escuela Politécnica Nacional.

Segovia, M., Font, Y., Regnier, M. M., Charvis, P., Nocquet, J. M., Galve, A., Hello, Y., Ogé, A., Jarrin, P., and Ruiz, M. C. (2015). Intense Microseismicity Associated with a SSE at La Plata Island in the Central Subduction Zone of Ecuador. In *AGU Fall Meeting Abstracts*, volume 2015, pages S31A–2736.

Segovia, M., Font, Y., Régnier, M., Charvis, P., Galve, A., Nocquet, J.-M., Jarrín, P., Hello, Y., Ruiz, M., and Pazmiño, A. (2018). Seismicity Distribution Near a Subducting Seamount in the Central Ecuadorian Subduction Zone, Space-Time Relation to a Slow-Slip Event. *Tectonics*, 37(7):2106–2123. _eprint: https://agupubs.onlinelibrary.wiley.com/doi/pdf/10.1029/2017TC004771.

Sella, G. F., Dixon, T. H., and Mao, A. (2002). REVEL: A model for Recent plate velocities from space geodesy. *Journal of Geophysical Research: Solid Earth*, 107(B4):ETG 11–1. Num Pages: ETG 11-30 Publisher: John Wiley & Sons, Ltd.

Sewnson, J. L. and Beck, S. L. (1996). Historical 1942 Ecuador and 1942 Peru subduction earthquakes and earthquake cycles along Colombia-Ecuador and Peru subduction segments. *pure and applied geophysics*, 146(1):67–101.

SGC (2020a). Catálogo Mecanismo Focal y Tensor Momento. Internet research 2020, Servicio Geológico Colombiano.

SGC (2021). Sismicidad Histórica de Colombia. Internet research 2021, Servicio Geológico Colombiano.

SGC, S. (2020b). Catálogo de Sismicidad. Internet research 2020, Servicio Geológico Colombiano.

Soler, T. and Marshall, J. (2003). A note on frame transformations with applications to geodetic datums. *GPS Solutions*, 7(1):23–32.

Stein, S. and Gordon, R. G. (1984). Statistical tests of additional plate boundaries from plate motion inversions. *Earth and Planetary Science Letters*, 69(2):401–412.

Stein, S. and Wysession, M. (2003). *An Introduction to Seismology, Earthquakes, and Earth Structure*. Wiley.

Suito, H. and Freymueller, J. (2009). A viscoelastic and afterslip postseismic deformation model for the 1964 Alaska earthquake. *Journal of Geophysical Research*, 114.

Suter, F., Sartori, M., Neuwerth, R., and Gorin, G. (2008). Structural imprints at the front of the Chocó-Panamá indenter: Field data from the North Cauca Valley Basin, Central Colombia. *Tectonophysics*, 460(1):134 – 157.

Suárez, G., Molnar, P., and Burchfiel, B. C. (1983). Seismicity, fault plane solutions, depth of faulting, and active tectonics of the Andes of Peru, Ecuador, and southern Colombia. *Journal of Geophysical Research: Solid Earth*, 88(B12):10403–10428. Publisher: John Wiley & Sons, Ltd.

Symithe, S., Calais, E., de Chabalier, J. B., Robertson, R., and Higgins, M. (2015). Current block motions and strain accumulation on active faults in the Caribbean. *Journal of Geophysical Research: Solid Earth*, 120(5):3748–3774. _eprint: https://agupubs.onlinelibrary.wiley.com/doi/pdf/10.1002/2014JB011779.

Syracuse, E. M., Maceira, M., Prieto, G. A., Zhang, H., and Ammon, C. J. (2016). Multiple plates subducting beneath Colombia, as illuminated by seismicity and velocity from the joint inversion of seismic and gravity data. *Earth and Planetary Science Letters*, 444:139–149.

Taboada, A., Rivera, L. A., Fuenzalida, A., Cisternas, A., Philip, H., Bijwaard, H., Olaya, J., and Rivera, C. (2000). Geodynamics of the northern Andes: Subductions and intracontinental deformation (Colombia). *Tectonics*, 19(5):787–813. _eprint: https://agupubs.onlinelibrary.wiley.com/doi/pdf/10.1029/2000TC900004.

Tarantola, A. (2005). *Inverse Problem Theory and Methods for Model Parameter Estimation*. Other Titles in Applied Mathematics. Society for Industrial and Applied Mathematics.

Tibaldi, A., Rovida, A., and Corazzato, C. (2007). Late Quaternary kinematics, slip-rate and segmentation of a major Cordillera-parallel transcurrent fault: The Cayambe-Afiladores-Sibundoy system, NW South America. *Journal of Structural Geology*, 29(4):664 – 680.

Trabant, C., Hutko, A. R., Bahavar, M., Karstens, R., Ahern, T., and Aster, R. (2012). Data Products at the IRIS DMC: Stepping Stones for Research and Other Applications. *Seismological Research Letters*, 83(5):846–854.

Tran, D. T. (2013). *Analyse rapide et robuste des solutions GPS pour la tectonique*. PhD thesis, Université de Nice.

Trenkamp, R., Kellogg, J. N., Freymueller, J. T., and Mora, H. P. (2002). Wide plate margin deformation, southern central america and northwestern south america, casa gps observations. *Journal of South American Earth Sciences*, 15:157–171.

UNAVCO (2004). Project Highlights 2004 - Easter Island IGS Station Install and Maintenance. Technical report, UNAVCO.

Vaca, S., Vallée, M., Nocquet, J.-M., and Alvarado, A. (2019). Active deformation in Ecuador enlightened by a new waveform-based catalog of earthquake focal mechanisms. *Journal of South American Earth Sciences*, 93:449 – 461.

Vaca, S., Vallée, M., Nocquet, J.-M., Battaglia, J., and Régnier, M. (2018). Recurrent slow slip events as a barrier to the northward rupture propagation of the 2016 Pedernales earthquake (Central Ecuador). *Tectonophysics*, 724-725:80–92.

Valladares, C. E. and Chau, J. L. (2012). The Low-Latitude Ionosphere Sensor Network: Initial results. *Radio Science*, 47(4). Publisher: John Wiley & Sons, Ltd.

Vallée, M., Nocquet, J.-M., Battaglia, J., Font, Y., Segovia, M., Regnier, M., Mothes, P., Jarrin, P., Cisneros, D., Vaca, S., Yepes, H., Martin, X., Béthoux, N., and Chlieh, M. (2013). Intense interface seismicity triggered by a shallow slow slip event in the central ecuador subduction zone. *Journal of Geophysical Research*, 118:2965–2981.

van Dam, T., Wahr, J., Milly, P. C. D., Shmakin, A. B., Blewitt, G., Lavallée, D., and Larson, K. M. (2001). Crustal displacements due to continental water loading. *Geophysical Research Letters*, 28(4):651–654.

Vargas, C. A. (2019). Subduction Geometries in Northwestern South America. Technical Report 58, Servicio Geológico Colombiano, Bogotá.

Velandia, F., Acosta, J., Terraza, R., and Villegas, H. (2005). The current tectonic motion of the Northern Andes along the Algeciras Fault System in SW Colombia. *Andean Geodynamics:*, 399(1):313–329.

Vezzoli, L. and Acocella, V. (2009). Easter Island, SE Pacific: An end-member type of hotspot volcanism. *GSA Bulletin*, 121(5-6):869–886.

Vigny, C., Rudloff, A., Ruegg, J.-C., Madariaga, R., Campos, J., and Alvarez, M. (2009). Upper plate deformation measured by GPS in the Coquimbo Gap, Chile. *Physics of the Earth and Planetary Interiors*, 175(1):86 – 95.

Vigny, C., Socquet, A., PEYRAT, S., Ruegg, J.-C., Metois, M., Madariaga, R., Morvan, S., Lancieri, M., Lacassin, R., Campos, J., Carrizo, D., Bejar-Pizarro, M., Barrientos, S., Armijo, R., Aranda, C., Valderas-Bermejo, M.-C., Ortega, I., Bondoux, F., Baize, S., Lyon-Caen, H., Pavez, A., Vilotte, J. P., Bevis, M., Brooks, B., Smalley, R., Parra, H., Baez, J.-C., Blanco, M., Cimbaro, S., and Kendrick, E. (2011). The 2010 M-w 8.8 Maule Megathrust Earthquake of Central Chile, Monitored by GPS. *Science*, 332:1417–1421.

Villegas-Lanza, J., Nocquet, J.-M., Rolandone, F., Vallée, M., Tavera, H., Bondoux, F., Tran, T., Martin, X., and Chlieh, M. (2016a). A mixed seismic–aseismic stress release episode in the Andean subduction zone. *Nature Geoscience*, 9(2):150–154.

Villegas-Lanza, J. C., Chlieh, M., Cavalié, O., Tavera, H., Baby, P., Chire-Chira, J., and Nocquet, J.-M. (2016b). Active tectonics of Peru: Heterogeneous interseismic coupling along the Nazca megathrust, rigid motion of the Peruvian Sliver, and Subandean shortening accommodation. *Journal of Geophysical Research: Solid Earth*, 121(10):7371–7394.

Wang, K., Hu, Y., Bevis, M., Kendrick, E., Smalley Jr., R., Vargas, R. B., and Lauría, E. (2007). Crustal motion in the zone of the 1960 Chile earthquake: Detangling earthquake-cycle deformation and forearc-sliver translation. *Geochemistry, Geophysics, Geosystems*, 8(10). _eprint: https://agupubs.onlinelibrary.wiley.com/doi/pdf/10.1029/2007GC001721.

Wdowinski, S., Bock, Y., Zhang, J., Fang, P., and Genrich, J. (1997). Southern california permanent gps geodetic array: Spatial filtering of daily positions for estimating coseismic and postseismic displacements induced by the 1992 landers earthquake. *Journal of Geophysical Research: Solid Earth*, 102(B8):18057–18070.

Weiss, J. R., Brooks, B. A., Foster, J. H., Bevis, M., Echalar, A., Caccamise, D., Heck, J., Kendrick, E., Ahlgren, K., Raleigh, D., Smalley Jr., R., and Vergani, G. (2016). Isolating active orogenic wedge deformation in the southern Subandes of Bolivia. *Journal of Geophysical Research: Solid Earth*, 121(8):6192–6218. Publisher: John Wiley & Sons, Ltd.

Wells, D. L. and Coppersmith, K. J. (1994). New empirical relationships among magnitude, rupture length, rupture width, rupture area, and surface displacement. *Bulletin of the Seismological Society of America*, 84(4):974–1002.

White, S. M., Trenkamp, R., and Kellogg, J. N. (2003). Recent crustal deformation and the earthquake cycle along the Ecuador–Colombia subduction zone. *Earth and Planetary Science Letters*, 216(3):231–242.

Williams, S. D. P. (2003a). The effect of coloured noise on the uncertainties of rates estimated from geodetic time series. *Journal of Geodesy*, 76(9):483–494.

Williams, S. D. P. (2003b). Offsets in global positioning system time series. *Journal of Geophysical Research: Solid Earth*, 108(B6).

Williams, S. D. P. (2008). CATS: GPS coordinate time series analysis software. *GPS Solutions*, 12(2):147–153.

Williams, S. D. P., Bock, Y., Fang, P., Jamason, P., Nikolaidis, R. M., Prawirodirdjo, L., Miller, M., and Johnson, D. J. (2004). Error analysis of continuous gps position time series. *Journal of Geophysical Research: Solid Earth*, 109(B3).

Winter, T., Avouac, J.-P., and Lavenu, A. (1993). Late Quaternary kinematics of the Pallatanga strike-slip fault (Central Ecuador) from topographic measurements of displaced morphological features. *Geophysical Journal International*, 115(3):905–920.

Witt, C., Bourgois, J., Michaud, F., Ordoñez, M., Jiménez, N., and Sosson, M. (2006). Development of the Gulf of Guayaquil (Ecuador) during the Quaternary as an effect of the North Andean block tectonic escape. *Tectonics*, 25(3). Publisher: John Wiley & Sons, Ltd.

Ye, L., Kanamori, H., Avouac, J.-P., Li, L., Cheung, K. F., and Lay, T. (2016). The 16 April 2016, MW7.8 (MS7.5) Ecuador earthquake: A quasi-repeat of the 1942 MS7.5 earthquake and partial re-rupture of the 1906 MS8.6 Colombia–Ecuador earthquake. *Earth and Planetary Science Letters*, 454:248 – 258.

Yepes, H., Audin, L., Alvarado, A., Beauval, C., Aguilar, J., Font, Y., and Cotton, F. (2016). A new view for the geodynamics of Ecuador: Implication in seismogenic source definition and seismic hazard assessment. *Tectonics*, 35(5):1249–1279. Publisher: John Wiley & Sons, Ltd.

Zhang, J., Bock, Y., Johnson, H., Fang, P., Williams, S., Genrich, J., Wdowinski, S., and Behr, J. (1997). Southern california permanent gps geodetic array: Error analysis of daily position estimates and site velocities. *Journal of Geophysical Research: Solid Earth*, 102(B8):18035–18055.

Zhang, T., Gordon, R. G., Mishra, J. K., and Wang, C. (2017). The Malpelo Plate Hypothesis and implications for nonclosure of the Cocos-Nazca-Pacific plate motion circuit. *Geophysical Research Letters*, 44(16):8213–8218. _eprint: https://agupubs.onlinelibrary.wiley.com/doi/pdf/10.1002/2017GL073704.

List of Figures

List of Tables